

# ИЗВЕСТИЯ ВЫСШИХ УЧЕБНЫХ ЗАВЕДЕНИЙ ЧЕРНАЯ МЕТАЛЛУРГИЯ

## IZVESTIYA. FERROUS METALLURGY

[fermet.misis.ru](http://fermet.misis.ru)

2024 Том 67 № 1  
Vol. No.

### МЕТАЛЛУРГИЧЕСКИЕ ТЕХНОЛОГИИ

Совместная переработка перовскитового и ильменитового концентратов. Сообщение 1

Механические свойства и микроструктура сплава Al-Mg (5052), обработанного методом равноканального углового прессования (РКУП) с вариациями методов РКУП и термической обработки

### МАТЕРИАЛОВЕДЕНИЕ

Исследование влияния водорода на стали в сероводородсодержащих и других средах на газовых объектах

### ИНФОРМАЦИОННЫЕ ТЕХНОЛОГИИ И АВТОМАТИЗАЦИЯ В ЧЕРНОЙ МЕТАЛЛУРГИИ

Математическое моделирование газодинамики и дожигания горючих компонентов над расплавом в плавильной печи-газификаторе

# ИЗВЕСТИЯ ВЫСШИХ УЧЕБНЫХ ЗАВЕДЕНИЙ ЧЕРНАЯ МЕТАЛЛУРГИЯ

Научно-технический журнал

Издается с января 1958 г. Выпускается 6 раз в год

2024 Том 67 № 1  
Vol. No.

# IZVESTIYA FERROUS METALLURGY

Scientific and Technical Journal

Published since January 1958. Issued 6 times a year

# IZVESTIYA FERROUS METALLURGY

www.fermet.misis.ru

ISSN 0368-0797 (Print) ISSN 2410-2091 (Online)

## Alternative title:

Izvestiya vuzov. Chernaya metallurgiya

## Founders:



## Editor-in-Chief:

**Leopol'd I. Leont'ev**, Academician, Adviser of the Russian Academy of Sciences; Dr. Sci. (Eng.), Prof., NUST "MISIS"; Chief Researcher, Institute of Metallurgy UB RAS, Moscow  
4 Leninskii Ave., Moscow 119049, Russian Federation  
National University of Science and Technology "MISIS"

## Deputy Editor-in-Chief:

**Evgenii V. Protopopov**, Dr. Sci. (Eng.), Prof., Siberian State Industrial University, Novokuznetsk

## Publisher:

National University of Science and Technology "MISIS"

## Editorial Office Address:

### in Moscow

4 Leninskii Ave., Moscow 119049, Russian Federation  
National University of Science and Technology "MISIS"  
Tel.: +7 (495) 638-44-11  
E-mail: fermet.misis@mail.ru, ferrous@sis.ru

### in Novokuznetsk

42 Kirova Str., Novokuznetsk, Kemerovo Region – Kuzbass  
654007, Russian Federation  
Siberian State Industrial University  
Tel.: +7 (3843) 74-86-28 E-mail: redjizvz@sibsiu.ru

## Editorial Board:

**Sailaubai O. Baisanov**, Dr. Sci. (Eng.), Prof., Abishev Chemical-Metallurgical Institute, Karaganda, Republic of Kazakhstan  
**Vladimir D. Belov**, Dr. Sci. (Eng.), Prof., NUST MISIS, Moscow  
**Anatolii A. Brodov**, Cand. Sci. (Econ.), Bardin Central Research Institute for Ferrous Metallurgy, Moscow  
**Il'ya V. Chumanov**, Dr. Sci. (Eng.), Prof., South Ural State Research University, Chelyabinsk  
**Andrei N. Dmitriev**, Dr. Sci. (Eng.), Prof., Academician, RANS, A.M. Prokhorov Academy of Engineering Sciences, Institute of Metallurgy, Ural Branch of RAS, Ural Federal University, Yekaterinburg  
**Aleksei V. Dub**, Dr. Sci. (Eng.), Prof., JSC "Science and Innovations", Moscow  
**Mikhail R. Filonov**, Dr. Sci. (Eng.), Prof., NUST MISIS, Moscow  
**Sergei M. Gorbatyuk**, Dr. Sci. (Eng.), Prof., NUST MISIS, Moscow  
**Konstantin V. Grigorovich**, Academician of RAS, Dr. Sci. (Eng.), Baikov Institute of Metallurgy and Materials Science of RAS, Moscow  
**Victor E. Gromov**, Dr. Sci. (Eng.), Prof., Siberian State Industrial University, Novokuznetsk  
**Aleksei G. Kolmakov**, Dr. Sci. (Eng.), Corresponding Member of RAS, Baikov Institute of Metallurgy and Materials Science of RAS, Moscow  
**Valerii M. Kolokol'tsev**, Dr. Sci. (Eng.), Prof., Magnitogorsk State Technical University, Magnitogorsk  
**Mariya V. Kostina**, Dr. Sci. (Eng.), Baikov Institute of Metallurgy and Materials Science of RAS, Moscow  
**Konstantin L. Kosyrev**, Dr. Sci. (Eng.), Academician of RANS, Electrosteel Heavy Engineering Works JSC, Moscow  
**Yuliya A. Kurganova**, Dr. Sci. (Eng.), Prof., Bauman Moscow State Technical University, Moscow  
**Linn Horst**, Linn High Therm GmbH, Hirschbach, Germany  
**Vladimir I. Lysak**, Academician of RAS, Dr. Sci. (Eng.), Prof., Rector, Volgograd State Technical University, Volgograd  
**Valerii P. Meshalkin**, Dr. Sci. (Eng.), Academician of RAS, Prof., D.I. Mendeleyev Russian Chemical-Technological University, Moscow  
**Radik R. Mulyukov**, Dr. Sci. (Phys.-Chem.), Prof., Corresponding Member of RAS, Institute of Metals Superplasticity Problems of RAS, Ufa

**Sergei A. Nikulin**, Dr. Sci. (Eng.), Prof., Corresponding Member of RANS, NUST MISIS, Moscow  
**Asylbek Kh. Nurumgaliev**, Dr. Sci. (Eng.), Prof., Karaganda State Industrial University, Karaganda, Republic of Kazakhstan  
**Oleg I. Ostrovski**, Dr. Sci. (Eng.), Prof., University of New South Wales, Sydney, Australia  
**Loris Pietrelli**, Dr., Scientist, Italian National Agency for New Technologies, Energy and Sustainable Economic Development, Rome, Italy  
**Igor' Yu. Pyshmintsev**, Dr. Sci. (Eng.), Russian Research Institute of the Pipe Industry, Chelyabinsk  
**Andrei I. Rudskoi**, Academician of RAS, Dr. Sci. (Eng.), Prof., Rector, Peter the Great Saint-Petersburg Polytechnic University, Saint-Petersburg  
**Oleg Yu. Sheshukov**, Dr. Sci. (Eng.), Prof., Ural Federal University, Yekaterinburg  
**Laura M. Simonyan**, Dr. Sci. (Eng.), Prof., NUST MISIS, Moscow  
**Robert F. Singer**, Dr. Sci. (Eng.), Prof., Friedrich-Alexander University, Germany  
**Boris A. Sivak**, Cand. Sci. (Eng.), Prof., VNIIMETMASH Holding Company, Moscow  
**Leonid A. Smirnov**, Dr. Sci. (Eng.), Prof., Academician of RAS, OJSC "Ural Institute of Metals", Yekaterinburg  
**Sergei V. Solodov**, Cand. Sci. (Eng.), NUST MISIS, Moscow  
**Speidel Marcus**, Dr. Natur. Sci., Prof., Swiss Academy of Materials, Switzerland  
**Nikolai A. Spirin**, Dr. Sci. (Eng.), Prof., Ural Federal University, Yekaterinburg  
**Tang Guoi**, Institute of Advanced Materials of Tsinghua University, Shenzhen, China  
**Mikhail V. Temlyantsev**, Dr. Sci. (Eng.), Prof., Siberian State Industrial University, Novokuznetsk  
**Ekaterina P. Volynkina**, Dr. Sci. (Eng.), Advisor, ALE "Kuzbass Association of Waste Processors", Novokuznetsk  
**Aleksei B. Yur'ev**, Dr. Sci. (Eng.), Rector, Siberian State Industrial University, Novokuznetsk  
**Vladimir S. Yusupov**, Dr. Sci. (Eng.), Prof., Baikov Institute of Metallurgy and Materials Science of RAS, Moscow  
**Vladimir I. Zhuchkov**, Dr. Sci. (Eng.), Prof., Institute of Metallurgy, Ural Branch of RAS, Ural Federal University, Yekaterinburg  
**Michael Zinigrad**, Dr. Sci. (Physical Chemistry), Prof., Rector, Ariel University, Israel  
**Vladimir I. Zolotukhin**, Dr. Sci. (Eng.), Prof., Tula State University, Tula

*In accordance with paragraph 5 of the Rules for the formation of the Higher Attestation Commission list journal "Izvestiya. Ferrous metallurgy" is included in the list of leading peer-reviewed scientific journals, publication in which is taken into account in the defense of candidate and doctoral dissertations, as indexed in international data bases.*

**Indexed:** Scopus, Russian Science Citation Index (RSCI), Research Bible, Chemical Abstracts, OCLC and Google Scholar  
Registered in Federal Service for Supervision in the Sphere of Mass Communications **PI number FS77-35456.**



Articles are available under Creative Commons Attribution 4.0 License.

# ИЗВЕСТИЯ ВЫСШИХ УЧЕБНЫХ ЗАВЕДЕНИЙ ЧЕРНАЯ МЕТАЛЛУРГИЯ

www.fermet.misis.ru

ISSN 0368-0797 (Print) ISSN 2410-2091 (Online)

## Варианты названия:

Известия вузов. Черная металлургия

Izvestiya. Ferrous Metallurgy

## Учредители:



## Редакционная коллегия:

**С. О. Байсанов**, д.т.н., профессор, ХМИ им. Ж.Абишева, г. Караганда, Республика Казахстан

**В. Д. Белов**, д.т.н., профессор, НИТУ МИСИС, г. Москва

**А. А. Бродов**, к.экон.н., ФГУП «ЦНИИчермет им. И.П. Бардина», г. Москва

**Е. П. Волынкина**, д.т.н., советник, ОЮЛ «Кузбасская Ассоциация переработчиков отходов», г. Новокузнецк

**С. М. Горбатько**, д.т.н., профессор, НИТУ МИСИС, г. Москва

**К. В. Григорович**, академик РАН, д.т.н., ИМЕТ им. А.А. Байкова РАН, г. Москва

**В. Е. Громов**, д.ф.-м.н., профессор, СибГИУ, г. Новокузнецк

**А. Н. Дмитриев**, д.т.н., профессор, академик РАЕН, академик АИН РФ, г. Екатеринбург

**А. В. Дуб**, д.т.н., профессор, ЗАО «Наука и инновации», г. Москва

**В. И. Жучков**, д.т.н., профессор, ИМЕТ УрО РАН, г. Екатеринбург

**Р. Ф. Зингер**, д.т.н., профессор, Институт Фридриха-Александра, Германия

**М. Зиниград**, д.т.н., профессор, Институт Ариэля, Израиль

**В. И. Золотухин**, д.т.н., профессор, ТулГУ, г. Тула

**А. Г. Колмаков**, д.т.н., чл.-корр. РАН, ИМЕТ им. А.А. Байкова РАН, г. Москва

**В. М. Колокольцев**, д.т.н., профессор, МГТУ им. Г.И. Носова, г. Магнитогорск

**М. В. Костина**, д.т.н., ИМЕТ им. А.А. Байкова РАН, г. Москва

**К. Л. Косырев**, д.т.н., академик РАЕН, ОАО «Электростальский завод тяжелого машиностроения», г. Москва

**Ю. А. Курганова**, д.т.н., профессор, МГТУ им. Н.Э. Баумана, г. Москва

**Х. Линн**, ООО «Линн Хай Терм», Германия

**В. И. Лысак**, академик РАН, д.т.н., профессор, ВолгГТУ, г. Волгоград

**В. П. Мешалкин**, академик РАН, д.т.н., профессор, РХТУ им. Д.И. Менделеева, г. Москва

В соответствии п. 5 Правил формирования перечня ВАК журнал «Известия вузов. Черная металлургия» входит в перечень ведущих рецензируемых научных журналов и изданий, публикация в которых учитывается при защитах кандидатских и докторских диссертаций как индексируемый в МБД.

## Главный редактор:

**Леопольд Игоревич Леонтьев**, академик РАН, советник, Президиум РАН; д.т.н., профессор, НИТУ «МИСИС»; главный научный сотрудник, Институт металлургии УрО РАН  
Россия, 119049, Москва, Ленинский просп., д. 4, стр. 1, Национальный исследовательский технологический университет «МИСИС»

## Заместитель главного редактора:

**Евгений Валентинович Протопопов**, д.т.н., профессор, Сибирский государственный индустриальный университет г. Новокузнецк

## Издатель:

Национальный исследовательский технологический университет «МИСИС»

## Адреса подразделений редакций:

### в Москве

Россия, 119049, Москва, Ленинский просп., д. 4, стр. 1  
Национальный исследовательский технологический университет «МИСИС»

Тел.: +7 (495) 638-44-11 E-mail: ferrous@sisis.ru

### в Новокузнецке

Россия, 654007, Новокузнецк,  
Кемеровская обл. – Кузбасс, ул. Кирова, зд. 42  
Сибирский государственный индустриальный университет  
Тел.: +7 (3843) 74-86-28 E-mail: redjizvz@sibsiu.ru

**Р. Р. Мулюков**, д.ф.м.-н., профессор, чл.-корр. ФГБУН ИПСМ РАН, г. Уфа  
**С. А. Никулин**, д.т.н., профессор, чл.-корр. РАЕН, НИТУ МИСИС, г. Москва  
**А. Х. Нурумгалиев**, д.т.н., профессор, КГИУ, г. Караганда, Республика Казахстан  
**О. И. Островский**, д.т.н., профессор, Университет Нового Южного Уэльса, Сидней, Австралия  
**Л. Пиетрелли**, д.т.н., Итальянское национальное агентство по новым технологиям, энергетике и устойчивому экономическому развитию, Рим, Италия  
**И. Ю. Пышминцев**, д.т.н., РосНИТИ, г. Челябинск  
**А. И. Рудской**, академик РАН, д.т.н., профессор, СПбПУ Петра Великого, г. Санкт-Петербург  
**Б. А. Сивак**, к.т.н., профессор, АО АХК «ВНИИМЕТМАШ», г. Москва  
**Л. М. Симонян**, д.т.н., профессор, НИТУ МИСИС, г. Москва  
**Л. А. Смирнов**, академик РАН, д.т.н., профессор, ОАО «Уральский институт металлов», г. Екатеринбург  
**С. В. Солодов**, к.т.н., НИТУ МИСИС, г. Москва  
**Н. А. Спирин**, д.т.н., профессор, УрФУ, г. Екатеринбург  
**Г. Танг**, Институт перспективных материалов университета Циньхуа, г. Шеньжень, Китай  
**М. В. Темлянецев**, д.т.н., профессор, СибГИУ, г. Новокузнецк  
**М. Р. Филонов**, д.т.н., профессор, НИТУ МИСИС, г. Москва  
**И. В. Чуманов**, д.т.н., профессор, ЮУрГУ, г. Челябинск  
**О. Ю. Шешуков**, д.т.н., профессор УрФУ, г. Екатеринбург  
**М. О. Шпайдель**, д.ест.н., профессор, Швейцарская академия материаловедения, Швейцария  
**А. Б. Юрьев**, д.т.н., ректор, СибГИУ, г. Новокузнецк  
**В. С. Юсупов**, д.т.н., профессор, ИМЕТ им. А.А. Байкова РАН, г. Москва

**Индексирование:** Scopus, Russian Science Citation Index (RSCI), Research Bible, Chemical Abstracts, OCLC и Google Scholar

Зарегистрирован Федеральной службой по надзору в сфере связи и массовых коммуникаций ПИ № ФС77-35456.



Статьи доступны под лицензией Creative Commons Attribution 4.0 License.



CONTENTS

СОДЕРЖАНИЕ

METALLURGICAL TECHNOLOGIES

- Vityaz' P.A., Zalesskii V.G., Pokrovskii A.I. Features of iron foundry production in Belarus and its prospects ..... 8
- Pavlovets V.M. Possibilities of heat-power spraying of wet charge during formation of structural properties of agglomerated iron ore materials ..... 19
- Fedorov S.A., Udоеva L.Yu., Pikulin K.V., Vusikhis A.S., Cherepanova L.A. Joint processing of perovskite and ilmenite concentrates. Part 1. Chemical-mineralogical (material) characteristics of perovskite and ilmenite concentrates ..... 27
- Puspasari V., Astawa I.N.G.P., Herbirowo S., Mabruuri E. Mechanical properties and microstructure of Al–Mg (5052) alloy processed by equal-channel angular pressing (ECAP) with variation of ECAP routes and heat treatment ..... 37

MATERIALS SCIENCE

- Gromov V.E., Konovalov S.V., Efimov M.O., Panchenko I.A., Chen X. Improvement of the Cantor alloy's mechanical properties by alloying with niobium and zirconium ..... 47
- Kantyukov R.R., Zapevalov D.N., Vagapov R.K. Effect of hydrogen on steels in hydrogen sulfide-containing and other environments at gas facilities ..... 53
- Kabaldin Yu.G., Chernigin M.A. Structure and its defects in additive manufacturing of stainless steels by laser melting and electric arc surfacing ..... 65

PHYSICO-CHEMICAL BASICS  
OF METALLURGICAL PROCESSES

- Adilov G., Kareva N.T., Roshchin V.E. Influence of copper and silicon on phase transformations in the iron–carbon system ..... 73

INNOVATIONS IN METALLURGICAL  
INDUSTRIAL AND LABORATORY  
EQUIPMENT, TECHNOLOGIES  
AND MATERIALS

- Leont'ev A.S., Rybenko I.A. Experience in implementing machine learning to calculate the quality and production of agglomerate ..... 76

МЕТАЛЛУРГИЧЕСКИЕ ТЕХНОЛОГИИ

- Витязь П.А., Залесский В.Г., Покровский А.И. Особенности чугунолитейного производства Беларуси и его перспективы ..... 8
- Павловец В.М. Возможности теплосилового напыления влажной шихты в процессе формирования структурных свойств окучкованных железорудных материалов ..... 19
- Федоров С.А., Удоева Л.Ю., Пикулин К.В., Вусихис А.С., Черепанова Л.А. Совместная переработка перовскитового и ильменитового концентратов. Сообщение 1. Химико-минералогическая (вещественная) характеристика перовскитового и ильменитового концентратов ..... 27
- Пуспасари В., Астава И.Н.Г.П., Хербирово С., Мабрури Э. Механические свойства и микроструктура сплава Al–Mg (5052), обработанного методом равноканального углового прессования (РКУП) с вариациями методов РКУП и термической обработки ..... 37

МАТЕРИАЛОВЕДЕНИЕ

- Громов В.Е., Коновалов С.В., Ефимов М.О., Панченко И.А., Чень С. Улучшение механических свойств сплава Кантора легированием ниобием и цирконием ..... 47
- Кантюков Р.Р., Запеевалов Д.Н., Вагапов Р.К. Исследование влияния водорода на стали в сероводородсодержащих и других средах на газовых объектах ..... 53
- Кабалдин Ю.Г., Чернигин М.А. Структура и ее дефекты при аддитивном выращивании нержавеющей сталей методами лазерного спекания и электродуговой наплавки ..... 65

ФИЗИКО-ХИМИЧЕСКИЕ ОСНОВЫ  
МЕТАЛЛУРГИЧЕСКИХ ПРОЦЕССОВ

- Адилев Г., Карева Н.Т., Рошин В.Е. Влияние меди и кремния на фазовые превращения в системе железо–углерод ..... 73

ИННОВАЦИИ В МЕТАЛЛУРГИЧЕСКОМ  
ПРОМЫШЛЕННОМ И ЛАБОРАТОРНОМ  
ОБОРУДОВАНИИ, ТЕХНОЛОГИЯХ  
И МАТЕРИАЛАХ

- Леонтьев А.С., Рыбенко И.А. Опыт внедрения машинного обучения для расчета качества и производства агломерата ..... 76

CONTENTS (Continuation)

СОДЕРЖАНИЕ (продолжение)

BASED ON THE MATERIALS  
OF THE INTERNATIONAL CONFERENCE  
“SCIENTIFIC AND PRACTICAL SCHOOL FOR  
YOUNG METALLURGISTS”

Salynova M.A., Uglunts T.V., Tolochko O.V. Effect of yttrium additions on microstructure and corrosion resistance of Incoloy 825 alloy ..... 83

INFORMATION TECHNOLOGIES  
AND AUTOMATIC CONTROL  
IN FERROUS METALLURGY

Ryabchikov M.Yu., Ryabchikova E.S., Novak V.S., Klimenko A.E. Investigation of performance limitations in continuous hot-dip galvanizing units associated with product defects ..... 89

Panasenko O.A., Khalezov A.O., Nukhov D.Sh. Investigating the effectiveness of changing calibration of input cone of rolls and lines of a piercing mill with tapered rolls using computer modeling ..... 106

Erokhov T.V., Levitskii I.A., Podgorodetskii G.S., Gorbunov V.B. Mathematical modeling of gas dynamics and off-gas post-combustion above the melt in a melter-gasifier furnace ..... 112

Shper V.L., Sheremet'yeva S.A., Smelov V.Yu., Khunuzidi E.I. Shewhart control charts – A simple but not easy tool for data analysis ..... 121

ПО МАТЕРИАЛАМ  
МЕЖДУНАРОДНОЙ КОНФЕРЕНЦИИ  
«НАУЧНО-ПРАКТИЧЕСКАЯ ШКОЛА  
ДЛЯ МОЛОДЫХ МЕТАЛЛУРГОВ»

Салынова М.А., Углунц Т.В., Толочко О.В. Оценка влияния добавок иттрия на микроструктуру и коррозионную стойкость сплава Incoloy 825 ..... 83

ИНФОРМАЦИОННЫЕ ТЕХНОЛОГИИ  
И АВТОМАТИЗАЦИЯ  
В ЧЕРНОЙ МЕТАЛЛУРГИИ

Рябчиков М.Ю., Рябчикова Е.С., Новак В.С., Клименко А.Е. Изучение ограничений производительности агрегатов непрерывного горячего оцинкования, связанных с дефектами продукции ..... 89

Панасенко О.А., Халезов А.О., Нухов Д.Ш. Исследование эффективности изменения калибровки входного конуса валков и линеек прошивного стана с грибовидными валками с помощью компьютерного моделирования ..... 106

Ерохов Т.В., Левицкий И.А., Подгородецкий Г.С., Горбунов В.Б. Математическое моделирование газодинамики и дожигания горючих компонентов над расплавом в плавильной печи-газификаторе ..... 112

Шпер В.Л., Шереметьева С.А., Смелов В.Ю., Хунузиди Е.И. Контрольные карты Шухарта – простой, но не лёгкий для применения инструмент анализа данных ..... 121



UDC 669.16:621.746

DOI 10.17073/0368-0797-2024-1-8-18



Review article

Обзорная статья

## FEATURES OF IRON FOUNDRY PRODUCTION IN BELARUS AND ITS PROSPECTS

P. A. Vityaz'<sup>1</sup>, V. G. Zaleskii<sup>2</sup>, A. I. Pokrovskii<sup>2</sup>

<sup>1</sup> Presidium of the National Academy of Sciences of Belarus (66 Nezavisimosti Ave., Minsk 220072, Republic of Belarus)

<sup>2</sup> Physico-Technical Institute, Belarus National Academy of Sciences (10 Kuprevicha Str., Minsk 220141, Republic of Belarus)

art@phti.by

**Abstract.** A historical overview of the development of iron foundry production in the world is presented. The modern level of the material structure in iron casting has an outstripping growth of ductile cast iron grades. The paper describes the features of iron foundry production in Belarus. Technologies and equipment are significantly inferior to foreign ones in terms of productivity and specific resource costs per unit of product. The specific character of Belarus lies in the still widespread use of cupolas, molds from sand-clay mixtures, predominant use of gray cast iron, and small volumes of ductile cast iron production. The total capacity of all foundries is 557.5 thousand tons of casting per year, but the peculiarity is that only about 250 thousand tons per year are actually produced. Development and implementation of the “Program for the Development of Foundry Industries of the Republic of Belarus for years 2017–2030” made it possible to ensure more efficient operation of the foundry industry in the country. In the near future Belorussian foundry industry will reproduce the global trend for critical casting products: transfer to ductile cast iron instead of gray one and further transition to ausferritic (bainitic) cast iron instead of rolled steel.

**Keywords:** casting, gray cast iron, ductile cast iron, bainitic cast iron, ausferritic cast iron

**Acknowledgements:** The work was performed at the Physico-Technical Institute of the National Academy of Sciences of Belarus within the framework of the State Scientific Research Program “Metallurgy”, task No. 2.01.

**For citation:** Vityaz' P.A., Zaleskii V.G., Pokrovskii A.I. Features of iron foundry production in Belarus and its prospects. *Izvestiya. Ferrous Metallurgy*. 2024;67(1):8–18. <https://doi.org/10.17073/0368-0797-2024-1-8-18>

## ОСОБЕННОСТИ ЧУГУНОЛИТЕЙНОГО ПРОИЗВОДСТВА БЕЛАРУСИ И ЕГО ПЕРСПЕКТИВЫ

П. А. Витязь<sup>1</sup>, В. Г. Залесский<sup>2</sup>, А. И. Покровский<sup>2</sup>

<sup>1</sup> Президиум Национальной академии наук Беларуси (Республика Беларусь, 220072, Минск, пр-т Независимости, 66)

<sup>2</sup> Физико-технический институт НАН Беларуси (Республика Беларусь, 220141, Минск, ул. Купревича, 10)

art@phti.by

**Аннотация.** Представлен исторический обзор развития чугунолитейного производства в мире. Рассмотрен современный уровень материальной структуры литья чугунов, в котором наблюдается опережающий рост марок высокопрочных чугунов. Описаны особенности чугунолитейного производства Беларуси. Показано, что технологии и оборудование значительно уступают зарубежным по производительности и удельным затратам ресурсов на единицу изделия. Специфика Беларуси заключается во все еще широком применении вагранок, форм из песчано-глинистых смесей, преобладающем использовании серого чугуна, небольших объемах выплавки высокопрочного чугуна. Суммарные мощности всех литейных производств составляют 557,5 тыс. т литья в год, но особенностью является то, что фактически отливается только около 250 тыс. т в год. Разработка и введение в действие «Программы развития литейных производств Республики Беларусь на 2017 – 2030 гг.» позволили обеспечить более эффективную деятельность литейной отрасли республики. Показано, что в Беларуси в ближайшее время произойдет повторение мировой тенденции перехода ответственных изделий на отливки из высокопрочного чугуна взамен серого и дальнейший переход на аусферритный (бейнитный) чугун взамен стального проката.

**Ключевые слова:** литье, серый чугун, высокопрочный чугун, бейнитный чугун, аусферритный чугун

**Благодарности:** Работа выполнена в Физико-техническом институте НАН Беларуси в рамках ГПНИ «Металлургия», задание № 2.01.

**Для цитирования:** Витязь П.А., Залесский В.Г., Покровский А.И. Особенности чугунолитейного производства Беларуси и его перспективы. *Известия вузов. Черная металлургия*. 2024;67(1):8–18. <https://doi.org/10.17073/0368-0797-2024-1-8-18>

## INTRODUCTION

Cast irons, or high-carbon iron alloys, have been acknowledged and extensively utilized since the initial millennium BC.

It is widely held among scholars that the Russian phrase “cast iron” is derived from the Chinese words “zhu” (meaning “to cast (metal)”) and “gong” (meaning “work”). The advent of iron smelting technology in China is purported to trace back to the 5<sup>th</sup> to 3<sup>rd</sup> centuries BC. This process involved the use of ball iron and charcoal, with smelting occurring at temperatures exceeding 1200 °C over several days. Subsequently, Chinese metallurgists developed a specialized furnace for melting cast iron from either highly phosphoric iron ore or ball iron, known as the “Chinese” cupola. This furnace essentially functioned as a 1 m tall chimney, equipped with a forced-air system to enhance air flow.

China excelled in producing intricate castings from cast iron. A noteworthy example is the lion statue (Fig. 1)



**Fig. 1.** 44-ton solid cast iron casting of a lion made in 954 in China

**Рис. 1.** Цельнолитая чугунная отливка льва весом 44 т, изготовленная в 954 г. в Китае



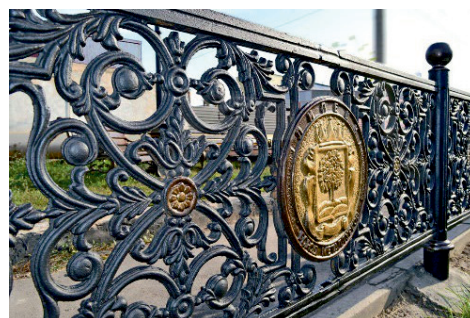
**Fig. 2.** The first cast iron bridge built in 1779 in England across Severn river

**Рис. 2.** Первый чугунный мост, построенный в 1779 г. в Англии через реку Северн

believed to have been cast in 954 and placed in the Jiangzhou district of Chongzuo Township, Guangxi Zhuang Autonomous Region. The dimensions of this casting, which is over a millennium old, continue to astonish metallurgists today. Replicating the statue presents a formidable challenge for many contemporary foundries (the sculpture measures 5.4 m in length, 3 m in width, 5.4 m in height, weighs 44 tons, and has wall thicknesses ranging from 4 to 20 cm). The figure was created using a life-sized clay model. Experts suggest that it was a single-piece casting, likely achieved by melting metal in multiple cupolas simultaneously, which then flowed through channels into one mold.

The earliest instances of cast-iron objects in Europe date back to the 14<sup>th</sup> century. The late 15<sup>th</sup> century saw the emergence of the first bloomery furnaces in Italy, the Netherlands, and Belgium. Fig. 2 illustrates the first cast-iron bridge, constructed in 1779 in England, spanning the River Severn.

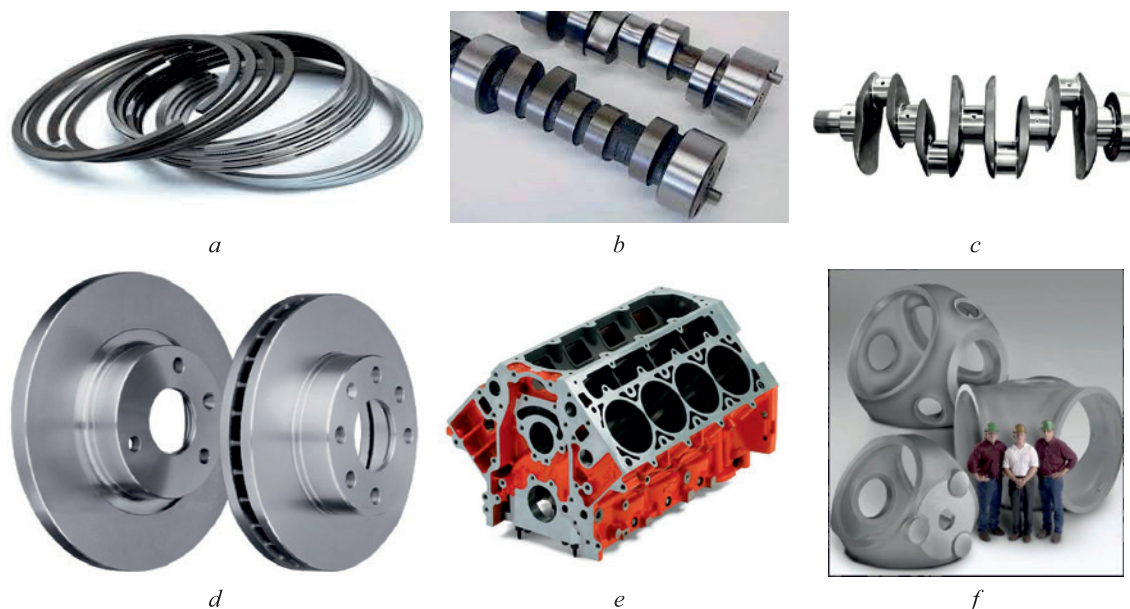
The production of cast iron in Russia commenced in the 16<sup>th</sup> century, with Russian artistic iron casting gaining widespread acclaim (Fig. 3).



**Fig. 3.** Examples of artistic castings

**Рис. 3.** Примеры художественного литья





**Fig. 4.** Examples of typical engineering parts made from cast iron:  
piston rings (a); camshafts (b); crankshaft (c); brake discs (d); cylinder block housing (e);  
cases of modern wind power plant (f)

**Рис. 4.** Примеры типовых машиностроительных деталей из чугуна:  
поршневые кольца (a); распределительные валы (b); коленчатый вал (c); тормозные диски (d);  
корпуса блока цилиндров (e); корпуса современной ветряной электростанции (f)

Into the 21<sup>st</sup> century, cast iron maintains its status as a primary and highly favored structural material [1]. Fig. 4 displays several examples of common mechanical engineering components made from cast iron, ranging from small piston rings to large casings for modern wind turbines.

This chart suggests a trend where environmentally harmful foundry operations are gradually relocating from advanced and wealthy nations to less developed ones. Japan's journey from being the third-largest producer of castings in the world during the 1970s to relocating its production to India, China, and Taiwan in more recent years exemplifies this trend.

#### CURRENT GLOBAL CASTING INDUSTRY:

##### A CONCISE SUMMARY

The World Foundry Organization [2] monitors casting activities globally, and Modern Casting magazine publishes comprehensive overviews. It's essential to recognize that statistical reports are subject to delays, meaning the most recent data might be one or sometimes two years old.

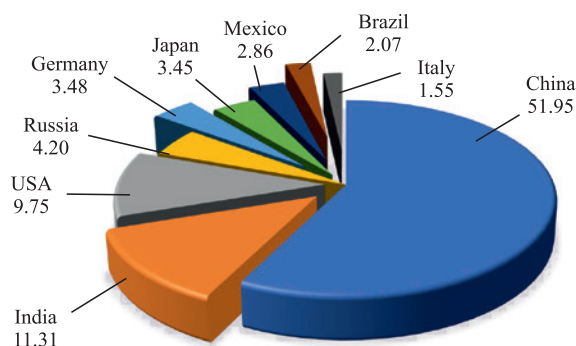
In 2018, the world experienced its peak in castings production, surpassing an impressive 112.7 million tons [3]. Recent years have seen a slight decrease in production, with figures showing a 4 – 6 % drop (109.1 million tons in 2019 compared to 105.5 million tons in 2020). Current data indicate that the global output for all casting grades consistently exceeds 100 million tons [4].

The distribution of casting output across various metallic materials in the top ten advanced countries for the year 2020 [3] reveals China as the leading nation, contributing more than half of the world's casting tonnage, followed by India and the USA, with Russia, Germany, Japan, Mexico, Brazil, and Italy (Fig. 5).

#### STATE OF GLOBAL IRON CASTING:

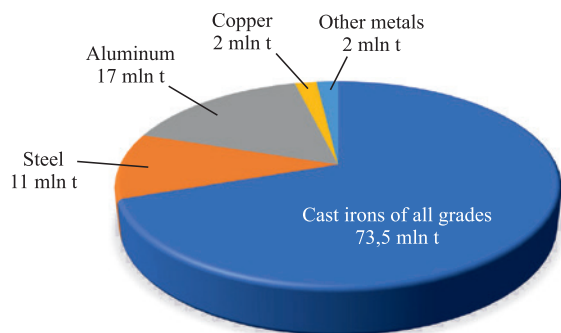
##### A CONTEMPORARY ANALYSIS

Within the material composition of all castings, cast iron notably surpasses all other casting materials, con-



**Fig. 5.** Distribution of casting output of all materials in ten most advanced countries of the world for 2020 [3]

**Рис. 5.** Распределение выпуска литья всех материалов по десяти наиболее передовым странам мира за 2020 г. [3]



**Fig. 6.** Structure of world production of castings by the type of material for 2020 [5]

**Рис. 6.** Структура мирового производства отливок по видам материалов за 2020 г. (по данным журнала Modern Casting [5])

stituting over 70 % of the total production. Following cast iron, aluminum castings hold the second spot in output volume, and steel castings are in the third position on a global scale (Fig. 6).

#### INCREASING PREVALENCE OF HIGH-QUALITY AND DUCTILE IRON OVER GRAY CAST IRON

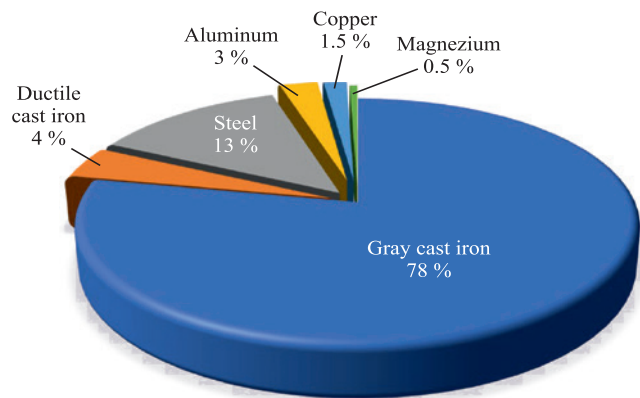
The shift in production from gray cast iron (GI) to ductile cast iron (DI) became prominent around the late 1970s and early 1980s. This transition was significantly influenced by the discovery made by Keith Dwight Millis. On May 7, 1948, Millis presented his groundbreaking work at a convention of American foundrymen. He demonstrated that the introduction of small quantities of magnesium into molten iron during casting resulted in the formation of spherical graphite inclusions within the iron. This change in the microstructure leads to a marked improvement in the strength properties of the material, potentially doubling its toughness. K. Millis' patent [5] marked the beginning of the ductile cast iron age.

Fig. 7 reveals significant shifts in the composition of materials used for castings internationally across five decades, from 1996 to 2016.

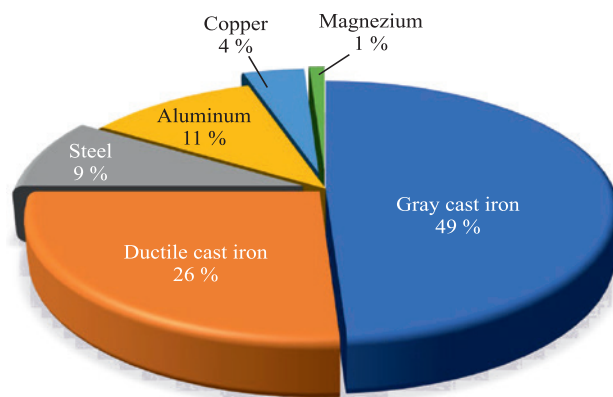
The data illustrated in these diagrams indicates a slight decrease in steel castings production, contrasted with a significant rise in the production of DI castings. Currently, ductile iron castings comprise more than 25 % of all global castings (Fig. 7, *b*), with the increase largely owing to the enhanced durability of certain cast iron grades.

Furthermore, the trend line in Fig. 8 affirms that, despite various global economic challenges, the production of DI has shown a remarkably stable increase over the recent years [6].

This graph serves as a crucial visual aid for metallurgists, enabling the prediction of an increased demand for ductile iron in the forthcoming years.



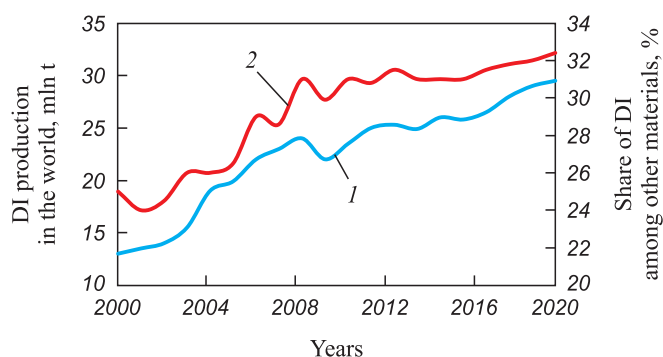
*a*



*b*

**Fig. 7.** Comparison of material structure of the world casting production with an interval of 50 years [6]: in 1996 (*a*) and in 2016 (*b*)

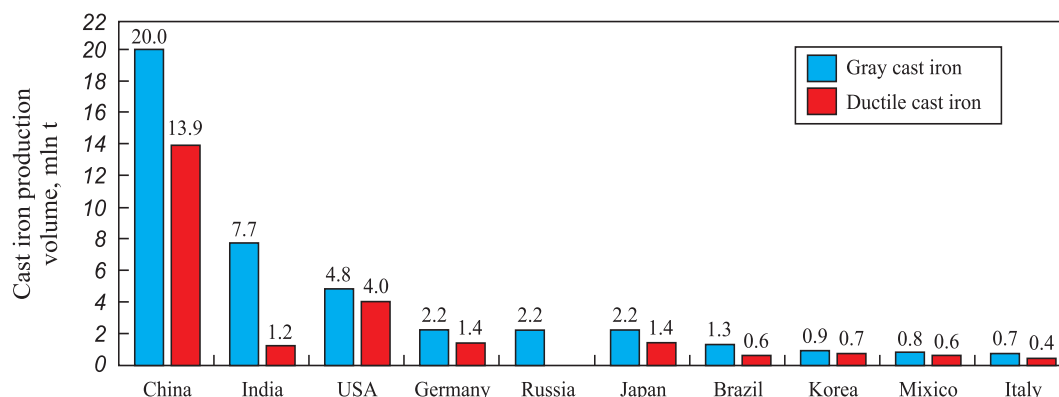
**Рис. 7.** Сравнение материальной структуры мирового производства отливок с интервалом в 50 лет [6]: в 1996 г. (*a*) и в 2016 г. (*b*)



**Fig. 8.** Dynamics of world production of ductile iron in natural (million tons) (*1*) and percentage (*2*) terms (share of all other cast materials) in recent years [5]

**Рис. 8.** Динамика мирового производства высокопрочного чугуна в натуральном (млн т) (*1*) и процентном (*2*) выражении (доля от всех других литых материалов) за последние годы [7]

Fig. 9 illustrates the production ratio between GI and DI in ten of the leading countries in this industry globally.



**Fig. 9.** Ratio of production of gray cast and ductile iron for ten most advanced countries in the world for 2019 [7].  
Russia provided summary data without separating gray and ductile irons

**Рис. 9.** Соотношение производства серого и высокопрочного чугуна по десяти наиболее передовым странам мира (данные Modern Casting за 2019 г. [7]). Россия предоставила суммарные данные, не разделяя СЧ и ВЧ

In numerous nations, the output of DI constitutes at least half of the production of GI. Notably, in several developed countries, the production of DI surpasses that of GI by a substantial margin. For example, in 2019 Austria's production of DI reached 104,700 tons, dwarfing its GI output of 42,300 tons, while Spain manufactured 663,000 tons of DI compared to 362,600 tons of GI.

This trend indicates a renaissance for cast irons, as their use pivots to high-loaded components within crucial technical sectors such as the automotive industry, railroad, pipeline transport, machine tool production, and shipbuilding. Cast irons are no longer confined to traditional applications like cylinder blocks, piston rings, crankshafts, and camshafts. Recent advancements have broadened their applications, including parts once deemed unsuitable for ductile iron. Internationally, companies such as Ford and Chrysler utilize DI in heavy trucks' final drive pinions, Zanardi uses it in railway coach suspension parts, and it's a choice material for soil cultivation implements, among others. Interestingly, due to its superior workability and robust strength characteristics, cast material is starting to replace alloyed steel rolled products that undergo multiple metallurgical processes, a shift particularly noticeable in the leading sectors of mechanical engineering.

#### ANALYSIS OF THE CAST IRON INDUSTRY IN BELARUS

During the era of the Soviet Union, Belarus was often referred to as the country's "assembly shop" due to its highly developed manufacturing sector, particularly in blank production and the foundry industry. In the 1980s, Belarus's annual output exceeded 1 million tons of various types of castings, with iron castings making up approximately 700,000 tons of this total. In 1985, the per capita production of castings in Belarus was 100 kg, ranking the country third in the world at that time based on this metric.

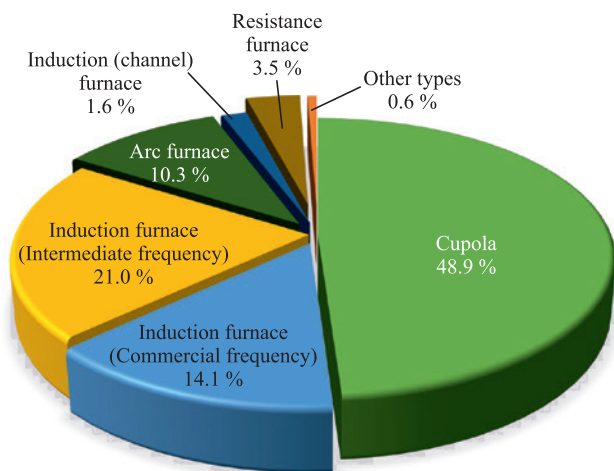
At present, the output of castings in Belarus has diminished to a quarter of what it was during its peak production years. In 2018, the country's total casting production was just 250,000 tons.

Several characteristics define the current state of the iron foundry industry in Belarus:

- the technologies and equipment in Belarusian foundries are generally less productive and more resource-intensive per product unit compared to those abroad;
- over half of the iron castings are made using mechanized casting conveyors that are equipped with outdated machinery;
- the capital assets are extensively worn and outdated, with a low rate of renewal (2 – 3 %), and the furnace fleet is antiquated;
- foundry operations consume a high amount of energy;
- there is a minimal inflow of direct investment and technology;
- the foundries are not operating at full capacity; they currently produce 250,000 tons of castings, yet have the capacity to produce 557,500 tons;
- the capacity at Belarusian foundries allows for the production of 345,700 tons of gray iron castings and 73,100 tons of ductile iron castings annually.

The majority of GI and DI castings are produced at key plants such as:

- OJSC "Minsk Tractor Works";
- OJSC "Minsk Automobile Plant" – Managing Company of "Belavtomaz" Holding;
- OJSC "Centrolite" Gomel Foundry";
- OJSC "Gomel plant of casting and normals";
- OJSC "Mogilevliftmash" – Managing Company of the Holding";



**Fig. 10.** Distribution of castings in Belarus according to the smelting method

**Рис. 10.** Распределение литья в Беларуси по методу плавки

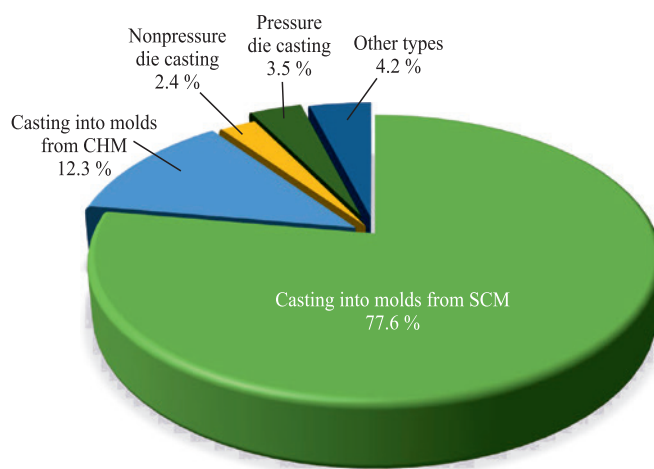
– OJSC “Managing Company of the Holding, Minsk Motor Plant”, Stowbtsy.

The remainder of the cast iron production, accounting for about 25 %, comes from other enterprises in the country.

Fig. 10’s diagram detailing the distribution of casting methods indicates that cupolas, comprising half of the foundry furnace fleet in Belarus, are incapable of producing high-grade cast iron and are significant contributors to dust and gas emissions. The other half of the furnace infrastructure consists of induction furnaces, which are subdivided almost equally among commercial frequency, intermediate frequency, and channel furnaces.

Yet, modern intermediate frequency induction furnaces have been adopted by several enterprises within Belarus, including: CJSC “Altant” subsidiary – Baranovich Machine-Tool Plant, OJSC “Minsk Tractor Works”, “Minsk Automobile Plant” – Managing Company of “Belavtomaz” Holding, OJSC “Gomel plant of casting and normals”, OJSC “Centrolite” Gomel Foundry”, OJSC “BELAZ” – Managing Company “BELAZ-HOLDING”, OJSC “Lida Foundry and Mechanical Plant” and OJSC “Managing Company of the Holding “Minsk Motor Plant”.

The analysis of casting distribution by molding methods (Fig. 11) reveals that approximately 78 % of molds are fashioned from sand-clay mixtures. This method is prevalent due to the low cost of raw materials. However, it has significant disadvantages, including high energy consumption, the cost per ton of castings, and less precise casting surfaces. Castings produced in cold-hardening mixtures (CHM) molds constitute about 12 % and offer cleaner surfaces and more accurate geometric dimensions. Despite this advantage, the preparation of these



**Fig. 11.** Distribution of casting in Belarus by forming methods

**Рис. 11.** Распределение литья в Беларуси по методам формообразования

mixtures often involves technologies and equipment that fall short of contemporary standards for molding and core sand mixtures.

Currently, around 10 vortex-type mixers are operational within Belarus, notably at enterprises such as OJSC “Minsk Automobile Plant” – Managing Company of “Belavtomaz” Holding and OJSC “Centrolite” Gomel Foundry”. These mixers have significantly optimized energy usage, cutting it by 1.5 times per ton of mixture, and reduced the need for binding components by 15 – 20 %.

The Belarusian foundry industry has also embraced other technological advancements:

– automatic molding lines are in use at several facilities, including OJSC “Minsk Tractor Works”, OJSC “Gomel plant of casting and normals”, CJSC “Altant” subsidiary – “Baranovich Machine-Tool Plant”, and OJSC “Centrolite” Gomel Foundry”;

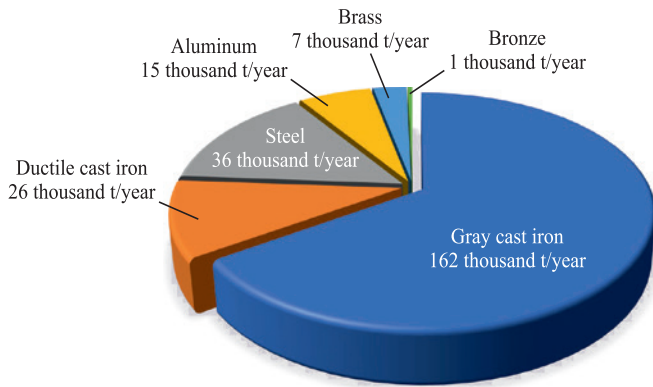
– core making machines, specifically employing the “cold-box-amine process,” have been implemented, with OJSC “Minsk Tractor Works” operating more than 30 machines and “Minsk Automobile Plant” – Managing Company of “Belavtomaz” Holding utilizing 4 machines developed by OJSC “BELNIIIT”.

Gray cast iron predominates in the material structure of Belarusian castings (Fig. 12).

In 2017, the “Foundry Development Program for the period 2017 – 2030” was launched, targeting significant enhancements in the sector’s efficiency and overcoming the aforementioned issues. The program’s primary objectives include:

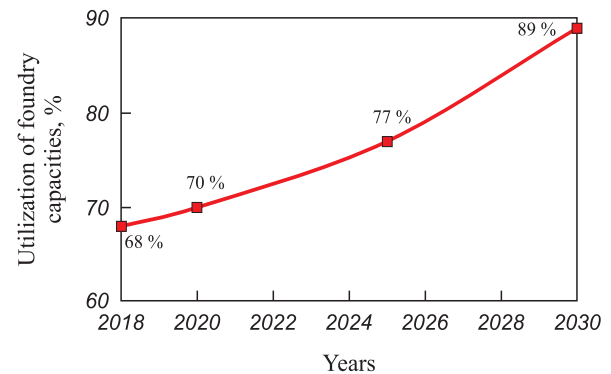
– optimizing the operations of existing foundries, enhancing product quality, lowering production costs, and maximizing the utilization of foundry capacities;





**Fig. 12.** Structure of castings produced in Belarus by types of materials for 2018 according to the Belarus “Foundry Development Program for the period 2017 – 2030”

**Рис. 12.** Структура производимого в Беларуси литья по видам материалов (данные за 2018 г.) из «Программы развития литейного производства Беларуси на период 2017 – 2030 гг.»



**Fig. 13.** Dynamics (actual and forecast for 2023 – 2030) of changes in the utilization of capacity of the basic foundry enterprises in Belarus

**Рис. 13.** Динамика (факт и прогноз на 2023 – 2030 гг.) изменения загрузки литейных мощностей базовых литейных предприятий Беларуси

- fostering the growth of financial and economic performance indicators within organizations;
- producing competitive products that fulfill consumer requirements;
- improving working conditions, minimizing environmental impact from production activities, continuously enhancing environmental standards, and promoting the efficient use of resources.

Initially, an audit of the existing production facilities’ technical standards was conducted as part of this program. Foundries that either met or were close to meeting the technological requirements for castings and could be updated with minimal expense were identified as basic foundries. This classification was in line with the Ministry of Industry’s Order No. 449, issued on December 9, 2016, titled “On Optimization of Foundries.” Focusing on the development of these basic foundries is expected to significantly enhance the foundry industry’s performance in Belarus, enabling the fulfillment of international orders, generating foreign currency revenue, and establishing a reliable reputation for producing quality products at reasonable prices.

#### INITIATIVES FOR THE DEVELOPMENT AND MODERNIZATION OF PRIMARY FOUNDRIES IN BELARUS

Following the directives from the Ministry of Industry’s Order No. 449, issued on December 9, 2016, updates were made to the modernization plans for foundries through to 2030. This involved revising the list of foundries scheduled for preservation or integration into base organizations by transferring their production lines, including the assortment of castings, as well as their melting, molding, mixing, and additional foundry equipment.

A Table details the operational parameters and capacity utilization of primary enterprises involved in the production of gray and ductile iron as of October 1, 2022.

Fig. 13 illustrates the comparative analysis of both actual and projected capacity utilization across the foundational foundries in Belarus, encompassing all casting categories.

The “Foundry Development Program for the period 2017 – 2030” includes investment initiatives and actions aimed at the establishment of new facilities and the enhancement of existing foundries within principal organizations.

It is proposed to incrementally reallocate the current product spectrum to these central entities and discontinue foundry operations at locations including OJSC “Minsk Automatic Lines Plant” named after P.M. Mashe-rov, OJSC “Gomel Radio Plant”, OJSC “MPOVT”, among others. Furthermore, due to economic non-viability, OJSC “Bobruisk Machine-Building Plant” and JSC “Managing Company of Lidselmash Holding” will cease the production of gray iron castings.

#### HUMAN WORKFORCE STRATEGY IN BELARUSIAN FOUNDRY INDUSTRY

In the Republic of Belarus, the training of personnel for the foundry industry is conducted by the following higher education institutions:

- the Faculty of Mechanics and Technology at the Belarusian National Technical University offers degree in: “Machines and technology of foundry production”, “Metallurgical production and material processing”, with specialization in “Foundry of ferrous and non-ferrous metals”;
- the Faculty of Mechanics and Technology at Sukhoi State Technical University of Gomel offers degree in

### Characteristics and utilization of capacity of the foundry production of basic enterprises for gray and ductile irons for October 1, 2022

#### Характеристика и загрузка мощностей литейного производства базовых предприятий по производству серого и высокопрочного чугуна на 1 октября 2022 г.

Alloy grade	Company name	Installed capacity, t/year	Actual production, tons, for three quarters of 2022	Capacity utilization, % from the beginning of the year
Gray iron casting (GI 10-30)	OJSC “Minsk Tractor Works”	110,000.00	44,812.72	54.32
	“Minsk Automobile Plant” – Managing Company of “Belavtomaz” Holding	12,336.41	5059.40	54.68
	OJSC “Centrolite” Gomel Foundry”	21,200.00	7833.85	49.27
	OJSC “Mogilevliftmash – Managing Company of the Holding”	10,600.00	6465.55	81.33
	OJSC “Gomel plant of casting and normals”	8716.50	5065.05	77.48
	OJSC “Lida Foundry and Mechanical Plant”	8620.00	6315.03	97.68
	OJSC “Mogilev Metallurgical Works”	17,679.00	6138.00	46.29
	OJSC “Legmash Plant”	400.00	94.82	31.61
	OJSC “Mogilev Plant Strommashina”	0	0	0
	OJSC “Managing Company of the Holding, “Minsk Motor Plant”, Stowbtsy	10,000.00	466.41	6.22
	TOTAL:	<b>199,551.91</b>	<b>82,250.33</b>	<b>54.96</b>
Ductile iron castings (DI 50)	OJSC “Minsk Tractor Works”	10,000.00	6240.38	83.20
	“Minsk Automobile Plant” – Managing Company of “Belavtomaz” Holding	11,920.00	3852.50	43.09
	OJSC “Gomel plant of casting and normals”	816.50	4930.05	75.41
	OJSC “Managing Company of the Holding, “Minsk Motor Plant”, Stowbtsy	8000.00	1568.04	26.13
	TOTAL:	<b>38,636.50</b>	<b>16 590.37</b>	<b>57.25</b>

“Machinery and technology of foundry production”, with specializations in “Technical operation of foundry equipment”, “Organization and management of foundry production”, “Metallurgical production and material processing” and “Electrometallurgy of ferrous and non-ferrous metals”;

– Gomel State Machine-Building College offers secondary vocational education with a major in “Metallurgical Production and Material Processing,” specializing in “Foundry Production of Ferrous and Non-Ferrous Metals”.

The state sector-specific educational institution of the Ministry of Industry of the Republic of Belarus, named “Institute of Professional Development and Retraining of Managers and Specialists “Industrial Personnel”, is responsible for the advanced training and retraining of managers and specialists within the engineering and technical services sector.

#### EXAMPLES OF FOUNDRY MODERNIZATION IN BELARUS

Examples of basic foundries’ modernization efforts in the Republic of Belarus as of January 1, 2023, include:

*OJSC “Minsk Tractor Works”.* Modernization efforts in Foundry Shop No. 1, including the molding and melting sections, and the melting section of Shop No. 2, have led to the procurement and installation of two induction furnaces along with charge preparation equipment. Construction and installation works are nearing completion, with commissioning 60 % finished. Completion is anticipated within 2023.

*OJSC “Minsk Automobile Plant”.* The reconstruction of the iron foundry block, targeting the gray iron section, commenced in 2021, with a projected completion in 2026. Additionally, the ductile iron section began reconstruction in 2023, with an expected finish in 2026.

*OJSC “Centrolite” Gomel Foundry*. The continuous mixer with a capacity of 30 t/h aimed at modernizing the heavy casting section, is being installed with an expected completion between 2018 and 2023. For the small casting shop, aiming to enhance competitiveness in large-format casting production, a molding line is acquired with a completion timeframe from 2025 to 2030. The smelting shop is undergoing upgrades by replacing three induction crucible furnaces IChT10 with a complex of intermediate frequency induction furnaces with an 8 t/h capacity.

*OJSC “Mogilevliftmash”*. Replacing a commercial frequency induction crucible furnace (IChT10) with an intermediate frequency induction furnace, with modernization extending from Q4 2022 to Q4 2023. The core-making section’s upgrade is planned for Q1 2024 to Q1 2025.

*OJSC “Mogilev Metallurgical Works”*. The foundry shop being reconstructed to accommodate the production of castings from gray and ductile cast iron, with a projected completion from Q1 2026 to Q4 2030.

*OJSC “Gomel plant of casting and normals”*. Acquisition and installation of a medium-frequency melting furnace with a 20 – 25 tons capacity are part of the ductile iron shop’s smelting section modernization, aiming to replace an outdated commercial frequency induction furnace. Completion is expected between 2024 and 2027.

*OJSC “Managing Company of the Holding, “Minsk Motor Plant”, Stowbtsy*. The “Production of high-precision ductile iron castings” investment project has been implemented, with completion spanning from 2012 to 2025. The facility is operational, with start-up and commissioning works fully completed as of September 2, 2020. The contract with GUSS-EX (Poland) has been fulfilled, and the setup for producing castings in the small series casting section using the Hardening Tag-Sand Process is underway, aiming for design capacity by Q4 2022.

#### **FUTURE DIRECTIONS FOR AUSFERRITIC CAST IRON APPLICATION IN BELARUS**

The global market is currently experiencing a surge in the production of Austempered Ductile Iron (ADI), a variant of ductile cast iron that undergoes a specific heat treatment to achieve an ausferritic metal matrix structure. This material effectively competes with high-quality rolled alloys steels, boasting strengths up to 1400 MPa. Industrially, hundreds of different part sizes are being produced, notably by corporations such as General Motors and Ford, with gears being one of the most extensively manufactured products internationally.

In Belarus, efforts by L.R. Dudetskaya and A.I. Pokrovsky have been made to adopt bainitic cast iron for manufacturing specific components, particularly medium

and large gears, within the foundry shop of Minsk Automobile Plant. The technology was applied to the production of rear axle differential gears for the MAZ 5336 model: the axle drive gear (No. 5336-2402050) and the pinion gear (No. 5336-2402055) [8 – 12]. The findings from these applications demonstrated that bainitic cast iron could serve as a viable alternative to the traditionally used 20KhN3A steel for gears. A number of bainitic and ausferritic cast iron compositions have been patented [13 – 17].

The appraisal survey conducted in November 2016, under the directive of the Ministry of Industry of the Republic of Belarus and distributed to over 70 subordinate organizations, identified a yearly demand for bainitic cast iron of approximately 10 thousand ton.

#### **CONCLUSIONS**

The foundry sector in Belarus is contending with outdated technologies and equipment that lead to lower productivity and higher specific resource consumption per product unit compared to international counterparts. Characteristically, the industry heavily relies on traditional practices such as the use of cupolas and sand-clay mixture molds, with a predominant focus on gray cast iron and limited ductile cast iron production.

A notable issue within Belarusian foundries is the underutilization of capacity. With a total capacity of 557.5 thousand tons for casting annually, the current production stands at only approximately 250 thousand tons – a gap that reflects a significant underuse of available resources. This situation presents an opportunity to align with global trends and fill the capacity with orders from technologically advanced nations, leveraging the shifts in countries like India and China, which are expanding their foundry productions. Efforts must be concentrated on attracting more customers and investors interested in contributing to the advancement of new technologies within the foundry in Belarus.

Efforts to mitigate these challenges are embodied in the “Foundry Development Program for the period 2017 – 2030”. This initiative aims to modernize the entire foundry landscape, designate and revitalize the most competitive foundries as primary operations, devise remodeling plans, and enhance overall efficiency. The program’s implementation is structured to boost the nation’s foundry industry, secure international orders, and enhance foreign currency inflows.

A key direction for modernizing the foundry industry in Belarus involves relocating foundry operations away from Minsk, such as those at Minsk Tractor Works and Minsk Automobile Plant, and establishing modern, high-tech production facilities built from the ground up to meet the latest global standards. A prime example of this initia-

tive is the construction of the Belarusian Metallurgical Plant in Zhlobin.

Belarus boasts a robust educational framework for metallurgy and casting, with professional training provided by the Faculties of Mechanics and Technology at both the Belarusian National Technical University and Sukhoi State Technical University of Gomel, as well as at Gomel State Mechanical Engineering College and Zhlobin State Metallurgical College. The “Foundry Development Program for the period 2017 – 2030” stipulates the targeted number of student enrollments in these disciplines. Additionally, the “Institute of Professional Development and Retraining of Managers and Specialists ‘Industrial Personnel’” oversees the continual professional development and skill enhancement of technical service managers and specialists.

Looking ahead, it is anticipated that Belarus will align with the international shift towards manufacturing critical castings predominantly from ductile cast iron instead of gray cast iron and will progressively move towards using ausferritic (bainitic) cast iron as an alternative to rolled steel. Thus, it is crucial to prepare the industrial infrastructure and the specialists within the field.

## REFERENCES / СПИСОК ЛИТЕРАТУРЫ

- Svidunovich N.A., Vityaz' P.A., Voitov I.V., Kuis D.V., Myurek M.N. Selection and Applications of Materials: A Tutorial. Vol. 5: Selection and Applications of Cast Irons. Minsk: Belaruskaya navuka; 2020:425. (In Russ.).  
Свидуневич Н.А., Витязь П.А., Войтов И.В., Куис Д.В., Мюрек М.Н. Выбор и применение материалов: Учебное пособие. Т. 5. Выбор и применение чугунов. Минск: Беларуская навука; 2020:425.
- World Foundry Organization – WFO. Available at URL: <https://www.thewfo.com/>
- Total casting tons hits 112 million. *Modern Casting*. 2019;(December):22–25.
- Global casting production worldwide. Available at URL: <https://www.statista.com/statistics/237526/casting-production-worldwide-by-country>
- Patent US2485760. *Cast ferrous alloy*. Millis K.D., etc. Oct. 25, 1949.
- Global casting production growth stalls. *Modern Casting*. 2017;(December):24–28.
- Total casting tons dip in 2019. *Modern Casting*. 2021;(January):28–30.
- Dudetskaya L.R., Pokrovskii A.I., Gaukhshtein I.S., Demin M.I., Gurchenko P.S. Bainitic cast iron: experience in production and application. *Avtomobil'naya promyshlennost'*. 2001;(11):33–35. (In Russ.).  
Дудецкая Л.Р., Покровский А.И., Гаухштейн И.С., Демин М.И., Гурченко П.С. Бейнитный чугун: опыт получения и применения. *Автомобильная промышленность*. 2001;(11):33–35.
- Dudetskaya L.R., Pokrovskii A.I., Gaukhshtein I.S., Demin M.I., Gurchenko P.S. Heat treatment for bainitic structure of cast iron parts. *Lit'e i metallurgiya*. 2002;(1):45–49. (In Russ.).
- Dudetskaya L.R., Pokrovskii A.I., Gaukhshtein I.S., Demin M.I., Gurchenko P.S. Thermoprocessing of bainitic structure of cast iron parts. *Lit'e i metallurgiya*. 2002;(1):45–49.
- Pokrovskii A.I., Dudetskaya L.R. Use of ductile bainitic cast iron for making gears. *Lit'e i metallurgiya*. 2015;(2(79)):126–134. (In Russ.).  
Покровский А.И., Дудецкая Л.Р. Использование высокопрочного бейнитного чугуна для изготовления зубчатых колес. *Литье и металлургия*. 2015;(2(79)):126–134.
- Pokrovskii A.I. Prospects for the use of austenite-bainitic cast iron (ADI) in Belarus. *Inzhener-mekhanik*. 2016;(4(73)):16–29. (In Russ.).  
Покровский А.И. Перспективы использования аустенито-бейнитного чугуна (ADI) в Беларуси. *Инженер-механик*. 2016;(4(73)):16–29.
- Pokrovskii A.I., Chaus A.S., Kunovskii E.B. Effect of the shape of graphite inclusions on acoustic characteristics of articles from cast and deformed iron. *Metal Science and Heat Treatment*. 2011;53(7-8):311–317.  
<https://doi.org/10.1007/s11041-011-9388-9>
- Dudetskaya L.R., Pokrovskii A.I., Danil'chik I.K. *Cast iron*. Patent 4427, Republic of Belarus. C1 BY МПК7 C22C37/00. No. 970656; applied 27.11.1997, publ. 30.06.2002. *Official Bulletin, National Center of Intellectual Property*. 2002;(2):48. (In Russ.).  
Пат. 4427 Респ. Беларусь. Чугун. Дудецкая Л.Р., Покровский А.И., Данильчик И.К. C1 BY МПК7 C22C37/00. № 970656; заявл. 27.11.1997; опубл. 30.06.2002. *Афіц. бюл.* 2002;(2):48.
- Pokrovskii A.I. *Bainitic cast iron*. Patent 23331, Republic of Belarus, МПК (2006.01) C 22C 37/10; No. a 20180359; applied 24.07.2018, published 30.12.2019. *Official Bulletin, National Center of Intellectual Property*. 2019;(6):98. (In Russ.).  
Пат. 22823 Респ. Беларусь. Бейнитный чугун. Покровский А.И.; МПК (2006.01) C 22C 37/10. № а 20180359; заявл. 24.07.2018; опубл. 30.12.2019. *Афіц. бюл.* 2019;(6):98.
- Pokrovskii A.I. *Bainitic cast iron*. Patent 23331, Republic of Belarus, МПК (2006.01) C 22C 37/10; No. a 20190368; applied 24.07.2018, published 28.02.2021. *Official Bulletin, National Center of Intellectual Property*. 2021;(1):57. (In Russ.).  
Пат. 23331 Респ. Беларусь. Бейнитный чугун. Покровский А.И.; МПК (2006.01) C 22C 37/10. № а 20190368; заявл. 24.07.2018, опубл. 28.02.2021. *Афіц. бюл.* 2021;(1):57.
- Pokrovskii A.I. *Ausferritic cast iron*. Patent 23389, Republic of Belarus, МПК (2006.01) C 22C 37/10; No. a 20200022; applied 27.01.2020, published 30.04.2021. *Official Bulletin, National Center of Intellectual Property*. 2021(2):50. (In Russ.).  
Пат. 23389 Респ. Беларусь. Аусферритный чугун. Покровский А.И.; МПК (2006.01) C 22C 37/10. № а 20200022; заявл. 27.01.2020, опубл. 30.04.2021. *Афіц. бюл.* 2021(2):50.
- Pokrovskii A.I. *Ausferritic cast iron*. Patent 23393, Republic of Belarus, МПК (2006.01) C 22C 37/10; No. a 20200023; applied 27.01.2020, published 30.04.2021. *Official Bulletin, National Center of Intellectual Property*. 2021(2):50. (In Russ.).  
Пат. 23393 Респ. Беларусь. Аусферритный чугун. Покровский А.И.; МПК (2006.01) C 22C 37/10. № а 20200023; заявл. 27.01.2020, опубл. 30.04.2021. *Афіц. бюл.* 2021(2):50.



## Information about the Authors

## Сведения об авторах

**Petr A. Vityaz'**, Academician, Chief of Staff of NAS of Belarus, Dr. Sci. (Eng.), Prof., Presidium of the National Academy of Sciences of Belarus  
**E-mail:** [vityaz@presidium.bas-net.byn](mailto:vityaz@presidium.bas-net.byn)

**Vitalii G. Zaleskii**, Dr. Sci. (Phys.–Math.), Assist. Prof., Director, Physico-Technical Institute, Belarus National Academy of Sciences  
**E-mail:** [vzalesski@mail.ru](mailto:vzalesski@mail.ru)

**Artur I. Pokrovskii**, Cand. Sci. (Eng.), Assist. Prof., Head of the Laboratory, Physico-Technical Institute, Belarus National Academy of Sciences  
**E-mail:** [art@phti.by](mailto:art@phti.by)

**Петр Александрович Витязь**, академик, руководитель аппарата НАН Беларуси, д.т.н., профессор, Президиум Национальной академии наук Беларуси

**E-mail:** [vityaz@presidium.bas-net.byn](mailto:vityaz@presidium.bas-net.byn)

**Виталий Геннадьевич Залесский**, д.ф.-м.н., доцент, директор, Физико-технический институт НАН Беларуси

**E-mail:** [vzalesski@mail.ru](mailto:vzalesski@mail.ru)

**Артур Игоревич Покровский**, к.т.н., доцент, заведующий лабораторией, Физико-технический институт НАН Беларуси

**E-mail:** [art@phti.by](mailto:art@phti.by)

Received 25.05.2023

Revised 28.08.2023

Accepted 11.12.2023

Поступила в редакцию 25.05.2023

После доработки 28.08.2023

Принята к публикации 11.12.2023



UDC 669.162

DOI 10.17073/0368-0797-2024-1-19-26



Original article

Оригинальная статья

## POSSIBILITIES OF HEAT-POWER SPRAYING OF WET CHARGE DURING FORMATION OF STRUCTURAL PROPERTIES OF AGGLOMERATED IRON ORE MATERIALS

V. M. Pavlovets

Siberian State Industrial University (42 Kirova Str., Novokuznetsk, Kemerovo Region – Kuzbass 654007, Russian Federation)

✉ [pawlowets.victor@yandex.ru](mailto:pawlowets.victor@yandex.ru)

**Abstract.** The substantiated problem of improving the structural properties of agglomerated metallurgical raw materials is associated with the formation of a favorable pore structure in iron ore pellets. The author analyzed various methods for the formation of structural properties of molded dispersed materials in various industries. The paper presents the technological capabilities of promising technologies for production of iron ore pellets based on the heat-power spraying of wet charge on pelletizer's charge skull and pelletized materials. The physical possibilities of heat-power spraying of wet charge in the forced nucleation and in the process of forming the iron ore pellets' structural properties are disclosed at the stage of pelletizing. The technical features and production operations of the main technologies for wet charge spraying and the design features of devices for obtaining pellets are shown. The paper describes the experimental unit and technology for the forced nucleation. The macro- and microstructure of the germ mass at forced nucleation were studied. Principles of the formation of regulated structure and improved metallurgical properties in iron ore pellets were substantiated. The article presents the description and characteristics of structural changes on the surface of the sprayed charge layer. A hypothesis was put forward about the structural correspondence of geometric dimensions and relief of charge lappings and cavities in the sprayed layer with the nature of porosity and germ structure. The germ mass affects the pellets' structural properties. The author obtained the dependences of structural changes' relative values on the sprayed layer surface on pressure of air-charge jet and particle size of the sprayed charge. There is relationship between geometric dimensions of the sprayed charge layer and the structural changes' size. A probable mechanism of porosity formation in the germ mass during heat-power spraying of a wet charge onto the pelletizer skull was formulated. The aerodynamic characteristics of air-charge jet influence the formation of porosity. New possibilities of heat-power spraying of wet charge can intensify pellets production and improve their quality.

**Keywords:** structural properties, agglomerated metallurgical raw materials, iron ore pellets, thermal-power heat-power spraying of wet charge, germ mass, forced nucleation

**For citation:** Pavlovets V.M. Possibilities of heat-power spraying of wet charge during formation of structural properties of agglomerated iron ore materials. *Izvestiya. Ferrous Metallurgy*. 2024;67(1):19–26. <https://doi.org/10.17073/0368-0797-2024-1-19-26>

## ВОЗМОЖНОСТИ ТЕПЛОСИЛОВОГО НАПЫЛЕНИЯ ВЛАЖНОЙ ШИХТЫ В ПРОЦЕССЕ ФОРМИРОВАНИЯ СТРУКТУРНЫХ СВОЙСТВ ОКУСКОВАННЫХ ЖЕЛЕЗОРУДНЫХ МАТЕРИАЛОВ

В. М. Павловец ✉

Сибирский государственный индустриальный университет (Россия, 654007, Кемеровская обл. – Кузбасс, Новокузнецк, ул. Кирова, 42)

✉ [pawlowets.victor@yandex.ru](mailto:pawlowets.victor@yandex.ru)

**Аннотация.** Повышение структурных свойств окучкованного металлургического сырья за счет формирования благоприятной поровой структуры у железорудных окатышей является актуальной задачей. Методы формирования структурных свойств у сформированных дисперсных материалов проанализированы применительно к различным отраслям промышленности. В работе представлены технологические возможности перспективных технологий производства железорудных окатышей на основе теплосилового напыления влажной шихты на шихтовый гарнизаж окомкователя и комкуемые материалы. Теплосиловое напыление влажной шихты в технике принудительного зародышеобразования позволяет формировать структурные свойства железорудных окатышей на стадии окомкования. Конструктивные особенности устройств для получения окатышей зависят от применяемых производственных технологий напыления влажной шихты на ограждения окомкователя. Методики экспериментов зависят от техники принудительного зародышеобразования. Технологии принудительного зародышеобразования влияют на макро- и микроструктуры зародышевой массы. Принципы регламентированного структурообразования позволяют формировать улучшенные металлургические свойства окатышей. На поверхности напыленного слоя шихты

образуются структурные изменения в форме углублений и шихтовых напылов. Высказана гипотеза о структурном соответствии геометрических размеров, рельефа шихтовых напылов и углублений у напыленного слоя с характером пористости и структуры зародышей. Количество зародышевой массы внутри окатышей влияет на их структурные свойства. Относительная величина структурных изменений на поверхности напыленного слоя шихты и их количество определяются давлением воздушно-шихтовой струи и размером напыляемых частиц. Вероятный механизм формирования пористости зародышевой массы в процессе теплосилового напыления влажной шихты на гарнисаж окомкователя зависит от параметров технологии. Обоснован сдвиговый механизм образования открытой пористости в структуре зародышевой массы. Аэродинамические характеристики воздушно-шихтовой струи влияют на формирование пористости. Новые технологии теплосилового напыления влажной шихты позволяют интенсифицировать производство и улучшать качество окатышей.

**Ключевые слова:** структурные свойства, окускованное металлургическое сырье, железорудные окатыши, теплосиловое напыление влажной шихты, зародышевая масса, технология принудительного зародышеобразования

**Для цитирования:** Павловец В.М. Возможности теплосилового напыления влажной шихты в процессе формирования структурных свойств окускованных железорудных материалов. *Известия вузов. Черная металлургия*. 2024;67(1):19–26.  
<https://doi.org/10.17073/0368-0797-2024-1-19-26>

## INTRODUCTION

Various techniques, including intensive modes of heat treatment, foaming, combustible additives, special pore-forming and ore-forming compositions, and other materials, are used to determine special structural properties of the majority of molded porous products across various branches of engineering, such as metallurgy, the manufacture of refractory products, construction operations, etc. [1 – 3]. The increased requirements to pelletized metallurgical raw materials in terms of iron content considerably limit the application of pore-forming additives and expand the use of methods for forming pores in the structure of iron ore pellets [4 – 7]. One way to improve the structural properties of pellets without using pore-forming additives is to apply a two-step technology. One of its steps enables the formation of most of the pellet mass by heat-power spraying of wet charge at the pelletizing stage [8; 9]. As a structure- and form-forming energy carrier, this technology uses an air charge jet (ACJ)

based on cold or heated up to 100 – 150 °C compressed air, which enables the formation of a wet charge sprayed layer (SL) on almost any technological surface [8; 9]. The raw pellets production based on the spraying technique also includes the operations of charge pelletizing and after-pelletizing of germs. Numerous experimentally proven combined technologies have been successfully explored in laboratories and have shown high practical efficiency [8; 9]. Some technical indicators of the mentioned technologies, in comparison with the traditional method, are given in the Table below [8 – 10].

Flow schemes for pellets production based on heat-power spraying of wet charge onto the charge skull of the plate pelletizer are illustrated in Fig. 1, *a*. The spraying schemes for pelletized materials are depicted in Fig. 1, *b*, *c*. The process of pellet production employing the forced nucleation technology (NSA) has been most thoroughly investigated under laboratory conditions. This technique involves forming the germinal

### Technical indicators of pelletizing technologies

#### Технические показатели технологий получения окатышей

Technical indicators	Pelletizing technologies			
	NP	NSA	NPSA	NPS
Spraying area, % of the plate area	–	30 – 40	20 – 30	15 – 25
Area occupied by pelletized materials, %	40 – 50	70 – 90	50 – 55	40 – 50
Relative productivity, %	100	115 – 130	105 – 115	110 – 120
Weight percentage of sprayed material in the pellet structure, %	–	up to 70	up to 40	up to 50
Spraying efficiency, %	–	up to 90	up to 70	up to 60
Pellet weight growth rate, g/s	0.01 – 0.03	0.08 – 0.24	0.05 – 0.14	0.08 – 0.31
Dehumidification of pellets after pelletizing, %	–	0.4 – 1.2	0.4 – 1.0	0.5 – 0.9
Moisture removal intensity in the process of nucleation, kg/(m <sup>2</sup> ·s)	–	(4 – 8)·10 <sup>–3</sup>	(5 – 10)·10 <sup>–3</sup>	(5 – 10)·10 <sup>–3</sup>
Crack formation temperature, °C	550 – 580	600 – 740	580 – 650	580 – 620
Total porosity of pellets, %	23 – 28	28 – 35	26 – 32	28 – 34
Number of open pores, %	20 – 25	25 – 30	22 – 26	24 – 28
Relative strength of pellets, %	100	90 – 110	90 – 100	85 – 95

part of pellets and their pore structure through heat-power spraying of wet charge onto the bottom charge skull in the idle zone of the pelletizer (Fig. 1, *a*) [8; 9]. Using this technique, the SL and germs exhibit reduced moisture content and a favorable pore structure, characterized by an increased number (up to 40 %) of open pores with low tortuosity [9]. The operations to produce suitable pellets include the mechanical division of SL into germs, spheroidization of germs, and their after-pelletizing in the rerolling mode. The NSA technology enables the achievement of superior performance characteristics and pellet properties (refer to the table). In the NPS and NPSF technologies, the germs are small pellets ranging in size from 4 to 12 mm. According to the NPSF technology, as the pellet mass forms, an internal charge sprayed layer is created on the surfaces of 4 – 7 mm germs, positioned between the germ and the shell. The mass of the sprayed layer can account for up to 40 % of the total (Fig. 1, *b*). During the NPS process, the pellet shell forms on the surfaces of larger pellets, 8 – 12 mm in size, that are grouped in the circulation zone of the pelletizer by spraying wet material onto the pelletized materials. Here, spraying serves as a finishing technique, after which the pellets achieve their standard size (14 – 16 mm) (Fig. 1, *c*). The strength of the surface shell can be increased by 5 – 15 % compared to the traditional industrial NP technology, albeit at the expense of some structural characteristics of the pellets. When employing these technologies, the germ mass is formed by pelletizing the wet charge in the rerolling mode, eliminating the need for mechanical follow-up elements. However, the efficiency of spraying, the weight percentage of the sprayed layer in the pellets, and some process specifications slightly lag behind the NSA technique. The processes developed can be easily integrated into existing facilities with minimal adjust-

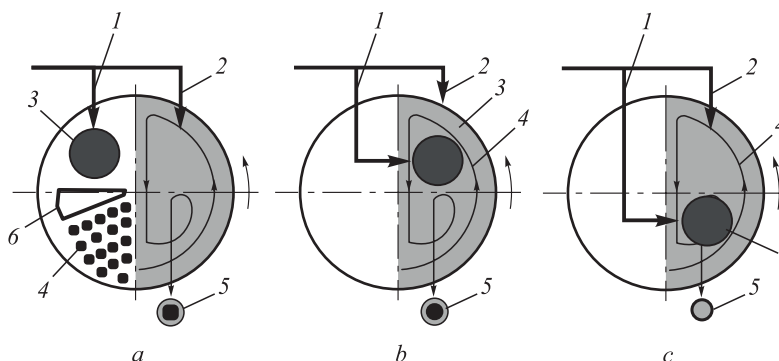
ments. Additionally, if needed, reverting to the conventional technology (NP), which relies on wet charge drip nucleation followed by after-pelletizing in the rerolling mode, is straightforward.

The spraying technique is extensively utilized across various manufacturing processes [11; 12], enabling the formation of structural properties in a broad array of sprayed materials [13 – 15]. Technologies based on spraying offer several technical benefits and are distinguished by numerous control actions, both in the manufacturing process itself and in terms of enhancing and broadening the consumer properties of the processed products. This is especially relevant to pellet production, where the technique of wet charge spraying using an air charge jet (ACJ) opens significant potential for influencing the structure of germs and pellets [8 – 10].

The aim of this paper is to explore the mechanism of structure formation in the germinal centers of pellets produced through the technology of heat-power spraying of wet charge onto the pelletizer's bottom skull.

## MATERIALS AND METHODS

The experiments were conducted on a laboratory semi-industrial pelletizer with a diameter of 0.62 m, inclined at a 45° angle to the horizon, and rotating at a speed of 12 rpm. The sprayed charge, with a moisture content of 5.0; 7.5; 10.0 %, consisted of iron ore concentrate from the Teysk deposit and 1 % of bentonite as a binder. The wet charge was sprayed onto the charge skull using compressed air at a pressure of 0.2 MPa and a flow rate of 0.6 m<sup>3</sup>/min. After spraying, the geometric dimensions of the SL were measured. Samples taken from the SL using the cutting ring method (GOST 5180 – 84) were utilized to evaluate compressive strength (GOST 17245 – 79



**Fig. 1.** Schemes for obtaining pellets based on heat-power spraying of wet charge on the charge skull of a plate pelletizer (*a*) and pelletized materials (*b*, *c*):

1, 2 – independent flows of the loaded charge; 3 – sprayed layer (*a*), spraying area (*b*, *c*) in the layer of pelletized materials; 4 – germs; 5 – suitable pellets; 6 – divider of sprayed layer (SL)

**Рис. 1.** Схемы получения окатышей на основе теплосилового напыления влажной шихты на шихтовый гарнизан тарельчатого окомкователя (*a*) и комкуемые материалы (*b*, *c*):

1, 2 – самостоятельные потоки загружаемой шихты; 3 – напыленный слой (*a*) и область напыления (*b*, *c*) в слое комкуемых материалов; 4 – зародыши; 5 – годные окатыши; 6 – делитель НС

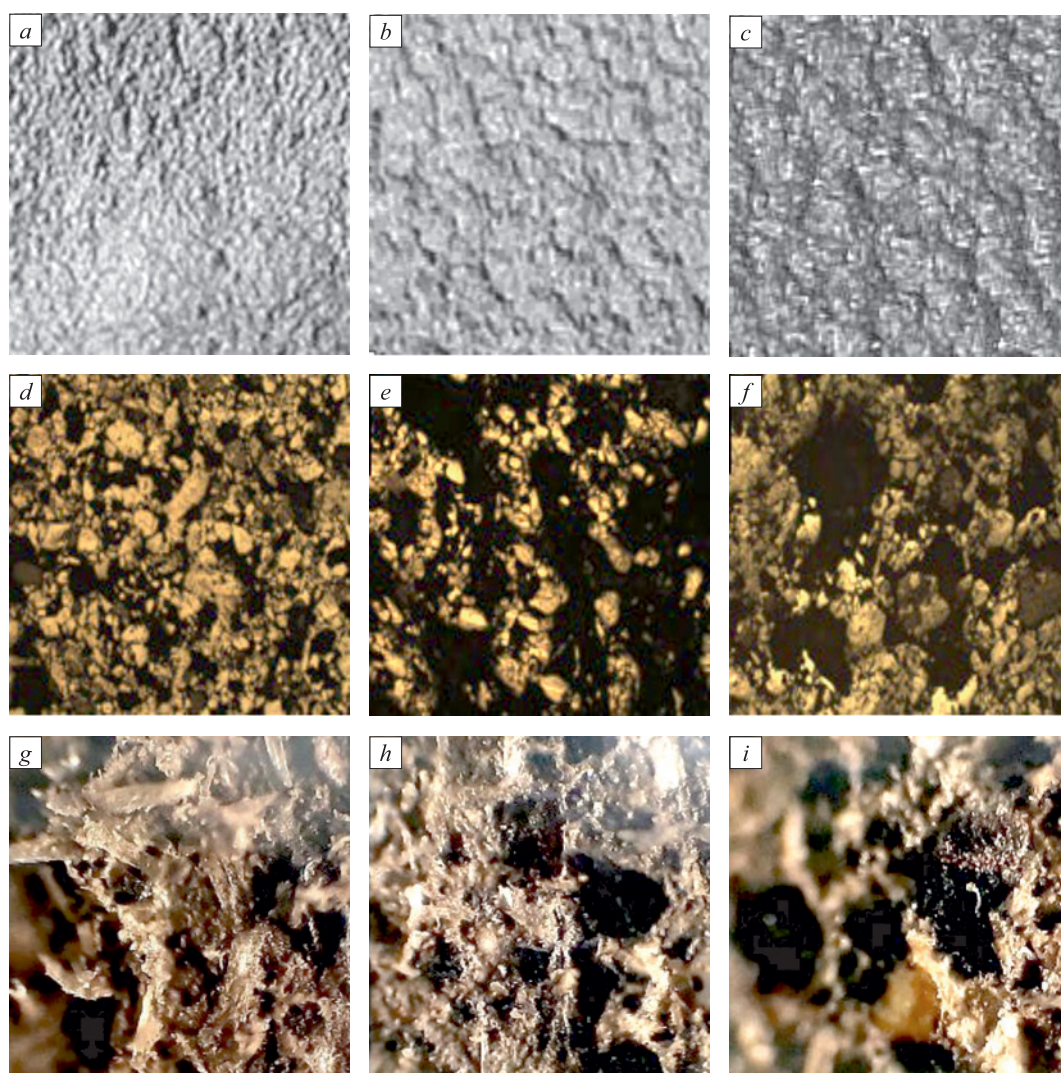


and 26447 – 85) and density. In each SL zone, defined by a relative diameter  $\delta$  equal to  $0 \pm 0.2$ , samples were collected with samplers (cutting ring) 10 mm in diameter, amounting to 10 – 15 samples per zone. The procedure is elaborated upon in references [8; 9]. The analysis of the germ structure formation mechanism during heat-power spraying of charge focused on:

- the macrostructure of the SL surface formed after spraying;
- the surface microstructure of the SL samples on their horizontal plane parallel to the sprayed base and on their vertical plane perpendicular to the sprayed base (Fig. 2).

Samples for microstructure analysis were fired in an electric furnace at 800 °C.

Structural alterations on the surface of the sprayed charge layer included cavities and charge lappings, arising from the dynamic impact of the ACJ on the SL surface. This interaction results in the formation of a wave-like relief on the surface, characterized by alternating cavities and lappings (Fig. 2, *a, b, c*). These structural changes, with varying geometric dimensions, shapes, locations, and tortuosities, serve as external indicators of the process, facilitating the analysis of pore formation within the germ [8]. Structural cavities in the SL are concentric channels with low tortuosity, arranged along a circular path between charge lappings around the axis of the circular SL, with the jet angle of attack ( $\beta$ ) set to 90°. These channels often form a loop, with some being intermittent. In macrostructure photographs, they appear as dark



**Fig. 2.** Macrostructure and microstructure of SL surface after spraying on horizontal and vertical planes of the samples: *a, b, c* – SL surface,  $\times 10$ ; *d, e, f* – thin section in the horizontal plane,  $\times 100$ ; *g, h, i* – thin section in the vertical plane,  $\times 100$ ; *a, d, g* – SL central zone  $\delta = 0$ ;  $\beta = 90^\circ$ ; *b, e, h* – intermediate zone  $\delta = 0.5$ ;  $\beta = 90^\circ$ ; *c, f, i* – peripheral zone  $\delta = 0.7$ ;  $\beta = 90^\circ$

**Рис. 2.** Макроструктура поверхности НС после напыления и микроструктуры поверхности образцов НС на горизонтальной и вертикальной плоскостях образцов:

- a, b, c* – поверхность НС,  $\times 10$ ; *d, e, f* – поверхность шлифа в горизонтальной плоскости,  $\times 100$ ;
- g, h, i* – поверхность шлифа в вертикальной плоскости,  $\times 100$ ; *a, d, g* – центральная зона НС,  $\delta = 0$ ,  $\beta = 90^\circ$ ;
- b, e, h* – промежуточная зона,  $\delta = 0,5$ ,  $\beta = 90^\circ$ ; *c, f, i* – периферийная зона,  $\delta = 0,7$ ,  $\beta = 90^\circ$

lines ranging from 0.1 to 2.5 mm in width. The charge lappings, in contrast, are wider, measuring 1 to 5 mm across. They feature a sloping surface on the side facing the ACJ attack and a steep slope on the opposite (shadow) side. These structural changes make it possible to establish a structural congruence between the SL surface relief and the pore structure of the germ mass [8]. Such surface formations of sprayed coatings have attracted the attention of both domestic [16; 17] and international researchers [18 – 21].

For analyzing the SL macrostructure, two parameters were employed: the relative value of the structural cavities of the SL  $\theta_{ho}$  and the relative number of structural cavities  $\theta_N$ , amount/m<sup>2</sup> (1/m<sup>2</sup>), on its surface. The relative width of the structural cavities can be determined using the expression

$$\theta_{ho} = \frac{h_o}{h},$$

where  $h_o$  is the average width of structural cavities, mm;  $h$  is the average height of the sprayed layer on its axis, mm.

The relative number of structural cavities is calculated using the expression

$$\theta_N = \frac{N}{f_{SL}},$$

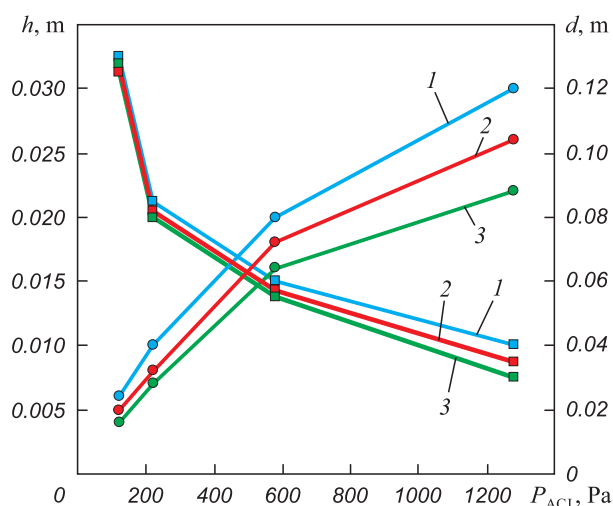
where  $N$  is the average number of structural cavities, determined by the number of concentric shadow channels in the SL;  $f_{SL}$  is the area of the SL with a diameter of  $d$ , m<sup>2</sup>.

The technique of measuring structural changes is detailed in [9]. These parameters,  $\theta_{ho}$  and  $\theta_N$ , are evaluated in relation to variables such as the ACJ pressure  $P_{ACJ}$ , moisture content  $W_c$  and the average particle size  $d_p$  of the sprayed charge. The ACJ pressure is determined based on a nomographic chart that considers both the charge parameters and the characteristics of the jet device [8].

## RESULTS AND DISCUSSION

The experimental findings are depicted in Figs. 3 and 4. Specifically, the parameter  $\theta_{ho}$  shows a marked decrease as the ACJ pressure increases to 800 Pa, beyond which it declines more gradually (Fig. 4, *a*). with increasing ACJ pressure, the dimensions of structural cavities diminish, while concurrently, the average height of the sprayed layer on its axis expands (Fig. 3). A similar impact is observed with the reduction in particle size of the sprayed charge on the SL's structural parameters (Fig. 4, *b*), where the rate of decrease in  $h_o$  outpaces the growth in the sprayed layer's height  $h$ . This implies a significant influence of both the moisture content

of the sprayed charge and the presence of mobile charge pulp (hydromix) on the surface of the SL, which is generated when the charge mixes with water expelled from the depth to the surface of the SL by the ACJ pressure [8]. At a low moisture content  $W_c = 5.0\%$  and an ACJ pressure of 200 Pa and higher, it is postulated that charge pulp is not formed in this mode of spraying, thereby not affecting the structure formation of the SL. In such conditions, the surface of the SL predominantly features low lappings and small structural cavities ( $h_o < 0.1 - 0.2$  mm), whose dimensions can be measured and analyzed under sufficient magnification. Conversely, at a moisture content of  $W_c = 7.5\%$ , the quantity of mobile charge pulp increases during spraying, leading to a decrease in the viscosity of the charge on the surface. This condition facilitates the creation of larger charge lappings and structural cavities, which become visually observable. As the ACJ pressure exceeds 800 – 1000 Pa and the charge moisture content reaches  $W_c = 10.0\%$ , there is a significant increase in the amount of mobile charge pulp of lower viscosity. This pulp readily fills the cavities, leading to the formation of a relatively uniform structural relief on the surface of the SL with a plethora of small pore channels. The appearance of charge pulp on the surface during the pellet production process serves as an indicator of impact pelletization, a phenomenon where the physical impact of spraying influences the formation and characteristics of pellets [1; 4]. Interestingly, the pattern of these findings bears resemblance to those observed in the plasma spraying of metal powders [16; 17].



**Fig. 3.** Dependence of the average height (●, ●, ●) and diameter of the sprayed layer of charge (■, ■, ■) on pressure of air-charge jet (ACJ), moisture content of the charge: 1 – 10.0 %; 2 – 7.5 %; 3 – 5.0 % at the average charge particle size of 0.068 mm

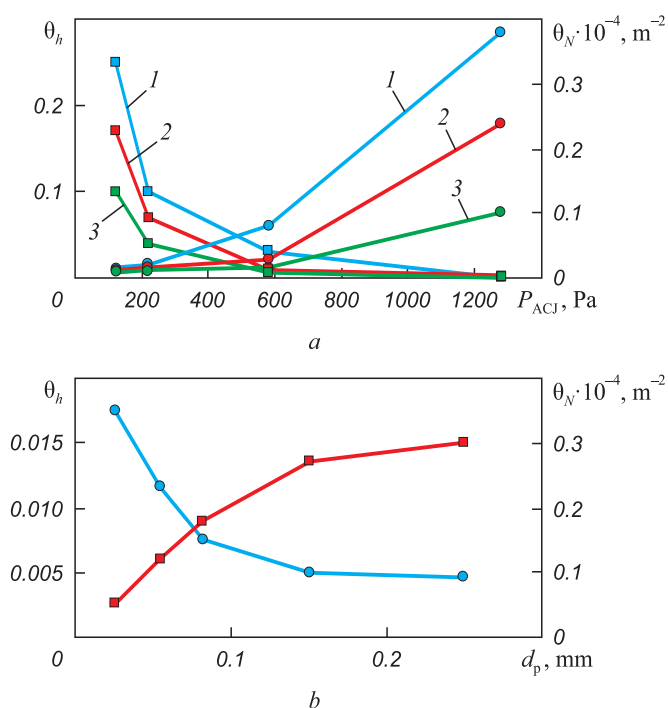
**Рис. 3.** Зависимость средней высоты (●, ●, ●) и диаметра напыленного слоя шихты (■, ■, ■) от давления ВШС при влажности шихты: 1 – 10,0 %; 2 – 7,5 %; 3 – 5,0 %, средний размер частиц шихты 0,068 мм



The parameter  $\theta_N$ , which represents the relative number of concentric structural cavities on the surface of the SL, varies with  $P_{ACJ}$  pressure (Fig. 4). A notable increase in  $\theta_N$  nearly fourfold, is observed as the charge moisture content rises from 5.0 to 10.0 % at a  $P_{ACJ} = 1280$  Pa. This phenomenon is attributed to the increased ACJ pressure, which not only escalates the number of structural cavities but does so at a rate much faster than the growth in the diameter  $d$  of the SL and its area  $f_{SL}$  (Fig. 3). Under these conditions, the mobile charge pulp is capable of flowing into adjacent zones of the SL in the direction of the air movement, consequently altering the size of cavities on the SL surface.

Analyzing the parameter  $\theta_F$ , which is defined as the ratio of the sizes of structural cavities to the surface area of the sprayed layer ( $\theta_F = h_o/F$ ,  $m^{-1}$ ), reveals that at a moisture content of 10.0 %  $\theta_F$  remains constant across a wide range of ACJ pressures, maintaining a value of 0.1. This consistency in  $\theta_F$  suggests that the ACJ pressure proportionally affects both the sizes of structural cavities and the dimensions of the sprayed layer (SL) itself. In contrast, for sprayed charges with moisture contents of 7.5 and 5.0 %,  $\theta_F$  decreases to 0.07 and 0.05, respectively, within the same ACJ pressure range. This indicates that the formation of the SL's shape and structure from charges with lower moisture content is significantly less favorable compared to those with higher moisture content due to the smaller sizes of cavities and lappings. As the moisture content of the charge increases, so do the mass and dimensions of the SL, leading to its expansion over a larger area and the enlargement of lappings and cavities. Conversely, with decreasing charge moisture, the mass, diameter, and height of the SL grow at a slower pace, resulting in smaller lappings and cavities. However, the number and concentration of these features within the area  $F$  increase, as structural cavities become more densely packed. It is noted that starting from ACJ pressures of 800 – 1000 Pa, the geometric dimensions of lappings and cavities decrease regardless of the moisture content.

The formation of air cavities (pores) on the surface of the SL is most likely to occur at the base of the structural cavities, where the adhesion of the charge lapping to the sprayed base is at its strongest. Under the influence of ACJ pressure, the crest of the lapping, being more mobile due to its specific geometric shape, is subjected to greater deformation. This mobility and deformability allow the lapping crest to potentially block voids in areas that are inaccessible to ACJ pressure. If the charge lappings lack sufficient mobility for this first mechanism of pore formation to take place, an alternative mechanism can occur, whereby voids are formed through the mechanical overlapping of structural cavities by the sprayed charge. The feasibility of this mechanism of structure formation has been supported by research findings pre-



**Fig. 4.** Dependence of the relative size (●, ■, ▲) and relative number of structural cavities of the sprayed charge layer (□, ■, ▲) on pressure of ACJ at moisture content of the charge: 1 – 10.0 %; 2 – 7.5 %; 3 – 5.0 % (a) and average particle size at  $P_{ACJ} = 580$  Pa,  $W_c = 10.0$  % (b), the average charge particle size of 0.068 mm

**Рис. 4.** Зависимость относительной величины структурных углублений (●, ■, ▲) и относительного количества структурных углублений напыленного слоя шихты (□, ■, ▲) от давления ВШС при влажности шихты: 1 – 10,0 %; 2 – 7,5 %; 3 – 5,0 % (a) и среднего размера частиц при  $P_{ACJ} = 580$  Па,  $W_c = 10,0$  % (b), средний размер частиц шихты 0,068 мм

sented in publications [8; 9]. These studies have demonstrated that defects in pellets and irregularities in the SL can be mitigated through the application of a hardening charge coating created by gas spraying. During the spraying process, the ACJ not only applies to the surface but also exerts dynamic shear forces on the deeper layers of the SL, extending from its axis to its periphery. It is this action that is believed to lead to the emergence of elongated pore channels (Fig. 2, g, h, i) which contributes to the formation of open pores within the germ structure. Interestingly, these pores are oriented with a slight inclination in the direction opposite to the ACJ's point of impact.

In the central zone of the SL, channels are densely packed and exhibit minimal sizes, a characteristic attributed to the high-velocity force pressure of the ACJ moving across the SL surface and the increased fluidity of the mobile charge pulp extruded from the SL's depth to its surface. This same mechanism is implicated in the formation of porosity within the depth of the SL. The aggregation of the SL undergoes shear power loads

due to the dynamic pressure of the ACJ, which is directed from the SL axis towards the periphery, leading to a characteristic inclination of the pores in the direction opposite to the jet's attack. In the intermediate zone of the SL, where the ACJ dynamic pressure reaches its maximum, cavities become larger but much shorter, and their tortuosity and density increase. This zone also features a mix of open pores and a smaller number of irregularly shaped, closed-type pores. Towards the peripheral zone of the SL, total porosity significantly rises, with the number of channel-type pores sharply decreasing and only forming at the beginning of the zone. The pores at the end of this zone are predominantly of the closed type, larger, and their longitudinal and transverse dimensions vary substantially. To enhance the structural uniformity of germs in the SL peripheral zone and reduce the sizes of structural cavities and overall porosity of the sprayed mass, certain techniques have been suggested. These include increasing the charge moisture content, employing multi-jet spraying, and introducing stabilizing additives into the ACJ [8; 9]. The continued influence of the ACJ on the SL suggests that structure formation within its depth, regarding changes in pore sizes, their configuration, and spheroidization, can persist. The elongated shape of pores in the SL's horizontal cross-section (Fig. 2, *d, e, f*), which closely mirrors the projection of structural cavities on the SL surface (Fig. 2, *a, b, c*) indirectly supports this mechanism of structure formation. However, the complexity of these processes, occurring dynamically within a closed system and potentially influenced by the force effect of production unit enclosures and other related phenomena [22; 23]. As these processes occurring in the dynamic state in the closed system are complex and multifaceted, all the described mechanisms of structure formation are probabilistic in nature.

## CONCLUSIONS

The paper effectively elucidates the impact of heat-power spraying of wet charge on the intensification of production processes and the formation of structural properties of iron ore pellets. By presenting detailed investigations into the macro- and microstructures of germs, the study highlights the application of forced nucleation technology as a method to regulate structure formation and improve the metallurgical properties of iron ore pellets. A probable mechanism for porosity formation within the germ mass during the forming process, facilitated by heat-power spraying of wet charge onto the pelletizer skull, is meticulously outlined. Further, the paper delves into the potential of shaping the structural properties of iron ore pellets by manipulating the parameters of the germ mass through this technology, alongside the selection of appropriate technological characteristics for the sprayed material. The conducted research substantiates the involvement of the shear mechanism and

the movement of mobile charge pulp in the formation of germs' porosity, which is predicated on the dynamic influence of the air-charge jet on wet charge materials.

## REFERENCES / СПИСОК ЛИТЕРАТУРЫ

1. Pavlovets V.M. Pellets in Technology of Metals Extraction from Ores. Moscow, Vologda: Infra-Ingenierya; 2022:284.  
Павловец В.М. Окатыши в технологии экстракции металлов из руд. Москва, Вологда: Инфра-Инженерия; 2022:284.
2. Pavlovets V.M. Refractory and Heat-Insulating Materials. Novokuznetsk: SibSIU; 2015:334.  
Павловец В.М. Огнеупорные и теплоизоляционные материалы. Новокузнецк: СибГИУ; 2015:334.
3. Pivinskii Yu.E., Rozhkov E.V. Ceramic castables – final stage in the evolution of low-cement refractory castables. Part 3. *Refractories and Industrial Ceramics*. 2003;44(3):134–140.  
<https://doi.org/10.1023/A:1026391915300>
4. Abzalov V.M., etc. Physico-Chemical and Thermal Engineering Fundamentals for Iron Ore Pellets Production. Ekaterinburg: NPVP "TOREX"; 2012:340.  
Абзалов В.М. и др. Физико-химические и теплотехнические основы производства железорудных окатышей. Екатеринбург: НПВП «ТОРЕКС»; 2012:340.
5. Okeke S.I., Onukwuli O.D. Effect of basicity on metallurgical properties of pellets produced from Itakpe iron ore concentrates. *Discovery and Innovation*. 1999;11(3):170–176.  
<https://doi.org/10.4314/dai.v11i3.15549>
6. Frantes K. North American iron mines running flat out to meet domestic and worldwide demand. *Skullings' Mining Review*. 2005;94(7):6–21.
7. Basics in Mineral Processing. Metso: Outotec, 2015:752. Available at URL: [https://www.metso.com/globalassets/insights/ebooks/mo-basics-in-mineral-processing-handbook\\_lowres.pdf](https://www.metso.com/globalassets/insights/ebooks/mo-basics-in-mineral-processing-handbook_lowres.pdf)
8. Pavlovets V.M. Expanding the Functionality of Units for Preparing Iron Ore Raw Materials for Metallurgical Smelting. Moscow, Vologda: Infra-Ingenierya, 2023:328.  
Павловец В.М. Расширение функциональных возможностей агрегатов для подготовки железорудного сырья к металлургической плавке. Москва, Вологда: Инфра-Инженерия, 2023:328.
9. Pavlovets V.M. Development of Equipment and Technology for Pelletizing Iron Ore Raw Materials in Metallurgy. Moscow, Vologda: Infra-Engineering; 2022:336.  
Павловец В.М. Развитие техники и технологии окомкования железорудного сырья в металлургии. Москва, Вологда: Инфра-Инженерия; 2022:336.
10. Pavlovets V.M. Formation of the structure of iron ore pellets produced using heat-spraying of wet charge. *Izvestiya. Ferrous Metallurgy*. 2016;59(12):857–863. (In Russ.).  
<https://doi.org/10.17073/0368-0797-2016-12-857-863>  
Павловец В.М. Формирование структуры железорудных окатышей, полученных с использованием теплосилового напыления влажной шихты. *Известия вузов. Черная металлургия*. 2016;59(12):857–863.  
<https://doi.org/10.17073/0368-0797-2016-12-857-863>
11. Kudinov V.V., Bobrov G.V. Spray Coating, Theory, Technology and Equipment. Moscow: Metallurgiya; 1992:412.



- Кудинов В.В., Бобров Г.В. Нанесение покрытий напылением, теория, технология и оборудование. Москва: Металлургия; 1992:412.
12. Baldaev L.Kh., etc. Thermal Spraying. Moscow: Market DS; 2007:344.  
Балдаев Л.Х. и др. Газотермическое напыление. Москва: Маркет ДС; 2007:344.
  13. Poveromo J.J. Grade pellet quality and supply. AISTech (Assoc. Iron & Steel Technology). Annual Meeting. Indianapolis; 2015:751–762.
  14. Forsmo S.P.E., Samskog P.O., Bjorkman M.T. A study on plasticity and compression strength in wet iron ore green pellets related to real process variations in raw material fineness. *Powder Technology*. 2008;181(3):321–330.  
<https://doi.org/10.1016/j.powtec.2007.05.023>
  15. Wang Z.C., Chu M.S., Chen S.Q., Liu Z.G., Tang J., Xue X.X. Effects of B-Mg additive on metallurgical properties of oxidized pellets. *Advanced Materials Research*. 2011;284–286:1232–1236.  
<https://doi.org/10.4028/www.scientific.net/AMR.284-286.1232>
  16. Gnezdovets A.G., Kalita V.I. Model of formation of coatings macrostructure during plasma spraying. *Fizika i khimiya obrabotki materialov*. 2007;(1):30–39. (In Russ.).  
Гнездовец А.Г., Калита В.И. Модель формирования макроструктуры покрытий при плазменном напылении. *Физика и химия обработки материалов*. 2007;(1):30–39.
  17. Калита В.И., Комлев Д.И. Механизм формирования аморфной структуры в металлических сплавах при плазменном напылении. *Металлы*. 2003;(6):30–37.
  - Kalita V.I., Komlev D.I. Mechanism of formation of an amorphous structure in metal alloys during plasma spraying. *Metally*. 2003;(6):30–37. (In Russ.).
  18. Goejen J.G., Miller R.A., Brindley W.J., Leissler G.W. A simulation technique for predicting defects of thermal sprayed coatings: NASA Technical Memorandum TM-106939, 1995.
  19. Hansbo A., Nylén P. Models for the simulation of spray deposition and robot motion optimization in thermal spraying of rotating objects. *Surface and Coatings Technology*. 1999;122(3-4):191–201.  
[https://doi.org/10.1016/S0257-8972\(99\)00255-8](https://doi.org/10.1016/S0257-8972(99)00255-8)
  20. Enszt M.T., Griffith M.L., Reckaway D.E. Critical issues for functionally graded material deposition by laser engineered net shaping. Available at URL: <http://edge.cs.drexel.edu/GICL/people/schroeder/referenc es/mpif02me.pdf>
  21. De Los Santos Valladares L., Domínguez A.B., Félix L.L., Kargin J.B., Mukhambetov D.G., Kozlovskiy A.L., Moreno N.O., Santibañez J.F., Cabrera R.C., Barnes C.H.W. Characterization and magnetic properties of hollow  $\alpha$ -Fe<sub>2</sub>O<sub>3</sub> microspheres obtained by sol gel and spray roasting methods. *Journal of Science: Advanced Materials and Devices*. 2019;4(3):483–491.  
<https://doi.org/10.1016/j.jsamd.2019.07.004>
  22. Kamijo C., Hara M., Kawaguchi T., etc. Sinter feed granulation improvement technique by pan pelletizer. *Zairyo to Prosesu = CAMP ISIJ*. 2010;23(1):5.
  23. Watanabe K., Yasukawa M., Kamisaka C., etc. Improvement of productivity by installing P-type separate granulation process at Wakayama no. 5 sintering plant. *Zairyo to Prosesu = CAMP ISIJ*. 2010;23(1):6.

## Information about the Author

## Сведения об авторе

**Viktor M. Pavlovets**, Cand. Sci. (Eng.), Assist. Prof. of the Chair "Thermal Power and Ecology", Siberian State Industrial University  
E-mail: [pawlowets.victor@yandex.ru](mailto:pawlowets.victor@yandex.ru)

**Виктор Михайлович Павловец**, к.т.н., доцент кафедры теплоэнергетики и экологии, Сибирский государственный индустриальный университет  
E-mail: [pawlowets.victor@yandex.ru](mailto:pawlowets.victor@yandex.ru)

Received 11.05.2022  
Revised 16.11.2022  
Accepted 11.12.2023

Поступила в редакцию 11.05.2022  
После доработки 16.11.2022  
Принята к публикации 11.12.2023



UDC 669.052

DOI 10.17073/0368-0797-2024-1-27-36



Original article

Оригинальная статья

## JOINT PROCESSING OF PEROVSKITE AND ILMENITE CONCENTRATES. PART 1. CHEMICAL-MINERALOGICAL (MATERIAL) CHARACTERISTICS OF PEROVSKITE AND ILMENITE CONCENTRATES

S. A. Fedorov<sup>✉</sup>, L. Yu. Udoeva, A. S. Vusikhis,  
K. V. Pikulin, L. A. Cherepanova

Institute of Metallurgy, Ural Branch of the Russian Academy of Sciences (101 Amundsena Str., Yekaterinburg 620016, Russian Federation)

✉ saf13d@mail.ru

**Abstract.** Russia has an impressive titanium mineral resource while the contribution into the global production of titanium concentrates is quite insignificant. The current annual demand of Russian enterprises for titanium raw materials is 40 times higher than its production. To improve and launch the processing of domestic titanium raw materials characterized by low quality and complex polymineral composition, new process solutions are required. These solutions should aim at the full extraction of  $\text{TiO}_2$  and related valuable components from the ore deposits whose development is planned or already started (for example, Afrikanda – perovskite-titanomagnetite deposit located on the Kola Peninsula). This report presents the results of studying the chemical and mineral compositions of perovskite and ilmenite concentrates with the purpose to assess the possibility of their joint processing using carbothermic reduction melting. Emission spectrometry,  $X$ -ray diffraction, electron microscopy, and  $X$ -ray spectral microanalysis were applied in these studies. It was found that the basis of the ilmenite gravity concentrate sample is modified ilmenite represented by leucoxenization products – pseudorutile and rutile, with their total content in the concentrate to be about 80 wt. %. Composition of other minerals (alumochromite, chromite, magnetite) includes titanium in the form of impurities – 2 – 3 wt. %. In the perovskite flotation concentrate sample titanium is contained in perovskite and titanite making up the bulk of the ore minerals of the concentrate. As for rare and rare-earth elements contained in the ilmenite sample – monazite having up to 33 wt. % Ce, and zircon were found. Perovskite sample contains rare-earth elements (REE concentration in wt. %) in loparite-(Ce) (22.8), aluminocerite-(Ce) (46.2), ancylite-(Ce) (51.3), torite (22.3), as well as in the main mineral – perovskite (2.8). With the exception of perovskite and loparite-(Ce), other REE-containing minerals are rare, and their share in total does not exceed 1 wt. %.

**Keywords:** titanium raw materials, ilmenite, pseudorutile, perovskite, concentrate, chemical composition, mineral composition, microstructure

**Acknowledgements:** The work was performed according to the State task of the Institute of Metallurgy of Ural Branch of the Russian Academy of Sciences (no. of the state registration: 122020100404-2) using the equipment of the Center for Collective Use “Ural-M”.

**For citation:** Fedorov S.A., Udoeva L.Yu., Pikulin K.V., Vusikhis A.S., Cherepanova L.A. Joint processing of perovskite and ilmenite concentrates. Part 1. Chemical-mineralogical (material) characteristics of perovskite and ilmenite concentrates. *Izvestiya. Ferrous Metallurgy*. 2024;67(1):27–36. <https://doi.org/10.17073/0368-0797-2024-1-27-36>

# СОВМЕСТНАЯ ПЕРЕРАБОТКА ПЕРОВСКИТОВОГО И ИЛЬМЕНИТОВОГО КОНЦЕНТРАТОВ. СООБЩЕНИЕ 1. ХИМИКО-МИНЕРАЛОГИЧЕСКАЯ (ВЕЩЕСТВЕННАЯ) ХАРАКТЕРИСТИКА ПЕРОВСКИТОВОГО И ИЛЬМЕНИТОВОГО КОНЦЕНТРАТОВ

С. А. Федоров<sup>✉</sup>, Л. Ю. Удоева, А. С. Вусихис,  
К. В. Пикулин, Л. А. Черепанова

■ Институт металлургии Уральского отделения РАН (Россия, 620016, Екатеринбург, ул. Амундсена, 101)

✉ saf13d@mail.ru

**Аннотация.** Россия обладает внушительной минерально-сырьевой базой титана, при этом ее вклад в мировое производство титановых концентратов ничтожно мал. Текущая годовая потребность российских предприятий в титановом сырье в 40 раз выше его производства. Для вовлечения в переработку отечественного титанового сырья, для которого характерно низкое качество и сложный полиминеральный состав, необходимы новые технологические решения, позволяющие полноценно извлекать  $\text{TiO}_2$  и сопутствующие ценные компоненты из руд месторождений, освоение которых планируется или уже началось (например, перовскит-титаномagnetитовое месторождение Африканда на Кольском полуострове). В настоящем сообщении представлены результаты изучения химического и минерального составов перовскитового и ильменитового концентратов для оценки возможности их совместной переработки путем карботермической восстановительной плавки. В исследованиях использованы методы эмиссионной спектроскопии, рентгеновской дифракции, электронной микроскопии и рентгеноспектрального микроанализа. Установлено, что в пробе ильменитового гравитационного концентрата основу составляет измененный ильменит, представленный продуктами лейкоксенизации – псевдорутилом и рутилом, суммарная доля которых в концентрате около 80 мас. %. В незначительных количествах титан встречается в составе других минералов (алюмохромит, хромит, магнетит) в качестве примесей (2 – 3 мас. %). В пробе перовскитового флотоконцентрата титан содержится в перовските и титаните, составляющих основную часть рудных минералов концентрата. Из минералов редких и редкоземельных элементов (РЗЭ) в ильменитовой пробе обнаружены монацит, содержащий до 33 мас. % Се, и циркон. В перовскитовой пробе РЗЭ находятся (концентрация РЗЭ в мас. %) в лопарите-(Се) (22,8), алюиноцерите-(Се) (46,2), анкилите-(Се) (51,3), торите (22,3), а также в основном минерале – перовските (2,8). За исключением перовскита и лопарита-(Се), другие РЗЭ-содержащие минералы встречаются редко, и их доля в сумме не превышает 1 мас. %.

**Ключевые слова:** титановое сырье, ильменит, псевдорутил, перовскит, концентрат, химический состав, минеральный состав, микроструктура

**Благодарности:** Работа выполнена по Государственному заданию ИМЕТ УрО РАН (№ гос. регистрации темы: 122020100404-2) с использованием оборудования ЦКП «Урал-М».

**Для цитирования:** Федоров С.А., Удоева Л.Ю., Пикулин К.В., Вусихис А.С., Черепанова Л.А. Совместная переработка перовскитового и ильменитового концентратов. Сообщение 1. Химико-минералогическая (вещественная) характеристика перовскитового и ильменитового концентратов. *Известия вузов. Черная металлургия*. 2024;67(1):28–36. <https://doi.org/10.17073/0368-0797-2024-1-27-36>

## INTRODUCTION

Russia possesses a significant titanium mineral resource [1; 2]. According to 2019 data from the Ministry of Natural Resources and Environment, Russia accounts for 12.5 % of the world's reserves. However, its contribution to the global production of titanium concentrates is relatively minor – only 0.04 % (about 9000 tons). Tugansky MPP “Ilmenite,” the sole producer of titanium concentrate in Russia, manages this production. Concurrently, data from FSBI VIMS indicates that the current annual demand for titanium raw materials by Russian enterprises is approximately 365,000 tons. Nearly all of this demand is met by imported ilmenite (about 340,000 tons) and rutile (about 12,000 tons) concentrates. Only 13,000 tons of domestic raw material, the loparite concentrate, are supplied to Russian companies.

The primary reason for this situation is that the main reserves of titanium in the Russian Federation, estimated

at 587.6 million tons of  $\text{TiO}_2$  as of January 2022, are found in polymetallic ores. The efficiency of processing these ores is determined by the potential for associated extraction of other valuable components. One of the unique Russian deposits of complex polymetallic ores is located on the Kola Peninsula, in the Afrikanda settlement. These ores are perovskite-titanomagnetite, containing not only titanium and iron but also rare elements (tantalum, niobium), rare-earth elements (lanthanum, cerium, etc.), and radioactive metals (thorium), with total reserves exceeding 626 million tons. The content of perovskite is 21.5 %, and titanomagnetite is 2.5 % [4 – 6]. The Afrikanda deposit was discovered a century ago, in 1917. In the 1930s, there was an attempt to obtain concentrates for titanium and thorium production, and in the 1950s, for the needs of ferrous metallurgy. Both projects failed, and in 1972, the titanium ore reserves of Afrikanda were removed from the State Register of Reserves.

The current economic and social level of the Kola Region allows for the reconsideration of the cost-effective development of the Afrikanda deposit. The Kola Scientific Center of the Russian Academy of Sciences has developed an effective magnetic-flotation scheme for enriching perovskite-titanomagnetite ores. This scheme includes magnetic separation of the initial ore to extract titanomagnetite concentrate and flotation of the non-magnetic fraction to extract perovskite concentrate [5; 6]. The titanomagnetite concentrate, containing up to 8 %  $\text{TiO}_2$ , is primarily of interest as raw material for ferrous metallurgy, suitable for processing in a classic manner, including blast furnace smelting, as well as using the electro-thermal method with the potential for associated extraction of vanadium [8 – 10].

Perovskite concentrates represent unconventional titanium raw materials that necessitate complex processing to produce titanium dioxide and compounds of associated components. For Afrikanda concentrates, several hydrometallurgical technologies have been developed. These technologies involve decomposing the concentrates with mineral acids, converting all components into salt solutions or hydrate products, and then extracting titanium dioxide, rare metals, and rare-earth elements [11; 12]. The proposed schemes, which have been tested on a pilot scale, are realistic and hold promise. However, like all hydrometallurgical technologies, they entail lengthy multi-stage processes, including leaching, precipitation, thickening, filtration, etc., and lead to the accumulation of hazardous effluents needing disposal. Researchers [13] have explored pyrometallurgical solutions to the processing of perovskite concentrates, attempting to address the challenges associated with hydrometallurgical methods. One proposal involves obtaining titanium carbide and metallic calcium through a two-stage reduction smelting process. It is important to note that perovskite raw materials are not utilized for titanium production outside of Russia.

Ilmenite ores, which are significantly found in the Gremyakha-Vyrmes Massif on the Kola Peninsula, differ from perovskite ores in that they satisfy approximately 90 % of the global demand for titanium-containing raw materials used in the production of metallic titanium, titanium dioxide, and carbide. To process the relatively resistant ilmenite mineral, various methods are employed, including pyrometallurgical processes, acid decomposition at high temperatures, and combined approaches [14 – 16]. Most pyrometallurgical technologies rely on reduction smelting using carbon-containing [17 – 19] or combined [20] reducing agents, which is enhanced by the pre-oxidation of the ilmenite concentrate [21; 22]. It is observed [23] that electric smelting of ilmenite concentrates with coal results in the formation of slags with a titanium content similar to that of perovskite but are more readily dissolved by acids. To lower the reduction smelting temperature of ilmenite in the ore-thermal furnace, calcium oxide is added to the mixture. This addition helps to adjust

the ratio of  $\text{TiO}_2$  and  $\text{CaTiO}_3$ , ensuring a slag melting temperature of 1400 – 1450 °C [24]. It is proposed that achieving the desired  $\text{TiO}_2/\text{CaTiO}_3$  in the titanium slag could be more efficiently accomplished by incorporating perovskite concentrate, based on calcium titanate  $\text{CaTiO}_3$ , rather than calcium oxide, into the ilmenite concentrate smelting charge. This approach will not significantly alter the titanium content in the slag but will facilitate the processing of titanium raw materials with diverse mineral compositions of the concentrate ore components within a unified workflow system.

In our study, we explored the feasibility of jointly processing perovskite and ilmenite concentrates through carbothermic reduction smelting. This method aims to extract rare metals into cast iron and generate a titanium-rich slag that is amenable to the hydrometallurgical extraction of titanium and rare earth elements. Given that the phase composition and distribution of components within the mineral components of titanium-containing concentrates play a crucial role in dictating the interaction mechanisms during processing, the initial phase of our research concentrated on determining the chemical and material compositions. We also examined the microstructure of perovskite and ilmenite concentrate samples selected for analysis.

## MATERIALS AND METHODS

To conduct chemical analysis of the averaged concentrate samples, a Spectroflame Modula S inductively coupled plasma atomic emission spectrometer (ICP-AES) was utilized.

The phase composition of the samples was determined using X-ray powder diffraction (XRD) with a Shimadzu XRD 7000C diffractometer. The diffractometer operated under the following conditions:  $\text{CuK}_\alpha$  radiation ( $\lambda = 0.154051$  nm), with a voltage of 34 kV and a current of 40 mA. Data were collected across a  $2\theta$  range from 20 to 80 – 90°, in 0.02° increments, with a point exposure time of 2.0 s. Phase identification was performed using the International Centre for Diffraction Data (ICDD) PDF-4 database [25]. The quantitative assessment of the phase composition was carried out through Rietveld full-profile analysis [26], employing the TOPAS software [27].

For the investigation of the microstructure and the elemental analysis of minerals composing the concentrates, a Carl Zeiss EVO 40 scanning electron microscope (SEM) equipped with an HKL Channel 5 EBSD (Premium) energy dispersive attachment was used. The images of the samples' microstructure were captured using the backscattered electrons (BSE) detector.

## RESULTS AND DISCUSSION

The ilmenite sample closely mirrors the major elements found in the gravity concentrate from the Gremyakha-Vyrmes deposit [28], while the perovskite mate-



**Table 1. Chemical composition of the ilmenite and perovskite concentrates**

**Таблица 1. Химический состав ильменитового и перовскитового концентратов**

Concentrate	Content of main components, wt. %								
	TiO <sub>2</sub>	Fe <sub>tot</sub>	Al <sub>2</sub> O <sub>3</sub>	CaO	MgO	Cr <sub>2</sub> O <sub>3</sub>	CeO <sub>2</sub>	SiO <sub>2</sub>	Nb <sub>2</sub> O <sub>5</sub>
Ilmenite	69.11	18.90	2.89	0.18	0.36	0.88	–	1.92	–
Perovskite	34.66	7.23	1.34	23.49	2.77	–	0.60	11.23	1.16

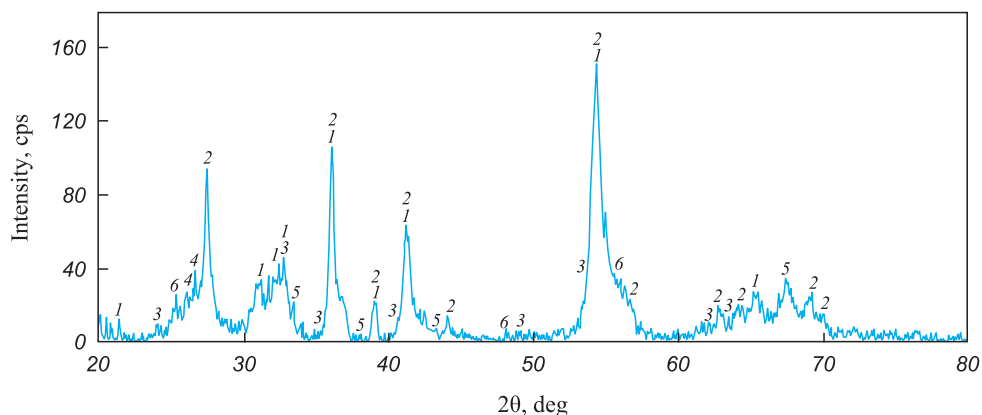
rial corresponds to a rough flotation concentrate from the Afrikanda deposit [29]. The chemical analysis results of the concentrate samples are presented in Table 1.

According to the X-ray phase study (Fig. 1, Table 2), the ilmenite concentrate primarily consists of Fe<sub>2</sub>Ti<sub>3</sub>O<sub>9</sub> pseudorutile (48 wt. %) and rutile (29 wt. %). This composition is typical for concentrates of the so-called altered ilmenite, which forms as a result of its leucogenization. The actual content of ilmenite in the concentrate is only 7 wt. %. Aluminum and silicon are concentrated in staurolite and sillimanite. The main mineral constituents of the perovskite concentrate (Fig. 2, Table 3) are perovskite (56 %), calcite (13 %), and titanite (11 %).

Iron is present in the forms of magnetite, ulvospinel, and fayalite, while silicon is found in fayalite and quartz.

Overall, the mineral composition of the investigated materials aligns with their chemical composition.

The ilmenite concentrate sample is a loose, fine-grained material obtained during the gravity concentration of the original ore. The majority of the grains exhibit a well-pelletized shape, with their sizes ranging from 10 to 300 μm. For most grains, this parameter lies between 150 and 200 μm (Fig. 3). The concentrate is primarily composed of pseudorutile, rutile, staurolite, and quartz. The study also revealed the presence of minerals from the spinel group (including picotite, alumochromite, chromite, hercynite, aluminomagnetite, gahnite, and magnetite), monazite, Mg and Fe aluminosilicates, sillimanite, and zircon. This complex assortment of ore components is characteristic of ilmenite placers [30].



**Fig.1.** XRD pattern of the ilmenite concentrate:

1, 3 – Fe<sub>2</sub>Ti<sub>3</sub>O<sub>9</sub>; 2 – TiO<sub>2</sub> (rutile); 4 – FeTiO<sub>3</sub>; 5 – Al[AlSiO<sub>5</sub>]; 6 – (Fe, Mg)<sub>2</sub>Al<sub>2</sub>[(Si, Al)O<sub>4</sub>]<sub>4</sub>O<sub>4</sub>[OH]<sub>2</sub>; 7 – TiO<sub>2</sub> (anatase)

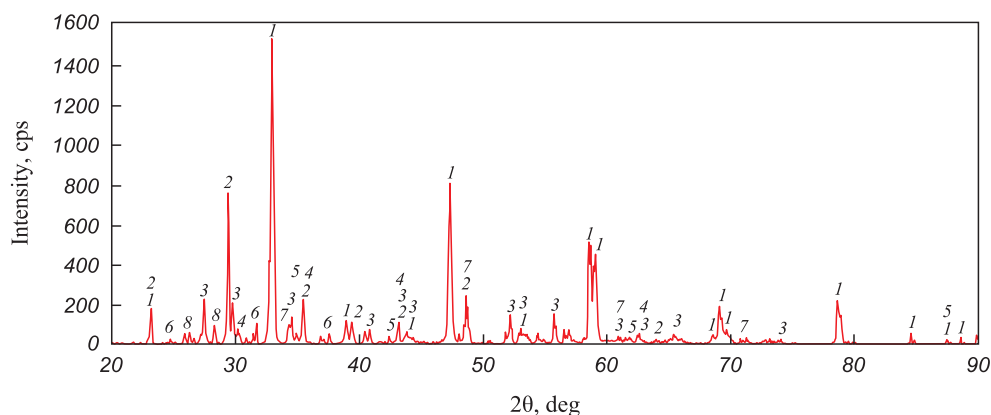
**Рис. 1.** Дифрактограмма ильменитового концентрата:

1, 3 – Fe<sub>2</sub>Ti<sub>3</sub>O<sub>9</sub>; 2 – TiO<sub>2</sub> (рутил); 4 – FeTiO<sub>3</sub>; 5 – Al[AlSiO<sub>5</sub>]; 6 – (Fe, Mg)<sub>2</sub>Al<sub>2</sub>[(Si, Al)O<sub>4</sub>]<sub>4</sub>O<sub>4</sub>[OH]<sub>2</sub>; 7 – TiO<sub>2</sub> (анатаз)

**Table 2. Phase composition of the ilmenite concentrate (phase numbering according to Fig. 1)**

**Таблица 2. Фазовый состав ильменитового концентрата (нумерация фаз по рис. 1)**

Phase	Mineral	Formula	Content, wt. %
1, 3	Pseudorutile	Fe <sub>2</sub> Ti <sub>3</sub> O <sub>9</sub>	48
2	Rutile	TiO <sub>2</sub>	29
4	Ilmenite	FeTiO <sub>3</sub>	7
5	Sillimanite	Al [AlSiO <sub>5</sub> ]	7
6	Staurolite	(Fe, Mg) <sub>2</sub> Al <sub>2</sub> [(Si, Al)O <sub>4</sub> ] <sub>4</sub> O <sub>4</sub> [OH] <sub>2</sub>	5
7	Anatase	TiO <sub>2</sub>	4



**Fig. 2.** XRD pattern of the perovskite concentrate:

1, 7 –  $\text{CaTiO}_3$ ; 2 –  $\text{CaCO}_3$ ; 3 –  $\text{CaTi}[\text{SiO}_4]\text{O}$ ; 4 –  $\text{Fe}_3\text{O}_4$ ; 5 –  $\text{Fe}_2\text{TiO}_4$ ; 6 –  $\text{Fe}_2[\text{SiO}_4]$ ; 8 –  $\text{SiO}_2$

**Рис. 2.** Дифрактограмма перовскитового концентрата:

1, 7 –  $\text{CaTiO}_3$ ; 2 –  $\text{CaCO}_3$ ; 3 –  $\text{CaTi}[\text{SiO}_4]\text{O}$ ; 4 –  $\text{Fe}_3\text{O}_4$ ; 5 –  $\text{Fe}_2\text{TiO}_4$ ; 6 –  $\text{Fe}_2[\text{SiO}_4]$ ; 8 –  $\text{SiO}_2$

**Table 3.** Phase composition of the perovskite concentrate (phase numbering according to Fig. 2)

**Таблица 3.** Фазовый состав перовскитового концентрата (нумерация фаз по рис. 2)

Phase	Mineral	Formula	Content, wt. %
1, 7	Perovskite	$\text{CaTiO}_3$	56
2	Calcite	$\text{CaCO}_3$	13
3	Titanite	$\text{CaTi}[\text{SiO}_4]\text{O}$	11
4	Magnetite	$\text{Fe}_3\text{O}_4$	5
5	Ulvospinel	$\text{Fe}_2\text{TiO}_4$	7
6	Fayalite	$\text{Fe}_2\text{SiO}_4$	2
8	Quartz	$\text{SiO}_2$	6

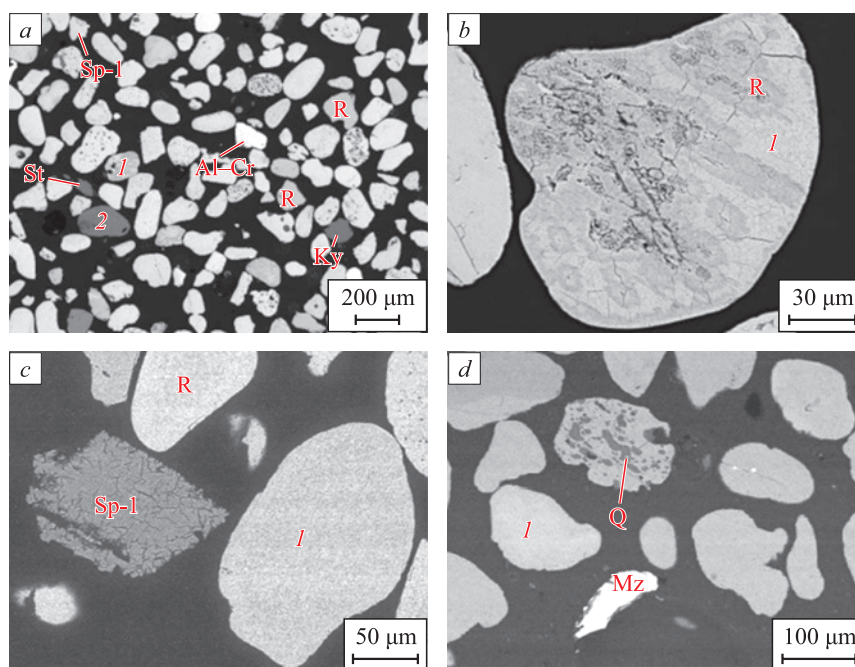
Pseudorutile is characterized by well-rounded grains (Fig. 3, *a*), which are often ellipsoidal and spherical in shape, according to the A.V. Khabakov scale [31]. Quartz inclusions, as well as less frequently zircon and magnetite inclusions, occupy the recesses on the surfaces of pseudorutile grains and fill voids of irregular or prismatic shapes. Some grains exhibit a large number of unfilled pores, indicating a porous texture. The chemical composition of the mineral varies, with magnesium admixtures reaching up to 1.2 wt. %, and manganese up to 2.6 wt. %.

Rutile, another major titanium mineral in the concentrate, appears in elongated, prismatic, and isometric shapes, ranging from well- to medium-rounded grains (Fig. 3, *a*). These grains are comparable in size to pseudorutile grains, measuring 100 – 200  $\mu\text{m}$ . Rutile contains iron impurities, with a maximum content of 9.6 wt. % and an average of 2.2 wt. %. Some medium-rounded grains, which have a cross-sectional shape close to rhombic, are likely to be anatase, another polymorphic modification of  $\text{TiO}_2$ . It is noteworthy that polymineral grains with clear signs of secondary alteration of ilmenite, known as

leucoxenization, are present. These grains are composed of pseudorutile and rutile and often include quartz inclusions (Fig. 3, *b*). To identify the products of ilmenite leucoxenization, we utilized the criterion proposed in [32], specifically the ratio of  $\text{Ti}/(\text{Ti} + \text{Fe})$ , which averaged 0.68 for pseudorutile grains and 0.96 for rutile in the studied sample of ilmenite concentrate.

In the studied sample of ilmenite concentrate, seven minerals from the spinel group were identified: picotite ( $(\text{Fe}, \text{Mg})(\text{Al}, \text{Cr})_2\text{O}_4$ ), aluminochromite ( $\text{Fe}(\text{Cr}, \text{Al})_2\text{O}_4$ ), chromite ( $\text{FeCr}_2\text{O}_4$ ), ganite ( $\text{ZnAl}_2\text{O}_4$ ), hercynite ( $\text{FeAl}_2\text{O}_4$ ), aluminomagnetite ( $\text{Fe}^{2+}(\text{Fe}^{3+}, \text{Al})_2\text{O}_4$ ) and magnetite ( $\text{Fe}^{2+}\text{Fe}_2^{3+}\text{O}_4$ ). The grains of these minerals ranging in size from 50 to 200  $\mu\text{m}$ , are poorly rounded and have an isometric shape. Octahedral crystals and their fragments also occur (Fig. 3, *a*). The chemical composition of minerals varies within the plane of section. Picotite, most commonly found in association with rutile and pseudorutile (Fig. 3, *c*), shows variability in its composition. Aluminochromite and chromite, with titanium admixtures of 0.2 – 3.0 wt. % and 2.6 wt. % respectively, are encountered less frequently. Ganite and magnetite, both with a titanium admixture of 2.6 wt. %, along with spinel exhibiting a zonal structure, are observed as singular grains. The core of the spinel is composed of hercynite, while the periphery consists of aluminomagnetite.

Among the accessory and other ore minerals, monazite ( $\text{CePO}_4$ ) and zircon ( $\text{Zr}[\text{SiO}_4]$ ) were identified. Monazite is represented by elongated wedge-shaped grains, 150 – 200  $\mu\text{m}$  in length, associated with pseudorutile (Fig. 4, *d*). It contains cerium (27.5 – 47.3 wt. %) and impurities such as lanthanum (up to 13.7 wt. %), neodymium (up to 12.5 wt. %), thorium (up to 7.1 wt. %), and praseodymium (up to 4.3 wt. %). Zircon, found as inclusions in pseudorutile, exhibits a shape close to a tetragonal prism, with grain sizes ranging from 1 to 10  $\mu\text{m}$  in length and up to 5  $\mu\text{m}$  in cross section.

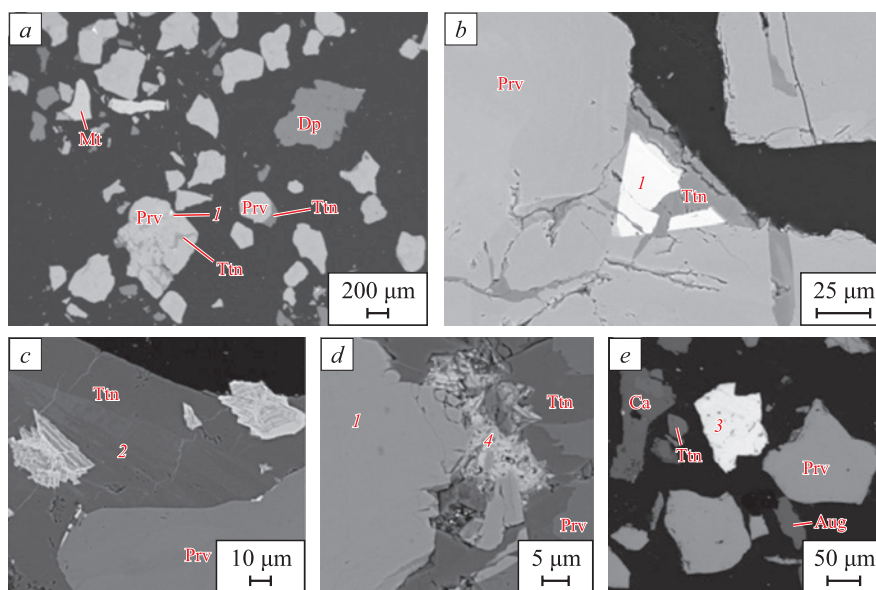


**Fig. 3.** BSE-images of the ilmenite concentrate:

*a* – general view (*I* – pseudorutile, *R* – rutile, Al–Cr – aluminochromite, *St* – staurolite, *Ky* – sillimanite, *Sp-1* – picotite, 2 – Mg and Fe aluminosilicate); *b* – grain of modified ilmenite, consisting of pseudorutile and rutile; *c* – octahedral crystal of picotite (*Sp-1*), covered with cracks; *d* – monazite grain (*Mz*), close to tabular shape, *Q* – quartz

**Рис. 3.** BSE-изображения ильменитового концентрата:

*a* – общий вид (*I* – псевдорутит, *R* – рутил, Al–Cr – алюмохромит, *St* – ставролит, *Ky* – силлиманит, *Sp-1* – пикотит, 2 – алюмосиликат Mg и Fe); *b* – зерно измененного ильменита, состоящее из псевдорутита и рутила; *c* – октаэдрический кристалл пикотита (*Sp-1*), покрытый трещинами; *d* – зерно монацита (*Mz*), близкое к таблитчатой форме, *Q* – кварц



**Fig. 4.** BSE-images of the perovskite concentrate:

*a* – general view (*Prv* – perovskite, *Mt* – magnetite with an impurity of titanium, *Dp* – diopside, *Ttn* – titanite, *I* – loparite-(Ce)); *b* – loparite-(Ce) intergrown with perovskite and titanite; *c* – aluminocerite-(Ce) grains (2) as inclusions in titanite associated with perovskite; *d* – prismatic thorite crystals (4) in association with loparite-(Ce), titanite, and perovskite; *e* – ancyrite-(Ce) grain (3) in association with calcite (*Ca*), perovskite, and augite (*Aug*)

**Рис. 4.** BSE-изображения перовскитового концентрата:

*a* – общий вид (*Prv* – перовскит, *Mt* – магнетит с примесью титана, *Dp* – диопсид, *Ttn* – титанит, *I* – лопарит-(Ce)); *b* – лопарит-(Ce) в ростке с перовскитом и титанитом; *c* – зерна алюиноцерита-(Ce) (2) в виде включений в титаните, ассоциированном с перовскитом; *d* – призматические кристаллы торита (4) в ассоциации с лопаритом-(Ce), титанитом и перовскитом; *e* – зерно анкилита-(Ce) (3) в ассоциации с кальцитом (*Ca*), перовскитом и авгитом (*Aug*)

The concentrate also contains rock-forming minerals such as Mg and Fe aluminosilicate, sillimanite, staurolite, and quartz. Aluminosilicate is present in both isometric and elongated grains, nearing prismatic in shape, with grain sizes ranging from 150 to 300  $\mu\text{m}$ . Sillimanite and staurolite form grains that are poorly to medium rounded and prismatic in shape, with their sizes not exceeding 100 – 200  $\mu\text{m}$  and 200 – 300  $\mu\text{m}$ , respectively. Quartz (Q) occurs exclusively as inclusions in pseudorutile, with sizes ranging from less than 1 to 60  $\mu\text{m}$  (Fig. 3, *d*).

The perovskite concentrate, a rough flotation concentrate from the Afrikanda deposit, is a loose, crushed material with the grain size ranging from 20 to 300  $\mu\text{m}$  (Fig. 4, *a*). The grains, predominantly isometric, irregular, and prismatic, are prevalent. The concentrate contains two major titanium minerals, perovskite and titanite, along with loparite-(Ce), aluminocerite-(Ce), ancylite-(Ce), thorite, magnetite, diopside, calcite, ulvospinel, fayalite, phlogopite, enstatite, aegirine, and augite. Perovskite is the most abundant mineral in the concentrate, forming isometric grains that range in size from 20 to 1000  $\mu\text{m}$  (Fig. 4, *b*), and its shape is sometimes close to cubic. The cracks in perovskite are mostly filled with titanite and rare earth elements, and these cracks can exceed 100  $\mu\text{m}$ .

Titanite is the second most abundant titanium mineral in the sample. It often fills cracks and cavities in perovskite (Fig. 4), but individual wedge-shaped crystals are also found, with sizes ranging from a few micrometers to 200  $\mu\text{m}$ . The mineral contains impurities of iron (0.7 – 5.0 wt. %) and aluminum (0.3 – 2.5 wt. %). Another titanium-bearing mineral, loparite-(Ce), with the general formula  $(\text{Ce}, \text{Na}, \text{Ca})(\text{Ti}, \text{Nb})\text{O}_3$ , forms crystals that are close in shape to octahedrons and cubes, with sizes ranging from 50 to 120  $\mu\text{m}$  (Fig. 4, *b*). These crystals occur in very small quantities as impregnations and intergrowths with perovskite and titanite, and less frequently as intergrowths with magnetite. The impregnations can be up to 100  $\mu\text{m}$  in size. Loparite-(Ce) contains cerium (15.4 – 20.5 wt. %), neodymium impurities (3.5 – 6.8 wt. %), thorium (1.2 – 1.6 wt. %), and occasional grains of niobium (3.1 – 8.2 wt. %).

In addition to loparite-(Ce), the perovskite concentrate sample contains three other rare earth element (REE)-bearing minerals in the form of single grains: aluminocerite-(Ce), ancylite-(Ce), and thorite, as indicated by elemental analysis. Aluminocerite-(Ce), with the formula  $(\text{Ce}, \text{Ca})_9\text{Al}[\text{SiO}_4]_3[\text{SiO}_3(\text{OH})]_4(\text{OH})_3$ , forms isometrically shaped grains ranging in size from 5 to 100  $\mu\text{m}$  (Fig. 4, *c*). At high magnification, some of these grains exhibit a layered texture, composed of oriented tabular crystals, zoning, and a structure reminiscent of solid solution decomposition. Ancylite-(Ce) is sometimes found in the central part of the grain. The major impurities in aluminocerite-(Ce) include lanthanum (6.8 – 14.1 wt. %), neodymium (5.8 – 9.8 wt. %), and thorium (1.3 – 3.7 wt. %), with cerium content ranging from 24.3 to 42.1 wt. %.

Ancylite-(Ce), with the formula  $\text{CeSr}(\text{CO}_3)_2(\text{OH})\cdot\text{H}_2\text{O}$ , is characterized by isometric grains and irregularly shaped particles of varying sizes, from less than 2 to 150  $\mu\text{m}$  (Fig. 4, *e*). It forms inclusions in titanite and perovskite, as well as individual large grains and crystalline aggregates. The cerium content in this mineral ranges from 25.3 to 30.1 wt. %, with impurities including lanthanum (14.4 – 18.3 wt. %) and neodymium (5.7 – 10.4 wt. %). Thorite is represented by prismatic, zonal crystals and their aggregates, with lengths up to 5  $\mu\text{m}$  and thicknesses up to 2  $\mu\text{m}$  (Fig. 4, *d*). This mineral fills voids and cracks in titanite and perovskite, containing impurities such as yttrium (5.2 – 7.8 wt. %), gadolinium (2.8 – 3.5 wt. %), phosphorus (0.8 – 1.2 wt. %), and aluminum (0.4 – 0.6 wt. %). However, some of the rare earth elements in its chemical composition may be attributable to the surrounding perovskite and loparite.

The last of the ore minerals in the perovskite concentrate is magnetite, which occurs as isometric grains and fragments of octahedral crystals. The surface of the magnetite displays signs of dissolution, and the mineral contains small admixtures of titanium (0.5 – 0.7 wt. %). In some grains, the lamellar structure resulting from the decomposition of the titanium-magnetite solid solution was observed, with the formation of ulvospinel veinlets.

The rock-forming minerals in the perovskite concentrate sample include calcite, fayalite with a small admixture of magnesium  $(\text{Fe}, \text{Mg})_2[\text{SiO}_4]$ , phlogopite  $\text{KMg}_3\text{AlSi}_3\text{O}_{10}(\text{OH})_2$ , enstatite  $\text{Mg}_2[\text{Si}_2\text{O}_6]$ , aegirine  $\text{NaFe}[\text{Si}_2\text{O}_6]$  and augite  $(\text{Ca}, \text{Mg}, \text{Fe})_2[(\text{Si}, \text{Al})_2\text{O}_6]$ . Calcite is frequently found in the sample, forming large rhombohedral crystals and their aggregates (more than 1 mm). The other minerals are present in very small quantities, appearing as prismatic or tabular grains in the form of inclusions or aggregates with titanite or perovskite. Calcite also sometimes forms a crust around magnetite grains and fills cracks in the mineral.

In general, the investigation of the material composition of the perovskite concentrate sample yielded results consistent with data from literary sources [33; 34], except for the minerals containing REE (aluminocerite-(Ce), ancylite-(Ce), and thorite).

## CONCLUSIONS

The investigations into the chemical and mineralogical composition of ilmenite and perovskite concentrates, along with the assessment of the distribution of their valuable components by structural elements, have enabled us to draw the following conclusions.

Almost all of the titanium in the ilmenite sample is concentrated in pseudorutile and rutile – products of the leucoxenization of ilmenite, i.e., its alteration (weathering), which accounts for a significant portion of the concentrate. Titanium is also found as an impurity



in aluminochromite, chromite, and magnetite, with its content not exceeding 2–3 wt. %.

The non-metallic part of the ilmenite sample comprises seven minerals from the spinel group, nearly half of which are chromspinelids. Additionally, we found monazite, containing up to 33 wt. % Ce, and zircon; the former occurs as single grains and is found more frequently than zircon.

In the perovskite sample, titanium is primarily represented by the main ore minerals of the concentrate – perovskite and titanite. The rare-earth element cerium is present in the form of specific minerals (loparite-(Ce), aluminocerite-(Ce), ancyllite-(Ce), thorite) or as an admixture in perovskite (2.8 wt. % Ce). Except for perovskite and loparite-(Ce), REE-bearing minerals are rare, and their total share in the concentrate does not exceed 1 wt. %. Loparite-(Ce) comprises cerium (18.0 wt. %), neodymium impurities (5.2 wt. %), thorium (1.4 wt. %), and isolated grains of niobium (up to 8.2 wt. %).

## REFERENCES / СПИСОК ЛИТЕРАТУРЫ

1. Nikolaev A.I., Larichkin F.D., Gerasimova L.G., etc. Titanium and Its Compounds: Resources, Production, Markets, Prospects. Apatity: Kola Science Centre, RAS; 2011:152. (In Russ.).  
Николаев А.И., Ларичкин Ф.Д., Герасимова Л.Г. и др. Титан и его соединения: ресурсы, производство, рынки, перспективы. Апатиты: КНЦ РАН; 2011:152.
2. Bykhovskii L.Z., Tiginov L.P. Titanium raw materials of Russia. *Rossiiskii Khimicheskii Zhurnal*. 2010;(2(54)): 73–86. (In Russ.).  
Быховский Л.З., Тигунов Л.П. Титановое сырье России. *Российский химический журнал*. 2010;(2(54)):73–86.
3. State report on the state and use of mineral resources of the Russian Federation in 2019. Moscow: Ministry of Natural Resources and Ecology of the Russian Federation. 2020:493. (In Russ.).  
Государственный доклад о состоянии и использовании минерально-сырьевых ресурсов Российской Федерации в 2019 году. Москва: Министерство природных ресурсов и экологии Российской Федерации; 2020:493.
4. Tochilo M.V., Fedoseev S.V., Larichkin F.D., Novosel'tseva V.D., Gorbovskikh A.V. Prospects and approaches to forming the strategy for the development of the titanium industry in the north-west region of Russia. *Sever i Rynok: Formirovanie ekonomicheskogo poriadka*. 2019;(3(65)): 99–108. (In Russ.).  
Точилю М.В., Федосеев С.В., Ларичкин Ф.Д., Новосельцева В.Д., Горбовских А.В. Перспективы и подходы к формированию стратегии развития титановой промышленности в северо-западном регионе России. *Север и рынок: формирование экономического порядка*. 2019;(3(65)):99–108.
5. Andronov G.P., Filimonova N.M., Khokhulya M.S. Separation of titanium-containing minerals by magnetic separation. *Vestnik MGTU*. 2019;(1(22)):109–119. (In Russ.).  
<https://doi.org/10.21443/1560-9278-2019-22-1-109-119>  
Андронов Г.П., Филимонова Н.М., Хохуля М.С. Разделение титаносодержащих минералов магнитной сепарацией. *Вестник МГТУ*. 2019;(1(22)):109–119.  
<https://doi.org/10.21443/1560-9278-2019-22-1-109-119>
6. Khokhulya M.S., Gerasimova L.G., Nikolaev A.I. New technological solutions for the preparation and processing of perovskite. In: *Trudy Kol'skogo Nauchnogo Tsentra RAN*. 2018:196–200. (In Russ.).  
Хохуля М.С., Герасимова Л.Г., Николаев А.И. Новые технологические решения подготовки и переработки перовскита. *Труды Кольского научного центра РАН*. 2018:196–200.
7. Leont'ev L.I., Vatolin N.A., Shavrin S.L., Shumakov N.S. Pyrometallurgical Processing of Complex Ores. Moscow: Metallurgiya; 1997:432. (In Russ.).  
Леонтьев Л.И., Ватолин Н.А., Шаврин С.Л., Шумаков Н.С. Пирометаллургическая переработка комплексных руд. Москва: Metallurgiya; 1997:432.
8. Grishin N.N., Rakitina E.Yu. New elements of technology for processing titanomagnetites of the Kola Peninsula. *Trudy Fersmanovskoi Nauchnoi Sessii GI KNTS RAN*. 2017;(14):228–231. (In Russ.).  
Гришин Н.Н., Ракитина Е.Ю. Новые элементы технологии переработки титаномагнетитов Кольского полуострова. *Труды Ферсмановской научной сессии ГИ КНЦ РАН*. 2017;(14):228–231.
9. Wang S., Chen M., Guo Y., Jiang T., Zhao B. Reduction and smelting of vanadium titanomagnetite metallized pellets. *JOM*. 2019;71:1144–1149.  
<https://doi.org/10.1007/s11837-018-2863-7>
10. Wang S., Guo Y., Chen F., Zheng F., Yang L., Tang M. Behavior of tantalum during the smelting of vanadium titanomagnetite metallized pellets in an electric furnace. *JOM*. 2019; 71:323–328. <https://doi.org/10.1007/s11837-018-2932-y>
11. Kiselev Yu.G., Shchukina E.S. Solubility of the hydrated product obtained by nitric acid treatment of perovskite in sulfuric acid. *Vestnik Kol'skogo Nauchnogo Tsentra RAN*. 2017;(2):81–86. (In Russ.).  
Киселев Ю.Г., Щукина Е.С. Растворимость гидратного продукта, полученного при азотнокислотной обработке перовскита, в серной кислоте. *Вестник Кольского научного центра РАН*. 2017;(2):81–86.
12. Nikolaev A.I., Gerasimova L.G., Petrov V.B., Maierov V.G. Perovskite concentrate as a promising non-traditional raw material for production of titanium and rare metal products. *Kompleksnoe ispol'zovanie mineral'nogo syr'ya*. 2015;(2):26–34. (In Russ.).  
Николаев А.И., Герасимова Л.Г., Петров В.Б., Майоров В.Г. Перовскитовый концентрат — перспективное нетрадиционное сырье для производства титановой и редкометаллической продукции. *Комплексное использование минерального сырья*. 2015;(2):26–34.
13. Budin O.N., Kropachev A.N., Cherepov V.V. Study of technology for producing titanium carbide and calcium metal from perovskite concentrate by carbothermic method. *Metallurg*. 2020;(4):56–64. (In Russ.).  
Будин О.Н., Кропачев А.Н., Черепов В.В. Исследование технологии получения карбида титана и металлического кальция из перовскитового концентрата карботермическим способом. *Металлург*. 2020;(4):56–64.
14. Zhang W., Zhu Z., Chen C.Y. Literature review of titanium metallurgical processes. *Hydrometallurgy*. 2011;108: 177–188. <https://doi.org/10.1016/j.hydromet.2011.04.005>
15. Ogasawara T., Veloso de Araujo R.V. Hydrochloric acid leaching of a pre-reduced Brazilian ilmenite concentrate in

- an autoclave. *Hydrometallurgy*. 2000;56(2):203–216.  
[https://doi.org/10.1016/S0304-386X\(00\)00074-8](https://doi.org/10.1016/S0304-386X(00)00074-8)
16. Amer A.M. Alkaline pressure leaching of mechanically activated Rosetta ilmenite concentrate. *Hydrometallurgy*. 2002;67(2): 125–133. [https://doi.org/10.1016/S0304-386X\(02\)00164-0](https://doi.org/10.1016/S0304-386X(02)00164-0)
  17. Wang Y.-M., Yuan Z.-F., Guo Z.-C., Tan Q.-Q., Li Z.-Y., Jiang W.-Z. Reduction mechanism of natural ilmenite with graphite. *Transactions of Nonferrous Metals Society of China*. 2008;18(4):962–968.  
[https://doi.org/10.1016/S1003-6326\(08\)60166-1](https://doi.org/10.1016/S1003-6326(08)60166-1)
  18. Gou H.-P., Zhang G.-H., Hu X.-J., Chou K.-Ch. Kinetic study on carbothermic reduction of ilmenite with activated carbon. *Transactions of Nonferrous Metals Society of China*. 2017;27(8):1856–1861.  
[https://doi.org/10.1016/S1003-6326\(17\)60209-7](https://doi.org/10.1016/S1003-6326(17)60209-7)
  19. Lv W., Bai C., Lv X., Hu K., Lv X., Xiang J., Song B. Carbothermic reduction of ilmenite concentrate in semi-molten state by adding sodium sulfate. *Powder Technology*. 2018;340:354–361.  
<https://doi.org/10.1016/j.powtec.2018.09.043>
  20. Samal S.K., Mishra B., Mishra S.C. Carboaluminothermic production of ferrotitanium from ilmenite through thermal plasma. *Journal of Sustainable Metallurgy*. 2020;(6): 563–575. <https://doi.org/10.1007/s40831-020-00292-5>
  21. Zhang G., Ostrovski O. Effect of pre-oxidation and sintering on properties of ilmenite concentrates. *International Journal of Mineral Processing*. 2002;64(4):201–218.  
[https://doi.org/10.1016/S0301-7516\(01\)00055-2](https://doi.org/10.1016/S0301-7516(01)00055-2)
  22. Gou H.P., Zhang G.H., Chou K.C. Influence of pre-oxidation on carbothermic reduction process of ilmenite concentrate. *ISIJ International*. 2015;55(5):928–933.  
<https://doi.org/10.2355/isijinternational.55.928>
  23. Reznichenko V.A., Shabalin L.I. Titanomagnetites: Deposits, Metallurgy, Chemical Technology. Moscow: Nauka; 1986:297. (In Russ.).  
Резниченко В.А., Шабалин Л.И. Титаномагнетиты: месторождения, металлургия, химическая технология. Москва: Наука; 1986:297.
  24. Slag Atlas, 2<sup>nd</sup> ed. Düsseldorf: Verlag Stahleisen GmbH; 1995:618.
  25. Powder Diffraction File PDF4+ ICDD. Release 2016.
  26. Rietveld H.M. Line profiles of neutron powder-diffraction peaks for structure refinement. *Acta Crystallographica*. 1967;22(1):151–152.  
<https://doi.org/10.1107/S0365110X67000234>
  27. DIFFRACPlus: TOPASBruker AXS GmbH. Karlsruhe, Germany; 2008.
  28. Reznichenko V.A., Averin V.V., Olyunina T.V. Titanates: Scientific Foundations, Technology, Production. Moscow: Nauka; 2010:267. (In Russ.).  
Резниченко В.А., Аверин В.В., Олюнина Т.В. Титанаты: научные основы, технология, производство. Москва: Наука; 2010:267.
  29. Gerasimova L.G., Mel'nik N.A., Nikolaev A.I., Petrov V.B., etc. Hydrochloric acid technology of perovskite concentrate and its radiation assessment. *Ekologiya promyshlennogo proizvodstva*. 2015;(1(89)):54–58. (In Russ.).  
Герасимова Л.Г., Мельник Н.А., Николаев А.И., Петров В.Б. и др. Солянокислотная технология перовскитового концентрата и ее радиационная оценка. *Экология промышленного производства*. 2015; (1(89)):54–58.
  30. Levchenko E.N. Specific features of the mineral composition of titanium-zirconium placers in Russia. *Lithology and Mineral Resources*. 2006;41(2):117–136.  
<https://doi.org/10.1134/S0024490206020039>
  31. Kuznetsov A.G., Pashkova N.G. Morphology of large-block material of beaches of the shores of the Tarkhankut peninsula (Crimea). *Uchenye zapiski Krymskogo Federal'nogo Universiteta imeni V.I. Vernadskogo. Seriya "Geografiya. Geologiya"*. 2015;(1(67)):81–90. (In Russ.).  
Кузнецов А.Г., Пашкова Н.Г. Морфология крупнообломочного материала пляжей берегов Тарханкутского полуострова (Крым). *Ученые записки Крымского федерального университета имени В.И. Вернадского. Серия «География. Геология»*. 2015;(1(67)):81–90.
  32. Kotova O.B., Ozhogina E.G., Ponaryadov A.V. Technological mineralogy: development of a comprehensive assessment of titanium ores (exemplified by the Pizhenskoye deposit). *Journal of Mining Institute*. 2022;256:632–641. (In Russ.).  
<https://doi.org/10.31897/PMI.2022.78>  
Котова О.Б., Ожогина Е.Г., Понарядов А.В. Технологическая минералогия: развитие комплексной оценки титановых руд (на примере Пижемского месторождения). *Записки Горного института*. 2022;256:632–641.  
<https://doi.org/10.31897/PMI.2022.78>
  33. Sokolov S.V. Perovskite and titanite – possible unconventional sources of titanium (on the example of the Afrikanda deposit). In: *Technological Mineralogy in Assessing the Quality of Mineral Raw Materials of Natural and Man-Made Origin. Coll. of reports of the XIV Russ. Seminar on Technological Mineralogy, Moscow, April 5-6, 2022*. Petrozavodsk: Kola Science Centre, RAS; 2022:78–81. (In Russ.).  
Соколов С.В. Перовскит и титанит – возможные нетрадиционные источники титана (на примере месторождения Африканда). В кн.: *Технологическая минералогия в оценке качества минерального сырья природного и техногенного происхождения. Сборник докладов XIV Российского семинара по технологической минералогии, Москва, 5–6 апреля 2022 г.* Петрозаводск: Издательство КНЦ РАН; 2022:78–81.
  34. Potter N.J., Ferguson M.R., Kamenetsky V.S., Chakhmouradian A.R., Sharygin V.V., Thompson J.M., Goemann K. Textural evolution of perovskite in the Afrikanda alkaline-ultramafic complex, Kola Peninsula, Russia. *Contributions to Mineralogy and Petrology*. 2018;173:100.  
<https://doi.org/10.1007/s00410-018-1531-9>

## Information about the Authors

## Сведения об авторах

**Sergei A. Fedorov**, Cand. Sci. (Eng.), Senior Researcher of the Laboratory of Pyrometallurgy of Nonferrous Metals, Institute of Metallurgy, Ural Branch of the Russian Academy of Sciences  
**ORCID:** 0000-0002-4201-5177  
**E-mail:** saf13d@mail.ru

**Сергей Андреевич Федоров**, к.т.н., старший научный сотрудник лаборатории пирометаллургии цветных металлов, Институт металлургии Уральского отделения РАН  
**ORCID:** 0000-0002-4201-5177  
**E-mail:** saf13d@mail.ru

**Lyudmila Yu. Udоеva**, *Cand. Sci. (Eng.), Leading Researcher of the Laboratory of Rare Refractory Metals, Institute of Metallurgy, Ural Branch of the Russian Academy of Sciences*  
**E-mail:** lyuud@yandex.ru

**Aleksandr S. Vusikhis**, *Cand. Sci. (Eng.), Senior Researcher of the Laboratory of Pyrometallurgy of Non-Ferrous Metals, Institute of Metallurgy, Ural Branch of the Russian Academy of Science*  
**ORCID:** 0000-0002-6395-0834  
**E-mail:** vas58@mail.ru

**Kirill V. Pikulin**, *Cand. Sci. (Eng.), Senior Researcher of the Laboratory of Rare Refractory Metals, Institute of Metallurgy, Ural Branch of the Russian Academy of Sciences*  
**ORCID:** 0000-0002-5843-0041  
**E-mail:** pikulin.imet@gmail.com

**Lyubov' A. Cherepanova**, *Cand. Sci. (Chem.), Research Associate of the Laboratory of Statics and Kinetics of Processes, Institute of Metallurgy, Ural Branch of the Russian Academy of Sciences*  
**ORCID:** 0000-0002-3983-8922  
**E-mail:** freefly88@mail.ru

**Людмила Юрьевна Удоева**, к.т.н., ведущий научный сотрудник лаборатории редких тугоплавких металлов, Институт металлургии Уральского отделения РАН  
**E-mail:** lyuud@yandex.ru

**Александр Семенович Вусихис**, к.т.н., старший научный сотрудник лаборатории пирометаллургии цветных металлов, Институт металлургии Уральского отделения РАН  
**ORCID:** 0000-0002-6395-0834  
**E-mail:** vas58@mail.ru

**Кирилл Владимирович Пикулин**, к.т.н., старший научный сотрудник лаборатории редких тугоплавких металлов, Институт металлургии Уральского отделения РАН  
**ORCID:** 0000-0002-5843-0041  
**E-mail:** pikulin.imet@gmail.com

**Любовь Александровна Черепанова**, к.х.н., научный сотрудник лаборатории статистики и кинетики процессов, Институт металлургии Уральского отделения РАН  
**ORCID:** 0000-0002-3983-8922  
**E-mail:** freefly88@mail.ru

## Contribution of the Authors

## Вклад авторов

**S. A. Fedorov** – microstructure study (SEM, EBMA), data processing, text preparation.

**L. Yu. Udоеva** – formulation of the research task, analysis of literary data, text preparation, formation of conclusions.

**A. S. Vusikhis** – formulation of the research task, literary review, text preparation, formation of conclusions.

**K. V. Pikulin** – literary review, results processing, text preparation.

**L. A. Cherepanova** – phase composition study (X-ray diffraction).

**С. А. Федоров** – исследование микроструктуры (СЭМ, РСМА), обработка данных, подготовка текста.

**Л. Ю. Удоева** – постановка задачи исследования, анализ литературных данных, подготовка текста, формирование выводов.

**А. С. Вусихис** – постановка задачи исследования, литературный обзор, подготовка текста, формирование выводов.

**К. В. Пикулин** – литературный обзор, обработка результатов, подготовка текста.

**Л. А. Черепанова** – исследование фазового состава (РФА).

Received 04.09.2023

Revised 30.10.2023

Accepted 11.11.2023

Поступила в редакцию 04.09.2023

После доработки 30.10.2023

Принята к публикации 11.11.2023



UDC 669.017:669.71

DOI 10.17073/0368-0797-2024-1-37-46



Original article

Оригинальная статья

# MECHANICAL PROPERTIES AND MICROSTRUCTURE OF Al–Mg (5052) ALLOY PROCESSED BY EQUAL-CHANNEL ANGULAR PRESSING (ECAP) WITH VARIATION OF ECAP ROUTES AND HEAT TREATMENT

V. Puspasari<sup>1</sup>, I. N. G. P. Astawa<sup>1</sup>, S. Herbirowo<sup>2</sup>, E. Mabururi<sup>1</sup><sup>1</sup> Research Center for Metallurgy (KST BJ. Habibie Bld. 420, PUSPIPTEK, South Tangerang, Indonesia)<sup>2</sup> Research Center for Advanced Materials (KST BJ. Habibie Bld. 441, PUSPIPTEK, South Tangerang, Indonesia)

✉ vind001@brin.go.id

**Abstract.** Equal-Channel Angular Pressing (ECAP) has become an effective technique of severe plastic deformation designed to produce ultrafine grain metals with improved mechanical properties, such as a good combination of strength and ductility. A report on the effect of ECAP routes on the mechanical and microstructure of commercial 5052 aluminum alloy needs also to be included. This work has been undertaken, in order to obtain the results. In this work, several deformation routes were used to process the Al–Mg (5052) alloy, namely *A*, *Ba*, *Bc* and *C*. Deformation route *A* involved repeatedly pushing the sample into the ECAP die without rotation, route *Ba* was performed by rotating the sample through 90° in alternate directions between each pass, route *Bc* by rotating the sample 90° in the same sense between each pass and route *C* by rotating the sample 180° between passes. The addition of the pass number decreases the grain size of ECAP-processed samples when compared to the as-annealed sample. It also confirmed that the microstructure of the 8-pass samples shows a finer grain size than the as-annealed sample. Furthermore, the *Bc* route (samples rotated in the same sense by 90° between each pass) has been proven to be the most effective deformation route, in order to obtain equiaxed ultrafine grain structure when compared to other deformation routes. This phenomenon takes place due to the continuous deformation in all cubic planes. The restoration after the 4-pass number will lead to the rapid evolution of sub-grains to high-angle grain boundaries, forming equiaxed grains. The characterization of the hardness number also shows that the addition of the ECAP pass number increases the hardness number of 5052 aluminum alloy, where samples processed with the *Bc* route indicate the highest hardness number at 168.4 HB. Moreover, a similar phenomenon also suggests that the tensile strength of all ECAP deformation routes has comparable values. The effect of heat treatment for samples with the *Bc* route also shows that 200 °C annealed samples have the highest hardness number and tensile strength when compared to other samples.

**Keywords:** ECAP, Al–Mg (5052) alloy, deformation routes, microstructure, hardness number, tensile strength, heat treatment

**Acknowledgements:** The work was supported by the Ministry of Research and Technology of Indonesia through Master Research Scholarship. The authors express their gratitude to the Research Center for Metallurgy the National Research and Innovation Agency of Indonesia for permitting them to utilize the facilities for this research.

**For citation:** Puspasari V., Astawa I.N.G.P., Herbirowo S., Mabururi E. Mechanical properties and microstructure of Al–Mg (5052) alloy processed by equal-channel angular pressing (ECAP) with variation of ECAP routes and heat treatment. *Izvestiya. Ferrous Metallurgy*. 2024;67(1):37–46. <https://doi.org/10.17073/0368-0797-2024-1-37-46>



# МЕХАНИЧЕСКИЕ СВОЙСТВА И МИКРОСТРУКТУРА СПЛАВА Al–Mg (5052), ОБРАБОТАННОГО МЕТОДОМ РАВНОКАНАЛЬНОГО УГЛОВОГО ПРЕССОВАНИЯ (РКУП) С ВАРИАЦИЯМИ МЕТОДОВ РКУП И ТЕРМИЧЕСКОЙ ОБРАБОТКИ

В. Пуспасари<sup>1</sup>, И. Н. Г. П. Астава<sup>1</sup>, С. Хербирово<sup>2</sup>, Э. Мабрури<sup>1</sup>

<sup>1</sup> Исследовательский центр металлургии, Национальное агентство исследований и инноваций Индонезии (420 Серпонт, Южный Тангеранг, Индонезия)

<sup>2</sup> Исследовательский центр перспективных материалов (441 Серпонт, Южный Тангеранг, Индонезия)

✉ vind001@brin.go.id

**Аннотация.** Равноканальное угловое прессование (РКУП) стало эффективным методом интенсивной пластической деформации для производства сверхмелкозернистых металлов с улучшенными механическими свойствами, такими как хорошее сочетание прочности и пластичности. Сведения о влиянии маршрутов РКУП на механическую прочность и микроструктуру алюминиевого сплава 5052 отсутствуют. В данной работе для обработки сплава Al–Mg (5052) использовались несколько маршрутов деформации, а именно *A*, *Ba*, *Bc*, и *C*. Маршрут деформации *A* включал в себя многократное проталкивание образца в матрицу РКУП без вращения, маршрут *Ba* предполагал поворот образца на 90° в разных направлениях между проходами, маршрут *Bc* – поворот образца на 90° в одном направлении между проходами, а маршрут *C* – поворот образца на 180° между проходами. Добавление количества проходов уменьшает размер зерна образцов, обработанных РКУП, по сравнению с образцом после отжига. Исследование микроструктуры показало, что образцы после восьми проходов имеют более мелкий размер зерен, чем после отжига. Маршрут *Bc* зарекомендовал себя как наиболее эффективный для получения равноосной ультрамелкозернистой структуры по сравнению с другими маршрутами деформации. Это явление происходит из-за непрерывной деформации во всех кубических плоскостях и восстановление после четвертого прохода будет формировать быструю эволюцию субзерен к большеугловым границам зерен, образуя равноосные зерна. Добавление числа проходов РКУП увеличивает твердость алюминиевого сплава 5052. Образцы, обработанные по маршруту *Bc*, показывают самую высокую твердость – 168,4 НВ. Более того, подобное явление обнаруживается, когда предел прочности при растяжении всех путей деформации РКУП имеет сопоставимые значения. Влияние термической обработки образцов с маршрутом *Bc* также показывает, что отожженный при 200 °С образец имеет самый высокий показатель твердости и предел прочности на растяжение по сравнению с другими образцами.

**Ключевые слова:** РКУП, сплав Al–Mg (5052), маршрут деформации, микроструктура, число твердости, предел прочности, термообработка

**Благодарности:** Работа выполнена при поддержке Министерства исследований и технологий Индонезии на оборудовании Исследовательского центра металлургии Национального агентства исследований и инноваций Индонезии.

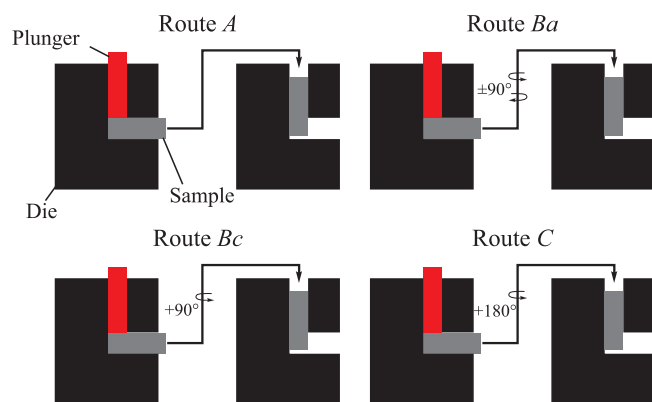
**Для цитирования:** Пуспасари В., Астава И.Н.Г.П., Хербирово С., Мабрури Э. Механические свойства и микроструктура сплава Al–Mg (5052), обработанного методом равноканального углового прессования (РКУП) с вариациями методов РКУП и термической обработки. *Известия вузов. Черная металлургия*. 2024;67(1):37–46. <https://doi.org/10.17073/0368-0797-2024-1-37-46>

## INTRODUCTION

Within the last two decades, Equal-Channel Angular Pressing (ECAP) has been intensively studied as an effective technique of severe plastic deformation (SPD) designed to produce ultrafine or even nanograin metals and alloys with considerably improved mechanical properties combining both strength and ductility [1]. Severe plastic deformation uses ECAP to produce large bulk samples free from residual stress where the samples are pressed to the die with an angled cavity without any change in the cross-sectional dimensions [2]. The samples are subjected to the shear phenomenon during the deformation process inside the ECAP die [3]. Another positive aspect of the ECAP process is the possibility of pressing repetition at the same cross-sectional area of samples [4]. This work applies several deformation routes to process the Al–Mg (5052) alloy, namely *A*, *Ba*, *Bc* and *C*. The different treatments of the sample are pressed continuously either without

any rotation, or by 90° in alternate directions between consecutive passes, or rotated in the same sense by 90° between each pass and rotated by 180° between passes, respectively [5]. The schematic illustration of ECAP routes can be seen in Fig. 1.

Due to their specific high-strength properties [6], aluminum and its alloys are widely used in numerous applications, such as automotive, aerospace, marine, and many others. Moreover, 5xxx-series aluminum alloys are commonly utilized in the industry due to their specific high strength, good formability, good weldability, and excellent corrosion resistance [7]. From the perspective of aluminum alloy applications, it is crucial to establish a suitable processing method which will enhance the mechanical properties and lead to the higher specific strength of materials [8]. Significant increases in mechanical properties of the alloys were achieved by the application of the ECAP process. Avcu et al. concluded that the ECAP process significantly increases the micro-



**Fig. 1.** Schematic illustration of ECAP routes variation in Al–Mg (5052) alloy ECAP process

**Рис. 1.** Схематическая иллюстрация изменения маршрутов РКУП в процессе РКУП сплава Al–Mg (5052)

hardness and wear resistance properties of 7075 aluminum alloy due to the fragmentation of precipitates and grain refinement phenomenon [9]. Nejadseyfi et al. also explained that ECAP, followed by the aging process, also enhances the mechanical performance of 6061 aluminum alloy, such as tensile strength, hardness, and corrosion resistance [10]. However, the study on the effect of variation of ECAP routes and heat treatment on the mechanical and microstructure properties of Al–Mg (5052) is still limited, although many researchers have reported the behavior of other alloys processed by ECAP.

The ECAP of Aluminium and other alloys with a variation of channel angles from 90 to 160° has been studied by numerous researchers [11]. The utilization of a large angle in the ECAP die affects the number of strains experienced by the sample in the ECAP pass [12]. The variation of deformation routes results in different microstructures and leads to the alteration of mechanical properties, such as hardness and tensile strength [13]. Studies by Ghosh et al. established that ECAP with a variation of deformation routes and numerous passes greatly influences the grain refinement. This thoroughly impacts the frequent change in shear plane and direction during the process [14]. Furthermore, Shaeri et al. also determined the enhancement quality of microstructure and texture of aluminium 7075 alloy using four passes variation and two routes of *Bc* and *A* at room temperature [15].

Yee et al. proved that the samples processed by the *Bc* route indicate better wear properties. However, they did not fully explain that the performance of this route is mechanically optimum for most of the application areas [16]. In another work, Valiev also stated that the *Bc* route is the most favorable route due to the amount of equiaxed ultrafine-grained morphology [17]. Further, Howeyze et al. also found that samp-

les processed with *A* route have a higher level of dislocation density, while samples processed using route *C* possessed higher amounts of high angle boundaries (HAGBs) [13]. However, other researchers also showed that routes *A* and *C* have a good level of performance in limited applications [18]. Therefore, it is crucial to study the effect of the ECAP routes on the microstructural and mechanical behavior of Al–Mg (5052) alloy, in order to obtain the best condition applicable in industrial applications, such as automotive, defense, and aerospace.

However, despite the enhancement of the mechanical properties in ECAP-processed samples, a decrease in elongation of the alloys was exhibited after ECAP in conventional cold working. With the increment of elongation of the ECAPed alloys, external energy is needed to reduce the dislocation density. Tański T. et al. investigated the strength and structure of AlMg<sub>3</sub> alloy, reporting the possibility of producing a UFG material with a combination of good mechanical properties and ductility. This was achieved by optimized ECAP deformation and heat treatment [19]. Meanwhile, Rominiyi A.L. et al. reported an optimum combination of properties of the 6061-aluminum alloy resulting from applying post-ECAP artificial aging [20]. This work investigated the effect of heat treatment temperature on the mechanical properties of ECAPed alloys, in the aim of achieving the best combination of strength and elongation. In addition, the pre-evaluation of ECAP deformation routes was conducted, in order to select the most effective route in obtaining the best combination of mechanical properties. The Al–Mg (5052) alloy was used in this work, since this type of aluminum was a non-heat treatable alloy that could only be strengthened by deformation. This obviated the complex mechanism of heat treatment after ECAP due to aging.

## RESEARCH MATERIALS AND METHODOLOGY

The material used for the ECAP experiments was a billet of aluminum alloys found commercially in the market with the chemical composition (wt. %), as listed in Table 1 according to Optical Emission Spectroscopy analysis. This chemical composition complied with Al–Mg or 5052 alloys. The samples for the ECAP experiments were cylindrical, 70 mm in length and 12.7 mm in diameter, made by machining the initial billet. The samples were annealed under argon gas flowing at 550 °C for 12 h before extrusion for internal stress releasing and texture removal of the as-received alloys. The ECAP was carried out at room temperature for up to 8 passes with deformation routes *A*, *Ba*, *Bc* and *C*.

Deformation route *A* was conducted by passing the sample into an ECAP die repetitively without rotation. Route *Ba* was performed by rotating the sample through 90° in alternate directions between each pass,

route *Bc* by rotating the sample 90° in the same sense between each pass and route *C* by rotating the sample 180° between passes. The ECAP facilities and the samples after ECAP deformation are shown in Fig. 1. The ECAP dies used in this work had internal angular channels with a diameter of 14 mm, channel angel ( $\phi$ ) 120° and corner angel ( $\phi$ ) 7°. The ECAP samples with *Bc* for four passes were subjected to heat treatment at 100, 200, and 300 °C for 30 min, in order to evaluate the effect of heat treatment.

All the samples were machined along the extrusion direction, in order to prepare the specimens for microstructure observation, hardness measurement, and tensile testing. The tensile specimens had a gauge length of 12 mm as per JIS Z 220. The tensile test was conducted at room temperature using a Universal Testing Machine with 12 mm gauge length samples according to JIS Z220. The hardness test was performed using a Hardness Brinell device at 5 varied points, in order to calculate the average and obtain a hardness number. Crystallite structure of the samples was also examined using Shimadzu X-Ray Diffraction machine, in order to identify crystalline phase in samples. Then, the 1×1 cm sample was grinded using silicon carbide paper with a 400 – 1500 grid mesh, followed by polishing and etching using Poulton's reagent for 5 – 10 s. The etched samples were washed with water and alcohol, dried, and

prepared to be examined using the Olympus U-MSSPG optical microscope for optical morphology characterization. The microstructure characterization was also held using JEOL JSM 6390 A machine, in order to examine the precipitate in the samples.

## RESEARCH RESULTS AND DISCUSSION

The ECAP process deforms the alloys plastically by inducing shear strains and changing the microstructure of the alloys accordingly. The microstructure developed in the ECAP alloys depends on the geometry of the die, the number of strains, the deformation routes, and the initial condition of the alloys [21]. In the present work, the number of passes and the deformation routes were evaluated with regard to the microstructure and the mechanical properties of the Al–Mg (5052) alloys. Fig. 3 shows the optical microstructure of Al–Mg (5052) alloys in the initial condition of annealed at 550 °C for 12 h and in ECAPed conditions for 2, 4 and 8 passes with various deformation routes. The microstructure of the initial alloys (0 pass) shows the typical annealed aluminum alloys with large grains. The annealing twins exist within several grains [22].

After the application of the ECAP process, the microstructure of the alloys changed. In general, the microstructure of the ECAP samples shows finer grain sizes than the initial sample. Routes *A* and *C* exhibit microstructure with elongated grains which increase with the addition of the number of passes. Route *Ba* results in a microstructure with wavy grains which became more prominent with a higher number of passes. For route *Bc*, the microstructure revealed broken grains without elongated or wavy grains, particularly for the 2 and 4 passes. Meanwhile, a wavy structure emerges for 8 passes due to heavy straining. The grain flow exhibited by the ECAPed samples can be explained by the shearing pattern developed associated with the deformation routes applied to the samples [5].

In route *A*, where the samples were not rotated, continuous shearing occurred in two cubic planes, and restoration of straining did not occur. The grains were elongated by shearing without restoration in all passes [23]. For route *C*, where the samples were rotated 180° repeatedly restoration should occur after 2<sup>nd</sup> pass. Regarding route *Bc* where the samples were rotated 90° repeatedly, continuous deformation was exhibited in all cubic planes. Restoration occurs after 4<sup>th</sup> pass, ensuring the rapid evolution of sub grains to high angle grain boundary, and forming equiaxed grains. Thus, route *Bc* is considered the most effective route to obtaining an equiaxed and fine-grain structure [24]. As can be seen in Fig. 3, the effect of several ECAP passes also affects the grain size of Al–Mg (5052) alloy. The addition of an ECAP pass will promote grain refinement in the Al–Mg (5052) alloy.

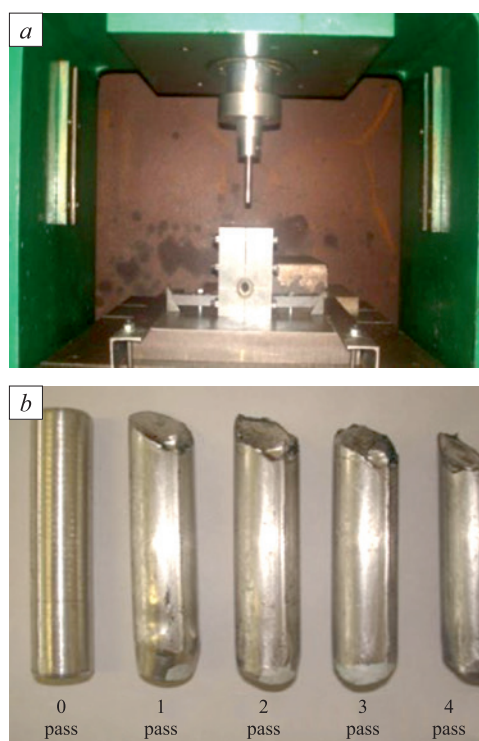
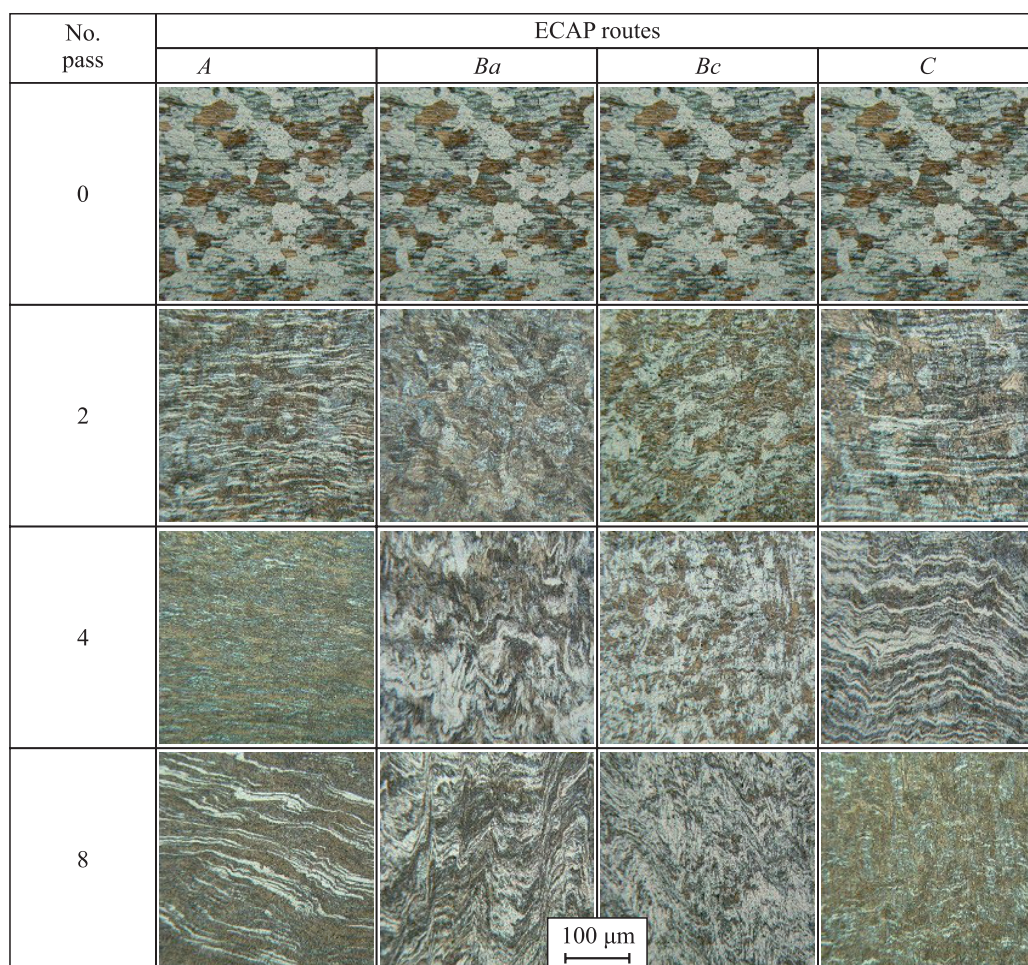


Fig. 2. ECAP equipment used in experiment (a) and samples after ECAP (b)

Рис. 2. Оборудование для РКУП, используемое в эксперименте (a), и образцы после прохождения процесса РКУП (b)





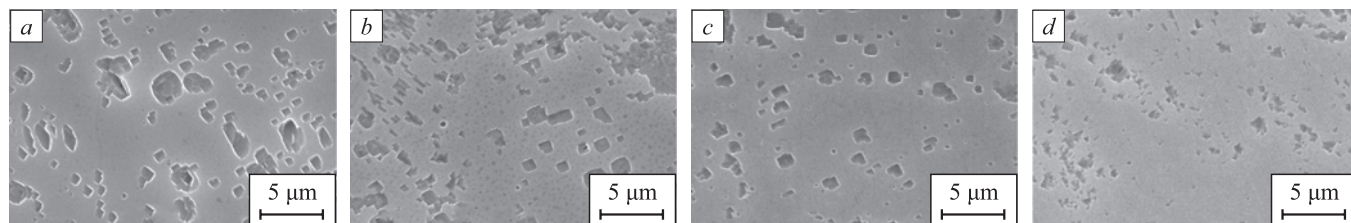
**Fig. 3.** Microstructure of Al–Mg (5052) alloy with a variation of routes and number of passes of ECAP

**Рис. 3.** Микроструктура сплава Al–Mg (5052) с изменением маршрутов РКУП и количества проходов

Fig. 4 reveals the results of Scanning Electron Microscope (SEM) Characterization of Al–Mg (5052) alloy with a *Bc* ECAP route and variation in the number of ECAP passes. The *Bc* orientation was chosen for SEM characterization due to the best results when compared to other routes where the samples have the equiaxial grain shape. The grain size in the Al–Mg (5052) alloy also becomes smaller with the addition of the ECAP pass number. The grain refinement phenomenon also answers the enhancement of hard-

ness numbers by adding the ECAP pass number. The microstructure in the sample is inhomogeneous. It consists of two different shapes of grain morphologies, such as elongated and equiaxial deformed grain.

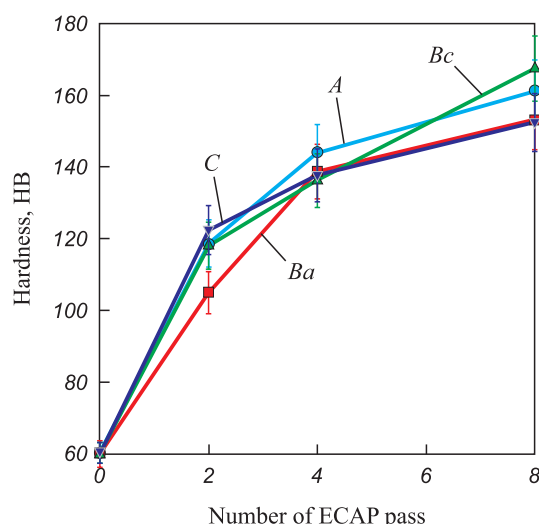
These shapes relate to the shear direction during the ECAP process; the short shear movement tends to create the equiaxed grains and align with the shear direction. The boundaries between the elongated grains are assimilated, forming a more or less strain-free



**Fig. 4.** SEM Characterization of Al–Mg (5052) alloy with a *Bc* ECAP route and variation of number of ECAP passes: *a* – 0; *b* – 2; *c* – 4; *d* – 8

**Рис. 4.** СЭМ-характеристика сплава Al–Mg (5052) с маршрутом *Bc* РКУП и изменением количества проходов: *a* – 0; *b* – 2; *c* – 4; *d* – 8



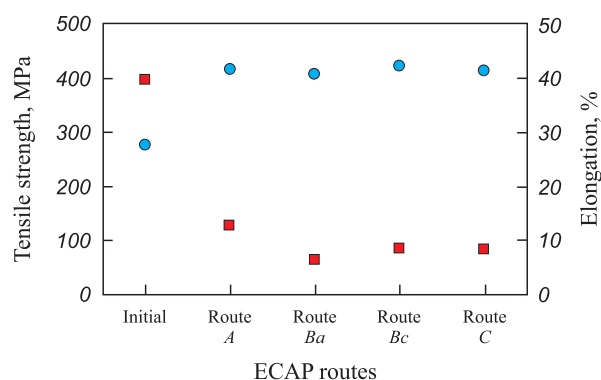


**Fig. 5.** Hardness properties of Al–Mg (5052) alloy with a variation of routes and number of passes of ECAP

**Рис. 5.** Твердость сплава Al–Mg (5052) при изменении маршрутов и количества проходов РКУП

area [22]. There are some agglomerated grains, where the sub-grains are formed within the elongated grains. After the first pass, the average distance between particles increases as the ECAP pass number rises [12].

Fig. 5 presents the Brinell hardness of the initial and the ECAPed Al–Mg (5052) samples for various passes with different deformation routes. The hardness of the alloys increases significantly after being subjected to one pass ECAP, when compared to that of the initial alloys for all deformation routes. The hardness of the alloys further increases with a reduced gradient with an increase in the number of passes [25]. At the first two passes, a significant increase in dislocation density occurs due to severe strains developed after ECAP. By increasing the number of passes, the dislocation density tends to be saturated gradually and renders the dislocation mobility causing only a slight increase in the hardness. This result is a common phenomenon and agrees with other results found in the literature [26]. Concerning deforma-

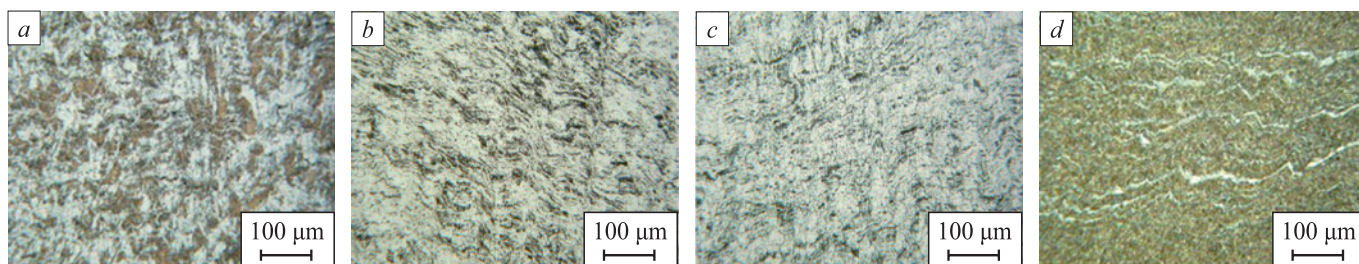


**Fig. 6.** ECAP route curve with tensile (●) and elongation (■)

**Рис. 6.** Кривая маршрута РКУП с указанием прочности на растяжение (●) и относительного удлинения (■)

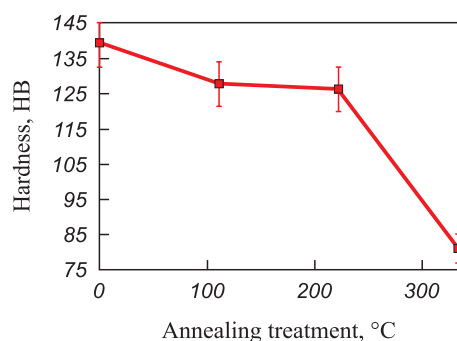
tion routes, Fig. 4 shows that the routes *A*, *Ba*, *Bc* and *C* applied in the ECAP experiments result in a relatively small difference in the hardness of the ECAP samples for all numbers of passes [27]. Similar phenomena are exhibited by the tensile strength of the alloys, where the strength was found to have comparable value among the deformation routes of ECAP as shown in Fig. 6.

Different routes produce values above 400 MPa, exceeding previous research only achieved below the tensile strength of this sample [21] (Fig. 6). The single crystallographic direction of deformation performed by route *A* results in the accumulation of dislocation in the same direction, and the annihilation of the dislocation which reduces the dislocation density. Thus, it eventually enhances the elongation [28]. The study of annealing temperature was also performed, in order to establish its effect on the microstructure of Al–Mg (5052) alloy. Fig. 7 shows that the variation of the annealing temperature (from 100 – 300 °C) affects the microstructure of Al–Mg (5052) alloy. The untreated sample indicates elongated grains, while the sample with an annealing treatment of 200 °C shows the recovery state where the grain becomes small and equiaxed due to the rearrangement of dislocation inside the annealed samples [29]. The increase of annealing temperature from 200 to 300 °C causes



**Fig. 7.** Microstructure of Al–Mg (5052) alloy with variation of annealing temperature: *a* – without treatment; *b* – annealing at 100 °C; *c* – annealing at 200 °C; *d* – annealing at 300 °C

**Рис. 7.** Микроструктура сплава Al–Mg (5052) при изменении температуры отжига: *a* – без обработки; *b* – отжиг при 100 °C; *c* – отжиг при 200 °C; *d* – отжиг при 300 °C



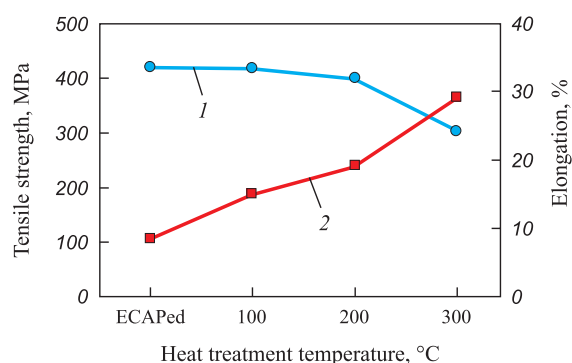
**Fig. 8.** Effect of heat treatment temperature after ECAP on hardness of Al–Mg (5052) alloy samples

**Рис. 8.** Влияние температуры термообработки после РКУП на твердость образцов сплава Al–Mg (5052)

the increment of the recrystallization process, in which the grain size becomes smaller, the grains dislocation-free, and the deformation substructure is also removed [30].

Figs. 8 and 9 reveal the effect of heat treatment after ECAP on the hardness and the tensile strength-elongation of the Al–Mg (5052) alloys, respectively. There is only a slight change which occurs in the hardness and the tensile strength of the ECAPed alloys after heat treatment at a temperature of 200 °C. The hardness and the tensile strength decrease significantly after heat treatment at a temperature of 300 °C. This implies that the heat treatment applied to the ECAPed alloys induced energy to release strain, and the saturated dislocation density gradually decreased until heat treatment at 200 °C [31]. After dislocation achieves the unsaturated condition, further strain release seems to accelerate the decrease of the dislocation density occurring at a heat treatment temperature of 300 °C. This agrees with the results of Y.H. Zhao [22], who calculated the dislocation density of ECAPed 7075 aluminum alloys during annealing. He found that there was no change in dislocation density when annealing up to 140 °C, along with a significant reduction in dislocation density from  $(0.94 \pm 0.08) \cdot 10^{15} \text{ m}^{-2}$  to about  $(0.05 \pm 0.04) \cdot 10^{15} \text{ m}^{-2}$  occurred when annealing at 300 °C.

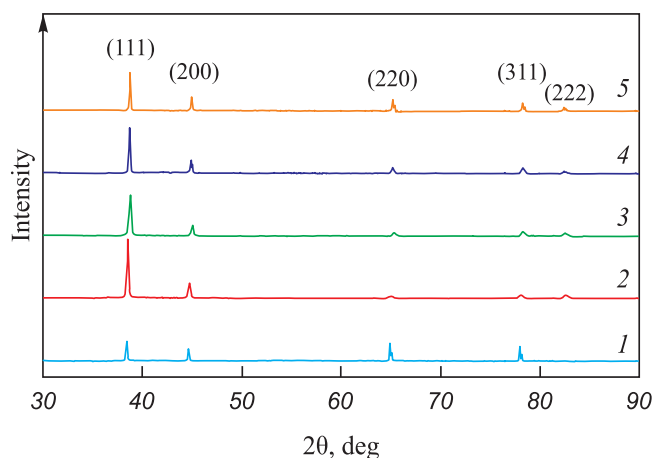
The different situation is shown by the response of the elongation of the alloys on the heat treatment after the ECAP process (Fig. 9). The elongation is consistent with increasing linearity for all temperatures of heat treatment concerned in this study. Consistent with a decrease in tensile strength with heat treatment temperature, the elongation shows a significant increase above 200 °C [31]. The heat treatment should be performed at a temperature which does not significantly decrease the tensile strength with sufficient elongation [32]. The best combination of mechanical properties of ECAPed Al–Mg (5052) alloys is achieved after heat treatment at a temperature of 200 °C for 30 min, i.e., 318 MPa for tensile strength and 19.16 % for elongation.



**Fig. 9.** Effect of heat treatment temperature after ECAP on tensile strength (1) and elongation (2) of Al–Mg (5052) alloy samples

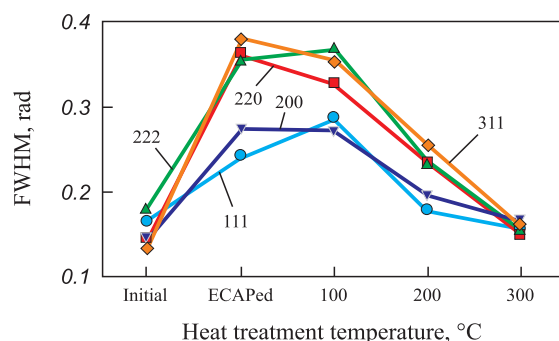
**Рис. 9.** Влияние температуры термообработки после РКУП на предел прочности при растяжении (1) и относительное удлинение (2) образцов сплава Al–Mg (5052)

Fig. 10 shows the XRD pattern of the Al–Mg (5052) alloy in the condition of initial: after ECAP deformation, and after heat treatment of ECAPed samples. In general, the XRD pattern of all samples reveals the peaks of lattice planes (111), (200), (220), (311), and (222), except for the absence of (222) in the initial sample. It can be seen from the Figure that in the ECAPed sample, the intensity of the (111) plane increases significantly when compared to that in the initial sample. This is concomitant with the fact that aluminum alloys have high *stacking fault energy* ( $\gamma_{\text{SFE}}$ ), wherein the fcc crystal structure, and the dislocation slip on the (111) plane is the primary deformation mechanism [33]. Hence, this close-packed plane (111) is the primary slip plane for dislocation glide during the ECAP deformation of the aluminum alloys. Another phenomenon that can be observed from Fig. 10 is the broadening of peaks for all crystal



**Fig. 10.** XRD peaks of Al–Mg (5052) alloy in conditions of initial (1), ECAPed (2), and heat treated after ECAP at 100 (3), 200 (4) and 300 °C (5)

**Рис. 10.** Рентгеновские пики сплава Al–Mg (5052) в исходном состоянии (1), после РКУП (2) и термообработки после РКУП при 100 (3), 200 (4) и 300 °C (5)



**Fig. 11.** FWHM of Al–Mg (5052) alloy in conditions of initial, ECAPed, heat treated after ECAP at 100, 200 and 300 °C

**Рис. 11.** Полная ширина на половине высоты сплава Al–Mg (5052) в исходном состоянии, после РКУП и термообработки после РКУП при 100, 200 и 300 °C

planes of samples after ECAP deformation. This peak broadening relates to increasing lattice defects, particularly dislocation density occurring during ECAP deformation [24; 25]. The peak broadening decreases in the heat-treated sample following the decreasing dislocation density caused by heat treatment.

The grain refining of the ECAPed samples can be evaluated qualitatively from the peak broadening by measuring the width of the XRD peaks of the ECAPed samples when compared to those of the initial samples. Since peak width relates inversely to crystallite size (considered as grain size) according to the Scherrer Equation [34], the larger peak width indicates the finer size of the crystallite. Fig. 11 shows the peak width (expressed by the FWHM/*Full Width at Half Maximum*) of Al–Mg (5052) alloys in different conditions of initial, ECAPed, and heat treated at 100, 200 and 300 °C. It can be seen from this Figure that the FWHM of the samples after ECAP increases about two-fold for all crystal planes when compared with initial samples. This indicates that grain refinement occurs in the ECAPed samples. The FWHM of the samples decreases again after being subjected to heat treatment and reaches almost the initial values after heat treatment at a temperature of 300 °C, with a significant reduction in dislocation density.

## CONCLUSIONS

The effect of ECAP routes and heat treatment temperature after ECAP on the microstructure and mechanical properties of Al–Mg (5052) alloys was investigated in this work. In general, the microstructure of the ECAPed samples showed finer grain sizes than that of the initial sample. The *Bc* deformation route was considered the most effective route, in order to obtain and equiaxed ultrafine grain structure. It was exhibited that the mechanical properties of the alloys had comparable values to those which resulted from all the defor-

mation routes of ECAP. The heat treatment to which the ECAP samples were subjected resulted in decreasing the mechanical properties, reaching almost the initial values after heat treatment at 300 °C. The best combination of mechanical properties of ECAPed Al–Mg (5052) alloys was achieved after heat treatment at temperature 200 °C, i.e., 318 MPa for tensile strength and 19.16 % for elongation. Further, the peak broadening of the ECAPed samples was observed on the XRD pattern indicating grain refinement. The peak broadening decreased by heat treatment and reached almost initial values after heat treatment at a temperature of 300 °C.

## REFERENCES / СПИСОК ЛИТЕРАТУРЫ

1. Tsuji N., Gholizadeh R., Ueji R., Kamikawa N., Zhao L., Tian Y., Bai Y., Shibata A. Formation mechanism of ultrafine grained microstructures: Various possibilities for fabricating bulk nanostructured metals and alloys. *Materials Transactions*. 2019;60(8):1518–1532. <https://doi.org/10.2320/matertrans.MF201936>
2. Agarwal K.M., Tyagi R.K., Choubey V., Saxena K.K. Mechanical behaviour of Aluminium Alloy AA6063 processed through ECAP with optimum die design parameters. *Advances in Materials and Processing Technologies*. 2022;8(2): 1901–1915. <https://doi.org/10.1080/2374068X.2021.1878705>
3. Kumar S.R., Gudimetla K., Venkatachalam P., Ravisankar B., Jayasankar K. Microstructural and mechanical properties of Al 7075 alloy processed by Equal Channel Angular Pressing. *Materials Science and Engineering: A*. 2012;533:50–54. <https://doi.org/10.1016/j.msea.2011.11.031>
4. Van Thuong N., Zuhailawati H., Seman A.A., Huy T.D., Dhindaw B.K. Microstructural evolution and wear characteristics of equal channel angular pressing processed semi-solid-cast hypoeutectic aluminum alloys. *Materials & Design*. 2015;67:448–456. <https://doi.org/10.1016/j.matdes.2014.11.054>
5. Sankuru A.B., Sunkara H., Sethuraman S., Gudimetla K., Ravisankar B., Kumares Babu S.P. Effect of processing route on microstructure, mechanical and dry sliding wear behavior of commercially pure magnesium processed by ECAP with back pressure. *Transactions of the Indian Institute of Metals*. 2021;74(11):2659–2669. <https://doi.org/10.1007/s12666-021-02340-4>
6. Dursun T., Soutis C. Recent developments in advanced aircraft aluminium alloys. *Materials & Design*. 2014;56: 862–871. <https://doi.org/10.1016/j.matdes.2013.12.002>
7. Dubyna A., Mogucheva A., Kaibyshev R. Hall-petch relationship in an Al–Mg–Sc alloy subjected to ECAP. *Advanced Materials Research*. 2014;922:120–125. <https://doi.org/10.4028/www.scientific.net/AMR.922.120>
8. Valiev R.Z., Enikeev N.A., Murashkin M.Y., Kazykhanov V.U., Sauvage X. On the origin of the extremely high strength of ultrafine-grained Al alloys produced by severe plastic deformation. *Scripta Materialia*. 2010;63(9):949–952. <https://doi.org/10.1016/j.scriptamat.2010.07.014>
9. Avcu E. The influences of ECAP on the dry sliding wear behaviour of AA7075 aluminium alloy. *Tribology International*. 2017;110:173–184. <https://doi.org/10.1016/j.triboint.2017.02.023>



10. Nejadseyfi O., Shokuhfar A., Dabiri A., Azimi A. Combining equal-channel angular pressing and heat treatment to obtain enhanced corrosion resistance in 6061 aluminum alloy. *Journal of Alloys and Compounds*. 2015;648:912–918. <https://doi.org/10.1016/j.jallcom.2015.05.177>
11. Zou D., He L., Xiao D., Zhao Y., Qiu Z., Lu C., Liu F. Microstructure and mechanical properties of fine grained uranium prepared by ECAP and subsequent intermediate heat treatment. *Transactions of Nonferrous Metals Society of China*. 2020;30(10):2749–2756. [https://doi.org/10.1016/S1003-6326\(20\)65417-6](https://doi.org/10.1016/S1003-6326(20)65417-6)
12. Alateyah A.I., Ahmed M.M.Z., Alawad M.O., Elkhatny S., Zedan Y., Nassef A., El-Garaihy W.H. Effect of ECAP die angle on the strain homogeneity, microstructural evolution, crystallographic texture and mechanical properties of pure magnesium: numerical simulation and experimental approach. *Journal of Materials Research and Technology*. 2022;17: 1491–1511. <https://doi.org/10.1016/j.jmrt.2022.01.088>
13. Howeyze M., Eivani A.R., Arabi H., Jafarian H.R. Effects of deformation routes on the evolution of microstructure, texture and tensile properties of AA5052 aluminum alloy. *Materials Science and Engineering: A*. 2018;732:120–128. <https://doi.org/10.1016/j.msea.2018.06.081>
14. Ghosh A., Ghosh M. 3D FEM simulation of Al–Zn–Mg–Cu alloy during multi-pass ECAP with varying processing routes. *Materials Today Communications*. 2020;26:102112. <https://doi.org/10.1016/j.mtcomm.2021.102112>
15. Shaeri M.H., Salehi M.T., Seyyedein S.H., Abutalebi M.R., Park J.K. Microstructure and mechanical properties of Al–7075 alloy processed by equal channel angular pressing combined with aging treatment. *Materials & Design*. 2014; 57:250–257 <https://doi.org/10.1016/j.matdes.2014.01.008>
16. Yee S.V., Hussain Z., Seman A.A., Syukron M., Almanar I.P. The influence of ECAP pass through Bc route on mechanical properties of aluminum alloy 6061. *Advanced Materials Research*. 2014;1024:219–222. <https://doi.org/10.4028/www.scientific.net/AMR.1024.219>
17. Valiev R.Z., Islamgaliev R.K., Alexandrov I.V. Bulk nanostructured materials from severe plastic deformation. *Progress in Materials Science*. 2000;45:103–189.
18. Rifai M., Miyamoto H., Fujiwara H. The effect of ECAP deformation route on microstructure, mechanical and electrochemical properties of low CN Fe–20%Cr alloy. *Materials Sciences and Applications*. 2014;5(8):568–578. <https://doi.org/10.4236/msa.2014.58059>
19. Tański T., Snopiński P., Borek W. Strength and structure of AlMg<sub>3</sub> alloy after ECAP and post-ECAP processing. *Materials and Manufacturing Processes*. 2017;32(12):1368–1374. <https://doi.org/10.1080/10426914.2016.1257131>
20. Rominiyi A.L., Oluwasegun K.M., Olawale J.O., Shongwe M.B., Adetunji A.R. Effect of post-ECAP aging on the microstructure, hardness and impact behaviour of 6061 Al alloy. *Materials Today Proceedings*. 2021;38: 2:1031–1034. <https://doi.org/10.1016/j.matpr.2020.05.670>
21. Kim W.J., Wang J.Y. Microstructure of the post-ECAP aging processed 6061 Al alloys. *Materials Science and Engineering: A*. 2007;464(1–2):23–27. <https://doi.org/10.1016/j.msea.2007.03.074>
22. Venkatachalam P., Ramesh Kumar S., Ravisankar B., Thomas Paul V., Vijayalakshmi M. Effect of processing routes on microstructure and mechanical properties of 2014 Al alloy processed by equal channel angular pressing. *Transactions of Nonferrous Metals Society of China*. 2010;20(10): 1822–1828. [https://doi.org/10.1016/S1003-6326\(09\)60380-0](https://doi.org/10.1016/S1003-6326(09)60380-0)
23. Segal V. Review: Modes and processes of severe plastic deformation (SPD). *Materials*. 2018;11(7):1175. <https://doi.org/10.3390/ma11071175>
24. Cabibbo M. A TEM Kikuchi pattern study of ECAP AA1200 via routes A, C, B<sub>c</sub>. *Materials Characterization*. 2010;61(6): 613–625. <https://doi.org/10.1016/j.matchar.2010.03.007>
25. Shivashankara B.S., Gopi K.R., Pradeep S., Raghavendra Rao R. Investigation of mechanical properties of ECAP processed AL7068 aluminium alloy. *IOP Conference Series: Materials Science and Engineering*. 2021;1189(1):012027. <https://doi.org/10.1088/1757-899x/1189/1/012027>
26. Venkatachalam P., Roy S., Ravisankar B., Paul V.T., Vijayalakshmi M., Suwas S. Effect of processing routes on evolution of texture heterogeneity in 2014 aluminium alloy deformed by equal channel angular pressing (ECAP). *Materials Science and Technology*. 2012;28(12):1445–1458. <https://doi.org/10.1179/1743284712Y.00000000045>
27. El-Shenawy M., Ahmed M.M.Z., Nassef A., El-Hadek M., Alzahrani B., Zedan Y., El-Garaihy H. Effect of ecap on the plastic strain homogeneity, microstructural evolution, crystallographic texture and mechanical properties of AA2xxx aluminum alloy. *Metals*. 2021;11(6):1–23. <https://doi.org/10.3390/met11060938>
28. Megahed N.E., Rashad M. Improvement of mechanical properties and electrical conductivity of 7075 Al alloy using ECAP process. *Journal of Engineering Research*. 2023;7(2):161–168. <https://doi.org/10.21608/ERJENG.2023.208328.1176>
29. Zhao Y.H., Liao X.Z., Jin Z., Valiev R.Z., Zhu Y.T. Microstructures and mechanical properties of ultrafine grained 7075 Al alloy processed by ECAP and their evolutions during annealing. *Acta Materialia*. 2004;52(15):4589–4599. <https://doi.org/10.1016/j.actamat.2004.06.017>
30. Khelfa T., Lachhab R., Azzeddine H., Chen Z., Muñoz J.A., Cabrera-Marrero J.M., Brisset F., Helbert A.-L., Baudin T., Khitouni M. Effect of ECAP and subsequent annealing on microstructure, texture, and microhardness of an AA6060 aluminum alloy. *Journal of Materials Engineering and Performance*. 2022;31(4):2606–2623. <https://doi.org/10.1007/s11665-021-06404-w>
31. Mao J., Kang S.B., Park J.O. Grain refinement, thermal stability and tensile properties of 2024 aluminum alloy after equal-channel angular pressing. *Journal of Materials Processing Technology*. 2005;159(3):314–320. <https://doi.org/10.1016/j.jmatprotec.2004.05.020>
32. Sjölander E., Seifeddine S. The heat treatment of Al–Si–Cu–Mg casting alloys. *Journal of Materials Processing Technology*. 2010;210(10):1249–1259. <https://doi.org/10.1016/j.jmatprotec.2010.03.020>
33. Liu H., Gao B., Yang Y., Xu M., Li X., Li C., Pan H., Yang J., Zhou H., Zhu X., Zhu Y. Strain hardening behavior and microstructure evolution of gradient-structured Cu–Al alloys with low stack fault energy. *Journal of Materials Research and Technology*. 2022;19:220–229. <https://doi.org/10.1016/j.jmrt.2022.05.027>
34. Akbari B., Tavandashti M.P., Zandrahimi M. Particle size characterization of nanoparticles – a practical approach. *Iranian Journal of Materials Science and Engineering*. 2011;8(2):48–56.



## Information about the Authors

## Сведения об авторах

**Vinda Puspasari**, M. Sci. (Eng.), Researcher, Research Center for Metallurgy

ORCID: 0000-0002-4757-0348

E-mail: vind001@brin.go.id

**I. Nyoman Gede Putrayasa Astawa**, M. Sci. (Eng.), Researcher, Research Center for Metallurgy

E-mail: inyo009@brin.go.id

**Satrio Herbirowo**, M. Sci. (Eng.), Researcher, Research Center for Advanced Materials

E-mail: satr009@brin.go.id

**Efendi Mabruuri**, Dr. Sci. (Eng.), Prof., Researcher, Research Center for Metallurgy

E-mail: efen002@brin.go.id

**Винда Пуспасари**, магистр технических наук, научный сотрудник, Исследовательский центр металлургии

ORCID: 0000-0002-4757-0348

E-mail: vind001@brin.go.id

**И. Нуоман Геде Путраяса Астава**, магистр технических наук, научный сотрудник, Исследовательский центр металлургии

E-mail: inyo009@brin.go.id

**Сатрио Хербиrowo**, магистр технических наук, научный сотрудник, Исследовательский центр перспективных материалов

E-mail: satr009@brin.go.id

**Эфенди Мабрури**, д.т.н., профессор, научный сотрудник, Исследовательский центр металлургии

E-mail: efen002@brin.go.id

## Contribution of the Authors

## Вклад авторов

**V. Puspasari** – writing the text, literary review, consolidation of experimental data, interpretation of results, formulation of conclusions.

**I. N. G. P. Astawa** – preparation of research material, literary review, performing X-ray diffraction and electron microscopic studies, performing studies on mechanical properties and corrosion resistance.

**S. Herbirowo** – development and review of the manuscript, interpretation of results, formulation of conclusions.

**E. Mabruuri** – determination of research concept, literary review, consolidation of experimental data, interpretation of results, formulation of conclusions.

**В. Пуспасари** – написание текста статьи, литературный обзор, обобщение экспериментальных данных, интерпретация результатов, формулировка выводов.

**И. Н. Г. П. Астава** – подготовка материала исследования, литературный обзор, проведение рентгеноструктурных и электронно-микроскопических исследований, проведение исследований механических свойств и коррозионной стойкости.

**С. Хербиrowo** – написание и редакция рукописи, интерпретация результатов, формулировка выводов.

**Э. Мабрури** – определение концепции исследования, литературный обзор, обобщение экспериментальных данных, интерпретация результатов, формулировка выводов.

Received 31.07.2023

Revised 15.11.2023

Accepted 11.12.2023

Поступила в редакцию 31.07.2023

После доработки 15.11.2023

Принята к публикации 11.12.2023



UDC 536.425:539.25:539.351

DOI 10.17073/0368-0797-2024-1-47-52



Review article

Обзорная статья

## IMPROVEMENT OF THE CANTOR ALLOY'S MECHANICAL PROPERTIES BY ALLOYING WITH NIOBIUM AND ZIRCONIUM

V. E. Gromov<sup>1</sup>, S. V. Konovalov<sup>1</sup>, M. O. Efimov<sup>1</sup>,  
I. A. Panchenko<sup>1</sup>, X. Chen<sup>2</sup>

<sup>1</sup> Siberian State Industrial University (42 Kirova Str., Novokuznetsk, Kemerovo Region – Kuzbass 654007, Russian Federation)

<sup>2</sup> Wenzhou University (Changshan, Zhejiang Province 325035, China)

✉ gromov@physics.sibsiu.ru

**Abstract.** Created in 2004, the high-entropy (HEA) five-component Cantor alloy CoCrFeNiMn is still in the focus of attention of researchers in the field of physical materials science due to a good combination of strength and plastic properties, which open up prospects for its use in various high-tech industries. We performed a brief review of recent publications by domestic and foreign researchers on improving the mechanical properties of the Cantor alloy by alloying with niobium and zirconium, which proved themselves well in alloying traditional alloys. Zirconium alloying leads to a lower melting point due to the formation of eutectic with all elements of the Cantor alloy. Alloying with niobium atoms in the range of 0 – 16 at. % ensures the formation of a volume fraction of the Laves phases and  $\sigma$ -phase up to 42 %, which, in turn, is responsible for a fivefold increase in the yield strength from 202 to 1010 MPa. The work on the joint alloying of the Cantor alloy with Zr + Ti + Y<sub>2</sub>O<sub>3</sub>, Nb + C, Nb + V systems was analyzed. With complex alloying, the mechanical properties are significantly improved. The paper reveals and discusses the physical mechanisms of hardening. Microalloying of 0.2 % Nb alloy with 1.3 % C provides an excellent combination of yield strength (~1096 MPa) and elongation (~12 %) after annealing at 700 °C.

**Keywords:** alloying, niobium, zirconium, Cantor alloy, hardening

**Acknowledgements:** The research was supported by the Russian Science Foundation, grant No. 23-49-00015, <https://rscf.ru/project/23-49-00015/>.

**For citation:** Gromov V.E., Konovalov S.V., Efimov M.O., Panchenko I.A., Chen X. Improvement of the Cantor alloy's mechanical properties by alloying with niobium and zirconium. *Izvestiya. Ferrous Metallurgy*. 2024;67(1):47–52. <https://doi.org/10.17073/0368-0797-2024-1-47-52>

## УЛУЧШЕНИЕ МЕХАНИЧЕСКИХ СВОЙСТВ СПЛАВА КАНТОРА ЛЕГИРОВАНИЕМ НИОБИЕМ И ЦИРКОНИЕМ

В. Е. Громов<sup>1</sup>, С. В. Коновалов<sup>1</sup>, М. О. Ефимов<sup>1</sup>,  
И. А. Панченко<sup>1</sup>, С. Чень<sup>2</sup>

<sup>1</sup> Сибирский государственный индустриальный университет (Россия, 654007, Кемеровская область – Кузбасс, Новокузнецк, ул. Кирова, 42)

<sup>2</sup> Университет Вэньчжоу (Китай, 325035, провинция Чжэнсян, г. Чаньшань)

✉ gromov@physics.sibsiu.ru

**Аннотация.** Созданный в 2004 году высокоэнтروпийный (ВЭС) пятикомпонентный сплав Кантора CoCrFeNiMn по-прежнему находится в фокусе внимания исследователей в области физического материаловедения благодаря хорошему сочетанию прочностных и пластических свойств, которые открывают перспективы его использования в различных наукоемких отраслях промышленности. Выполнен краткий обзор публикаций последних лет отечественных и зарубежных исследователей по улучшению механических свойств сплава Кантора путем легирования ниобием и цирконием, хорошо зарекомендовавшими себя при легировании традиционных сплавов. Легирование цирконием приводит к более низкой температуре плавления из-за образования эвтектики со всеми элементами сплава Кантора. Легирование атомами ниобия в диапазоне 0 – 16 ат. % обеспечивает образование объемной доли фаз Лавеса и  $\sigma$ -фазы до 42 %, что, в свою очередь, ответственно за пятикратное увеличение предела текучести от 202 до 1010 МПа. Проанализированы работы по совместному легированию сплава Кантора системами Zr + Ti + Y<sub>2</sub>O<sub>3</sub>, Nb + C, Nb + V. При комплексном легировании значительно улучшаются механические свойства. В работе раскрыты и обсуждены физические механизмы упрочнения. Микролегирование 0,2 % Nb сплава с 1,3 % C обеспечивает превосходное сочетание предела текучести (~1096 МПа) и относительного удлинения (~12 %) после отжига при 700 °C.

**Ключевые слова:** легирование, ниобий, цирконий, сплав Кантора, упрочнение

**Благодарности:** Исследование выполнено за счет гранта Российского научного фонда № 23-49-00015, <https://rscf.ru/project/23-49-00015/>.

**Для цитирования:** Громов В.Е., Коновалов С.В., Ефимов М.О., Панченко И.А., Чень С. Улучшение механических свойств сплава Кантора легированием ниобием и цирконием. *Известия вузов. Черная металлургия*. 2024;67(1):47–52.  
<https://doi.org/10.17073/0368-0797-2024-1-47-52>

## INTRODUCTION

High-entropy alloys (HEAs), a novel class of metallic materials discovered towards the end of the 20<sup>th</sup> century, comprise 5 to 6 elements, each at concentrations ranging from 5 to 35 % [1; 2]. These alloys have attracted significant research interest due to their outstanding characteristics, such as high strength, ductility, corrosion resistance, and suitability for extreme temperature conditions, as well as their ease of machining. The potential applications of HEAs span a wide range, from the fabrication of cutting tools and molds to components for the nuclear power and aerospace industries [3 – 8]. According to Scopus, over 30,000 articles on HEAs have been published in the last quarter-century. Among this vast repository of research, the Cantor alloy (CoCrFeNiMn) occupies a prominent position, having been thoroughly investigated for its properties at ambient, high, and low temperatures since 2004 [1; 2]. Remarkably, the Cantor alloy can exhibit an elongation to fracture of approximately 71 % at room temperature, though its yield strength and toughness are relatively low at 215 MPa and 491 MPa, respectively [1; 2]. The practical application of this alloy is somewhat limited by the challenge of balancing strength and ductility, a hurdle that might be overcome through alloying techniques without inducing embrittlement.

The quest to enhance the mechanical properties of HEAs continues to be a key focus for researchers in the field of material science. Review articles [9; 10] have examined two main approaches to address this challenge: firstly, through the development of a nanocrystalline structure and surface hardening via external energy treatments [11; 12], and secondly, through computer modeling to predict high-performance properties, utilizing the CALPHAD software package designed for calculating phase diagrams [13 – 15]. Additionally, the traditional method of alloying with elements well-established in the fabrication of steels and other alloys is also being explored.

The enhancement of both mechanical and functional properties of Cantor HEAs can be achieved through the strategic incorporation of well-investigated elements such as niobium and zirconium [2; 9; 16]. The technique of microalloying with these elements is a well-established practice for hardening conventional steels and alloys. The underlying principles and mechanisms of this hardening process have been the subject of extensive research, particularly within the realm of rail steel from

the late last century through the early years of the current century [17 – 19]. Niobium, recognized for its potent carbide- and nitride-forming capabilities, interacts with carbon and nitrogen to generate ultrafine, nano-sized carbides and carbonitrides. Nevertheless, it's important to note that micron-sized particles can adversely affect impact toughness by facilitating a pronounced intergranular fracture mode. Such fractures are among the least energy-intensive and thereby the most hazardous, as the energy absorbed during fracture primarily reflects the properties of the weakened grain boundaries within the polycrystalline structure, rather than the intrinsic characteristics of the metal itself.

During the cooling phase following hot rolling, niobium precipitates as niobium carbide and/or niobium nitride, enhancing the pearlitic structure's hardness (strength) through dispersion hardening and bolstering wear resistance and resilience against internal fatigue failure. Furthermore, niobium plays a crucial role in averting the softening of the heat-affected zone in welds: niobium carbide or nitride consistently forms in the heat-affected zone across a broad temperature spectrum, upon reheating to temperatures at or below the  $A_{c1}$  point. Nonetheless, when the niobium concentration falls below 0.001 %, these benefits are not realized to a meaningful degree, leading to no discernible enhancement in the hardness (strength) of the pearlitic structure. Conversely, a niobium content exceeding 0.050 % results in over-intensification of dispersion hardening due to niobium carbide or nitride, rendering the pearlite structure brittle and diminishing the rail's internal fatigue resistance. Therefore, the optimal niobium concentration lies between 0.001 and 0.050 %.

When niobium is incorporated into a complex multi-element alloy like the Cantor alloy, the impact of such alloying additives on the structure and properties of the HEA can only be fully understood through nanoscale investigation using transmission electron microscopy.

The scarcity of publications on this topic means that a unified understanding of how niobium and zirconium influence the alloy's characteristics is still developing. Nevertheless, the existing research efforts dedicated to this area highlight both its importance and practical relevance to the scientific community.

The aim of this article is to briefly review recent studies on the enhancement of mechanical properties in the Cantor alloy through the alloying with niobium and zirconium.

## RESULTS AND DISCUSSION

The role of 5 % zirconium additives in the recrystallization process of the equiatomic Cantor composition was scrutinized in a study [20]. The analysis focused on the cold-rolled alloy subjected to annealing for 30 min at elevated temperatures ranging from 750 to 1125 °C to examine the kinetics of recrystallization. This research aimed to understand the evolution of grain boundaries and grain size from the cast state to the recrystallized condition. It was found that the primary force driving the recrystallization of the dendritic microstructure is the eradication of the dislocation substructure engendered during cold rolling. Alloying with zirconium resulted in more effective solid-solution hardening than the non-alloyed counterpart, maintaining a single-phase HEA structure. The dendritic microstructure transitioned into a fine-grained polycrystalline structure, facilitating CoCrFeNiMn + 5 % Zr HEA's application at cryogenic temperatures.

The zirconium alloying effect was markedly improved by concurrently introducing titanium and yttrium oxide  $Y_2O_3$ , each at 1 wt. %, through mechanical alloying followed by plasma sintering [21]. This modified alloy possessed a FCC lattice with a high density of various oxide morphologies (up to  $2.01 \cdot 10^{21} \text{ m}^{-3}$ ), contributing to its exceptional mechanical properties. The average grain size was around 130 nm, with oxides forming hexagonal ( $YTiO_2$ ), orthorhombic ( $Y_2TiO_5$ ), and monoclinic ( $Ti_2O_3$ ,  $Y_2Zr_2O_7$ ) structures. This high density of oxides and small grain size yielded outstanding microhardness, yield strength, and toughness values of 449 HV, 1309 MPa, and 2231 MPa, respectively. The predominant hardening mechanisms were identified as grain boundary hardening and Orowan hardening.

Comprehensive analysis of how alloying with various elements influences the mechanical properties of the Cantor alloy was presented in [2; 22]. The studies revealed an increase in hardness with the addition of niobium [23] and zirconium [24], attributable to solid-solution hardening and the formation of second phases. Notably, as the niobium content ranged from 0.1 to 0.8 wt. %, hardness linearly escalated to 712 HV, with Laves phases playing a crucial role. Concurrently, an investigation [25] reported a significant increase in yield strength from 1373 to 2473 MPa with a niobium concentration boost from 0 to 5 wt. %. The mechanism of dislocation motion obstruction was identified as a key factor in this enhancement.

In the study documented in [24], CoCrFeNiZr<sub>x</sub> alloys with varying zirconium concentrations were synthesized using vacuum-arc melting. A distinct eutectic microstructure was observed in the cast alloy when  $x = 0.5$ . The research demonstrated that the alloys comprise a FCC solid solution and a Laves C15 phase, appearing in lamellar formations. The crystallographic orientation relationship between these two phases was established.

As the volume fraction of the Laves C15 phase increased, the alloys exhibited enhanced strength but showed increased brittleness at room temperature; the mode of fracture transitioned from ductile inter-lamellar to brittle trans-lamellar. However, with elevated test temperatures, fractures tended to be more ductile, indicating that the eutectic microstructure is capable of enduring significant plastic deformation. This characteristic suggests their potential utility in engineering applications at higher temperatures [24]. The impact of alloying is notably amplified when niobium and vanadium (Nb + V) or niobium and carbon (Nb + C) are introduced together [27].

A study [28] delves into the complexities and challenges involved in analyzing hardness changes in CoCrFeNi alloys alloyed with 1 – 4 wt. % zirconium. It was observed that, following annealing at temperatures below 700 °C, the initially formed nanocrystalline grains maintained their size of approximately 10 nm and a hardness of around 500 HV. However, a significant increase in grain size was noted at temperatures of 900 °C and above, reaching up to 250 nm at 900 °C and transitioning to micron-sized grains at 1100 °C. This variation in grain size distribution may provide avenues for developing HEAs with a superior blend of properties by integrating large grains within a fine-grained matrix.

The influence of zirconium on the melting temperature, microstructure, recrystallization, and mechanical properties of the Cantor HEAs is particularly noteworthy, as discussed in article [29]. The research utilized samples prepared through vacuum arc melting of pre-mechanically alloyed powders, followed by 90 % cold rolling and recrystallization annealing at 1143 K. The incorporation of zirconium yielded several benefits, including a faster induction melting process under vacuum conditions, a reduced melting temperature due to zirconium's eutectic formation with the Cantor alloy elements, improved chemical homogeneity, and enhanced mechanical properties of the recrystallized grains. The zirconium-altered HEA exhibited a higher recrystallization temperature and reduced grain size post-recrystallization, which contributed to increased hardness and strength of the alloy.

The beneficial role of niobium microalloying in a carbon-containing Cantor alloy was explored in article [30]. Such fine-grained, carbon-alloyed HEAs demonstrated an optimal mix of yield strength and ductility. Nonetheless, these carbon-infused HEAs are prone to decomposing into intermetallic compounds under intermediate temperatures, presenting a challenge to their structural stability and performance. The integration of a mere 0.2 % niobium into the CoCrFeMnNi – 1.3 % C (Nb – HEA) alloy markedly enhances mechanical performance at room temperature while averting thermal decomposition at intermediate temperatures. Niobium's microalloying role in carbon-enriched high-entropy alloys is crucial, facilitating the release of NbC carbides at tem-



peratures between 700 and 900 °C, thus inducing hardening. The Nb – HEA alloy, particularly after annealing at 700 °C for 1 h, exhibits an impressive synergy of yield strength (approximately 1096 MPa) and relative elongation (approximately 12 %). Furthermore, niobium microalloying curtails the disintegration of the FCC matrix at intermediate temperatures (500 °C), significantly reducing the emergence of brittle  $\sigma$ -phase, while restraining the proliferation of L10 and BCC/B2 phases.

The CALPHAD software suite serves as a predictive tool for behavior of the Cantor's HEA during alloying processes [23]. Through computer-aided thermodynamic analyses, a pseudo-eutectic binary CoCrFeNiNb<sub>x</sub> alloy series (with  $x$  values of 0.10, 0.25, 0.50 and 0.80) was devised. Experimental findings reveal that these eutectic alloys comprise a ductile face-centered cubic (FCC) phase alongside a solid Laves phase, characterized by a fine lamellar structure, thereby endowing the alloys with superior mechanical attributes in terms of both plasticity and strength. For the CoCrFeNiNb<sub>0.5</sub> variant, tensile strength under compression and strain-to-fracture metrics exceeds 2300 MPa and 23.6 %, respectively. Informed by CALPHAD projections [26], a septenary eutectic high-entropy alloy (comprising Fe, Ni, Cr, V, Co, Mn, and Nb) was synthesized via a melting approach. The configurational entropy calculated for the dual-phase microstructure qualifies the alloy as a high-entropy alloy. Notably, when niobium concentration surpasses 9.7 wt. %, the microstructural paradigm shifts from pre-eutectic with primary FCC to hypereutectic with dominant Laves phase.

The structural phase states and hardness of two distinct non-equiatom HEAs, namely Cantor and Cantor + NbC, were meticulously explored in [27]. The empirical evidence aligns with CALPHAD-based theoretical predictions, suggesting the presence of two solid solutions characterized by high entropy and a FCC crystalline structure post-centrifugal casting. Microscopic examinations and hardness assessments detected minimal structural variance across the thickness of both alloys, depicting a dendritic configuration with iron and manganese segregating within dendritic zones, whilst inter-dendritic spaces concentrated cobalt, chromium, and nickel. Niobium-rich nano-precipitates exhibiting spherical and oval shapes were discernible in interdendritic areas. Differential thermal analysis did not register any peak up to the melting point, indicating the solid solution structures' high temperature resilience.

The beneficial impact of Laves phases on the mechanical properties of HEAs has been underscored across various studies. A particular investigation [31] traced the microstructural evolution and mechanical performance of (CoCrFeNiMn)<sub>100-x</sub>Nb<sub>x</sub>;  $0 \leq x \leq 16$  at. % under compression. This study demonstrates that the volumetric fraction of secondary phases (Laves and  $\sigma$ -phases) esca-

lated from 0 to 42 %, correlating with a yield strength increase from 202 to 1010 MPa.

The lamellar structures have transient mechanical properties. Although the mechanical properties deteriorate as these structures degrade after annealing at 900 °C, HCEs from CoCrFeNiNb<sub>x</sub> retain good mechanical properties.

## CONCLUSIONS

This brief review synthesizes the findings from recent domestic and international research articles on modification of the Cantor alloy through alloying with zirconium, niobium, and complex alloying using systems such as Nb + V, Nb + C, Zr + Ti + V<sub>2</sub>O. The discussions in these studies primarily focus on the physical mechanisms of hardening induced by these alloying processes.

## REFERENCES / СПИСОК ЛИТЕРАТУРЫ

1. Cantor B., Chang I.T.H., Knight P., Vincent A.J.B. Microstructural development in equiatomic multicomponent alloys. *Materials Science and Engineering: A*. 2004;375–377: 213–218. <https://doi.org/10.1016/j.msea.2003.10.257>
  2. Gromov V.E., Konovalov S.V., Ivanov Yu.F., Osintsev K.A. Advanced structured materials. In: *Structure and Properties of High-Entropy Alloys*. Springer; 2021:107–110.
  3. Gludovatz B., Hohenwarter A., Catoor D., Chang E.H., George E.P., Ritchie R.O. A fracture-resistant high-entropy alloy for cryogenic applications. *Science*. 2014;345(6201): 1153–1158. <https://doi.org/10.1126/science.1254581>
  4. Xia S.Q., Yang X., Yang T.F., Liu S., Zhang Y. Irradiation resistance in Al<sub>x</sub>CoCrFeNi high entropy alloys. *JOM*. 2015; 67:2340–2344. <https://doi.org/10.1007/s11837-015-1568-4>
  5. Chuang M.-H., Tsai M.-H., Wang W.-R., Lin S.-J., Yeh J.-W. Microstructure and wear behavior of Al<sub>x</sub>Co<sub>1.5</sub>CrFeNi<sub>1.5</sub>Ti<sub>y</sub> high-entropy alloys. *Acta Materialia*. 2011;59(16):6308–6317. <https://doi.org/10.1016/j.actamat.2011.06.041>
  6. Senkov O.N., Wilks G.B., Miracle D.B., Chuang C.P., Liaw P.K. Refractory high-entropy alloys. *Intermetallics*. 2010;18(9): 1758–1765. <https://doi.org/10.1016/j.intermet.2010.05.014>
  7. Zou Y., Maiti S., Steurer W., Spolenak R. Size-dependent plasticity in an Nb<sub>25</sub>Mo<sub>25</sub>Ta<sub>25</sub>W<sub>25</sub> refractory high-entropy alloy. *Acta Materialia*. 2014;65:85–97. <https://doi.org/10.1016/j.actamat.2013.11.049>
  8. Maiti S., Steurer W. Structural-disorder and its effect on mechanical properties in single-phase TaNbHfZr high-entropy alloy. *Acta Materialia*. 2016;106:87–97. <https://doi.org/10.1016/j.actamat.2016.01.018>
  9. Osintsev K.A., Gromov V.E., Konovalov S.V., Ivanov Yu.F., Panchenko I.A. High-entropy alloys: Structure, mechanical properties, deformation mechanisms and application. *Izvestiya. Ferrous Metallurgy*. 2021;64(4):249–258. (In Russ.). <https://doi.org/10.17073/0368-0797-2021-4-249-258>
- Осинцев К.А., Громов В.Е., Коновалов С.В., Иванов Ю.Ф., Панченко И.А. Высокоэнтропийные сплавы: структура, механические свойства, механизмы деформации и применение. *Известия вузов. Черная металлургия*. 2021;64(4): 249–258. <https://doi.org/10.17073/0368-0797-2021-4-249-258>

10. Gromov V.E., Rubannikova Yu.A., Kononov S.V., Osintsev K.A., Vorob'ev S.V. Generation of increased mechanical properties of Cantor high-entropy alloy. *Izvestiya. Ferrous Metallurgy*. 2021;64(8):599–605. (In Russ.). <https://doi.org/10.17073/0368-0797-2021-8-599-605>  
Громов В.Е., Рубанникова Ю.А., Коновалов С.В., Осинцев К.А., Воробьев С.В. Формирование улучшенных механических свойств высокоэнтروпийного сплава Cantor. *Известия вузов. Черная металлургия*. 2021;64(8):599–605. <https://doi.org/10.17073/0368-0797-2021-8-599-605>
11. Ivanov Yu.F., Gromov V.E., Efimov M.O., Shlyarova Yu.A., Panchenko I.A., Kononov S.V. The structure of the contact zone of the surfacing-substrate subjected to electron-beam processing. *Technical Physics Letters*. 2023;49(6):26–31. (In Russ.). <https://doi.org/10.21883/PJTF.2023.06.54813.19410>  
Иванов Ю.Ф., Громов В.Е., Ефимов М.О., Шлярова Ю.А., Панченко И.А., Коновалов С.В. Структура зоны контакта наплавка-подложка, подвергнутой электронно-пучковой обработке. *Письма в ЖТФ*. 2023;49(6):26–31. <https://doi.org/10.21883/PJTF.2023.06.54813.19410>
12. Ivanov Yu.F., Gromov V.E., Kononov S.V., Shugurov V.V., Efimov M.O., Teresov A.D., Petrikova E.A., Panchenko I.A., Shlyarova Yu.A. Structure and properties of a high-entropy alloy subjected to electron-ion-plasma treatment. *Problemy chernoi metallurgii i materialovedeniya*. 2022;(4):102–116. (In Russ.). [https://doi.org/10.54826/19979258\\_2022\\_4\\_102](https://doi.org/10.54826/19979258_2022_4_102)  
Иванов Ю.Ф., Громов В.Е., Коновалов С.В., Шугуров В.В., Ефимов М.О., Тересов А.Д., Петрикова Е.А., Панченко И.А., Шлярова Ю.А. Структура и свойства высокоэнтропийного сплава, подвергнутого электронно-ионно-плазменной обработке. *Проблемы черной металлургии и материаловедения*. 2022;(4):102–116. [https://doi.org/10.54826/19979258\\_2022\\_4\\_102](https://doi.org/10.54826/19979258_2022_4_102)
13. Senkov O.N., Zhang C., Pilchak A.L., Payton E.J., Woodward C., Zhang F. CALPHAD-aided development of quaternary multi-principal element refractory alloys based on NbTiZr. *Journal of Alloys and Compounds*. 2019;783:729–742. <https://doi.org/10.1016/j.jallcom.2018.12.325>
14. Menou E., Tancet F., Toda-Caraballo I., Ramstein G., Castany P., Bertrand E., Gautier N., Rivera Díaz-Del-Castillo P.E.J. Computational design of light and strong high entropy alloys (HEA): Obtainment of an extremely high specific solid solution hardening. *Scripta Materialia*. 2018;156:120–123. <https://doi.org/10.1016/j.scriptamat.2018.07.024>
15. Tapia A.J.S.E., Yim D., Kim H.S., Lee B.-J. An approach for screening single phase high-entropy alloys using an in-house thermodynamic database. *Intermetallics*. 2018;101:56–63. <https://doi.org/10.1016/j.intermet.2018.07.009>
16. Zeng Z., Xiang M., Zhang D., Shi J., Wang W., Tang X., Tang W., Wang Ye, Ma X., Chen Z., Ma W., Morita K. Mechanical properties of Cantor alloys driven by additional elements: a review. *Journal of Materials Research and Technology*. 2021;15:1920–1934. <https://doi.org/10.1016/j.jmrt.2021.09.019>
17. Tushinskii L.I., Plokhov A.V., Mochalina N.S. Macro-, meso- and nanostructural foundations for creating optimal structures of carbon steels with controlled thermoplastic hardening. *Materialovedenie*. 2008;(5):31–35. (In Russ.).  
Тушинский Л.И., Плохов А.В., Мочалина Н.С. Макро-, мезо- и наноструктурные основы создания оптимальных структур углеродистых сталей при регулируемом термопластическом упрочнении. *Материаловедение*. 2008;(5):31–35.
18. Tushinskii L.I., Mochalina N.S., Plokhov A.V., Kuz'min N.G. Properties of steel after controlled thermoplastic hardening during structure formation at macro-, meso- and nanoscale levels. *Izvestiya. Ferrous Metallurgy*. 2010;53(4):37–40. (In Russ.).  
Тушинский Л.И., Мочалина Н.С., Плохов А.В., Кузьмин Н.Г. Свойства стали после регулируемого термопластического упрочнения при формировании структуры на макро-, мезо- и наномасштабах. *Известия вузов. Черная металлургия*. 2010;53(4):37–40.
19. Mochalina N.S. Formation of nanodisperse hardening phases during controlled thermoplastic hardening of microalloyed steel and their effect on structural strength. In: *Modern Problems in Mechanical Engineering Technology*. Novosibirsk: NSTU; 2009:213–214.  
Мочалина Н.С. Формирование нанодисперсных упрочняющих фаз в процессе регулируемого термопластического упрочнения микролегированной стали и их влияние на конструктивную прочность. В кн.: *Современные проблемы в технологии машиностроения*. Новосибирск: изд. НГТУ; 2009:213–214.
20. Colombini E., Garzoni A., Giovanardi R., Veronesi P., Casagrande A. Al, Cu and Zr addition to high entropy alloys: The effect on recrystallization temperature. *Materials Science Forum*. 2018;941:1137–1142. <https://doi.org/10.4028/www.scientific.net/MSF.941.1137>
21. Peng S., Lu Z., Gao S., Li H. Improved microstructure and mechanical properties of ODS-CoCrFeNiMn high entropy alloys by different Ti, Zr and Y<sub>2</sub>O<sub>3</sub> addition. *Journal of Alloys and Compounds*. 2023;935(2):168166. <https://doi.org/10.1016/j.jallcom.2022.168166>
22. Gromov V.E., Shlyarova Yu.A., Kononov S.V., Vorob'ev S.V., Peregudov O.A. Application of high-entropy alloys. *Izvestiya. Ferrous Metallurgy*. 2021;64(10):747–754. (In Russ.). <https://doi.org/10.17073/0368-0797-2021-10-747-754>  
Громов В.Е., Шлярова Ю.А., Коновалов С.В., Воробьев С.В., Перегудов О.А. Применение высокоэнтропийных сплавов. *Известия вузов. Черная металлургия*. 2021;64(10): 747–754. <https://doi.org/10.17073/0368-0797-2021-10-747-754>
23. He F., Wang Z., Cheng P., Wang Q., Li J., Dang Y., Wang J., Liu C.T. Designing eutectic high entropy alloys of CoCrFeNiNb<sub>x</sub>. *Journal of Alloys and Compounds*. 2016;656:284–289. <https://doi.org/10.1016/j.jallcom.2015.09.153>
24. Huo W., Zhou H., Fang F., Xie Z., Jiang J. Microstructure and mechanical properties of CoCrFeNiZr<sub>x</sub> eutectic high-entropy alloys. *Materials & Design*. 2017;134:226–233. <https://doi.org/10.1016/j.matdes.2017.08.030>
25. Ma S.G., Zhang Y. Effect of Nb addition on the microstructure and properties of AlCoCrFeNi high-entropy alloy. *Materials Science and Engineering: A*. 2012;532:480–486. <https://doi.org/10.1016/j.msea.2011.10.110>
26. Rahul M.R., Phanikumar G. Design of a seven-component eutectic high-entropy alloy. *Metallurgical and Materials Transactions A*. 2019;50:2594–2598. <https://doi.org/10.1007/s11661-019-05210-3>
27. Abbasi E., Dehghani K. Phase prediction and microstructure of centrifugally cast non-equiatomic Co-Cr-Fe-Mn-Ni(Nb,C)

- high entropy alloys. *Journal of Alloys and Compounds*. 2019; 783:292–299. <https://doi.org/10.1016/j.jallcom.2018.12.329>
28. Tekin M., Polat G., Kotan H. An investigation of abnormal grain growth in Zr doped CoCrFeNi HEAs through in-situ formed oxide phases. *Intermetallics*. 2022;146:107588. <https://doi.org/10.1016/j.intermet.2022.107588>
  29. Campari E.G., Casagrande A., Colombini E., Gualtieri M.L., Veronesi P. The effect of Zr addition on melting temperature, microstructure, recrystallization and mechanical properties of a Cantor high entropy alloy. *Materials*. 2021;14(20):5994. <https://doi.org/10.3390/ma14205994>
  30. Wang M., Zhan L., Peng J. Nb micro-alloying on enhancing yield strength and hindering intermediate temperature decomposition of a carbon-doped high-entropy alloy. *Journal of Alloys and Compounds*. 2023;940:168896. <https://doi.org/10.1016/j.jallcom.2023.168896>
  31. Qin G., Li Z., Chen R., Zheng H., Fan C., Wang L., Su Y., Ding H., Guo J., Fu H. CoCrFeMnNi high-entropy alloys reinforced with Laves phase by adding Nb and Ti elements. *Journal of Materials Research*. 2019;34(6):1011–1020. <https://doi.org/10.1557/jmr.2018.468>
  32. He F., Wang Z., Shang X., Leng C., Li J., Wang J. Stability of lamellar structures in CoCrFeNiNb<sub>x</sub> eutectic high entropy alloys at elevated temperatures. *Materials & Design*. 2016;104:259–264. <https://doi.org/10.1016/j.matdes.2016.05.044>

## Information about the Authors

**Viktor E. Gromov**, Dr. Sci. (Phys.-Math.), Prof., Head of the Chair of Science named after V.M. Finkel', Siberian State Industrial University  
**ORCID:** 0000-0002-5147-5343  
**E-mail:** gromov@physics.sibsiu.ru

**Sergei V. Konovalov**, Dr. Sci. (Eng.), Prof., Vice-Rector for Research and Innovation, Siberian State Industrial University  
**ORCID:** 0000-0003-4809-8660  
**E-mail:** konovserg@gmail.com

**Mikhail O. Efimov**, Candidates for a degree of Cand. Sci. (Eng.) of the Chair of Science named after V.M. Finkel', Siberian State Industrial University  
**ORCID:** 0000-0002-4890-3730  
**E-mail:** moefimov@mail.ru

**Irina A. Panchenko**, Cand. Sci. (Eng.), Head of the Laboratory of Electron Microscopy and Image Processing, Siberian State Industrial University  
**ORCID:** 0000-0002-1631-9644  
**E-mail:** i.i.ss@yandex.ru

**Xinzhang Chen**, Prof., Wenzhou University  
**ORCID:** 0000-0003-1649-1820  
**E-mail:** chenxinzhang@wzu.edu.cn

## Сведения об авторах

**Виктор Евгеньевич Громов**, д.ф.-м.н., профессор, заведующий кафедрой естественнонаучных дисциплин им. профессора В.М. Финкеля, Сибирский государственный индустриальный университет  
**ORCID:** 0000-0002-5147-5343  
**E-mail:** gromov@physics.sibsiu.ru

**Сергей Валерьевич Коновалов**, д.т.н., профессор, проректор по научной и инновационной деятельности, Сибирский государственный индустриальный университет  
**ORCID:** 0000-0003-4809-8660  
**E-mail:** konovserg@gmail.com

**Михаил Олегович Ефимов**, соискатель степени к.т.н. кафедры естественнонаучных дисциплин им. профессора В.М. Финкеля, Сибирский государственный индустриальный университет  
**ORCID:** 0000-0002-4890-3730  
**E-mail:** moefimov@mail.ru

**Ирина Алексеевна Панченко**, к.т.н., заведующий лабораторией электронной микроскопии и обработки изображений, Сибирский государственный индустриальный университет  
**ORCID:** 0000-0002-1631-9644  
**E-mail:** i.i.ss@yandex.ru

**Сичжан Чень**, профессор, Университет Вэньжоу  
**ORCID:** 0000-0003-1649-1820  
**E-mail:** chenxinzhang@wzu.edu.cn

## Contribution of the Authors

**V. E. Gromov** – conceptualization of the article, justification of application fields of the Cantor HEA, writing the text.  
**S. V. Konovalov** – selection and analysis of foreign articles containing information on the latest areas of use of the Cantor alloy in high-tech technologies.  
**M. O. Efimov** – analysis of articles on the combined effect of niobium, zirconium and other elements on the Cantor alloy's properties.  
**I. A. Panchenko** – analysis of influence of niobium and zirconium on the Cantor alloy's mechanical properties.  
**X. Chen** – analysis of the Chinese articles, writing the article final version.

## Вклад авторов

**В. Е. Громов** – концепция статьи, обоснование областей применения ВЭС Кантора, написание чернового варианта статьи.  
**С. В. Коновалов** – подбор и анализ зарубежных статей, содержащих сведения о последних областях использования сплава Кантора в наукоемких технологиях.  
**М. О. Ефимов** – анализ статей по совместному влиянию ниобия, циркония и других элементов на свойства сплава Кантора.  
**И. А. Панченко** – анализ природы влияния ниобия и циркония на механические свойства сплава Кантора.  
**С. Чень** – анализ работ китайских авторов, написание окончательного варианта статьи.

Received 10.11.2023  
 Revised 04.12.2023  
 Accepted 18.12.2023

Поступила в редакцию 10.11.2023  
 После доработки 04.12.2023  
 Принята к публикации 18.12.2023





UDC 620.197.3

DOI 10.17073/0368-0797-2024-1-53-64



Original article

Оригинальная статья

## EFFECT OF HYDROGEN ON STEELS IN HYDROGEN SULFIDE-CONTAINING AND OTHER ENVIRONMENTS AT GAS FACILITIES

R. R. Kantyukov, D. N. Zapevalov, R. K. Vagapov

LLC “Scientific-Research Institute of Natural Gases and Gas Technologies – Gazprom VNIIGAZ” (Razvilka Village, Moscow Region 142717, Russian Federation)

✉ R\_Vagapov@vniigaz.gazprom.ru

**Abstract.** The impact of hydrogen sulfide raw materials on steel equipment and pipelines is known and is associated not only with internal corrosion processes, but also with the hydrogenation of carbon and low-alloy steels used. Penetration of hydrogen into steel can lead to the loss of its strength properties and subsequent destruction of gas pipelines operated under high pressure conditions. The manifestations of cracking characteristic of hydrogen sulfide environments, which are a consequence of the penetration of hydrogen into steel, are the most dangerous from the point of view of the safety and reliability of the operation of facilities for the production and transportation of corrosive gas. The effect of  $H_2S$  on the decrease in ductility of the main types of structural steels was studied based on the results of simulation tests. The formation of blisters (bloatings) and cracks on the surface of steels due to the effect of hydrogen on steel was recorded. The study of the phase composition and properties of corrosion products was carried out in order to assess their possible influence on the processes of steel hydrogenation. The formation of evenly distributed on the surface and the densest corrosion deposits will hinder both the corrosion processes and the penetration of hydrogen into steel. A decrease in the plastic properties of steel is also observed when exposed to hydrogen, which can be transported both separately and together with methane through the main gas pipelines. The main possible means of protecting steels that are unstable to hydrogenation is the use of corrosion inhibitors. It was established that the most effective corrosion inhibitors with rational technologies of application and dosage can protect steels from penetration of hydrogen into them and their destructive effect.

**Keywords:** gas pipeline, steel microstructure, blistering, hydrogenation, steel cracking, corrosion products, corrosion inhibitor

**For citation:** Kantyukov R.R., Zapevalov D.N., Vagapov R.K. Effect of hydrogen on steels in hydrogen sulfide-containing and other environments at gas facilities. *Izvestiya. Ferrous Metallurgy*. 2024;67(1):53–64. <https://doi.org/10.17073/0368-0797-2024-1-53-64>

## ИССЛЕДОВАНИЕ ВЛИЯНИЯ ВОДОРОДА НА СТАЛИ В СЕРОВОДОРОДСОДЕРЖАЩИХ И ДРУГИХ СРЕДАХ НА ГАЗОВЫХ ОБЪЕКТАХ

Р. Р. Кантюков, Д. Н. Запеевалов, Р. К. Вагапов

ООО «Научно-исследовательский институт природных газов и газовых технологий – Газпром ВНИИГАЗ» (Россия, 142717, Московская область, п. Развилка)

✉ R\_Vagapov@vniigaz.gazprom.ru

**Аннотация.** Воздействие сероводородного сырья на стальное оборудование и трубопроводы известно и связано не только с процессами внутренней коррозии, но и с наводороживанием применяемых углеродистых и низколегированных сталей. Проникновение водорода в сталь может приводить к потере ее прочностных свойств и последующему разрушению газопроводов, эксплуатируемых в условиях повышенных давлений. Характерные для сероводородных сред проявления растрескивания, являющиеся последствием проникновения водорода в сталь, наиболее опасны с точки зрения безопасности и надежности работы объектов по добыче и транспортировке коррозионно-агрессивного газа. Исследовано воздействие  $H_2S$  на снижение пластичности основных видов конструкционных сталей по результатам имитационных испытаний. Зафиксировано образование блистерингов (вздутий) и трещин на поверхности сталей вследствие воздействия водорода на сталь. Проведено изучение фазового состава и свойств продуктов коррозии с целью оценки их возможного влияния на процессы наводороживания стали. Образование равномерно расположенных по поверхности и наиболее плотных коррозионных отложений будет затруднять процессы коррозии и проникновение водорода в сталь. Снижение пластических свойств стали наблюдается и при воздействии водорода, который может транспортироваться как в отдельности, так и совместно с метаном по магистральным газопроводам. Основным возможным средством защиты сталей, нестойких к наводороживанию, является применение ингибиторов коррозии. Установлено, что наиболее эффективные ингибиторы коррозии с рациональными технологиями применения и дозировкой могут обеспечить защиту сталей от проникновения в них водорода и его разрушительного действия.



**Ключевые слова:** газопровод, микроструктура стали, блистеринг, наводороживание, растрескивание стали, продукты коррозии, ингибитор коррозии

**Для цитирования:** Кантюков Р.Р., Запечалов Д.Н., Вагапов Р.К. Исследование влияния водорода на стали в сероводородсодержащих и других средах на газовых объектах. *Известия вузов. Черная металлургия*. 2024;67(1):53–64.

<https://doi.org/10.17073/0368-0797-2024-1-53-64>

## INTRODUCTION

The reliable and secure functioning of infrastructure is essential for the effective exploitation of oil and gas reserves. Corrosive components like carbon dioxide ( $\text{CO}_2$ ) and hydrogen sulfide ( $\text{H}_2\text{S}$ ), especially when water is present (either formation water or from condensation), can lead to widespread or localized corrosion and fractures [1].

Environments containing  $\text{H}_2\text{S}$  are notably aggressive, leading to the hydrogenation of steel and causing both localized and general hydrogen sulfide corrosion (HSC) [2]. The permeation of hydrogen into steel poses a heightened risk, and thus the durability of steel structures and pipelines in high  $\text{H}_2\text{S}$  environments is evaluated with consideration of the potential for hydrogen induced cracking [3].

It is important to recognize that the operational conditions at oil and gas facilities vary depending on whether the primary extracted fluids are oil or gas/gas condensate. These differences affect the types of corrosion that occur within pipelines. Previous research [4] has indicated that a particularly hazardous form of internal corrosion in gas pipelines involves localized corrosion at the top of the pipe where moisture condenses, collects, and then flows along the lower external curve of the pipe.

The Orenburg and Astrakhan gas condensate fields are examples where conditions conducive to HSC complications are present [2]. These sites are not unique in their susceptibility to HSC and hydrogenation issues. Moreover, pipeline systems for the reinjection of “sour gases” (a mixture of  $\text{H}_2\text{S}$  and  $\text{CO}_2$  extracted from fluids during processing) are being developed at the Astrakhan field for disposal and enhanced condensate recovery in later production stages [5]. The  $\text{H}_2\text{S}$  concentration in the gases transported through these pipelines will be considerably higher than in the initial extraction.

There is also growing interest in hydrogen as a fuel and its combined transportation with natural gas through main pipelines, as well as in the storage of hydrogen in underground facilities [6 – 7]. The use of hydrogen raises inevitable concerns regarding its explosive nature and its effect on the mechanical integrity of pipelines made from carbon/low alloy steel.

Some studies [8] suggest that hydrogen-containing gases could impact steel in a manner similar to  $\text{H}_2\text{S}$ : atomic hydrogen is generated, diffuses into the steel from the surface, and then dissociates, causing local dis-

integration of the metal’s crystal lattice. This can lead to the development of hydrogen-induced microcracks, which, under the high pressure of the gas pipeline and continued hydrogen exposure, may result in hydrogen cracking. As mentioned in [9], storing hydrogen in underground gas storage (UGS) facilities, along with natural gas, might induce a variety of effects, including steel hydrogenation, thereby intensifying the internal corrosion of steel structures and pipelines. The potential effects of hydrogen on steel during transportation and storage are not thoroughly understood and are vital subjects for future research.

Therefore, it is imperative to explore the trends, progression, and mechanisms of corrosion damage, along with the protective strategies employed at gas processing facilities to counteract HSC and steel hydrogenation. The corrosive effects of  $\text{H}_2\text{S}$  and hydrogen ions, generated during the cathodic process, impact steel not only in the liquid phase but also in the vapor phase. This dual-phase impact requires careful consideration when evaluating the corrosive risks of an environment and choosing appropriate protective measures.

## MATERIALS AND METHODS

The following types of carbon and low-alloy steels were selected for testing: 09G2S, St20, S–75, X42SS, and 30KhMA. These steels are commonly utilized in different components and segments of wellhead equipment and pipeline systems within gas field operations.

To assess their performance under HSC conditions and to collect corrosion products for subsequent analysis, tests were carried out in controlled environments using autoclaves. These simulated conditions mimicked the effects of mineral content in the environment and the partial pressures ( $P$ , MPa) of  $\text{CO}_2$  and/or  $\text{H}_2\text{S}$ , allowing for the replication of the corrosion rates observed in actual field conditions. The autoclave tests were conducted for 120 h at temperatures ( $T$ ) of 30 or 90 °C. Aqueous environment with mineralization level of 100 (MB1) and 200 g/l (MB2), with the addition of 0.25 g/l of  $\text{CH}_3\text{COOH}$ , were used. A 0.5 % NaCl solution was used for the tests in the presence of hydrogen. The total corrosion rate ( $K$ , mm/yr) was determined based on the weight loss of the samples from the test results. The effect of hydrogenation was evaluated by the steel’s ability to retain plasticity before and after exposure to the corrosive environment, measured by the number of kinks in wire samples (SV08A steel) before destruction accor-

ding to GOST 1579 – 93 [10]. The decrease in plasticity ( $Pl$ , %) was determined by the number of steel wire kinks after autoclave tests compared to the initial value.

Metallographic analysis of the steels included determining the microstructure according to GOST 8233 [11]. A Zeiss Axio.Vert A1 inverted metallurgical microscope with the Thixomet image analyzer was used for metallographic studies at magnifications of 100 – 1000 times.

The technique for analyzing the phase composition of corrosion products by  $X$ -ray diffraction (XRD) method, based on registering the dependence of  $X$ -ray reflection intensity (reflections) by the crystal lattices of compounds on the diffraction angle, was described earlier in paper [2], with subsequent interpretation of the diffraction pattern.

## RESULTS AND DISCUSSION

The microstructure of steels significantly influences in the development of corrosion defects and hydrogen permeation into the metal in scenarios involving HSC. According to [12], the highest amount of hydrogen diffuses into the sample of heat-treated carbon steel API X65, a commonly used foreign pipe steel grades, that exhibits a microstructure with an increased proportion of pearlite and a reduced amount of ferrite, akin to the types studied by the authors. This specific microstructural composition leads to diminished steel strength and plasticity. Notably, within the pearlite phase – characterized by its lamellar structure of alternating cementite and ferrite – gaps between the lamellae act as channels that facilitate the diffusion and accumulation of hydrogen. The occurrence of microcracking as a result of hydrogen sulfide embrittlement within the steel's crystalline structure may limit further permeation of hydrogen into steel. This phenomenon could partly account for the non-uniform distribution of hydrogen across the steel's thickness, with the highest concentrations typically found in the surface layer. The presence of corrosion-active non-metallic inclusions (CANMIs) in the steel can also contribute to the deterioration of steel strength properties in instances of internal corrosion. Manganese compounds such as  $MnS$ , often found in combination with aluminum inclusions in steel, serve as notable examples of CANMIs that function as hydrogen “traps” [13]. The interface between these inclusions and the steel matrix acts as a repository for hydrogen atoms, providing a locale for these atoms to recombine into molecular  $H_2$ .

This interaction highlights a critical mechanism through which the microstructure of steel, influenced by the presence of such inclusions, can impact the overall resilience and integrity of the material in corrosive environments, particularly those encountered in gas fields (Figure).

The microstructure of the samples is as follows:

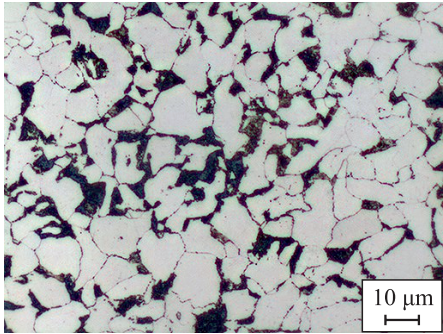

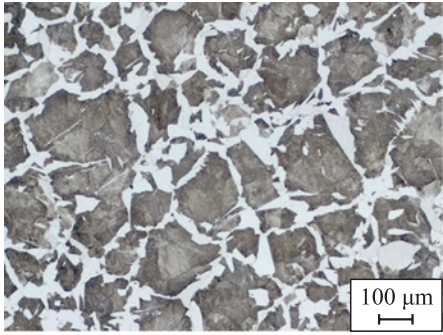

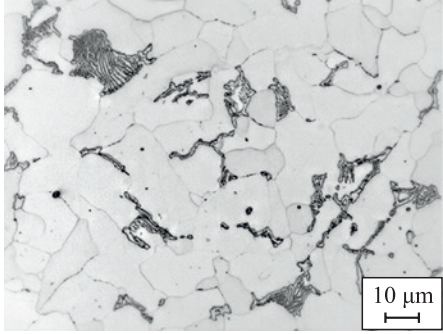

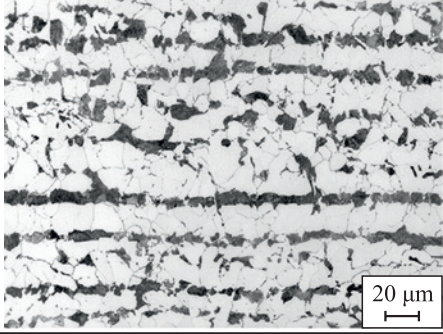

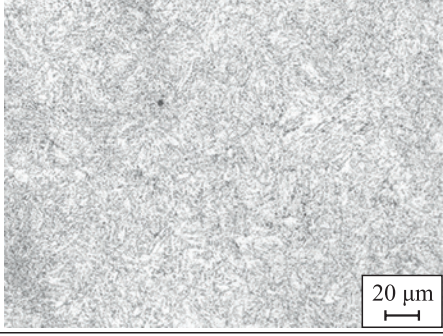
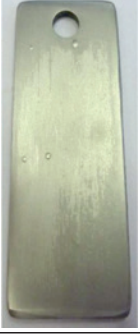
- S75 steel exhibits finely dispersed secondary sorbite that has retained martensitic orientation;
- X42SS is a ferritic-perlitic steel;
- St20 is a ferritic-perlitic steel with non-uniform distribution of lamellar pearlite;
- 30KhMA is a coarse-grained ferritic-perlitic steel where ferrite forms a network at the boundaries of primary austenitic grains, and ferrite needles grow from the ferrite network into perlite;
- 09G2S is a fine-grained ferritic-perlitic steel.

Hydrogen permeation has visibly altered the appearance of the steel samples, as evidenced by the formation of blisters of varying sizes on the surface of most steels under examination, with 09G2S steel presenting the smallest blisters. The surface of the 30KhMA steel is extensively marked with small cracks, and sporadic blistering is also evident. These blisters, when subjected to critical hydrogen pressure levels, rupture and lead to crack formation.

The inherent stresses in the steel's crystal structure, along with the pre-existing microstructural characteristics, are implicated in the initiation and expansion of microcracks [14]. According to the findings in [15], the occurrence of blisters on 13KhFA and 05KhGB steels is related to the presence of complex corrosion-active non-metallic inclusions within the metal, which also predispose these steels to cracking.

Subsequent tests were conducted on St20 steel, which exhibited the highest blister count [2], and 09G2S steel, which is predominantly used in gas infrastructure. Both St20 and 09G2S steels possess a ferritic-perlitic microstructure with a non-uniform distribution of these phases, contributing to their heterogeneous nature. This heterogeneity compromises their resistance to both corrosion and hydrogenation.

Table 1 reveals that the  $K$  value of the samples made from St20 and 09G2S steels after the tests in and above the MB2 aqueous solution ranges from 0.319 to 0.569 mm/yr (for the aqueous phase) and from 0.156 to 0.227 mm/yr (for the vapor phase). In a different MB1 environment, the  $K$  value is higher: 0.8 and 0.52 – 0.55 mm/yr in and above the aqueous electrolyte, respectively. The probable reason is that solubility of corrosive  $H_2S$  in the higher mineralized MB2 solution is limited. High mineralization can result in lower evaporation and condensation of such water required for HSC to propagate on the samples in the vapor phase. However, despite this, localized corrosion defects are observed on the steel surface of the sample tested above the MB1 solution (Table 2). Tests conducted by the authors under the conditions of forced moisture condensation on carbon steels with  $H_2S$  purging showed [16] that in the humidified

Steel	Microstructure	Appearance
09G2S		
30KhMA		
St20		
X42SS		
S75		

Microstructure and appearance of various structural steels after simulation tests in the MB2 environment at  $P_{\text{CO}_2} = 0.13 \text{ MPa}$  and  $P_{\text{H}_2\text{S}} = 0.54 \text{ MPa}$

Микроструктура и внешний вид различных конструкционных сталей после имитационных испытаний в среде MB2 при  $P_{\text{CO}_2} = 0,13 \text{ МПа}$  и  $P_{\text{H}_2\text{S}} = 0,54 \text{ МПа}$



Table 1. Conditions and results of simulation tests in H<sub>2</sub>S-containing environmentsТаблица 1. Условия и результаты имитационных испытаний в H<sub>2</sub>S-содержащих средах

Number of the test conditions	Steel	Phase	$P$ , MPa		$T$ , °C	$K$ , mm/yr	$Pl$ , %
			H <sub>2</sub> S	CO <sub>2</sub>			
MB2 solution							
1	St20	Aqueous	0.54	0.13	30	0.458	71
2	09G2S	Aqueous	0.54	0.13	30	0.465	
3	St20	Vapor	0.54	0.13	30	0.156	35
4	St20	Aqueous	0.60	–	30	0.319	60
5	St20	Vapor	0.60	–	30	0.227	57
6	09G2S	Aqueous	0.13	0.54	30	0.569	–
7	09G2S	Aqueous	0.60	0.54	30	0.525	60
8	St20	Aqueous	0.60	0.54	30	0.454	
MB1 solution							
9	St20	Aqueous	1.50	0.80	30	0.797	74
10	St20	Vapor	1.50	0.80	30	0.817	66
11	St20	Aqueous	1.50	0.80	90	0.529	40
12	St20	Vapor	1.50	0.80	90	0.557	32

vapor phase, the local *K* value, calculated by the depth of pittings formed, reached 1.232 – 1.366 mm/yr.

The microstructural characteristics of steel, particularly the inclusion of CANMIs such as manganese sulfides, are pivotal in the development of pitting lesions in HSC scenarios [17]. These CANMIs, due to their dissimilarity with the steel matrix, act as precursors for the formation of localized corrosion defects. This typically occurs either through the dissolution of the CANMIs themselves or the steel immediately surrounding them. One of the primary reasons behind the corrosive influence of CANMIs is their heterogeneity, which induces elevated stress levels in the adjacent steel matrix. This stress is a result of the mismatched thermal expansion coefficients between the CANMIs and the steel matrix during the steel's production, which involves cycles of heating and subsequent cooling [18]. After the steel cools the region with increased tensile stresses may form around the CANMIs, accelerating internal corrosion.

The effect of steel hydrogenation was evaluated by the reduction of its plastic properties, subsequently resulting in hydrogen embrittlement, and deterioration of metal strength characteristics. As shown in Table 1, the *PI* value after tests at 30 °C in both environments with H<sub>2</sub>S ranges from 60 to 74 % for the aqueous phase and from 35 to 66 % for the vapor phase. Traces of blistering are observed on the surface of the samples after exposure to the aggressive environment (Table 2). It should be noted that in both phases for the MB2 environment, when the test temperature is increased to 90 °C, the *K* value decreases by 33 %, and *PI* drops by 45 to 50 % (Table 1).

Hydrogenation may slightly decrease as the temperature rises due to higher rates of conjugated electrochemical reactions: the cathodic process of hydrogen atom molization on the steel surface is intensified, reducing their ability to permeate inside the metal, as observed by the authors [19]. Another reason why hydrogen permeation and HSC are limited may be the fact that at elevated temperatures, densely packed and evenly distributed corrosion products form faster, acting as a barrier that creates obstacles preventing corrosion components from permeating to the steel surface.

The assessment of the samples' appearance after simulation tests and XRD analysis revealed (Table 2) that corrosion products in the vapor and water phases have different thicknesses and phase compositions. Precipitations in the vapor phase form when the water film is thin. It is suggested that in the vapor phase, only 40 % of the compounds of the corrosion products have a crystalline structure. The majority of them (60 %) did not have enough time to form and remained as looser and unconsolidated X-ray amorphous compounds. In the aqueous phase, the sediment film completely crystallized, becoming thicker and denser.

The results of XRD analysis (Table 2) indicate that in both phases, the main corrosion product is iron sulfide, represented by its two crystal forms: tetragonal FeS (mackinawite) and cubic FeS. The presence of cubic FeS distinguishes these results from the previously obtained data [2]. The results presented in this paper show significant differences, as CH<sub>3</sub>COOH was added to the aqueous environments. Such acidification of the environment



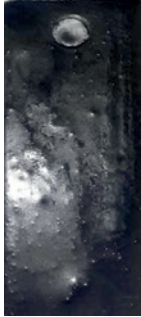



alters the composition of corrosion products and leads to the formation of cubic FeS in addition to the tetragonal form. As a volatile compound, CH<sub>3</sub>COOH evaporates along with H<sub>2</sub>S and contributes to steel fracture in the vapor phase. Additionally, in this phase, cubic FeS precipitates are also formed (Table 2). The formation of deposits with different crystal structures and different faces of FeS will make the film less cohesive and monolithic, thus reducing its barrier (protective) functionality.

The XRD method is based on the phenomenon of *X*-ray diffraction on a three-dimensional crystal lattice. In this case, *X*-rays scattering by crystals correlates with the arrangement of atoms in the crystal. Therefore, each crystalline substance is characterized by a set of peaks in the diffraction pattern, where the position of their reflections is constant, and the relative intensity depends on the substance's content in the mixture. The main factors causing changes in the width of the reflections are the structural features of phases (such as the size of crystallites – coherent scattering region (CSR)) or the structural features of the crystal lattice. The EXD data

facilitates the determination of the crystallite size distribution (CSD) within a polycrystal or identifies the minimum particle size maintaining an accurate crystal structure. The methodology for calculating the CSD relies on the analysis and application of the broadening of diffraction lines, represented by  $\beta$ , employing the Selyakov-Scherrer equation [20]. This technique underpins the evaluation of the CSD for FeS (T) compound particles. As illustrated in Table 2, the experimentally measured  $\beta$  values for the samples (post-exposure to aqueous and vapor phases) exhibit variations of different magnitudes from the standard value ( $\beta = 0.1697^\circ$ ), which is typical for the 001 peak position of mackinawite. These discrepancies suggest the occurrence of lattice defects (such as microstresses, isomorphism, etc.) in the samples. Additionally, it was observed that mackinawite crystals formed in the aqueous phase have a significantly larger CSD, up to eight times that of corrosion products formed in the vapor phase. As a result, the FeS film produced in the vapor phase is thinner and possesses inferior protective qualities compared to its aqueous phase counterpart. The findings imply that crystal growth is more rapid

**Table 2. Characteristics of the precipitate and crystal structure of the obtained compounds of mackinawite and appearance of steel (St20) samples for various test conditions (numbering of the experimental conditions is given in Table 1)**

**Таблица 2. Характеристика осадка и кристаллической структуры полученных соединений макинавита и внешний вид стальных (Ст20) образцов (нумерация приведена по табл. 1)**

Number of the test conditions	Ratio		$\beta$ (for <i>hkl</i> ***-peak FeS (T) – 001), deg	CSR, nm	With corrosion products	Without corrosion products
	phases, Cr/X*	of crystalline compounds**				
1	100/0	95 % FeS (T) 1 % FeS (K) 3 % NaCl 1 % CaSO <sub>4</sub> ·2H <sub>2</sub> O	0.1719	13,928		
3	40/60	28 % FeS (T) 8 % FeS (K) 4 % NaCl	0.1875	1,721		

\* Cr – crystal, X – X-ray amorphous.

\*\* T – tetragonal FeS (mackinawite) and C – cubic FeS.

*hkl* – crystallographic indices (Miller indices) characterizing the arrangement of atomic planes in the crystal (these are whole numbers equal to the number of parts into which the unit-cell edges *a*, *b*, *c* are divided).

in the aqueous phase than in the vapor phase. Moreover, as per [21], a temperature rise from 25 to 80 °C also contributes to an enlargement of crystal compound facets, particularly noticeable in the context of HSC in aqueous environments.

In HSC, corrosion products start to form immediately upon exposure to an aqueous environment containing hydrogen sulfide, a phenomenon observable through visual inspection during experiments. The composition and thickness of these corrosion products are influenced by the operational conditions. Numerous studies under HSC conditions have corroborated that the nature and consistency of the deposits significantly impact corrosion processes [22] and the capability of hydrogen to permeate into steel in aqueous environments [21].

Research documented in [23] indicates that the rate of hydrogen permeation during HSC is influenced by  $P_{\text{H}_2\text{S}}$ , which affects the morphology and structure of the corrosion films formed. Investigations on API X65 pipeline steel in environments containing  $\text{H}_2\text{S}$  have shown that the incidence of hydrogen cracking is contingent on both  $P_{\text{H}_2\text{S}}$  and the pH level [24]. As  $P_{\text{H}_2\text{S}}$  increased from 0.001 to 0.1 MPa, there's a predictable rise in the number of visible microcracks on the steel surface. However, the pH level exerts a more significant influence on hydrogen permeation; in acidic conditions (pH = 3.5), permeation rates surpass those in relatively neutral conditions (pH ranging from 5.5 to 6.5). For example, at  $P_{\text{H}_2\text{S}} = 0.1$  MPa and pH = 5.5, the amount of hydrogen absorbed by the steel decreased and, consequently, the effect of hydrogen cracking on the steel surface decreased. The authors attribute to the formation of denser and more uniformly distributed corrosion products (FeS) at the highest  $P_{\text{H}_2\text{S}} = 0.1$  MPa, which impede hydrogen permeation. Additionally, the formation of mackinawite may decelerate the anodic process of HSC, thereby slowing down the associated electrochemical reaction of hydrogen formation. Another study [25] has noted a reduction in hydrogen diffusion over time, resulting from the development of denser corrosion layers that obstruct the anodic-cathodic process of HSC on pipeline steel.

Visual examination of samples post-exposure to the MB2 environment (Table 3) reveals the formation of blisters of varying sizes on St20 steel in the absence of  $\text{H}_2\text{S}$  protection measures, like corrosion inhibitors, under identical conditions (11). This variability in blister formation is likely due to the unique microstructural features of St20 steel, which exhibits a notably uneven distribution of the pearlite phase. Within the ferritic matrix, pearlite manifests as both discrete particles and sizeable clusters. Such microstructural diversity creates varying sizes of hydrogen “traps,” thereby affecting the morphology of the resulting blisters.


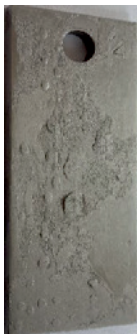
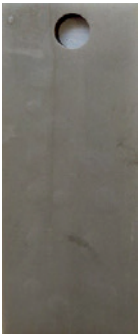
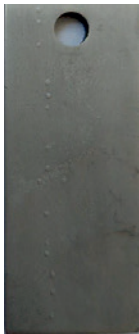




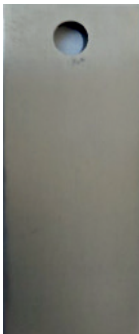
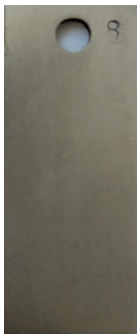
Recent developments in the pipeline transportation of hydrogen, including blends of hydrogen with methane, have seen significant interest. According to a review in paper [8], studies from abroad conducted over the past decade or so reveal that existing data on the operation of main gas pipelines for transporting methane-hydrogen mixtures are not comprehensive. This is primarily because the fundamental parameters, such as strength and steel composition, differ significantly, complicating the identification of consistent patterns regarding hydrogen's impact on steel. Furthermore, the operational performance of these pipelines has been deemed inadequate for future needs. The hydrogen content in these methane-hydrogen mixtures varies from a minimal 2 – 3 % to a maximum of 20 %, with transportation distances spanning several tens of kilometers, and the total pressure not surpassing 1 MPa. The authors of [8] suggest that the observed low performance is attributed to the utilization of older main gas pipelines, which were subject to operational limitations. This has led to varied data regarding the safe hydrogen content or the critical  $P_{\text{H}_2}$  value in the hydrogen-methane mixture. However, there is a consensus among researchers [26 – 27] that a higher  $\text{H}_2$  content could exacerbate the wear on pipeline steel, adversely affecting its plasticity, ductility, and resistance to crack propagation.

Furthermore, it was previously noted [28] that  $\text{CO}_2$  is commonly encountered at oil and gas facilities and may be transported alongside  $\text{H}_2$  through gas pipelines. This scenario becomes particularly relevant when free moisture is present, such as during condensation [4]. In such cases, the chemical interactions involving  $\text{H}_2$  (with  $\text{CO}_2$  present in the natural gas) can act as an additional source of reagents that initiate internal corrosion, further complicating the challenges associated with transporting these gases. The research cited in [9] identifies lower carboxylic acids as intermediate products of chemical interactions that acidify the environment, posing a corrosive threat to steel and potentially enhancing the cathodic process of steel hydrogenation [1]. During the transport of methane-hydrogen mixtures,  $\text{CO}_2$  can be present as an impurity, with up to 2.4 % allowed in natural gas through main gas pipelines. Studies [29] have demonstrated that the presence of both  $\text{H}_2$  and  $\text{CO}_2$  simultaneously increases the rate of fatigue crack growth more than in an environment containing only hydrogen. This suggests a synergistic effect of  $\text{CO}_2$  on hydrogen embrittlement, yet the mechanism behind this interaction remains poorly understood and warrants further investigation.

Subsequent experiments were conducted to examine wire plasticity in an  $\text{H}_2$  environment akin to the hydrogen sulfide conditions previously discussed. It was found (Table 4) that in an aqueous environment (0.5 % NaCl solution), steel plasticity is on average 50 – 60 % lower when 50 – 60 % lower when  $\text{H}_2$  and  $\text{CO}_2$  are present during

**Table 3. Appearance of the samples after testing in the MB1 environment and protective properties of the corrosion inhibitor (numbering of the experimental conditions is given in Table 1)**

**Таблица 3. Внешний вид образцов после испытаний в среде MB1 и защитные свойства ингибитора коррозии (нумерация условий эксперимента приведена по табл. 1)**

9	10	11		12
Without the corrosion inhibitor				
				
With the corrosion inhibitor				
				
$K = 0.013 \text{ mm/yr};$ $Pl = 8.8 \%$	$K = 0.026 \text{ mm/yr};$ $Pl = 4.1 \%$	$K = 0.038 \text{ mm/yr};$ $Pl = 12.9 \%$		$K = 0.070 \text{ mm/yr};$ $Pl = 21.7 \%$

together. However, these tests did not show any significant effect of  $\text{CO}_2$  on hydrogen permeation (Table 4), indicating that more research is needed in this area.

Interestingly, in the vapor phase of  $\text{H}_2$  and  $\text{CO}_2$  (without contact with water), no decrease in steel plasticity was observed, similar to conditions where the water is saturated with  $\text{CO}_2$  only. This suggests that the tests did not reveal any impact of hydrogen on steel's plastic properties in the vapor phase (Table 4) possibly due to the short duration of the tests (120 h). In contrast, hydrogenation and subsequent hydrogen embrittlement of steel occur much more rapidly in an  $\text{H}_2\text{S}$  environment (Table 1) than with  $\text{H}_2$  alone. According to [30], the increase in hydrogen cracking in an  $\text{H}_2$  environment is linked to the greater amount of hydrogen absorbed by the steel, with the time required for hydrogen to permeate into steel's dislocations being a critical factor. Thus, the duration of hydrogen exposure is a significant aspect to consider in future experimental designs.

The paper [31] further elucidates the impact of hydrogen on gas main pipelines, noting a reduction in plasticity and crack resistance of pipe steels by 20 – 60 %, and a significantly higher crack propagation rate. Simul-

taneously, the risk of hydrogen embrittlement increases as the hydrogen concentration in the hydrogen-methane mixture rises, leading to a corresponding increase in  $P_{\text{H}_2}$ . Research cited in [32] identifies a critical  $P_{\text{H}_2}$

**Table 4. Results of the studies in 0.5 % NaCl solution on change in plasticity of Sv08A wire after autoclave tests**

**Таблица 4. Результаты исследований в 0,5 %-ном растворе NaCl по изменению пластичности проволоки Св08А после автоклавных испытаний**

Phase	$P$ , MPa		$PI$ , %	
	$\text{H}_2$	$\text{CO}_2$	without the inhibitor	with the inhibitor
Aqueous	0.81	1.78	50 – 60	0
Vapor	0.81	1.78	0	0
Aqueous	1.40	2.13	60 – 64	0 – 16
Vapor	1.40	2.13	0 – 18	0
Aqueous	0.69	0.05	50 – 59	0
Aqueous	–	1.78	0 – 6	0



range of 0.05 to 0.1 MPa for austenitic stainless steel type 304SS, beyond which the material begins to exhibit embrittlement at room temperature in an inert gas environment containing hydrogen.

Studies [29; 31] have shown that hydrogen presence shifts the dominant failure mode of steel from ductile to brittle, thereby altering its mechanical properties. It's highlighted in [31] that both  $H_2$  and  $H_2S$  environments can reduce the plasticity of steel and intensify hydrogen embrittlement. Specifically, steel samples with a streaked ferritic-perlitic structure exhibited lower resistance to a hydrogen-methane mixture than those with a more uniform ferrite-bainite structure. Further findings [33] indicate that hydrogen crack initiation in X42 pipeline steel, exposed to a hydrogen ( $P_{H_2}$  ranging from 0.5 to 10 MPa) and natural gas mixture, tends to occur at the ferrite/perlite interface. This interface is a critical site for hydrogen diffusion, especially under local stress or strain along grain boundaries.

Mitigation strategies against the detrimental effects of hydrogen include modifying the steel's microstructure to reduce factors that contribute to  $H_2$  accumulation and employing corrosion inhibitors. Among the primary defenses against hydrogen sulfide cracking (HSC) is the use of corrosion inhibitors.

One of the main means of protection against HSC is the use of corrosion inhibitors. However, it should be noted that under such conditions the impact of hydrogen sulfide embrittlement on steel pipes and equipment seriously complicates the selection of potential corrosion inhibitors, in addition to aggravating corrosion [34 – 35].

Technologies for administering corrosion inhibitors encompass injecting them into the aqueous environment or forming an inhibitor coating to safeguard steel in the vapor phase. The conducted experiments reveal (Table 3) that the vapor-phase inhibitor coating can effectively protect the steel using the specified corrosion inhibitor (corrosion rate below 0.1 mm/yr), but it fails to entirely prevent defect formation on the steel's surface. Meanwhile, steel hydrogenation was found to be minimal: hydrogen uptake was 4.1 % at 30 °C and increased to 21.7 % at 90 °C. In contrast, inhibitor coatings from other chemicals not discussed in this document provided even less protection against hydrogen sulfide cracking (HSC) (corrosion rates ranging from 0.187 to 0.303 mm/yr) and hydrogenation (hydrogen uptake between 34 and 64 %), resulting in numerous pits on the steel surface.

When the most effective inhibitor was introduced into the aqueous environment, overall corrosion damage was minimal ( $K = 0.013 - 0.038$  mm/yr), and steel retained high plasticity ( $Pl = 8.8 - 12.9$  %) (Table 3). However, an initial inhibitor concentration of 100 mg/l proved to be insufficient at 90 °C, as localized damage occurred

on the steel surface. Increasing the inhibitor concentration in the aqueous phase by 2 to 3 times successfully prevented localized corrosion on the steel surface at elevated temperatures during the test (Table 3).

The occurrence of increased pitting corrosion might be attributed to either an inadequate concentration of the corrosion inhibitor, preventing the formation of a uniform protective layer on the steel, or a low adsorption rate on the metal surface compared to that of reactive iron sulfide (FeS). According to the study referenced in paper [34], the competitive adsorption between iron sulfide and the corrosion inhibitor on the steel surface might undermine the effectiveness of the inhibitor film.

Additionally, employing corrosion inhibitors in an aqueous environment saturated with  $H_2$  and  $CO_2$ , was also effective in preserving the plasticity of steel (Table 4).

Research aimed at improving steel properties and enhancing their resistance to hydrogen permeation is also ongoing. The paper [36] gives a positive example when the homogeneous ferrite-bainite microstructure of steel with enhanced resistance to hydrogen cracking is formed. The regulation of the thermal modes of steel quenching and tempering enables obtaining the metal structure with such levels of microstresses and dislocation density that resistance to cracking in the  $H_2S$  environment can be increased [37]. The studies [12] proved that the ratio of ferrite and pearlitic components can be changed by increasing the temperature from 850 to 1150 °C as API X65 pipe steel is formed. The content, stability, and sizes of the faces of ferrite grain increase, while simultaneously, the pearlite content in the steel decreases from 15 to 2 %. As the proportion of ferrite in the steel increases, there is a notable reduction in both cathodic and anodic reaction rates within  $H_2S$  environments, alongside a decrease in the accumulation of hydrogen within “traps”. To bolster the resistance of structural steels to cracking when exposed to  $H_2S$  environments, a comprehensive strategy is employed. This strategy involves the modification of steel through the addition of calcium and rare-earth elements, in conjunction with processes such as quenching followed by tempering. These modifications are aimed at preventing the formation of CANMIs, like iron sulfides, within the steel matrix. By inhibiting the development of these inclusions, the approach effectively reduces the emergence of microstresses in their vicinity. Consequently, this leads to a decrease in microcrack formation, thereby diminishing the risk of hydrogen-induced cracking in the steel.

## CONCLUSIONS

Research analysis and literature review reveal that steel's plasticity is adversely affected by hydrogenation in hydrogen sulfide environments, such as those encoun-



tered in gas fields, as well as in the presence of molecular hydrogen, whether alone or combined with other gases. The conditions prevalent in H<sub>2</sub>S-containing gas fields pose a significant aggressive influence on the cracking of pipelines and equipment constructed from carbon and low-alloy steels. This susceptibility to hydrogenation is manifested through the development of cracks and blisters on the surfaces of various steels. The propensity for hydrogen to permeate and be stored in steel is heightened and influenced by microstructural inhomogeneities, including CANMIs, as well as the distribution and dimensions of ferrite-perlite components within the steel. It has been noted that the corrosion film that forms on steel in vapor phase environments is significantly thinner than that formed in aqueous conditions. In environments that are acidified by acetic acid, the cubic form of iron sulfide emerges alongside mackinawite (tetragonal FeS, the primary corrosion product), resulting in a less compact film that diminishes its protective capabilities. The physical characteristics of these deposits, such as their density, compactness, presence of pores, and thickness, play a crucial role in determining their effectiveness as barriers against both HSC and the permeation of hydrogen into the steel. Employing corrosion inhibitors has been shown to effectively preserve the plasticity of steel at adequate levels in environments containing H<sub>2</sub> and H<sub>2</sub>S, including scenarios where CO<sub>2</sub> is also present.

## REFERENCES / СПИСОК ЛИТЕРАТУРЫ

1. Vagapov R.K. Corrosion destruction of steel equipment and pipelines at gas field facilities in the presence of aggressive components. *Steel in Translation*. 2023;53(1):5–10. <https://doi.org/10.3103/S0967091223010138>  
Вагатов Р.К. Коррозионное разрушение стального оборудования и трубопроводов на объектах газовых месторождений в присутствии агрессивных компонентов. *Технология металлов*. 2021;(3):47–54.
2. Kanyukov R.R., Zapevalov D.N., Vagapov R.K. Assessment of the effect of operating conditions on the resistance of steels used in H<sub>2</sub>S-containing environments at hydrocarbon production facilities. *Metallurgist*. 2022;65:1369–1380. <https://doi.org/10.1007/s11015-022-01284-4>  
Кантюков Р.Р., Запечалов Д.Н., Вагатов Р.К. Оценка влияния эксплуатационных условий на стойкость сталей, применяемых в H<sub>2</sub>S-содержащих средах на объектах добычи углеводородов. *Металлург*. 2021;(12):24–31. [https://doi.org/10.52351/00260827\\_2021\\_12\\_24](https://doi.org/10.52351/00260827_2021_12_24)
3. Ghosha G., Rostron P., Garg R., Panday A. Hydrogen induced cracking of pipeline and pressure vessel steels: A review. *Engineering Fracture Mechanics*. 2018;199:609–618. <https://doi.org/10.1016/j.engfracmech.2018.06.018>
4. Vagapov R.K., Kanyukov R.R., Zapevalov D.N. Investigation of the corrosiveness of moisture condensation conditions at gas production facilities in the presence of CO<sub>2</sub>. *International Journal of Corrosion and Scale Inhibition*. 2021;10(3):994–1010. <https://doi.org/10.17675/2305-6894-2021-10-3-11>
5. Zhirnov R.A., Derbenev V.A., Lyugai A.D., Polozkov K.A., Semikolenov T.G., Nikitin V.V., Dymochkina M.G. Prospects for acid gas re-injection into the formation to improve the efficiency of field development (on the example of the Astrakhan GCF). *Nauka i tekhnika v gazovoi promyshlennosti*. 2020;(1(81)):32–39. (In Russ.)  
Жирнов Р.А., Дербенёв В.А., Люгай А.Д., Полозков К.А., Семиколонов Т.Г., Никитин В.В., Дымочкина М.Г. Перспективы обратной закачки в пласт кислых газов для повышения эффективности разработки месторождений (на примере Астраханского ГКМ). *Наука и техника в газовой промышленности*. 2020;(1(81)):32–39.
6. Aksyutin O.E., Ishkov A.G., Romanov K.V., Teterevlev R.V. Methane-hydrogen energy for low-emission development. *Gazovaya promyshlennost'*. 2018;(11(777)):120–125. (In Russ.)  
Аксютин О.Е., Ишков А.Г., Романов К.В., Тетеревлев Р.В. Метано-водородная энергия для низкоэмиссионного развития. *Газовая промышленность*. 2018;(11(777)):120–125.
7. Messaoudani Z.L., Rigas F., Hamid M.D.B., Hassan C.R.C. Hazards, safety and knowledge gaps on hydrogen transmission via natural gas grid: A critical review. *International Journal of Hydrogen Energy*. 2016;41(39):17511–17525. <http://dx.doi.org/10.1016/j.ijhydene.2016.07.171>
8. Wu X., Zhang H., Yang M., Jia W., Qui Y., Lan L. From the perspective of new technology of blending hydrogen into natural gas pipelines transmission: Mechanism, experimental study, and suggestions for further work of hydrogen embrittlement in high-strength pipeline steels. *International Journal of Hydrogen Energy*. 2022;47(12):8071–8090. <https://doi.org/10.1016/j.ijhydene.2021.12.108>
9. Kireeva T.A., Berestovskaya Yu.Yu. Microbiological shifts in hydrogen-rich gases under storage. *Gazovaya promyshlennost'*. 2012;(5(684)):51–54. (In Russ.)  
Киреева Т.А., Берестовская Ю.Ю. Микробиологические изменения водородсодержащих газов при подземном хранении. *Газовая промышленность*. 2012;(5(684)):51–54.
10. GOST 1579-93 Wire. Bend test method. (In Russ.)  
ГОСТ 1579-93 Проволока. Метод испытания на перегиб.
11. GOST 8233-56 Steel. Microstructure standards. (In Russ.)  
ГОСТ 8233-56 Сталь. Эталоны микроструктуры.
12. Mousavi Anijdan S.H., Arab Gh., Sabzi M., Sadeghi M., Eivani A.R., Jafarian H.R. Sensitivity to hydrogen induced cracking, and corrosion performance of an API X65 pipeline steel in H<sub>2</sub>S containing environment: influence of heat treatment and its subsequent microstructural changes. *Journal of Materials Research and Technology*. 2021;15:1–16. <https://doi.org/10.1016/j.jmrt.2021.07.118>
13. Quispe-Avilés J.M., Pereira Fiori M.A., Hincapié-Ladino D., Prada Ramirez O.M., Gomes de Melo H. Effects of Mn and microalloying composition on corrosion and hydrogen-induced cracking of API 5L X65 steels. *Corrosion*. 2022;78(8):765–777. <https://doi.org/10.5006/3876>
14. Huang F., Li X.G., Liu J., Qu Y.M., Du C.W. Effects of alloying elements, microstructure, and inclusions on hydrogen induced cracking of X120 pipeline steel in wet H<sub>2</sub>S sour environment. *Materials and Corrosion*. 2012;63(1):59–66. <https://doi.org/10.1002/maco.201005649>
15. Naumenko V.V., Mursenkov E.S., Kudashov D.V., Udod K.A. Study of reasons for the blistering formation on metal surface

- after the tests on hydrogen induced cracking and classification of blisterings. *Steel in Translation*. 2022;52(2):263–269. <https://doi.org/10.3103/S0967091222020139>
- Науменко В.В., Мурсенков Е.С., Кудашов Д.В., Удод К.А. Исследование причин формирования блистерингов на поверхности металла после испытаний на водородное растрескивание и их классификация. *Сталь*. 2022;(2):44–49.
16. Ibatullin K.A., Vagapov R.K. Evaluation of the influence of various factors on the corrosion of steels during moisture condensation under the conditions of transportation of a corrosive gas. *Praktika protivokorroziionnoi zaschity*. 2022;27(3):31–46. (In Russ.).

Ибатуллин К.А., Вагапов Р.К. Оценка влияния различных факторов на коррозию сталей при конденсации влаги в условиях транспортировки коррозионно-агрессивного газа. *Практика противокоррозионной защиты*. 2022;27(3):31–46.

  17. Amezhnov A.V., Rodionova I.G. Effect of non-metallic inclusion chemical and phase composition on corrosion resistance of carbon and low alloy steels in water media typical for oilfield pipeline operating conditions. *Metallurgist*. 2019;63:717–726. <https://doi.org/10.1007/s11015-019-00881-0>

Амежнов А.В., Родионова И.Г. Влияние химического и фазового состава неметаллических включений на коррозионную стойкость углеродистых и низколегированных сталей в водных средах, характерных для условий эксплуатации нефтепромысловых трубопроводов. *Металлург*. 2019;(7):15–30.

  18. Golubtsov V.A., Ryabchikov I.V., Mizin, V.G. Influence of chemically active elements on the hydrogen cracking of pipe steel. *Steel in Translation*. 2016;46(3):220–223. <https://doi.org/10.3103/S0967091216030037>

Голубцов В.А., Рябчиков И.В., Мизин В.Г. Влияние химически активных элементов на водородное растрескивание стали для труб. *Сталь*. 2016;(3):50–53.

  19. Talukdar A., Rajaraman P.V. Effect of acetic acid in CO<sub>2</sub>-H<sub>2</sub>S corrosion of carbon steel at elevated temperature. *Materials Today: Proceedings*. 2022;57(4):1842–1845. <https://doi.org/10.1016/j.matpr.2022.01.036>
  20. Mikhalkina O.G., Fedorov P.P., Andreev P.O. Obtaining compounds of rare earth elements using sulfides. *Khimicheskaya Tekhnologiya*. 2011;12(12):706–710. (In Russ.).

Михалкина О.Г., Федоров П.П., Андреев П.О. Получение соединений редкоземельных элементов с использованием сульфидов. *Химическая технология*. 2011;12(12): 706–710.

  21. Zhou C., Chen X., Wang Z., Zheng S., Li X., Zhang S. Effects of environmental conditions on hydrogen permeation of X52 pipeline steel exposed to high H<sub>2</sub>S-containing solutions. *Corrosion Science*. 2014;89:30–37. <https://doi.org/10.1016/j.corsci.2014.07.061>
  22. Liu Z., Wang Y., Hai Y., Qiao Y., Zheng C., Wang D., Shi X., Lu H., Liu C. Corrosion behavior of low alloy steel used for new pipeline exposed to H<sub>2</sub>S-saturated solution. *International Journal of Hydrogen Energy*. 2022;47(77):33000–33013. <https://doi.org/10.1016/j.ijhydene.2022.07.203>
  23. Alanazi N.M., Al-Enezi A.A. The effect of the partial pressure of H<sub>2</sub>S and CO<sub>2</sub> on the permeation of hydrogen in carbon steel by using pressure buildup techniques. *Corrosion*. 2019;75(10):1207–1215. <https://doi.org/10.5006/3128>
  24. Kittel J., Smanio V., Fregonese M., Garnier L., Lefebvre X. Hydrogen induced cracking (HIC) testing of low alloy steel in sour environment: Impact of time of exposure on the extent of damage. *Corrosion Science*. 2010;52(4):1386–1392. <http://dx.doi.org/10.1016/j.corsci.2009.11.044>
  25. Huang B., Peng H., Chen X., Gong C., Li J. Study on the impact toughness and diffusible hydrogen of G105 drill pipe steel in wet H<sub>2</sub>S environment. *Corrosion Engineering, Science and Technology*. 2017;52(6):453–458. <https://doi.org/10.1080/1478422X.2017.1329247>
  26. Laureys A., Depraetere R., Cauwels M., Depover T., Hertelé S., Verbeken K. Use of existing steel pipeline infrastructure for gaseous hydrogen storage and transport: A review of factors affecting hydrogen induced degradation. *Journal of Natural Gas Science and Engineering*. 2022;101:104534. <https://doi.org/10.1016/j.jngse.2022.104534>
  27. Zhou D., Li T., Huang D., Wu Y., Huang Z., Xiao W., Wang Q., Wang X. The experiment study to assess the impact of hydrogen blended natural gas on the tensile properties and damage mechanism of X80 pipeline steel. *International Journal of Hydrogen Energy*. 2017;42(10):7407–7412. <https://doi.org/10.1016/j.ijhydene.2020.11.267>
  28. Kantukov R.R., Zapevalov D.N., Vagapov R.K. Media corrosiveness and materials resistance at presence of aggressive carbon dioxide. *Izvestiya. Ferrous Metallurgy*. 2021;64(11):793–801. (In Russ.). <https://doi.org/10.17073/0368-0797-2021-11-793-801>

Кантюков Р.Р., Запеевалов Д.Н., Вагапов Р.К. Исследование коррозионной активности сред и стойкости используемых материалов в условиях присутствия агрессивного диоксида углерода. *Известия вузов. Черная Металлургия*. 2021;64(11):793–801. <https://doi.org/10.17073/0368-0797-2021-11-793-801>

  29. Shang J., Chen W., Zheng J., Hua Z., Zhang L., Zhou C., Gu C. Enhanced hydrogen embrittlement of low-carbon steel to natural gas/hydrogen mixtures. *Scripta Materialia*. 2020;189:67–71. <https://doi.org/10.1016/j.scriptamat.2020.08.011>
  30. Song E.J., Baek S.-W., Nahm S.H., Baek U.B. Notched-tensile properties under high-pressure gaseous hydrogen: Comparison of pipeline steel X70 and austenitic stainless type 304L, 316L steels. *International Journal of Hydrogen Energy*. 2017;42(12):8075–8082. <http://dx.doi.org/10.1016/j.ijhydene.2016.12.069>
  31. Nastich S.Yu., Lopatkin V.A., Arabei A.B., Egorov V.A., Popkov A.S. Changes in the mechanical properties of metal pipes of main gas pipelines under the influence of hydrogen gas at high pressure. In: *Gas Transportation Systems: Present and Future (GTS-2023): Abstracts of Reports of the IX International Scientific and Technical Conference. Kazan, 03–07 April 2023*. Kazan: Gazprom VNIIGAZ; 2023:27. (In Russ.).

Настич С.Ю., Лопаткин В.А., Арабей А.Б., Егоров В.А., Попков А.С. Изменение механических свойств металла труб магистральных газопроводов под воздействием газообразного водорода при высоком давлении. В сб.: *Газотранспортные системы: настоящее и будущее (ГТС-2023): тезисы докладов IX Международной*

научно-технической конференции. Казань, 03–07 апреля 2023 г. Казань: Газпром ВНИИГАЗ; 2023:27.

32. Koide K., Minami T., Anraku T., Iwase A., Inoue H. Effect of hydrogen partial pressure on the hydrogen embrittlement susceptibility of type 304 stainless steel in high pressure H<sub>2</sub>/Ar mixed gas. *ISIJ International*. 2015;55(11):2477–2482. <http://dx.doi.org/10.2355/isijinternational.ISIJINT-2015-232>
33. Nguyen T.T., Park J.S., Nahm S.H., Baek U.B. Evaluation of hydrogen related degradation of API X42 pipeline under hydrogen/natural gas mixture conditions using small punch test. *Theoretical and Applied Fracture Mechanics*. 2021;113:102961. <https://doi.org/10.1016/j.tafmec.2021.102961>
34. Pessu F., Barker R., Chang F., Chen T., Neville A. Iron sulphide formation and interaction with corrosion inhibitor in H<sub>2</sub>S-containing environments. *Journal of Petroleum Science and Engineering*. 2021;207:109152. <https://doi.org/10.1016/j.petrol.2021.109152>
35. Tsygankova L.E., Uryadnikov A.A., Abramov A.E., Semyuk T.V. Inhibiting formulations against hydrogen sulfide corrosion of carbon steel. *International Journal of Corrosion*

and Scale Inhibition. 2022;11(1):102–110.

<https://doi.org/10.17675/2305-6894-2021-11-1-5>

36. Matrosov Yu.I., Kholodnyi A.A., Matrosov M.Yu., Popov E.S., Konovalov G.N., Sosin S.V. Effect of accelerated cooling parameters on microstructure and hydrogen cracking resistance of low-alloy pipe steels. *Metallurgist*. 2015;59:60–68. <https://doi.org/10.1007/s11015-015-0061-1>  
Матросов Ю.И., Холодный А.А., Матросов М.Ю. и др. Влияние параметров ускоренного охлаждения на микроструктуру и сопротивление водородному растрескиванию низколегированных трубных сталей. *Металлург*. 2015;(1):68–75.
37. Naumenko V.V., Muntin A.V., Baranova O.A., Smetanin K.S. Resistance to hydrogen cracking of rolled structural steel after heat processing. *Steel in Translation*. 2021;51(3): 211–216. <https://doi.org/10.3103/S0967091221030086>  
Науменко В.В., Мунтин А.В., Баранова О.А., Сметанин К.С. Стойкость против водородного растрескивания проката из конструкционной стали после термической обработки. *Сталь*. 2021;(3):44–49.

## Information about the Authors

## Сведения об авторах

**Rafael' R. Kantyukov**, Cand. Sci. (Eng.), Deputy General Director for Research, LLC "Scientific-Research Institute of Natural Gases and Gas Technologies – Gazprom VNIIGAZ"

ORCID: 0000-0003-3339-4774

E-mail: [vniigaz@vniigaz.gazprom.ru](mailto:vniigaz@vniigaz.gazprom.ru)

**Dmitry N. Zapevalov**, Cand. Sci. (Eng.), Head of the Corporate Scientific and Technical Center for Corrosion Monitoring and Protection, LLC "Scientific-Research Institute of Natural Gases and Gas Technologies – Gazprom VNIIGAZ"

ORCID: 0000-0002-2867-1995

E-mail: [D\\_Zapevalov@vniigaz.gazprom.ru](mailto:D_Zapevalov@vniigaz.gazprom.ru)

**Ruslan K. Vagapov**, Dr. Sci. (Eng.), Cand. Sci. (Chem.), Head of the Laboratory of Atmospheric and Internal Corrosion Protection, LLC "Scientific-Research Institute of Natural Gases and Gas Technologies – Gazprom VNIIGAZ"

ORCID: 0000-0002-8467-4103

E-mail: [R\\_Vagapov@vniigaz.gazprom.ru](mailto:R_Vagapov@vniigaz.gazprom.ru)

**Рафаэль Рафкатович Кантюков**, к.т.н., заместитель генерального директора по науке, ООО «Научно-исследовательский институт природных газов и газовых технологий – Газпром ВНИИГАЗ»

ORCID: 0000-0003-3339-4774

E-mail: [vniigaz@vniigaz.gazprom.ru](mailto:vniigaz@vniigaz.gazprom.ru)

**Дмитрий Николаевич Запевалов**, к.т.н., начальник Корпоративного научно-технического центра коррозионного мониторинга и защиты от коррозии, ООО «Научно-исследовательский институт природных газов и газовых технологий – Газпром ВНИИГАЗ»

ORCID: 0000-0002-2867-1995

E-mail: [D\\_Zapevalov@vniigaz.gazprom.ru](mailto:D_Zapevalov@vniigaz.gazprom.ru)

**Руслан Кизитович Вагапов**, д.т.н., к.х.н., начальник лаборатории защиты от атмосферной и внутренней коррозии, ООО «Научно-исследовательский институт природных газов и газовых технологий – Газпром ВНИИГАЗ»

ORCID: 0000-0002-8467-4103

E-mail: [R\\_Vagapov@vniigaz.gazprom.ru](mailto:R_Vagapov@vniigaz.gazprom.ru)

## Contribution of the Authors

## Вклад авторов

**R. R. Kantyukov** – formation of the article concept and abstract, goals and objectives of the study; correction of conclusions.

**D. N. Zapevalov** – scientific guidance, revision and correction of the text, formation of introduction and conclusions.

**R. K. Vagapov** – analysis of research results, writing the main text, search and analysis of literary data, text formatting and design.

**Р. Р. Кантюков** – формирование концепции статьи и аннотации, целей и задач исследования, корректировка выводов.

**Д. Н. Запевалов** – научное руководство, доработка и корректировка текста, формирование введения и выводов.

**Р. К. Вагапов** – анализ результатов исследований, написание основного текста статьи, поиск и анализ литературных данных, форматирование и оформление текста.

Received 30.05.2023

Revised 09.11.2023

Accepted 19.12.2023

Поступила в редакцию 30.05.2023

После доработки 09.11.2023

Принята к публикации 19.12.2023





UDC 621.791.927.5

DOI 10.17073/0368-0797-2024-1-65-72



Original article

Оригинальная статья

## STRUCTURE AND ITS DEFECTS IN ADDITIVE MANUFACTURING OF STAINLESS STEELS BY LASER MELTING AND ELECTRIC ARC SURFACING

Yu. G. Kabaldin, M. A. Chernigin

R.E. Alekseev Nizhny Novgorod State Technical University (24 Minina Str., Nizhny Novgorod 603022, Russian Federation)

honeybadger52@yandex.ru

**Abstract.** Currently, there is an active development and study of additive technologies. Metal 3D printing makes it possible to obtain parts and structures of complex configuration using a minimum of shaping operations, which can lead to a reduction in overall cost of the resulting products. In this paper, we studied the structure formation in manufacture of products made of stainless steels 10Cr12Ni10Ti (analogue of AISI 321) and 08Cr18Ni9 (analogue of AISI 304) by additive methods – SLM (*Selective Laser Melting*) and WAAM (*Wire Arc Additive Manufacturing*). In the course of microstructural analysis, it was found that during the manufacture of products using SLM technology, small austenitic grains oriented in the direction of heat removal are formed, and with WAAM method, austenite is formed mainly in form of dendrites. It is shown that porosity is formed during manufacture of the samples by SLM method, which is associated with non-melting of individual powder particles. When implementing additive manufacturing by WAAM (electric arc surfacing), there is no increased porosity. In the course of the study, a new defect of the structure formed during the manufacture of products by both methods was revealed – formation of interface boundaries between layers, which is associated with the technology of additive manufacturing itself. When manufacturing a WAAM product, it manifests itself more clearly than when obtaining metal by SLM. Boundaries of the surfacing rollers in the manufacture of products by SLM accumulate various intermetallics and structural defects more intensively, relative to WAAM. As a result of the small relative volume of one surfacing roller, compared with WAAM, accumulation of these defects and intermetallics can act as an effective barrier during movement of dislocations, which can lead to an increase in the strength properties of products.

**Keywords:** additive manufacturing, stainless steels, SLM, WAAM, sample structure, structural defects

**For citation:** Kabaldin Yu.G., Chernigin M.A. Structure and its defects in additive manufacturing of stainless steels by laser melting and electric arc surfacing. *Izvestiya. Ferrous Metallurgy*. 2024;67(1):65–72. <https://doi.org/10.17073/0368-0797-2024-1-65-72>

## СТРУКТУРА И ЕЕ ДЕФЕКТЫ ПРИ АДДИТИВНОМ ВЫРАЩИВАНИИ НЕРЖАВЕЮЩИХ СТАЛЕЙ МЕТОДАМИ ЛАЗЕРНОГО СПЕКАНИЯ И ЭЛЕКТРОДУГОВОЙ НАПЛАВКИ

Ю. Г. Кабалдин, М. А. Чернигин

Нижегородский государственный технический университет им. Р.Е. Алексеева (Россия, 603022, Нижний Новгород, ул. Минина, 24)

honeybadger52@yandex.ru

**Аннотация.** В настоящее время происходит активное развитие и изучение аддитивных технологий. Технологии 3D-печати металлами позволяют получать детали и конструкции сложной конфигурации с применением минимума формообразующих операций, что может приводить к снижению общей себестоимости получаемых изделий. В данной работе исследовалось структурообразование при изготовлении изделий из нержавеющей стали 10Х12Н10Т и 08Х18Н9 аддитивными методами – SLM (*Selective Laser Melting*, селективное лазерное спекание) и WAAM (*Wire Arc Additive Manufacturing*, электродуговое выращивание). В ходе микроструктурного анализа было установлено, что при изготовлении изделий по технологии SLM образуются мелкие аустенитные зерна, ориентированные по направлению отвода тепла, а при методе WAAM аустенит формируется преимущественно в виде дендритов. Показано, что при изготовлении образцов методом SLM образуется пористость, что связано с неплавлением отдельных частиц порошка. При реализации аддитивного выращивания методом WAAM (электродуговой наплавкой) повышенная пористость отсутствует. В ходе исследования выявлен новый дефект структуры, формирующийся при изготовлении изделий обоими методами – это образование границ раздела между слоями, что связано с самой технологией аддитивного выращивания. При выращивании изделия методом WAAM он проявляется более явно, чем при получении металла методом SLM. Границы наплавочных валиков при изготовлении изделий методом SLM более интенсивно накапливают различные интерметаллиды и структурные дефекты. Вследствие малого относительного объема одного наплавочного валика, по



сравнению с методом WAAM, скопление данных дефектов и интерметаллидов может выступать эффективным барьером при движении дислокаций и приводить к повышению прочностных свойств изделий.

**Ключевые слова:** аддитивное выращивание, нержавеющие стали, SLM, WAAM, структура образцов, дефекты структуры

**Для цитирования:** Кабалдин Ю.Г., Чернигин М.А. Структура и ее дефекты при аддитивном выращивании нержавеющей сталей методами лазерного спекания и электродуговой наплавки. *Известия вузов. Черная металлургия*. 2024;67(1):65–72.

<https://doi.org/10.17073/0368-0797-2024-1-65-72>

## INTRODUCTION

Additive technologies represent a burgeoning trend in digital technologies today [1 – 7]. However, the terminology for this trend has yet to be standardized, not only in Russia but globally. Currently, Russia is actively developing specialized GOST standards, which are partially harmonized with ISO and ASTM standards and, in some respects, surpass them.

Among the various technologies for additive manufacturing (AM) of products, Selective Laser Melting (SLM) and Wire Arc Additive Manufacturing (WAAM) techniques stand out as the most popular.

SLM is an additive production method that manufactures parts from an electronic geometric pattern by surfacing metal raw materials with laser radiation [1 – 6]. Both powder and wire can serve as the metal raw material.

Recently, Wire Arc Additive Manufacturing (WAAM) has also gained significant prominence. WAAM [5 – 8] has demonstrated the highest efficiency (up to 15 kg/h) and the capability to produce large-sized items. Domestic manufacturing companies are quite familiar with this technology, as electric arc surfacing and welding are commonplace in nearly any metal-involved production process.

It should be noted that in Russia, both technologies are relatively understudied, particularly in terms of defect formation during their application [1 – 2] during their implementation, which results in a drop of the metal mechanical properties, which leads to a degradation of the metal's mechanical properties. Therefore, the objective of this work is to investigate defect formation during the additive manufacturing of products (samples) using these methods.

## MATERIALS AND METHODS

Stainless steels are widely used in additive manufacturing due to their special properties [6; 9; 10], such as good weldability and corrosion resistance.

In this study, we examined stainless steels 12Cr18Ni10T and 08Cr18Ni9, which have an FCC structure. These materials are particularly favored for their layer weldability and melt fluidity.

The samples were manufactured using the SLM method, employing powder from 10Cr18Ni10Ti steel

with spherical particles ranging from 50 to 80  $\mu\text{m}$  in size. Various initial powders were used to produce several samples (samples 1 and 2). While both samples were surfaced using powder from the same manufacturer, sample 1 utilized powder from a newly opened package, whereas sample 2 used powder from a previously opened package. The chemical composition of the materials is provided in Table 1.

In the additive manufacturing process of the samples using the WAAM method, welding wire Sv-08Cr18Ni9 (ER308Lsi) was employed.

The test samples were produced in the form of bars on a Rusmelt 300M printer using the SLM method.

The WAAM blanks were manufactured as walls on a specially designed experimental bench. The papers [6; 11] describe a 3D printing technology utilizing electric arc surfacing, and the method employed on the bench is protected by patent RU 2696121C1. The 3D printing process was investigated with gas torch travel speeds of 350 and 400 mm/min in a  $\text{CO}_2$  shielding gas environment. The surfacing heat input varied within the range of 150 – 1200 J/mm.

Metallographic sections were prepared from the obtained samples to determine the structure of the printed blanks. The sections were mechanically sanded using sandpaper of varying grits and polished with pastes. A solution consisting of 5  $\text{cm}^3$   $\text{HNO}_3$ , 50  $\text{cm}^3$   $\text{HCl}$ , and 50  $\text{cm}^3$   $\text{H}_2\text{O}$  was used as a chemical etching reagent, following recommendations from reference sources [12 – 14].

Structural analysis was conducted using a KEYENCEVHX-1000 optical microscope. The fractographic investigation was conducted using a Tescan Vega 3 scanning electron microscope. The metal's chemical composition was analyzed using an ARL 3460 spectrometer.

**Table 1. Chemical composition of the samples obtained by SLM, %**

**Таблица 1. Химический состав образцов, изготовленных методом SLM, %**

C	Mn	Si	S	P	Ni	Cu	Mo	Cr
0.080	0.694	0.432	0.236	0.147	10.6	0.296	0.9913	17.1

## EXPERIMENTAL STUDIES

The optical emission analysis of the WAAM samples indicated negligible carbon and silicon loss. This phenomenon is attributed to the characteristics of the sample manufacturing technology and is typical of foundry and welding operations. Table 2 displays the chemical composition of the initial wire made from stainless steel 08Cr18Ni9 and the sample produced by the WAAM method.

According to Table 2, although the percentage content of several elements decreases during additive manufacturing, it remains within acceptable limits.

Typically, metal powders utilized for manufacturing products via the SLM method possess a high surface area, which inevitably results in sample porosity and the transfer of adsorbed contaminating agents from the powder surface into the finished product. Therefore, it was imperative to primarily investigate the porosity of the blanks and the structure of the metal produced by the SLM method.

We examined the surface of unetched sections manufactured by the SLM method to study the formation of metal porosity and contamination by non-metallic inclusions (Fig. 1). On several samples, metal porosity did not increase during the study. The degree of metal contamination with non-metallic inclusions was determined on the microsection at a magnification of 100 in accordance with GOST 1778 – 70. The results of the test for contamination with non-metallic inclusions are presented in Table 3.

Metallographic examination of the sample in the direction transverse to surfacing reveals sharp boundaries of surfacing rollers (Fig. 2). There are no pronounced signs of a dendritic structure characteristic of metal after 3D printing.

In general, the structure of the deposited metal formed by the SLM method comprises relatively small austenitic grains oriented in the direction of heat removal, with distinctly observed austenitic twins (Fig. 2). Closer to the boundaries where the layers melt, the structure

**Table 2. Chemical composition of 08Cr18Ni9 wire and metal deposited by WAAM, %**

**Таблица 2. Химический состав проволоки из стали 08X18H9 и наплавленного материала методом WAAM, %**

C	Mn	Si	S	P	Ni	Cu	Mo	Cr
Wire								
0.0019	1.95	0.9	0.012	0.200	9.90	0.05	0.06	19.79
Deposited material								
0.0100	1.80	0.8	0.012	0.013	10.00	0.10	0.10	20.00



**Fig. 1.** Unetched section of sample 1 obtained by SLM

**Рис. 1.** Нетравленный шлиф образца 1, полученного методом SLM

appears refined, displaying abnormally small austenitic grains also oriented in the direction of heat removal.

The microstructural analysis data obtained align with results presented in the works of other authors [15 – 18].

Examination of sample 2 revealed the presence of large individual pores and clusters thereof, as well as shrinkage cavities [19]. All identified discontinuity flaws are typical defects formed during metal casting or welding.

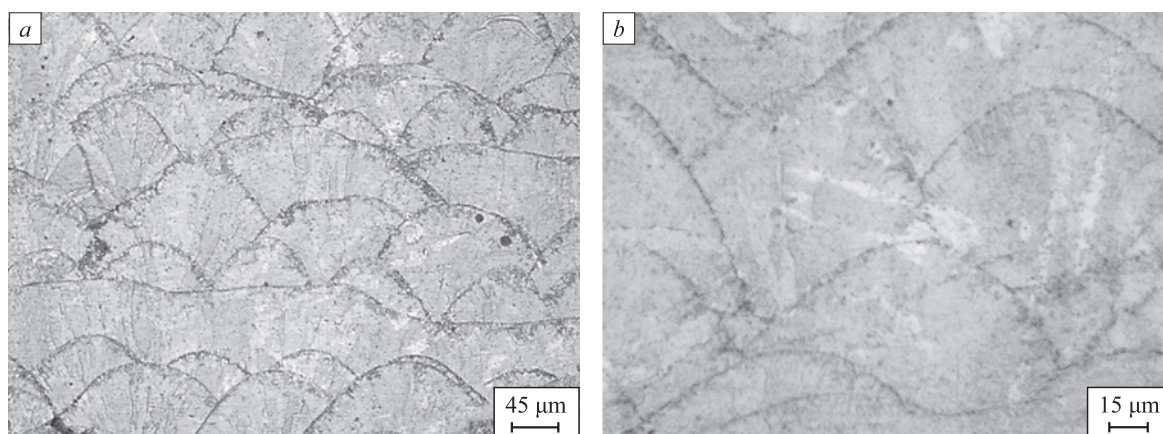
The average size of these discontinuity flaws was calculated at a magnification of 50 at various points on the unetched polished section, amounting to 94 μm (Fig. 3). Clusters of discontinuity flaws of this size can potentially exert a negative impact on the mechanical properties of the product.

Currently, the heightened porosity observed in samples obtained through the SLM method is attributed to powder contamination with various impurities or the explosive melting of powder particles. It is evident that the feed-

**Table 3. Points of contamination of the section with various non-metallic inclusions in accordance with GOST 1778**

**Таблица 3. Баллы загрязненности шлифа различными неметаллическим включениям в соответствии с ГОСТ 1778**

Type of inclusion	Score
Spot oxides	2
Line oxides	0
Spot nitrides	1
Line nitrides	0
Sulfides	0
Non-deformable, brittle and plastic silicates	0



**Fig. 2.** Structure of sample 1 obtained by SLM:  $\times 200$  (a);  $\times 500$  (b)

**Рис. 2.** Структура образца 1, полученного методом SLM:  $\times 200$  (a);  $\times 500$  (b)

stock used in manufacturing sample 2 may have been contaminated. The identified defects can be classified as typical flaws associated with this technology [20].

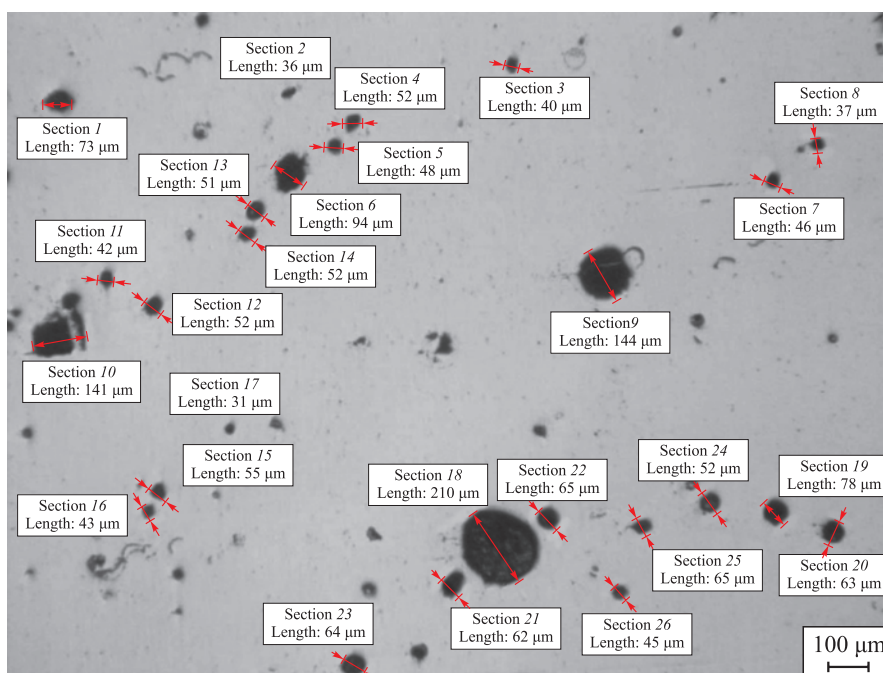
Fig. 4 illustrates an electron fractogram depicting the presence of spherical particles of unmelted powder of 12Cr18Ni10T steel on the fracture surface of sample 2.

Consequently, the metal of products manufactured by the SLM method tends to be porous primarily because powder particles fail to melt, either due to powder contamination or incorrect processing parameters.

The structure of the welded metal exhibits dendritic characteristics. Near the fusion boundary, the dendrites typically orient themselves towards it, possibly influenced

by temperature gradients. In the interior of the deposited metal, dendrites are randomly arranged. Irregular dendrites are shorter than their normally oriented counterparts, yet they possess a more developed boundary structure. Overall, the structure of the deposited metal bears resemblance to the microstructure resulting from the crystallization of austenitic steel.

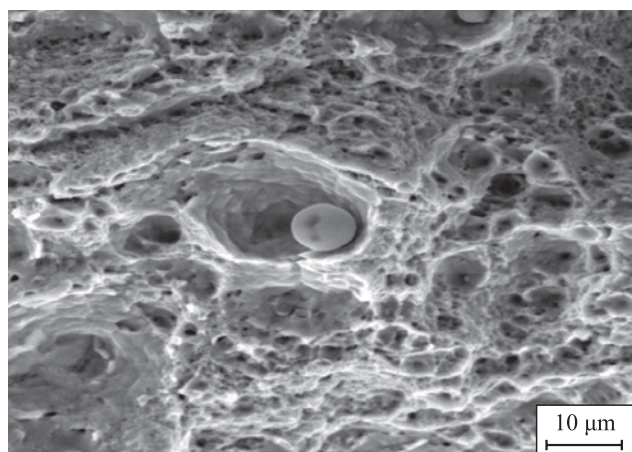
The metallographic analysis of sections from samples made of 08Cr18Ni9 steel via the WAAM method revealed minimal porosity. Fig. 6 depicts an unetched sample section. The level of metal contamination with non-metallic inclusions was assessed on the microsection at a magnification of 100 in accordance with GOST 1778 – 70.



**Fig. 3.** Unetched section of sample 2 obtained by SLM

**Рис. 3.** Нетравленный шлиф образца 2, полученного методом SLM





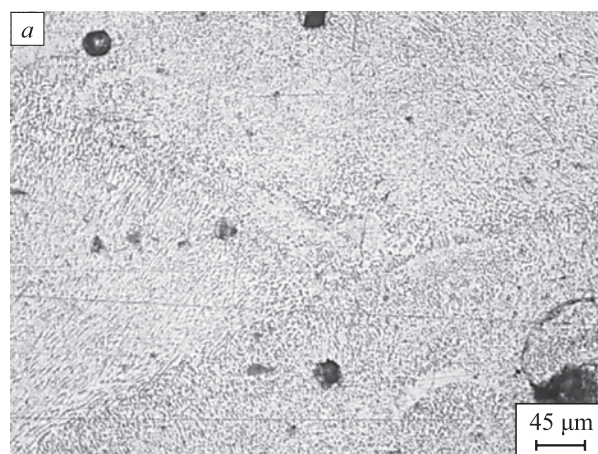
**Fig. 4.** Fractogram of the fracture of sample 2 obtained by SLM after its stretching

**Рис. 4.** Фрактограмма излома образца 2, полученного методом SLM, после его растяжения

The findings regarding contamination with non-metallic inclusions are detailed in Table 4.

Fig. 7 illustrates the microstructure of the metal produced via the WAAM method under optimal 3D printing conditions. The deposited metal's structure exhibits dendritic characteristics and changes as it moves from the fusion boundary into the depth of the deposited metal from cellular-dendritic to predominantly dendritic with a disordered orientation. Overall, the structure of the deposited metal bears resemblance to the microstructure resulting from the crystallization of austenitic steel or by additive manufacturing with other methods.

The analysis indicates that structural defects such as porosity and structural inhomogeneity are inherent in all known methods of metal production. However, with products manufactured by both methods, a new structural defect characteristic of additive manufacturing has emerged – the formation of interface boundaries between



**Fig. 5.** Structure of sample 2 obtained by SLM:  $\times 200$  (a);  $\times 500$  (b)

**Рис. 5.** Структура образца 2, полученного методом SLM:  $\times 200$  (a);  $\times 500$  (b)

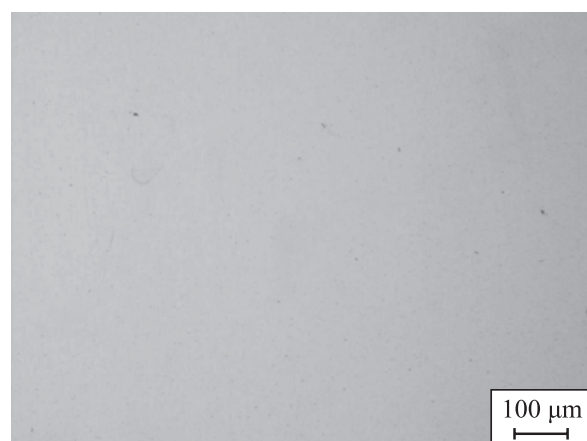
layers, attributed to the additive manufacturing technology itself.

Fig. 8 presents micrographs of the interface boundaries of displays micrographs of the interface boundaries

**Table 4.** Points of contamination of the section with various non-metallic inclusions in accordance with GOST 1778

**Таблица 4.** Баллы загрязненности шлифа различными неметаллическим включениям в соответствии с ГОСТ 1778

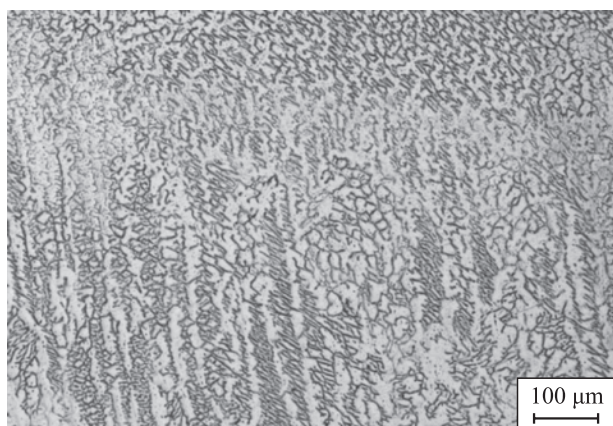
Type of inclusion	Score
Spot oxides	0.5
Line oxides	0
Spot nitrides	0
Line nitrides	0
Sulfides	0
Non-deformable, brittle and plastic silicates	0



**Fig. 6.** Unetched section of the sample obtained by WAAM

**Рис. 6.** Нетравленный шлиф образца, полученного методом WAAM





**Fig. 7.** Microstructure of metal of the sample obtained by WAAM from welding wire Sv-08Cr18Ni9 (ER308Lsi)

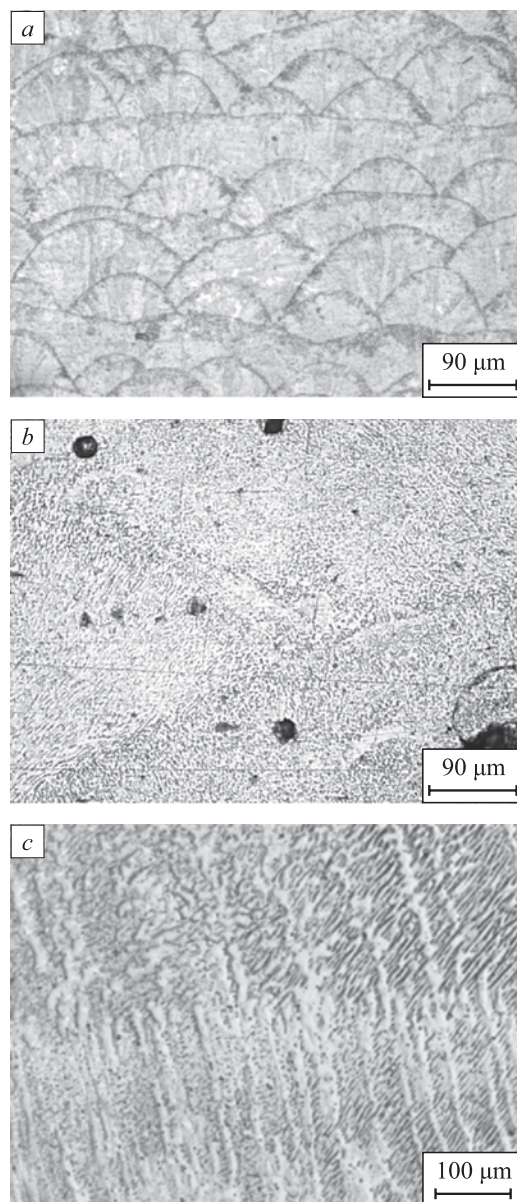
**Рис. 7.** Микроструктура металла образца, полученного методом WAAM из сварочной проволоки Св-08Х18Н9 (ER308Lsi)

of samples manufactured by both the WAAM and SLM methods, where porosity is also detected at these boundaries between layers.

Research findings indicate that the interface boundaries formed between layers introduce high internal stresses into the product. The WAAM method is characterized by greater internal stresses resulting from these interface boundaries compared to the SLM method. This discrepancy is attributed to the differing thicknesses of the layers generated by each method. In the SLM method, layers are typically 0.2 – 0.5 mm thick, whereas in the WAAM method, layers range from 0.8 – 0.9 mm thick.

Another undesired defect observed in additive manufacturing of steels is the presence of the  $\delta$ - and  $\sigma$ -phases. However, X-ray diffraction analysis [8] revealed that their content in samples produced by both methods does not exceed 4 %, remaining within acceptable limits.

In traditional welding technology, the weld often weakens the overall structure. However, metal produced by the SLM method exhibits greater strength than rolled steel. This effect is corroborated by several studies and can be attributed to the relatively small space occupied by each surfacing roller in relation to the entire deposited metal. This allows various intermetallics to concentrate within the roller, which, due to rapid cooling rates, do not have sufficient time to completely transform into welding slag and thus remain embedded within the metal surface – a phenomenon not observed in WAAM surfacing. The accumulation of various intermetallics and potential structural defects is clearly evident in Fig. 8, *a, b*. When samples obtained by the SLM method undergo stretching, defects and intermetallics accumulated along the boundaries of surfacing rollers can effectively impede dislocation motion. Consequently, this impediment results in enhanced strength properties.



**Fig. 8.** Micrographs of metal interface of the samples: SLM, sample 1 (*a*); SLM, sample 2 (*b*); WAAM (*c*)

**Рис. 8.** Микрофотографии границы раздела металла образцов: SLM, образец 1 (*a*); SLM, образец 2 (*b*); WAAM (*c*)

## CONCLUSIONS

The structure of stainless steels produced by the SLM method is austenitic, whereas the metal formed by the WAAM technique tends to exhibit a dendritic structure. Porosity, typically associated with the non-melting of individual powder particles, is observed during the manufacture of samples via the SLM method. To mitigate porosity in the products, stricter control over the raw materials used for surfacing is necessary. While the use of the WAAM method did not noticeably increase metal porosity, a new structural defect emerged in products manufactured by both methods – the formation of interface boundaries between layers, inherent to addi-

tive manufacturing technology itself. In SLM-produced products, porosity is evident at these interface boundaries, resulting in elevated internal stresses within the product. Moreover, in the SLM method, the accumulation of defects and intermetallics at the boundaries of surfacing rollers can effectively impede dislocation motion, thereby contributing to improved strength properties.

## СПИСОК ЛИТЕРАТУРЫ / REFERENCES

1. Grigoriyants A.G., Kolchanov D.S., Drenin A.A., Denezhkin A.O. Study of the influence of main parameters of the selective laser melting process on the porosity of aluminum alloy RS-300 samples. *BMSTU. Journal of Mechanical Engineering*. 2022;(8(749)):55–64. (In Russ.).  
<https://doi.org/10.18698/0536-1044-2022-8-55-64>  
Григорьянц А.Г. Колчанов Д.С., Дренин А.А., Денежкин А.О. Исследование влияния основных параметров процесса селективного лазерного плавления на пористость образцов из алюминиевого сплава RS-300. *Известия вузов. Машиностроение*. 2022;(8(749)):55–64.  
<https://doi.org/10.18698/0536-1044-2022-8-55-64>
2. Grigoriyants A.G., Lutchenko A.V. Modern problems of technological development of additive techniques in mechanical engineering. *Science Intensive Technologies in Mechanical Engineering*. 2022;(8(134)):27–30. (In Russ.).  
<https://doi.org/10.30987/2223-4608-2022-8-27-30>  
Григорьянц А.Г., Лутченко А.В. Современные проблемы развития аддитивных технологий в машиностроении. *Научные технологии в машиностроении*. 2022;(8(134)):27–30.  
<https://doi.org/10.30987/2223-4608-2022-8-27-30>
3. Turichin G.A., Zemlyakov E.V., Klimova O.G., Babkin K.D., Shamrai F.A., Kolodyazhnyi D.Yu. Direct laser manufacturing – a promising additive technology for aircraft engine production. *Svarka i Diagnostika*. 2015;(3):54–57. (In Russ.).  
Туричин Г.А., Земляков Е.В., Климова О.Г., Бабкин К.Д., Шамрай Ф.А., Колодяжный Д.Ю. Прямое лазерное выращивание – перспективная аддитивная технология для авиадвигателестроения. *Сварка и Диагностика*. 2015;(3):54–57.
4. Panchenko O., Kurushkin D., Mushnikov D., Khismatullin I., Popovich A.A. High-performance WAAM process for Al-Mg-Mn using controlled short-circuiting metal transfer at increased wire feed rate and increased travel speed. *Materials and Design*. 2020;195:35–45.  
<https://doi.org/10.1016/j.matdes.2020.109040>
5. Cunningham C.R., Wikshåland S., Xu F. Cost modelling and sensitivity analysis of wire and arc additive manufacturing. *Procedia Manufacturing*. 2017;11:650–657.  
<https://doi.org/10.1016/j.promfg.2017.07.163>
6. Kabaldin Y., Shatagin D., Ryabov D., Solovyov A., Kurkin A. Microstructure, phase composition, and mechanical properties of a layered bimetallic composite ER70S 6-ER309LSI obtained by the WAAM method. *Metals*. 2023;(13(5)):851.  
<https://doi.org/10.3390/met13050851>
7. Gulyaev A.P. *Metal Science*. Moscow: Metallurgiya; 1986: 544. (In Russ.).  
Гуляев А.П. *Металловедение*. Москва: Металлургия; 1986:544.
8. Gonchar A.V., Klyushnikov A.A., Mishakin V.V. The effect of plastic deformation and subsequent heat treatment on the acoustic and magnetic properties of 12Kh18N10T steel. *Industrial laboratory. Diagnostics of materials*. 2019;85(2):23–28. (In Russ.).  
<https://doi.org/10.26896/1028-6861-2019-85-2-23-28>  
Гончар А.В., Ключников А.А., Мишакин В.В. Влияние пластического деформирования и последующей термообработки на акустические и электромагнитные свойства стали 12Х18Н10Т. *Заводская лаборатория. Диагностика материалов*. 2019;85(2):23–28.  
<https://doi.org/10.26896/1028-6861-2019-85-2-23-28>
9. Fetisov G.P., Karpman M.G., etc. *Material Science and Technology of Metals*. Moscow: Vysshaya shkola; 2002:638. (In Russ.).  
Фетисов Г.П., Карпман М.Г. и др. *Материаловедение и технология металлов*. Москва: Высшая школа; 2002:638.
10. Chernigin M.A., Sorokina S.A., Vorobyev R.A. Study of the microstructure of metastable austenitic chromium manganese steel 14Kh15G9ND by optical and electron microscopy. *Industrial laboratory. Diagnostics of materials*. 2023;89(4):38–44. (In Russ.).  
<https://doi.org/10.26896/1028-6861-2023-89-4-38-44>  
Чернигин М.А., Сорокина С.А., Воробьев Р.А. Исследование микроструктуры метастабильной аустенитной хромомарганцевой стали 14Х15Г9НД методами оптической и электронной микроскопии. *Заводская лаборатория. Диагностика материалов*. 2023;89(4):38–44.  
<https://doi.org/10.26896/1028-6861-2023-89-4-38-44>
11. Anosov M.S., Shatagin D.A., Chernigin M.A., Mordovina Yu.S., Anosova E.S. Structure formation of Np-30KhGSA alloy in wire and arc additive manufacturing. *Izvestiya. Ferrous Metallurgy*. 2023;66(3):294–301. (In Russ.). <https://doi.org/10.17073/0368-0797-2023-3-294-301>  
Аносов М.С., Шатагин Д.А., Чернигин М.А., Мордовина Ю.С., Аносова Е.С. Структурообразование сплава Нп-30ХГСА при аддитивном электродуговом выращивании. *Известия вузов. Черная Металлургия*. 2023;66(3): 294–301. <https://doi.org/10.17073/0368-0797-2023-3-294-301>
12. Kovalenko V.S. *Metallographic Reagents: Handbook*. Moscow: Metallurgiya; 1981:120. (In Russ.).  
Коваленко В.С. *Металлографические реактивы: Справочник*. Москва: Металлургия; 1981:120.
13. Beckert M., Klemm H. *Handbook of Metallographic Etching Methods*. Leipzig: Veb Deutscher Verlag für Grundstoff; 1962.  
Беккерт М., Клемм Х. *Способы металлографического травления: Справочник*. Москва: Металлургия; 1988:400.
14. Panchenko E.V. *Metallographic Laboratory*. Moscow: Metallurgiya; 1965:441. (In Russ.).  
Панченко Е.В. *Лаборатория металлографии*. Москва: Металлургия; 1965: 441.
15. Gerov M., Kolmakov A., Prosvirnin D., Kayasova A., Zhdanova N., Prutskov M. Mechanical properties and fracture of austenitic steel fabricated by selective laser melting. *Russian Metallurgy (Metally)*. 2022;2022(10):1218–1226.  
<https://doi.org/10.1134/S0036029522100068>
16. Tascioglu E., Karabulut Y., Kaynak Y. Influence of heat treatment temperature on the microstructural, mechanical, and wear behavior of 316L stainless steel fabricated by laser

powder bed additive manufacturing. *International Journal of Advanced Manufacturing Technology*. 2020;107(5-6): 1947–1956. <https://doi.org/10.1007/s00170-020-04972-0>

17. Shin W.-S., Son B., Song W., Sohn H., Jang H., Kim Y.-J., Park C. Heat treatment effect on the microstructure, mechanical properties, and wear behaviors of stainless steel 316L prepared via selective laser melting. *Materials Science and Engineering*. 2021;806:140805. <https://doi.org/10.1016/j.msea.2021.140805>
18. Jeyaparakash N., Yang C.-H., Ramkumar K.R. Correlation of microstructural evolution with mechanical and tribological behavior of SS 304 specimens developed through SLM

technique. *Metals and Materials International*. 2021;27: 5179–5190. <https://doi.org/10.1007/s12540-020-00933-0>

19. Vasin O.E., etc. Atlas of Defects. Scientific and Technical Collector. Yekaterinburg: Izdatel'skie resheniya; 2008:56. (In Russ.).  
Васин О.Е. и др. Атлас дефектов. Научно-технический сборник. Екатеринбург: Издательские решения; 2008:56.
20. Jing G., Wang Z. Defects, densification mechanism and mechanical properties of 300M steel deposited by high power selective laser melting. *Additive Manufacturing*. 2021;38:101831. <https://doi.org/10.1016/j.addma.2020.101831>

## Information about the Authors

## Сведения об авторах

**Yurii G. Kabaldin**, Dr. Sci. (Eng.), Prof., Head of the Laboratory "Nanotechnology in Mechanical Engineering", R.E. Alekseev Nizhny Novgorod State Technical University  
**ORCID:** 0000-0003-4300-6659  
**E-mail:** [uru.40@mail.ru](mailto:uru.40@mail.ru)

**Mikhail A. Chernigin**, Engineer, R.E. Alekseev Nizhny Novgorod State Technical University  
**E-mail:** [honeybadger52@yandex.ru](mailto:honeybadger52@yandex.ru)

**Юрий Георгиевич Кабалдин**, д.т.н., профессор, руководитель лаборатории «Нанотехнологии в машиностроении», Нижегородский государственный технический университет им. Р.Е. Алексеева  
**ORCID:** 0000-0003-4300-6659  
**E-mail:** [uru.40@mail.ru](mailto:uru.40@mail.ru)

**Михаил Алексеевич Чернигин**, инженер, Нижегородский государственный технический университет им. Р.Е. Алексеева  
**E-mail:** [honeybadger52@yandex.ru](mailto:honeybadger52@yandex.ru)

Received 05.08.2023  
Revised 10.10.2023  
Accepted 11.12.2023

Поступила в редакцию 05.08.2023  
После доработки 10.10.2023  
Принята к публикации 11.12.2023





UDC 669.1+669.162.275.142

DOI 10.17073/0368-0797-2024-1-73-75

Short Report  
Краткое сообщение

## INFLUENCE OF COPPER AND SILICON ON PHASE TRANSFORMATIONS IN THE IRON – CARBON SYSTEM

G. Adilov, N. T. Kareva, V. E. Roshchin

■ South Ural State University (76 Lenina Ave., Chelyabinsk 454080, Russian Federation)

roshchinve@susu.ru

**Abstract.** To evaluate the phase and structural components of grinding media made of cast iron with a high content of copper and silicon obtained by extracting iron from copper-smelting slags, phase equilibria in the iron–carbon system were calculated with the addition of copper and silicon in various concentrations. The calculation was carried out using the ThermoCalc software package with construction of phase diagrams by the Calphad method. At the same time, temperatures of the beginning of phase transformations were estimated taking into account the presence of all thermodynamically possible phases in the system at various combinations of copper and silicon concentrations.

**Keywords:** copper smelting slag, cast iron, white cast iron, copper, iron, silicon, carbon, austenite, ferrite

**For citation:** Adilov G., Kareva N.T., Roshchin V.E. Influence of copper and silicon on phase transformations in the iron–carbon system. *Izvestiya. Ferrous Metallurgy*. 2024;67(1):73–75. <https://doi.org/10.17073/0368-0797-2024-1-73-75>

## ВЛИЯНИЕ МЕДИ И КРЕМНИЯ НА ФАЗОВЫЕ ПРЕВРАЩЕНИЯ В СИСТЕМЕ ЖЕЛЕЗО – УГЛЕРОД

Г. Адиллов, Н. Т. Карева, В. Е. Рошин

■ Южно-Уральский государственный университет (Россия, 454080, Челябинск, пр. Ленина, 76)

roshchinve@susu.ru

**Аннотация.** При извлечении железа из медеплавильных шлаков образуется чугу́н с повышенным содержанием меди и кремния. Для оценки фазового и структурного состава мелющих тел, произведенных из такого чугу́на, были рассчитаны фазовые равновесия в системе железо–углерод с добавлением разного количества меди и кремния. Расчеты были проведены с использованием программного комплекса ThermoCalc, который позволяет строить фазовые диаграммы по методу Calphad. В ходе расчетов были оценены температуры начала фазовых превращений с учетом всех возможных термодинамических фаз в системе при различных сочетаниях концентраций меди и кремния.

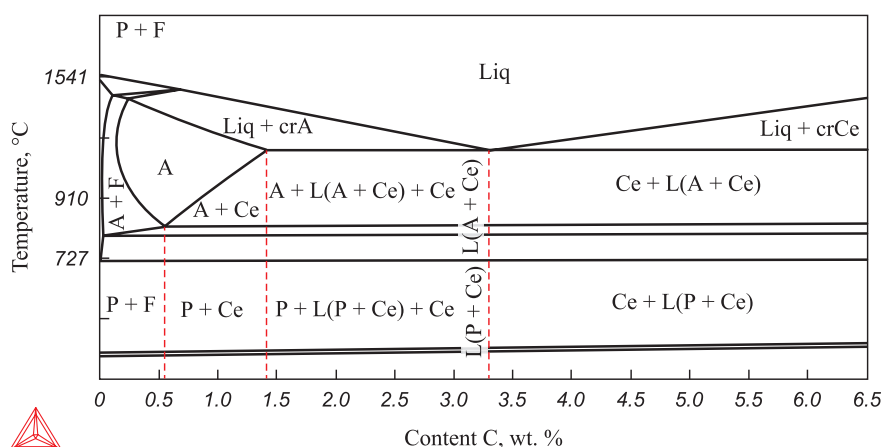
**Ключевые слова:** медеплавильный шлак, чугу́н, белый чугу́н, медь, железо, кремний, углерод, аустенит, феррит

**Для цитирования:** Адиллов Г., Карева Н.Т., Рошин В.Е. Влияние меди и кремния на фазовые превращения в системе железо–углерод. *Известия вузов. Черная металлургия*. 2024;67(1):73–75. <https://doi.org/10.17073/0368-0797-2024-1-73-75>

### INTRODUCTION

Large quantities of copper-smelting slag, primarily composed of iron, silicon, calcium, and aluminum oxides, have accumulated in waste dumps in areas where the non-ferrous metallurgy industry is well-developed. The slag also contains small amounts of compounds of copper, zinc, selenium, arsenic, and other elements. Among the elements present, iron has the highest value in the slag. When

iron is reduced by carbon under certain process conditions, alloys of iron-carbon or iron-carbon-silicon with high copper and sulfur content are produced. The high copper content, which traditional methods cannot remove, prevents the use of such metal in iron and steelmaking. Therefore, a process for the deep processing of copper-smelting slags is proposed to produce metal grinding media based on copper-containing iron-carbon-silicon alloys and ceramic proppants for the exploration and production sec-



Vertical section of the iron–carbon–copper system (1 %) with addition of silicon (3.5 %)

Вертикальный разрез системы железо–углерод–медь (1 %) при добавлении кремния (3,5 %)

tor [1]. Currently, white wear-resistant eutectic cast irons are employed in the manufacture of grinding media from copper-containing material [2; 3]. Additional knowledge about phase transformations in the iron-carbon system, in the presence of copper and silicon, is necessary to estimate the phase and structural composition of the alloys obtained from the processed slag material.

## RESEARCH METHOD

To construct the iron-carbon phase diagram with the presence of copper and silicon impurities, the Calphad method was employed using the ThermoCalc software package and the TCBD database: TC Binary Solutions v1.1<sup>1</sup>. The Calphad method within ThermoCalc leverages all available experimental data to derive the system's thermodynamic functions, which are represented as polynomials of chemical composition and temperature. Consequently, the values of the polynomial coefficients are determined using numerical optimization methods<sup>2</sup>. To ascertain the phase transformations in the iron-carbon phase diagram, copper in quantities ranging from 0 to 1.5 wt. % and silicon in the range of 0 to 3.5 wt. % were introduced into the system during the calculations. The pressure was set to 10<sup>5</sup> Pa, and the temperature was defined automatically.

## SIMULATION RESULT

The iron-carbon system, known for its five phases – ferrite (F), austenite (A), cementite (Ce), graphite, and one liquid phase—exhibits changes in carbon solubility when copper and silicon admixtures are present within specified limits. Copper, at quantities ranging from 0

to 1.5 %, marginally decreases carbon solubility in austenite, reducing it from 2.14 to 2.0 %.

Additionally, adding silicon from 0 to 3.5 % along a vertical section of the iron–carbon–copper system (at 1 % copper) lowers the carbon solubility in austenite's FCC lattice from 2.14 to 1.5 %. This addition also causes the ferrite phase region to expand and the eutectic point to shift towards a higher carbon concentration of 3.2 %, as illustrated in the accompanying figure.

## CONCLUSIONS

The calculations indicate that to produce white wear-resistant cast iron with a eutectic composition suitable for manufacturing high-performance grinding balls, the slag processing material must contain approximately 1 % copper, 3.5 % silicon, and 3.5 % carbon.

## REFERENCES / СПИСОК ЛИТЕРАТУРЫ

1. Roshchin V.E., Adilov G.A., Povolotckii A.D., Kapelyushin Y. Complex processing of copper smelting slags with obtaining of cast iron grinding media and proppants. In: *KnE Social Sciences. IV Congress "Fundamental Research and Applied Developing of Recycling and Utilization Processes of Technogenic Formations"*. 2020:462–471. <https://doi.org/10.18502/kms.v6i1.8126>
2. Steblov A.B., Berezov S.N., Kozlov A.A. Cast iron balls for materials grinding. *Lit'e i metallurgiya*. 2012;(3S(66)): 45–49. (In Russ.).  
Стеблов А.Б., Березов С.Н., Козлов А.А. Литые чугуновые шары для помола материалов. *Литье и металлургия*. 2012;(3S(66)):45–49.
3. Chizh E.V., Abenova M.B. Selection and analysis of grinding media manufacturing technology. *Teoriya i tekhnologiya metallurgicheskogo proizvodstva*. 2016;(2(19)):42–44. (In Russ.).  
Чиж Е.В., Абенова М.Б. Выбор и анализ технологии изготовления мелющих тел. *Теория и технология металлургического производства*. 2016;(2(19)):42–44.

<sup>1</sup> The CALPHAD methodology, Introduction to ThermoCalc. URL: <http://www.thermocalc.com> (Accessed 03.04.2023).

<sup>2</sup> Computational Thermodynamics. Calculation of Phase Diagrams using the CALPHAD Method. URL: [http://www.calphad.com/calphad\\_method.html](http://www.calphad.com/calphad_method.html) (Accessed 03.04.2023).

## Information about the Authors

## Сведения об авторах

**Galymzhan Adilov**, Research Associate of the Research Laboratory "Hydrogen Technologies in Metallurgy", South Ural State University  
**ORCID:** 0000-0002-1012-8097  
**E-mail:** adilovg@susu.ru

**Nadezhda T. Kareva**, Cand. Sci. (Eng.), Assist. Prof. of the Chair of Materials Science and Physical Chemistry of Materials, South Ural State University  
**E-mail:** karevant@susu.ru

**Vasilii E. Roshchin**, Dr. Sci. (Eng.), Prof. of the Chair of Pyrometallurgical and Foundry Technologies, South Ural State University  
**ORCID:** 0000-0003-3648-8821  
**E-mail:** roshchinve@susu.ru

**Галымжан Адиллов**, научный сотрудник научно-исследовательской лаборатории «Водородные технологии в металлургии», Южно-Уральский государственный университет  
**ORCID:** 0000-0002-1012-8097  
**E-mail:** adilovg@susu.ru

**Надежда Титовна Карева**, к.т.н., доцент кафедры материаловедения и физико-химии материалов, Южно-Уральский государственный университет  
**E-mail:** karevant@susu.ru

**Василий Ефимович Рошин**, д.т.н., профессор кафедры пирометаллургических и литейных технологий, Южно-Уральский государственный университет  
**ORCID:** 0000-0003-3648-8821  
**E-mail:** roshchinve@susu.ru

## Contribution of the Authors

## Вклад авторов

**G. Adilov** – analytical review on the article topic, modeling, preparation of the text and illustrations.

**N. T. Kareva** – statement and solution of the problem, analysis of modeling results, editing the text and illustrations.

**V. E. Roshchin** – scientific guidance, formation of the research goal and conclusions based on the modeling results.

**Г. Адиллов** – аналитический обзор по теме статьи, проведение моделирования, подготовка текста и иллюстраций статьи.

**Н. Т. Карева** – постановка и решение задачи, анализ результатов моделирования, редактирование текста и иллюстраций.

**В. Е. Рошин** – научное руководство, формирование цели исследования и выводов по результатам моделирования.

Received 03.04.2023

Revised 11.04.2023

Accepted 11.09.2023

Поступила в редакцию 03.04.2023

После доработки 11.04.2023

Принята к публикации 11.09.2023



INNOVATION IN METALLURGICAL  
INDUSTRIAL AND LABORATORY EQUIPMENT,  
TECHNOLOGIES AND MATERIALSИННОВАЦИИ В МЕТАЛЛУРГИЧЕСКОМ  
ПРОМЫШЛЕННОМ И ЛАБОРАТОРНОМ  
ОБОРУДОВАНИИ, ТЕХНОЛОГИЯХ И МАТЕРИАЛАХ

UDC 004.942

DOI 10.17073/0368-0797-2024-1-76-82



Original article

Оригинальная статья

EXPERIENCE IN IMPLEMENTING MACHINE LEARNING  
TO CALCULATE THE QUALITY AND PRODUCTION OF AGGLOMERATE

A. S. Leont'ev, I. A. Rybenko

Siberian State Industrial University (42 Kirova Str., Novokuznetsk, Kemerovo Region – Kuzbass 654007, Russian Federation)

rybenkoi@mail.ru

**Abstract.** In 2020, EVRAZ United West Siberian Metallurgical Combine JSC (EVRAZ ZSMK JSC) completed work on the creation of a mathematical modeling system for all processing units of the metallurgical plant. During testing of the system, a high error was found in the existing factor model for predicting agglomerate production, which was developed taking into account the specific sintering rate of individual concentrates. The paper proposes the use of linear regression to predict the productivity of sintering machines, which, unlike nonlinear methods, is optimal for integration into high-performance optimization systems. A feature of the work is forecasting, taking into account the proportion of the agglomeration charge. The model was tested at EVRAZ ZSMK JSC and showed sufficient accuracy ( $R^2 > 90$ ). A large economic effect is expected from the model. A separate study of existing agglomerate quality forecasting systems was conducted. Machine learning (ML) methods have recently made a great contribution to the development of forecasting models used to assess the quality of the agglomerate. This is due to the fact that the sintering process is a very complex dynamic with non-linearity and a large delay. The physico-chemical phenomena involved in this process are complex and numerous. The neural network can constantly adjust the parameters of the model to reflect changes in systemic causes. A linear method was also studied to predict the agglomerate quality. Due to the poor quality of the resulting linear model, the “random forest” machine learning method was applied. Currently, the model is being operated as part of the integrated optimization program SMM Prognoz for the entire plant. For the convenience of the user, when implementing the module, visualization of the model quality using historical data was added, as well as the statistical metrics obtained.

**Keywords:** agglomerate production, mathematical model, planning, machine learning, forecasting

**For citation:** Leont'ev A.S., Rybenko I.A. Experience in implementing machine learning to calculate the quality and production of agglomerate. *Izvestiya. Ferrous Metallurgy*. 2024;67(1):76–82. <https://doi.org/10.17073/0368-0797-2024-1-76-82>

ОПЫТ ВНЕДРЕНИЯ МАШИННОГО ОБУЧЕНИЯ  
ДЛЯ РАСЧЕТА КАЧЕСТВА И ПРОИЗВОДСТВА АГЛОМЕРАТА

А. С. Леонтьев, И. А. Рыбенко

Сибирский государственный индустриальный университет (Россия, 654007, Кемеровская обл. – Кузбасс, Новокузнецк, ул. Кирова, 42)

rybenkoi@mail.ru

**Аннотация.** В 2020 г. на АО «ЕВРАЗ Объединенный Западно-Сибирский металлургический комбинат» (АО «ЕВРАЗ ЗСМК») была завершена работа по созданию системы математического моделирования для всех переделов металлургического комбината. В процессе тестирования системы была обнаружена высокая погрешность существующей факторной модели прогнозирования производства агломерата, которая разрабатывалась с учетом удельной скорости спекания отдельных концентратов. В работе предлагается использование линейной регрессии для прогнозирования производительности агломашин, которая в отличие от нелинейных методов оптимальна для встраивания в высокопроизводительные системы оптимизации. Особенностью работы является прогнозирование с учетом долей шихты агломерации. Модель была опробована на АО «ЕВРАЗ ЗСМК» и показала достаточную точность ( $R^2 > 90$ ). От модели ожидается большой экономический эффект. Отдельно проведено исследование существующих систем прогнозирования качества агломерата. Методы машинного обучения (ML) в последнее время внесли большой вклад в развитие моделей прогнозирования, используемых для оценки качества агломерата. Это связано с тем, что процесс спекания – очень сложная динамика с нелинейностью и большим запаздыванием. Физико-химические явления, вовлеченные в этот процесс, сложны и многочисленны. Нейронная сеть может постоянно корректировать параметры модели, чтобы отразить изменение системных причин. Для прогнозирования качества агломерата используется линейный метод. Из-за низкого качества полученной линейной модели применяется метод машинного обучения «случайный лес». В настоящее время модель эксплуатируется в составе программы комплексной оптимизации всего комбината СММ «Прогноз». Для удобства пользователя при

внедрении модуля была добавлена визуализация качества модели с использованием исторических данных, а также полученные статистические метрики.

**Ключевые слова:** производство агломерата, математическая модель, планирование, машинное обучение, прогнозирование

**Для цитирования:** Леонтьев А.С., Рыбенко И.А. Опыт внедрения машинного обучения для расчета качества и производства агломерата. *Известия вузов. Черная металлургия.* 2024;67(1):76–82. <https://doi.org/10.17073/0368-0797-2024-1-76-82>

## INTRODUCTION

Presently, the primary manufacturers of steel are integrated full-cycle enterprises that function utilizing the sintering and blast furnace methodology [1]. The reduction process of iron, which facilitates the production of cast iron, is executed within blast furnaces. This is followed by the oxidation of impurities, which occurs in converters and electric furnaces, with further refinement conducted outside of the furnace [2].

It is established that for the production of cast iron in blast furnaces, agglomerates, pellets, and briquettes are utilized. Concurrently, the necessity to process fine ore and concentrate into larger aggregates is underscored, as their application in blast furnace smelting is pivotal for ensuring high gas permeability of the layer – a critical condition for the efficient operation of the blast furnace [3]. Among the trio of sintering methods – briquetting, agglomeration, and pelletizing – agglomeration emerges as the prevalent choice, presenting several notable benefits over the alternatives. Notably, agglomeration facilitates the integration of by-products and in-house waste (such as sludge, blast furnace dust, etc.) into the production cycle [4]. This incorporation aids in moisture retention and contributes to the diminution of harmful emissions into the atmosphere, thereby enhancing environmental sustainability.

Market analysis over the past five years has highlighted the significance of augmenting agglomerate production, primarily due to the cost-effectiveness of producing agglomerate from purchased concentrate in comparison to the acquisition costs of pellets. Generating an additional ton of agglomerate yields financial benefits for the enterprise through the substitution of the more expensive pellets, which are subject to limitations regarding their maximum proportion within the agglomeration charge. This limitation is attributed to the “swelling” phenomenon observed in pellets during the reduction process [5]. For instance, at EVRAZ United West Siberian Metallurgical Combine JSC (EVRAZ ZSMK JSC), the pellet proportion should not surpass 30 %. Therefore, to optimize cast iron production, merely procuring pellets is insufficient; there is a clear necessity to escalate the production of agglomerate.

The enhancement of agglomerate production is facilitated through several strategies [6]:

- expansion of agglomerate production capacity (extensive way);
- amplification of the sintering process efficiency (intensive way);

– improvement of the yield quality, achieved through enhancements in agglomerate quality, including the reduction of fines production;

– employment of sub-standard agglomerate in blast furnace smelting (compromise).

The optimization of the charge composition during sintering crucial for enhancing the quality of agglomerate and the efficiency of sintering machines, potentially increasing the enterprise’s profit margins at no extra cost [7 – 11].

This article presents the outcomes of mathematical modeling and optimization of the aglocharge forming process under the specific conditions at EVRAZ ZSMK JSC.

## DATA COLLECTION

For the purposes of this research, two distinct datasets were obtained from the operations of the sinter plant at EVRAZ ZSMK JSC. The initial dataset spans from 2018 to 2021, providing a detailed, shift-by-shift analysis of all relevant technical parameters for each of the three sintering machines. This includes data on operating time, pressure differential, temperature in the hearth, total material consumption measured by the main scales, layer height, as well as the volume and quality of the agglomerate produced, return volumes, among other technical metrics. The process of data collection for this dataset is fully automated and the information is stored within MSSQL databases.

The second dataset required the assembly of data concerning the consumption volumes of concentrates, fluxes, and fuels for each sintering machine, broken down on a daily basis. Initially, this data was manually collected and recorded in Excel files. However, during the preparation of this article, the data collection process was automated, with information systematically transferred to a database by recording the item numbers of materials and their respective consumption volumes.

The culmination of this effort resulted in a comprehensive dataset comprising raw, unprocessed data.

## DATA PROCESSING

The data was subjected to a day-by-day analysis under specific criteria:

- the volume of consumed fuel must not equal zero;
- the volume of produced agglomerate must not equal zero;
- the volume of returns must not exceed the volume of agglomerate produced.

Observations failing to meet any of these criteria were excluded. Except for consumed coke volume and agglomerate production, all indicators were set to zero in cases of missing data, treating such absences as zeroes.

Furthermore, to analyze model behavior with aggregated data, monthly dynamics indicators were derived from the dataset.

Given that the charge is not individually supplied to each sintering machine and is considered uniformly distributed, a proportional allocation of charge consumption and agglomerate production volumes was employed for individual machine analysis, based on data from the main scales at EVRAZ ZSMK JSC.

#### **RATIONALE FOR DEVELOPING A MATHEMATICAL MODEL OF THE AGGLOMERATE PRODUCTION PROCESS**

The enhancement of agglomerate production can be achieved through the construction of new facilities or the implementation of technical advancements, such as [4]:

- the application of lime and lime milk (hydrate  $\text{Ca}(\text{OH})_2$ , produced by  $\text{CaO}$  reacting with water) which exhibit strong binding qualities, significantly boosting the granulation speed of the charge and the robustness of the resulting granules. This enhancement in turn

#### **Factors of agglomerate production intensification**

#### **Факторы интенсификации производства агломерата**

Factor	Variation limits	Variation value	
		$\Delta a$	$\Delta \Pi$
Lime in charge, %	0 – 1.5	1.0	+3.5
	1.5 – 2.0	1.0	+2.0
	2.0 – 3.0	1.0	+1.0
Oxygen for ignition, $\text{mm}^3/\text{tonn}$	4 – 10	1	+0.2
Charge heating up, $^{\circ}\text{C}$	0 – 55	55	+15.0
Increase of the returns content in charge, %	30 – 45	1.0	–1.0
Increase of +5 mm fraction content in the returns, %	0 – 10	1.0	–0.4
Increase of the proportion of fine-grained concentrates, %	50	1.0	–0.3
Increase of depression in gas manifold, $\text{mmHg}$	750	100	+3.0
Increase of the height of the charge layer, mm	250 – 300	10	–0.6
Increase of $\text{FeO}$ content in agglomerate, %	14 – 18	1.0	–0.5
Increase of agglomerate basicity, unit fraction	0.90 – 1.20	0.05	–1.0
Increase of iron content in agglomerate, %	55 – 58	1.0	–1.5

improves the gas permeability of the sintered charge layer, leading to increased efficiency of the sintering machines;

- preheating the charge, typically with hot return and steam, is crucial especially when sintering finely ground concentrates to prepare the charge for sintering by preheating, thus preventing granule disintegration due to over-moistening;

- elevating the depression in the gas manifold, which augments the rate of fuel combustion and the vertical speed of sintering;

- diminishing the basicity of the agglomerate through a reduction in the consumption of fluxes such as lime, dolomite, and limestone.

The sintering process at EVRAZ ZSMK JSC is influenced by a variety of factors, some of which may conflict with one another. For instance, an increase in lime content can enhance production by 1.0 – 3.5 %, yet concurrently, it elevates the basicity of the agglomerate, adversely impacting productivity.

Furthermore, the specific productivity of sintering machines is affected differently by various concentrates. To refine the accuracy of the charge planning process, experimental sintering involving diverse concentrates was conducted, with the specific productivity assessed. The anonymized results, in compliance with commercial confidentiality requirements, are illustrated in Fig. 1. It was observed that productivity rates for sintering machines fluctuate markedly across different concentrates. From the test outcomes, a model for estimating charge productivity was formulated, delivering satisfactory performance. However, due to the substantial expense associated with the process (the cost of pilot sintering can approach 1 million rubles), these experiments have not been replicated nor the coefficients reevaluated for over a decade. A universal correction factor was incorporated into the model to facilitate its validation.

The variability in component composition of concentrates, as well as in the composition of fuel, fluxes, and the basicity and chemical composition of the produced agglomerate, during operations at sintering plants indicates that the specific productivity of concentrates alone is not adequate for accurately calculating the productivity of sintering machines. Simply revising the coefficients does not suffice to achieve the necessary precision in the model.

Consequently, the comprehensive assessment of the impact of all these factors on the productivity of sinter machines and the quality of agglomerate can only be accurately conducted through the application of machine learning techniques, utilizing archival data.

The review of literature [12 – 17] confirms the extensive application of machine learning not only in evaluating the quality of agglomerate but also in forecasting its production.

In 2021, EVRAZ ZSMK JSC initiated a project aimed at developing a mathematical model to evaluate the productivity of its sintering machines.



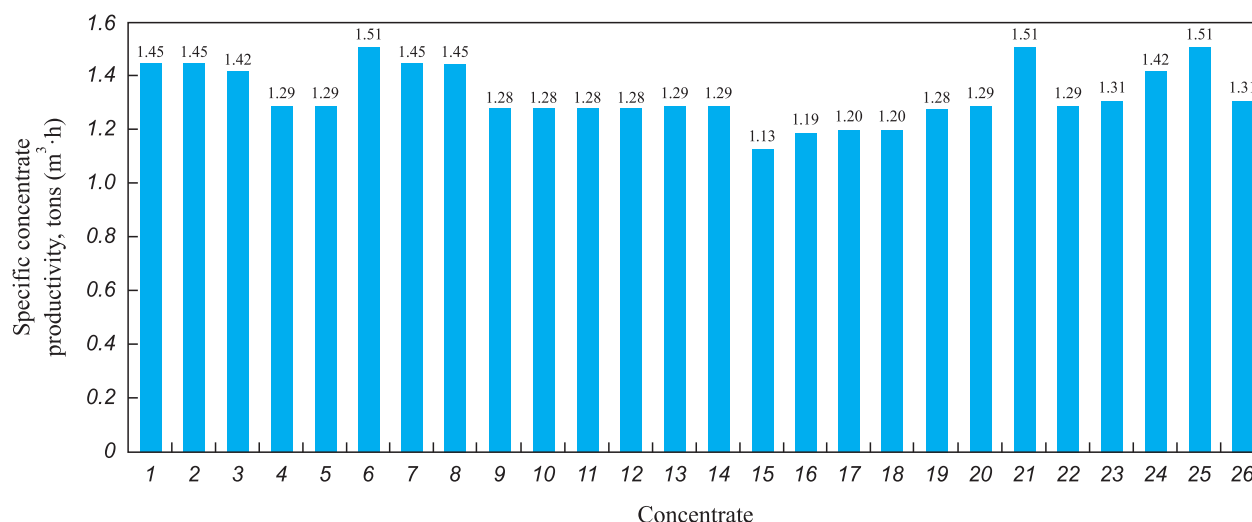


Fig. 1. Specific productivity of various concentrates at EVRAZ ZSMK JSC

Рис. 1. Удельная производительность различных концентратов на АО «ЕВРАЗ ЗСМК»

## DEFINING OBJECTIVES FOR APPLYING MACHINE LEARNING

The regression mathematical model for calculating the productivity of the sinter plant is as follows:

$$y = b_0 + b_1x_1 + b_2x_2 + \dots + b_nx_n, \quad (1)$$

where  $y$  the predicted volume of bin agglomerate, tonn;  $b_0$  is the intercept;  $b_1, b_2, b_n$  are the regression coefficients corresponding to the factors; and  $x_1, x_2, x_n$  are the factors influencing the volume of bin agglomerate.

The objective of this project is to refine a mathematical model through the training on historical data concerning concentrate consumption and sinter machine productivity, aiming to:

- enhance the precision of mathematical modeling;
- increase confidence in the system by allowing users to verify results against archived data;
- identify new charging modes for the charge to optimize agglomerate production.

The system prototype operates in a “Train the model” mode, performing the following functions:

- loading the specified period of sintering data;
- training a performance model utilizing the archived data;
- training a quality model based on the data;
- presenting a table/graph of actual versus predicted data;
- displaying model quality indicators, such as ( $R^2$ ).

Upon completion, the program notifies the user that the task is finished, detailing the outcomes of the most recent model training.

Users should also have the capability to toggle between different graphs to evaluate the model’s accuracy on various metrics (actual/forecast), including

agglomerate quality, sieve quantity, bin agglomerate, and skip agglomerate.

The input data for the model encompassed the following indicators:

- consumed concentrates clarification;
- volume of consumed concentrates, tonn;
- consumption of fluxes (limestone, dolomite, lime, brucite), tonn;
- fuel consumption;
- agglomerate strength;
- chemical composition of agglomerate (content of Fe, CaO, SiO<sub>2</sub>, basicity);
- sintering machine process parameters (layer height, depression in the header);
- volume of agglomerate production.

## FORECASTING AGGLOMERATE QUALITY

The *Random forest* method was employed for predicting agglomerate quality, given its superior forecasting accuracy compared to regression analysis. The *Random Forest* algorithm, developed by Leo Breiman and Adele Cutler, is a machine learning approach that employs an ensemble of decision trees. It integrates the Breiman Bagging method with the random subspace method introduced by Tin Kam Ho, making it versatile for classification, regression, and clustering tasks. The strength of this algorithm lies in its utilization of a large number of decision trees, each individually contributing to low classification accuracy. However, when aggregated, these trees produce significantly improved results [18]. Fig. 2 illustrates the correlation between actual agglomerate quality and the outcomes estimated by the model. With a coefficient of determination at 60 %, the model’s adequacy is affirmed, as the benchmark for the coefficient of determination is set at a minimum of 50 % [19].

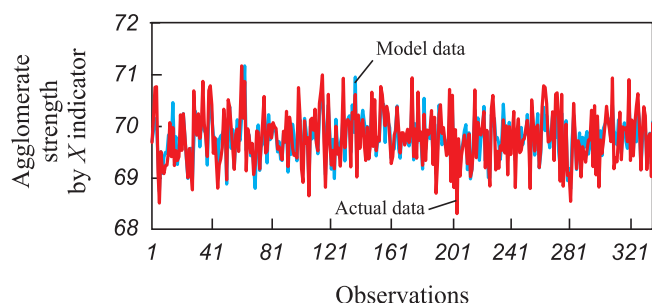


Fig. 2. Comparative analysis of model and actual data

Рис. 2. Сравнительный анализ модельных и фактических данных

This approach forms part of a comprehensive model that encapsulates both technical and economic aspects, delineating the interplay between chemical, thermodynamic, mechanical processes, and productivity, alongside considerations for product availability and logistics costs.

A notable characteristic of the Prognoz system is its capability to seamlessly incorporate third-party software modules into its computations. A screenshot presented in Fig. 3 displays the user interface of the Prognoz system in operation.

To enhance user experience, functionalities for visualizing the quality of the model were introduced alongside the

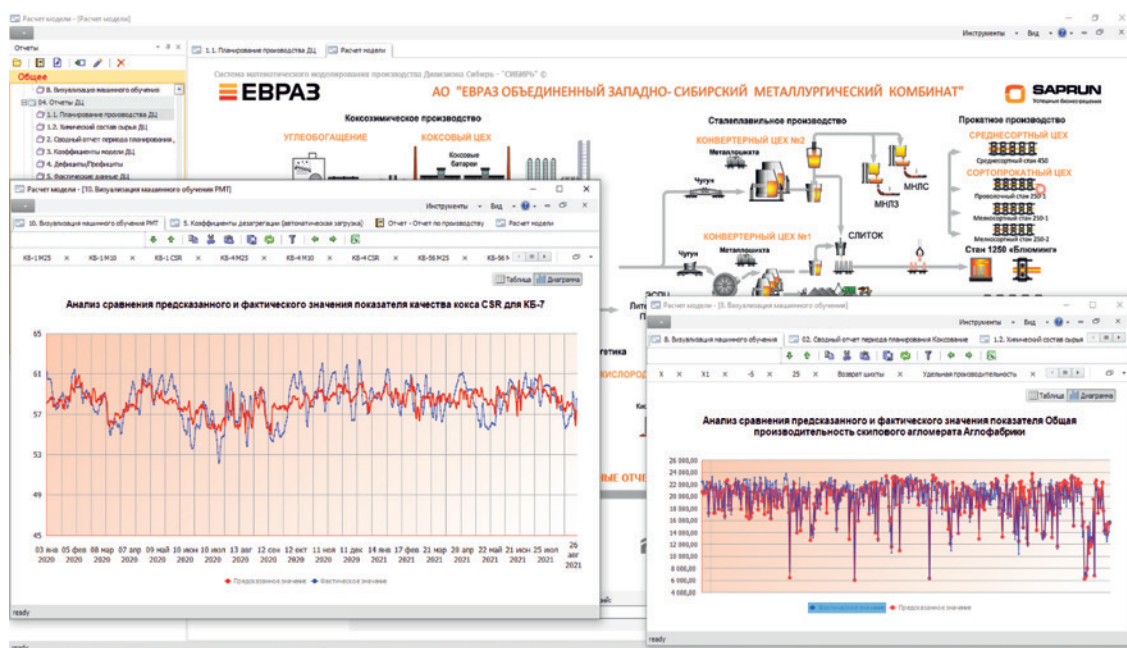


Fig. 3. Working window of the SMM system Prognoz

Рис. 3. Рабочее окно системы СММ «Прогноз»

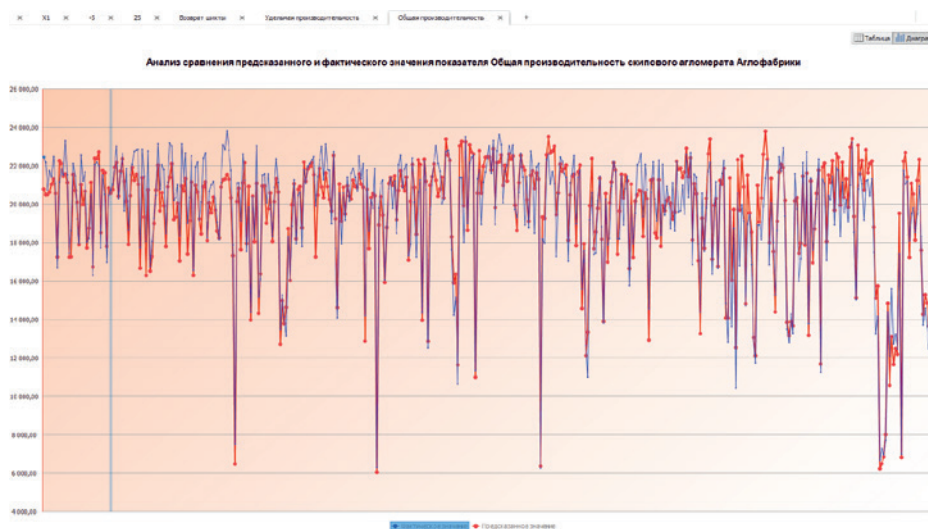


Fig. 4. Visualization of the learning quality of the model

Рис. 4. Визуализация качества обучения модели

Метрики KLD		Метрики AB		Метрики обучения Алгоритма					
Модель	R2	Ошибки	Процент_ошибки	Пользователь	Начало_периода	Конец_периода	Дата_расчета	Период	
ef_total_capacity	0.90777	870.98469	0.045	teontlev_as	01.01.2020 0:00:00	31.05.2021 0:00:00	30.09.2021 8:49:00	Алгоритм	
X	0.70046	0.21368	0.0031	teontlev_as	01.01.2020 0:00:00	31.06.2021 0:00:00	30.09.2021 8:49:00	Алгоритм	
X1	0.81444	0.05039	0.0125	teontlev_as	01.01.2020 0:00:00	31.06.2021 0:00:00	30.09.2021 8:49:00	Алгоритм	
Δ	0.60446	0.24918	0.0168	teontlev_as	01.01.2020 0:00:00	31.06.2021 0:00:00	30.09.2021 8:49:00	Алгоритм	
+25	0.87068	0.75338	0.0497	teontlev_as	01.01.2020 0:00:00	31.06.2021 0:00:00	30.09.2021 8:49:00	Алгоритм	
ef_return_rm	0.63601	860.26026	0.0785	teontlev_as	01.01.2020 0:00:00	31.12.2020 0:00:00	30.09.2021 8:46:17	Алгоритм	
ef_unit_capacity	0.0792	0.03967	0.0372	teontlev_as	01.01.2020 0:00:00	31.12.2020 0:00:00	30.09.2021 8:46:17	Алгоритм	
ef_total_capacity	0.88771	781.41505	0.038	teontlev_as	01.01.2020 0:00:00	31.12.2020 0:00:00	30.09.2021 8:46:17	Алгоритм	
X	0.68194	0.21904	0.0031	teontlev_as	01.01.2020 0:00:00	31.12.2020 0:00:00	30.09.2021 8:46:17	Алгоритм	
X1	0.89328	0.06786	0.0136	teontlev_as	01.01.2020 0:00:00	31.12.2020 0:00:00	30.09.2021 8:46:17	Алгоритм	
Δ	0.72332	0.21867	0.0148	teontlev_as	01.01.2020 0:00:00	31.12.2020 0:00:00	30.09.2021 8:46:17	Алгоритм	
+25	0.58075	0.70216	0.0449	teontlev_as	01.01.2020 0:00:00	31.12.2020 0:00:00	30.09.2021 8:46:17	Алгоритм	
ef_return_rm	0.70358	930.30077	0.0824	teontlev_as	01.01.2020 0:00:00	30.04.2021 0:00:00	30.09.2021 8:30:49	Алгоритм	
ef_unit_capacity	0.1645	0.0437	0.0417	teontlev_as	01.01.2020 0:00:00	30.04.2021 0:00:00	30.09.2021 8:30:49	Алгоритм	
ef_total_capacity	0.90788	843.86287	0.0432	teontlev_as	01.01.2020 0:00:00	30.04.2021 0:00:00	30.09.2021 8:30:49	Алгоритм	
X	0.72186	0.20758	0.003	teontlev_as	01.01.2020 0:00:00	30.04.2021 0:00:00	30.09.2021 8:30:49	Алгоритм	
X1	0.82863	0.06388	0.0126	teontlev_as	01.01.2020 0:00:00	30.04.2021 0:00:00	30.09.2021 8:30:49	Алгоритм	
Δ	0.81837	0.26471	0.0168	teontlev_as	01.01.2020 0:00:00	30.04.2021 0:00:00	30.09.2021 8:30:49	Алгоритм	
+25	0.68181	0.7131	0.047	teontlev_as	01.01.2020 0:00:00	30.04.2021 0:00:00	30.09.2021 8:30:49	Алгоритм	
ef_return_rm	0.63601	860.26026	0.0785	teontlev_as	01.01.2020 0:00:00	31.12.2020 0:00:00	30.09.2021 8:23:03	Алгоритм	
ef_unit_capacity	0.0792	0.03967	0.0372	teontlev_as	01.01.2020 0:00:00	31.12.2020 0:00:00	30.09.2021 8:23:03	Алгоритм	
ef_total_capacity	0.88771	781.41505	0.038	teontlev_as	01.01.2020 0:00:00	31.12.2020 0:00:00	30.09.2021 8:23:03	Алгоритм	
X	0.68361	0.22463	0.0032	teontlev_as	01.01.2020 0:00:00	31.12.2020 0:00:00	30.09.2021 8:23:03	Алгоритм	
X1	0.89949	0.06714	0.0134	teontlev_as	01.01.2020 0:00:00	31.12.2020 0:00:00	30.09.2021 8:23:03	Алгоритм	
Δ	0.71854	0.21765	0.0148	teontlev_as	01.01.2020 0:00:00	31.12.2020 0:00:00	30.09.2021 8:23:03	Алгоритм	
+25	0.58197	0.70214	0.0449	teontlev_as	01.01.2020 0:00:00	31.12.2020 0:00:00	30.09.2021 8:23:03	Алгоритм	
ef_return_rm	0.70358	930.30077	0.0824	teontlev_as	01.01.2020 0:00:00	30.04.2021 0:00:00	23.09.2021 11:07:11	Алгоритм	
ef_unit_capacity	0.1645	0.0437	0.0417	teontlev_as	01.01.2020 0:00:00	30.04.2021 0:00:00	23.09.2021 11:07:11	Алгоритм	
ef_total_capacity	0.90788	843.86287	0.0432	teontlev_as	01.01.2020 0:00:00	30.04.2021 0:00:00	23.09.2021 11:07:11	Алгоритм	
X	0.72339	0.20882	0.003	teontlev_as	01.01.2020 0:00:00	30.04.2021 0:00:00	23.09.2021 11:07:11	Алгоритм	
X1	0.81628	0.06436	0.0127	teontlev_as	01.01.2020 0:00:00	30.04.2021 0:00:00	23.09.2021 11:07:11	Алгоритм	
Δ	0.8029	0.24719	0.0162	teontlev_as	01.01.2020 0:00:00	30.04.2021 0:00:00	23.09.2021 11:07:11	Алгоритм	
+25	0.67763	0.70987	0.0457	teontlev_as	01.01.2020 0:00:00	30.04.2021 0:00:00	23.09.2021 11:07:11	Алгоритм	
ef_return_rm	0.70358	930.30077	0.0824	teontlev_as	01.01.2020 0:00:00	30.04.2021 0:00:00	23.09.2021 11:03:15	Алгоритм	
ef_unit_capacity	0.1645	0.0437	0.0417	teontlev_as	01.01.2020 0:00:00	30.04.2021 0:00:00	23.09.2021 11:03:15	Алгоритм	
ef_total_capacity	0.90788	843.86287	0.0432	teontlev_as	01.01.2020 0:00:00	30.04.2021 0:00:00	23.09.2021 11:03:15	Алгоритм	
X	0.71388	0.21223	0.003	teontlev_as	01.01.2020 0:00:00	30.04.2021 0:00:00	23.09.2021 11:03:15	Алгоритм	
X1	0.80816	0.06517	0.0129	teontlev_as	01.01.2020 0:00:00	30.04.2021 0:00:00	23.09.2021 11:03:15	Алгоритм	
Δ	0.81893	0.26411	0.0168	teontlev_as	01.01.2020 0:00:00	30.04.2021 0:00:00	23.09.2021 11:03:15	Алгоритм	
+25	0.67349	0.71413	0.047	teontlev_as	01.01.2020 0:00:00	30.04.2021 0:00:00	23.09.2021 11:03:15	Алгоритм	

Fig. 5. History of calculations and metrics

Рис. 5. История расчетов и метрик

module implementation (Fig. 4). Post-training, users have the facility to visually assess the training outcomes. Additionally, there's provision to review the history of model training, enabling users to select the optimal period for further training based on specific metrics (Fig. 5).

## CONCLUSIONS

Throughout this project, archival data from the sinter plant of EVRAZ ZSMK JSC was meticulously gathered and analyzed. Utilizing statistical methodologies, the study identified and quantified the relationships between various input factors – such as the consumption rates of charge components, operational technical parameters of the sinter machines, and the chemical composition of the agglomerate – and the resulting productivity and quality of the agglomerate. Both linear and nonlinear correlations were discovered, with the proportions of charge component consumption being highlighted as having a significant impact on forecasting accuracy. These insights were subsequently incorporated into the forecasting module of the SMM mathematical modeling system, Prognoz, developed for EVRAZ ZSMK JSC.

## REFERENCES / СПИСОК ЛИТЕРАТУРЫ

- Lisienko V.G., Solov'eva N.V., Trofimova O.G. Alternative Metallurgy: Problem of Alloying, Model Efficiency Estimates. Moscow: Teplotekhnika; 2007:440. (In Russ.).  
Лисиенко В.Г., Соловьева Н.В., Трофимова О.Г. Альтернативная металлургия: проблема легирования, модельные оценки эффективности. Москва: изд. Теплотехник; 2007:440.

- Protopopov E.V., Kalinogorskii A.N., Ganzer A.A. Steel-making production: Current state and directions of development. In: *Metallurgy: Technologies, Innovations, Quality. Proceedings of the XX Int. Sci. and Pract. Conf. Part 1*. Novokuznetsk: SibSIU; 2019:9–14. (In Russ.).

Протопопов Е.В., Калиногорский А.Н., Ганзер А.А. Сталеплавильное производство: современное состояние и направления развития. В кн.: *Металлургия: технологии, инновации, качество. Труды XX междунар. науч.-практ. конф. Ч. 1*. Новокузнецк: ИЦ СибГИУ; 2019:9–14.

- Spirin N.A., Ovchinnikov Yu.N., Shvydkii V.S., Yaroshenko Yu.G. Heat Exchange and Efficiency Improvement of Blast Furnace Smelting. Yekaterinburg: USTU; 1995:243. (In Russ.).

Спирин Н.А., Овчинников Ю.Н., Швыдкий В.С., Ярошенко Ю.Г. Теплообмен и повышение эффективности доменной плавки. Екатеринбург: УГТУ; 1995:243.

- Frolov Yu.A. Agglomeration. Technology, Heat Engineering. Moscow: Metallurgiya; 2006:600. (In Russ.).

Фролов Ю.А. Агломерация. Технология, теплотехника. Москва: Металлургия; 2006:600.

- Geerdes M. Modern Domain Process. Moscow: Metallurgizdat; 2016:273. (In Russ.).

Геердес М. Современный доменный процесс. Москва: Металлургиздат; 2016:273.

- Bizhanov A., Chizhikova V. Agglomeration in Metallurgy. Springer; 2020:453.

<http://doi.org/10.1007/978-3-030-26025-5>

- Rybenko I.A. Solving a task of metallurgical processes optimization by using instrumental system "Engineering-Metallurgy". *Ferrous Metallurgy. Bulletin of Scientific, Technical and Economic Information*. 2018;1(3):42–47. (In Russ.).

Рыбенко И.А. Решение задач оптимизации металлургических процессов с использованием инструментальной



- системы «Инжиниринг-Металлургия». *Черная металлургия. Бюллетень научно-технической и экономической информации*. 2018;1(3):42–47.
8. Rybenko I.A. Development of optimal technological modes of metal production processes using mathematic modeling methods and instrumental system. *Ferrous Metallurgy. Bulletin of Scientific, Technical and Economic Information*. 2018;1(2):57–61. (In Russ.).  
Рыбенко И.А. Разработка оптимальных технологических режимов получения металлов с использованием методов математического моделирования и инструментальных систем. *Черная металлургия. Бюллетень научно-технической и экономической информации*. 2018;1(2):57–61.
  9. Mitterlehner J., Loeffler G., Winter F., Hofbauer H., Schmid H., Zwittag E., Buerger T.H., Pammer O., Stiasny H. Modeling and simulation of heat front propagation in the iron ore sintering process. *ISIJ International*. 2004;44(1):11–20. <http://doi.org/10.2355/isijinternational.44.11>
  10. Yang W., Rui C., Choi S., Choi E., Lee D., Huh W. Modeling of combustion and heat transfer in an iron ore sintering bed with considerations of multiple solid phases. *ISIJ International*. 2004;44(3):492–499. <http://doi.org/10.2355/isijinternational.44.492>
  11. Fernandez-Gonzalez D., Martin-Duarte R., Ruiz-Bustanza I., González-Gasca C., Verdeja L.F. Optimization of sinter plant operating conditions using advanced multivariate statistics: Intelligent data processing. *JOM*. 2016;68:2089–2095. <http://doi.org/10.1007/s11837-016-2002-2>
  12. Silva T.P., da Silva A.M., Resende B.A., da Silva B.V. Prediction of sinter plant productivity by neural network. In: *6<sup>th</sup> Int. Congress on the Science and Technology of Ironmaking*. 2012;6(6):764–776.
  13. Mohanan S., Mohapatra P., Kumar C.A., Adepu R.K., Koranne V.M., Prasad Y.G.S., Reddy A.S., Ramna R.V. Prediction and optimization of internal return fines generation in iron ore sintering using machine learning. *Advances in Materials*. 2021;10(3):42–46. <http://doi.org/10.11648/j.am.20211003.12>
  14. Mochón J., Ruiz-Bustanza I., Cores A., Verdeja L., Robla J.I., García-Carcedo F. Iron ore sintering. Part 2. Quality indices and productivity. In: *DYNA*. 2014;81(183):168–177. <http://doi.org/10.15446/dyna.v81n183.41568>
  15. Shao H., Yi Z., Chen Z., Zhou Z., Deng Z. Application of artificial neural networks for prediction of sinter quality based on process parameters control. *Transactions of the Institute of Measurement and Control*. 2019;42(3):422–429. <https://doi.org/10.1177/0142331219883501>
  16. Mallick A., Dhara S., Rath S. Application of machine learning algorithms for prediction of sinter machine productivity. *Machine Learning with Applications*. 2021;6:100186. <https://doi.org/10.1016/j.mlwa.2021.100186>
  17. Song L., Qing L., Xiaojie L., Yanqin S. Synthetically predicting the quality index of sinter using machine learning model. *Ironmaking & Steelmaking Processes, Products and Applications*. 2020;47(7):828–836. <http://doi.org/10.1080/03019233.2019.1617573>
  18. Random Forrest. WIKIPEDIA. Available at URL: [https://ru.wikipedia.org/wiki/Random\\_forest](https://ru.wikipedia.org/wiki/Random_forest) (Accessed 05.01.2024).  
Случайный лес. Сайт интернет энциклопедии WIKIPEDIA. URL: [https://ru.wikipedia.org/wiki/Random\\_forest](https://ru.wikipedia.org/wiki/Random_forest) (дата обращения 05.01.2024).
  19. Coefficient of Determination. WIKIPEDIA. Available at URL: [https://ru.wikipedia.org/wiki/Коэффициент\\_детерминации](https://ru.wikipedia.org/wiki/Коэффициент_детерминации) (Accessed 05.01.2024).  
Коэффициент детерминации. Сайт интернет энциклопедии WIKIPEDIA. URL: [https://ru.wikipedia.org/wiki/Коэффициент\\_детерминации](https://ru.wikipedia.org/wiki/Коэффициент_детерминации) (дата обращения 05.01.2024).
  20. Leont'ev A.S., Rybenko I.A., Borisov A.S., Volkova I.V. Experience in development and application of a mathematical modeling system at EVRAZ ZSMK JSC. In: *Modeling and High-Tech Information Technologies in Technical and Socio-Economic Systems. Proceedings of the V All-Russ. Sci. and Pract. Conf. with Int. Participation*. Novokuznetsk: SibSIU;2021:250–255. (In Russ.).  
Леонтьев А.С., Рыбенко И.А., Борисов А.С., Волкова И.В. Опыт разработки и применения системы математического моделирования на «ЕВРАЗ ЗСМК». В кн.: *Моделирование и наукоемкие информационные технологии в технических и социально-экономических системах. Труды V всерос. науч.-практ. конф. с международным участием*. Новокузнецк: ИЦ СибГИУ;2021:250–255.

## Information about the Authors

**Aleksei S. Leont'ev**, Postgraduate of the Chair of Applied Information Technologies and Programming, Siberian State Industrial University  
E-mail: [aleksey.leontiev@evraz.com](mailto:aleksey.leontiev@evraz.com)

**Inna A. Rybenko**, Dr. Sci. (Eng.), Assist. Prof., Head of the Chair of Applied Information Technologies and Programming, Siberian State Industrial University  
ORCID: 0000-0003-1679-0839  
E-mail: [rybenkoi@mail.ru](mailto:rybenkoi@mail.ru)

## Сведения об авторах

**Алексей Сергеевич Леонтьев**, аспирант кафедры прикладных информационных технологий и программирования, Сибирский государственный индустриальный университет  
E-mail: [aleksey.leontiev@evraz.com](mailto:aleksey.leontiev@evraz.com)

**Инна Анатольевна Рыбенко**, д.т.н., доцент, заведующий кафедрой прикладных информационных технологий и программирования, Сибирский государственный индустриальный университет  
ORCID: 0000-0003-1679-0839  
E-mail: [rybenkoi@mail.ru](mailto:rybenkoi@mail.ru)

Received 12.01.2022  
Revised 19.05.2023  
Accepted 11.09.2023

Поступила в редакцию 12.01.2022  
После доработки 19.05.2023  
Принята к публикации 11.09.2023

ON THE MATERIALS OF THE INTERNATIONAL  
CONFERENCE "SCIENTIFIC AND PRACTICAL  
SCHOOL FOR YOUNG METALLURGISTS" – 2023ПО МАТЕРИАЛАМ МЕЖДУНАРОДНОЙ  
КОНФЕРЕНЦИИ «НАУЧНО-ПРАКТИЧЕСКАЯ  
ШКОЛА ДЛЯ МОЛОДЫХ МЕТАЛЛУРГОВ» – 2023

UDC 669.018:620.18:620.193

DOI 10.17073/0368-0797-2024-1-83-88



Original article

Оригинальная статья

## EFFECT OF YTTRIUM ADDITIONS ON MICROSTRUCTURE AND CORROSION RESISTANCE OF INCOLOY 825 ALLOY

M. A. Salynova<sup>1</sup>, T. V. Uglunts<sup>1</sup>, O. V. Tolochko<sup>1,2</sup><sup>1</sup> Peter the Great St. Petersburg Polytechnic University (29 Politekhnikeskaya Str., St. Petersburg 195251, Russian Federation)<sup>2</sup> State Marine Technical University (3 Lotsmanskaya Str., St. Petersburg 190121, Russian Federation)

✉ m.salynova21@gmail.com

**Abstract.** The work is devoted to the study of the effect of microalloying with yttrium (Y) additives to improve the corrosion resistance of Incoloy 825 superalloy. The influence of Y on microstructure was evaluated by metallographic methods using optical and scanning electron microscopes, resistance to pitting and intergranular corrosion was evaluated by electrochemical and chemical methods of analysis. The paper describes changes in the structure, phase composition and hardness of cast samples with yttrium content of 0, 0.01, 0.05 and 0.1 wt. %. The obtained data correlate with the results of thermodynamic calculations of phase formation during crystallization. The influence of additions on the structure after strain hardening was investigated. Small addition (up to 0.01 wt. %) promotes increase of mobility of recrystallized grain boundaries. With increasing Y amount, the grain size decreases and hardness increases. It is shown that the greatest deoxidizing ability is observed at small additions of Y in the amount up to 0.01 wt. %, while the total amount of dissolved [O] decreased five times. Increasing the Y content reduces the ability to remove heavy inclusions from the melt, resulting in an increase in the proportion of oxide inclusions. The effect of additives on nitrogen [N] was not observed, and the volume fraction of nitride inclusions did not change, but the size of nitride inclusions decreased and the character of their distribution changed to uniform than in the alloy without Y. The results of pitting and intergranular fracture resistance tests showed that Y is an element that can be used to improve the corrosion properties of Incoloy 825 alloy. The best combination of resistance to the two types of corrosion was observed for the 0.01 wt. % Y sample.

**Keywords:** Incoloy 825, rare earth metals (REM), non-metallic inclusions (NMI), corrosion resistance, intergranular corrosion (IGC), pitting corrosion, modification, microstructure, hardness

**Acknowledgements:** The research was partially funded by the Ministry of Science and Higher Education of the Russian Federation as part of the program "World-Class Research Center: Advanced Digital Technologies" (contract No. 075-15-2022-311 dated 20 April 2022).

**For citation:** Salynova M.A., Uglunts T.V., Tolochko O.V. Effect of yttrium additions on microstructure and corrosion resistance of Incoloy 825 alloy. *Izvestiya. Ferrous Metallurgy*. 2024;67(1):83–88. <https://doi.org/10.17073/0368-0797-2024-1-83-88>

## ОЦЕНКА ВЛИЯНИЯ ДОБАВОК ИТТРИЯ НА МИКРОСТРУКТУРУ И КОРРОЗИОННУЮ СТОЙКОСТЬ СПЛАВА INCOLOY 825

М. А. Салынова<sup>1</sup>, Т. В. Углунц<sup>1</sup>, О. В. Толочко<sup>1,2</sup><sup>1</sup> Санкт-Петербургский политехнический университет Петра Великого (Россия, 195251, Санкт-Петербург, ул. Политехническая, 29)<sup>2</sup> Санкт-Петербургский государственный морской технический университет (Россия, 190121, Санкт-Петербург, ул. Лощманская, 3)

✉ m.salynova21@gmail.com

**Аннотация.** Работа посвящена исследованию эффекта микролегирования присадками иттрия для повышения коррозионной стойкости высоколегированного сплава на основе никеля марки Incoloy 825. Влияние иттрия на микроструктуру оценивали металлографическими методами с помощью оптического и сканирующего электронного микроскопов, стойкость к питтинговой и межкристаллитной коррозии оценивали по известным методикам при помощи электрохимических и химических методов анализа. В работе показано изменение структуры, фазового состава и твердости литых образцов с содержанием иттрия 0; 0,01; 0,05 и 0,1 мас. %. Полученные данные коррелируют с результатами термодинамических расчетов фазообразования при кристаллизации. Исследовано влияние добавок на структуру после деформационного упрочнения. Малые добавки (до 0,01 мас. %) способствуют повышению подвижности границ рекристаллизованного зерна. С увеличением количества иттрия уменьшается размер зерна и увеличивается твердость. Показано, что наибольшая раскисляющая способность наблю-

дается при малых добавках иттрия (до 0,01 мас. %), при этом общее количество растворенного кислорода уменьшилось в 5 раз. Увеличение содержания иттрия снижает возможность удаления тяжелых включений из расплава, в результате растет доля оксидных включений. Эффекта присадок на азот не наблюдалось, и объемная доля нитридных включений не изменилась, однако уменьшился размер нитридных включений и характер их распределения изменился на равномерный, нежели в сплаве без иттрия. Результаты испытаний на стойкость сплава к питтинговому и межкристаллитному разрушению показали, что иттрий – это элемент, который может быть использован для улучшения коррозионных свойств сплава Incoloy 825. Наилучшее сочетание стойкости к двум типам коррозии наблюдалось у образца с 0,01 мас. % Y.

**Ключевые слова:** Incoloy 825, редкоземельные металлы (РЗМ), неметаллические включения (НВ), коррозионная стойкость, межкристаллитная коррозия (МКК), питтинговая коррозия, модифицирование, микроструктура, твердость

**Благодарности:** Исследование частично финансируется Министерством науки и высшего образования Российской Федерации в рамках программы «Научный центр мирового уровня: Передовые цифровые технологии (контракт № 075-15-2022-311 от 20 апреля 2022 г.).

**Для цитирования:** Салынова М.А., Углунц Т.В., Толочко О.В. Оценка влияния добавок иттрия на микроструктуру и коррозионную стойкость сплава Incoloy 825. *Известия вузов. Черная металлургия*. 2024;67(1):83–88. <https://doi.org/10.17073/0368-0797-2024-1-83-88>

## INTRODUCTION

The influence of catalysts, pressure, and temperature during oil refining induces alterations in the chemical composition of oil. Throughout the refining process, the constituents within crude oil undergo reactions facilitated by catalysts. The resultant compounds can cause detrimental effects on purification equipment, leading to severe corrosion [1].

This corrosion substantially diminishes process efficiency, necessitating careful selection of materials for equipment components. Superalloys, such as the foreign Incoloy 825 alloy, are recommended for manufacturing equipment [1 – 3].

The Incoloy 825 alloy possesses a distinctive set of properties, including resistance to stress corrosion, pitting in active media, and intergranular corrosion [3]. Nevertheless, the ever-increasing demands for alloy properties prompt researchers to explore new methods and avenues for enhancing alloy characteristics [4 – 6].

Several studies highlight the beneficial influence of rare earth metals (REMs) on the microstructural characteristics and mechanical properties of alloys, owing to their heightened sensitivity to oxygen and sulfur [7 – 12]. Cerium and yttrium are the most commonly utilized REMs in nickel superalloys, positively impacting mechanical properties at elevated temperatures through the mechanism of solid solution hardening [12 – 16]. Additionally, they contribute to the modification of carbides and eutectic phases [17; 18].

As per a patent [19], REM additions in conjunction with calcium and/or magnesium result in significant desulfurization of Ni–Cr alloys, facilitating sustained inhibition of hot workability deterioration in the low-temperature range. However, REMs are susceptible to oxidation; hence, they should be added to the pre-deoxidized melt in restricted amounts (0.010 to 0.074 %). As the content increases, a large number of finely dispersed, high-density rare earth metal (REM) oxide nonmetallic inclusions (NMIs) are formed. NMIs are difficult to remove from the melt and contribute to a reduction in material impact strength.

Similar conclusions were drawn by the authors of [13]. They found that the microstructure of a Ni–16Mo–7Cr–4Fe nickel-based alloy was significantly enhanced by the addition of 0.05 wt. % Y. The alloy's hardness and strength increased as solid solution hardening occurred with yttrium. However, when the yttrium content in the alloy exceeded 0.43 wt. %, the refractory intermetallic phase  $\text{Ni}_{17}\text{Y}_2$  could emerge and grow, leading to a sharp deterioration in mechanical properties.

The addition of yttrium at 0.05 wt. % to the IN–13C alloy positively impacted its high-temperature tensile properties [15]. Furthermore, in the as-cast condition, the ingot's crystallization texture was refined.

Research interest is currently focused on the REM impact on the corrosion properties of steels and alloys. However, there is no unanimous opinion regarding the influence of specific rare-earth elements on certain alloy properties. Most studies are dedicated to investigating the effect of the rare-earth element yttrium on the resistance of the Incoloy 825 alloy to pitting and intergranular corrosion.

## MATERIALS AND METHODS

To investigate the impact of yttrium microalloying on the corrosion and mechanical properties of Incoloy 825 alloy, a series of batches with varying additive content was melted. The experimental alloys were melted using a 15 kW open induction furnace in quartz crucibles. The chemical compositions of the alloy samples under investigation are provided in the Table.

Following melting, the ingots underwent homogenization and were subsequently forged on a press within a temperature range of 970 to 1150 °C. The forged samples were then annealed at a temperature of  $960 \pm 10$  °C for 1 h, followed by quenching in water. This procedure aligns with the standard technology used for producing parts from Incoloy 825 alloy.

The microstructures of the stabilized alloys were analyzed using scanning electron microscopy (SEM) in backscatter mode, utilizing a Tescan Mira SEM instru-



## Calculated chemical composition of the samples and actual content of nitrogen and oxygen in them, wt. %

## Расчетный химический состав образцов и фактическое содержание азота и кислорода в них, мас. %

Samples number	Ni	Cr	Fe	Mo	Cu	Ti	Mn	Si	Al	Y	[N]	[O]
1	40.0	21.0	res.	3.0	2.0	0.75	1.0	0.5	0.2	—	0.057	0.030
2										0.01	0.054	0.006
3										0.05	—	—
4										0.10	0.053	0.013

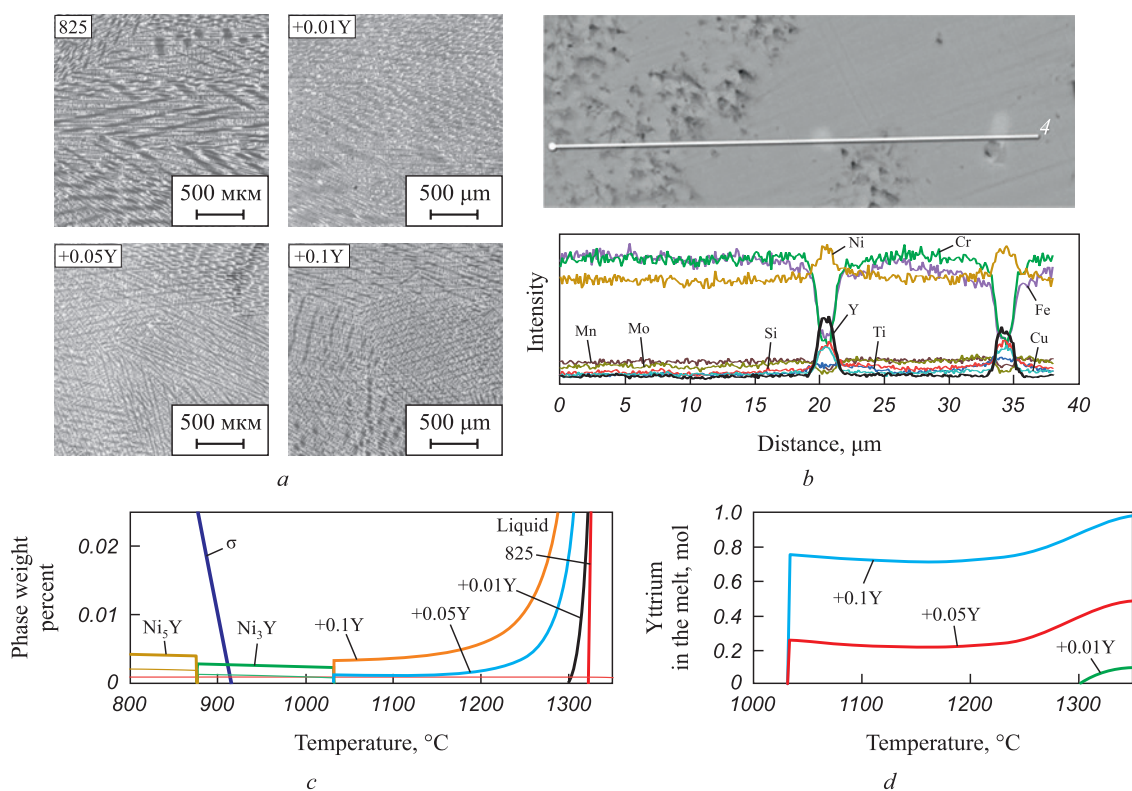
ment. Additionally, the phase composition was examined using a DRON-7 diffractometer.

To evaluate the resistance of the compositions to general and pitting corrosion, polarization curves were generated. These curves were instrumental in determining the steady-state corrosion potential ( $E_{\text{cor}}$ ) and pitting breakdown potential ( $E_{\text{pit}}$ ) [20]. Imaging was conducted in a 5 % NaCl electrolyte acidified with acetic acid to achieve a pH of  $3.00 \pm 0.02$  within an open, aerated electrochemical cell at room temperature. The polarization curve was obtained within potential ranges from  $-450$  to  $1100$  mV at a scan velocity of  $0.16$  mV/s. The standard silver-chloride electrode (AgCl) served as the reference electrode during testing.

The alloys underwent intergranular corrosion (IGC) testing following ASTM G28 [21] guidelines. Testing involved immersing the samples in a boiling solution comprising 50 %  $\text{H}_2\text{SO}_4$  and iron (III) sulfate for a duration of 120 h. Prior to testing, the samples were sensitized at  $700$  °C for 1 h. IGC values were determined through mass loss analysis and metallographic methods, with the depth of corrosion damage also being measured.

## ANALYSIS OF MICROSTRUCTURAL FEATURES

Fig. 1, *a* displays microstructure images of cast samples with varying amounts of yttrium. These images were captured at a distance equivalent to  $1/2$  the ingot radius. The original alloy sample, devoid of yttrium additions,



**Fig. 1.** Images of microstructure of ingots (*a*): interdendritic segregation of yttrium in the form of inclusions (*b*) and thermodynamics of their formation during crystallization (*c*, *d*)

**Рис. 1.** Изображения микроструктуры полученных отливок (*a*), междендритная сегрегация иттрия в виде включений (*b*) и термодинамика их образования при кристаллизации (*c*, *d*)

exhibits a region characterized by columnar crystals. However, upon the addition of yttrium at 0.01 wt. %, the dendritic structure of the alloy begins to refine during solidification. This effect becomes more pronounced with increasing additive content, resulting in a shift from predominantly columnar to predominantly equiaxial dendritic structure. It is noteworthy that subsequent thermomechanical processing of the alloy necessitates an equiaxial structure within the ingot, as it reduces the risk of defects during forging operations. Consequently, an equiaxial structure is deemed optimal. Following yttrium microalloying, the Vickers hardness value of the samples increases from 140 to 160 HV.

SEM analysis of the cast samples revealed finely dispersed yttrium-rich intermetallic inclusions, measuring up to 2  $\mu\text{m}$  in diameter, with nickel present in the interdendritic regions (Fig. 1, *b*). Thermodynamic calculations supported the notion that such inclusions could precipitate from the melt (Fig. 1, *c, d*). It was observed that even small additions of yttrium (0.01 wt. %) expanded the two-phase region during crystallization. With increased additive content, the solidus temperature notably decreases, resulting in oversaturation of the melt with yttrium. This facilitates the formation of high-temperature  $\text{Ni}_3\text{Y}$  inclusions, the abundance of which is contingent upon the quantity of yttrium added. The heightened hardness of ingots is likely attributable to these refractory inclusions.

Many researchers examining the impact of REMs on the microstructure of superalloys have analyzed cast samples and arrived at similar conclusions [4; 7]. However, there has been scarce investigation into the impact of REMs on the structure of alloys after strain hardening [12].

Fig. 2 illustrates how the size of the austenitic grain of samples, following forging and annealing, varies with the amount of added yttrium. In the sample containing the lowest yttrium additive content (0.01 wt. %), the grain size is 2.2 times larger than in the original alloy sample, measuring 28.4  $\mu\text{m}$ . Concurrently, the hardness value decreases by 15 %. With an increase in the amount of additive, there is a refinement of the recrystallized austenitic grain and an associated increase in hardness (Fig. 2).

As previously noted [4 – 6], the high sensitivity of REM elements to oxygen and sulfur contributes to a reduction in impurity content at grain boundaries, effectively “purifying” them and enhancing the mobility of grain boundaries, thereby increasing their size. This underscores how even a minute concentration of impurities can significantly influence the mobility of grain boundaries.

These findings align well with the total oxygen content values in the samples (as indicated in the Table) obtained through gas analysis, as well as with the assessment of NMIs in the samples.

#### ASSESSMENT OF NON-METALLIC INCLUSIONS AND CORROSION RESISTANCE

Yttrium additions play a significant role in reducing the oxygen content and deoxidizing the melt. Even with small yttrium additives, the total oxygen content decreased by a factor of five (as indicated in the Table), with the volume fraction of oxide NMIs amounting to  $0.0055 \pm 0.004$  %. Following the addition of yttrium, the composition and size of oxide inclusions transition to complex oxides of yttrium and titanium. As the additive

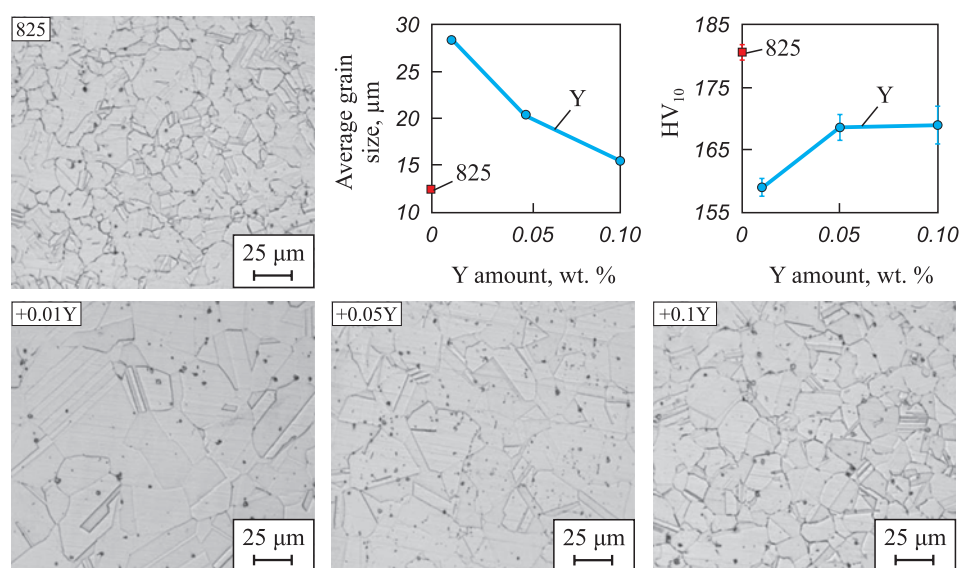


Fig. 2. Dependence of austenitic grain size of the samples after deformation and change of their hardness on Y amount, wt. %

Рис. 2. Зависимость размера аустенитного зерна деформировано упрочненных образцов и изменение их твердости от количества иттрия, мас. %

content increases, the total oxygen content and inclusion values grew to  $0.093 \pm 0.033$  %, yet they remain lower than those in the original alloy sample, where the oxide volume fraction is  $0.13 \pm 0.05$  %.

While yttrium does not influence the nitrogen content in the alloy (as shown in the table), and consequently, the volume fraction of carbonitride  $\text{Ti}(\text{C}, \text{N})$  NMIs, it does alter the morphology of these inclusions. In samples with yttrium microalloying, complex oxycarbonitride inclusions of the  $\text{Y}_2\text{O}_3 - \text{Ti}(\text{C}, \text{N})$  system are formed. In this scenario, finely dispersed deoxidation products, namely yttrium oxides, serve as a substrate for carbonitride formation (Fig. 3).

The results of electrochemical and chemical corrosion resistance tests are depicted in Fig. 3. An yttrium additive (0.01 wt. %) increased the pitting breakdown potential by 13 % and reduced the intergranular fracture rate by 20 %. However, as the additive amount increases, so does the proportion of oxide inclusions rich in titanium and yttrium, which diminishes the effect of melt stabilization by titanium and accounts for the decreased IGC resistance.

## CONCLUSIONS

In this study, we investigated the relationship between changes in the microstructure of cast samples after strain hardening, NMI characteristics and corrosion resistance of Incoloy 825 alloy with different content of yttrium additives.

Following stabilizing annealing, there were notable changes in the phase composition. Introduction of yttrium additives led to an expansion of the two-phase region during crystallization. Additionally, the liquid portion of the dendritic cell became oversaturated with yttrium, which transformed into high-temperature inclusions of  $\text{Ni}_3\text{Y}$  during solidification, as confirmed by calculations.

In the state, increasing yttrium additions resulted in a shift in solidification structure from predominantly columnar to predominantly equiaxial. Simultaneously, pressure treatment of the alloys proved to be more effective, yielding no cracks.

Yttrium acts as an active deoxidizing element; its impact is more pronounced with smaller additive amounts, as confirmed by gas analysis and measurement of grain size in samples after forging and annealing.

Yttrium additives altered the composition of NMIs in the alloy to yttrium-modified complex inclusions, characterized by a more rounded shape and smaller size. Such inclusions demonstrated enhanced chemical resistance in aggressive media during corrosion testing, with the sample containing 0.01 wt. % Y exhibiting the best corrosion resistance. Due to the increased grain size imparted by this composition, the alloy possesses higher

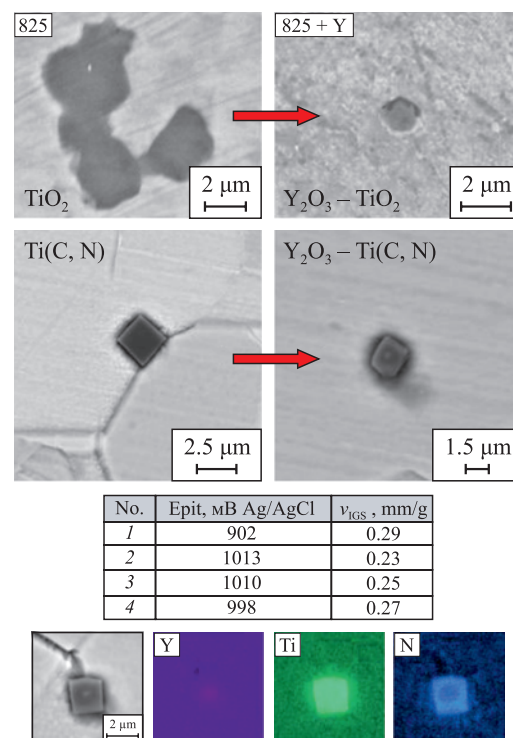


Fig. 3. Variation of non-metallic inclusions and corrosion resistance at different Y amounts

Рис. 3. Изменение НВ и коррозионной стойкости при разном количестве иттрия

ductility, necessitating the selection of a new heat treatment regimen.

## REFERENCES / СПИСОК ЛИТЕРАТУРЫ

1. Reed R.C. The Superalloys: Fundamentals and Applications. Cambridge University Press; 2008:392.
2. Mankins W.L., Lamb S. Nickel and nickel alloys. In: *ASM Metals Handbook. Vol. 2: Properties and Selection: Nonferrous Alloys and Special-Purpose Materials*. Materials Park, OH, USA: ASM International; 1990:428–445.
3. ASTM B564 Standard Specification for Ni-Fe-Cr-MoCu Alloy (UNS N08825 and UNS N08221) Rod and 108 Bar. West Conshohocken, PA: ASTM International; 2011.
4. Botinha J., Krämer J., Genchev G., Bosch C., Alves H. Effect of sensitization on the corrosion resistance of an advanced version of alloy UNS N08825. In: *Proceedings of the NACE Int. Corrosion Conf., Nashville, TN, USA, 24–28 March 2019*:1–12.
5. Shoemaker L., Crum J. Processing and fabricating alloy 825 for optimized properties and corrosion resistance. In: *Proceedings of the NACE Corrosion Conf., Houston, TX, USA, 13–17 March 2011*:1–13.
6. Raymond E.L. Mechanisms of sensitization and stablization of Incoloy nickel-iron-chromium alloy 825. *Corrosion*. 1968; 24(6):180–188. <https://doi.org/10.5006/0010-9312-24.6.180>
7. Li J.-P., Zhang H.-R., Gao M., Li Q.-L. Mechanism of yttrium in deep desulfurization of NiCoCrAlY alloy during vacuum induction melting process. *Rare Metals*. 2022;41(3): 218–225. <https://doi.org/10.1007/s12598-018-1103-1>
8. Du T., Wang L., Liu A., Wu Y., Zhang Y. Thermodynamics and phase equilibria for cerium and yttrium in the presence



- of oxygen and sulphur in nickel-base solutions. *Journal of Alloys and Compounds*. 1993;193(1–2):38–40. [https://doi.org/10.1016/0925-8388\(93\)90303-5](https://doi.org/10.1016/0925-8388(93)90303-5)
9. Ishii F., Ban-Ya S. Equilibrium between yttrium and oxygen in liquid iron and nickel. *ISIJ International*. 1995;35(3): 280–285. <https://doi.org/10.2355/isijinternational.35.280>
  10. Dan T., Gunji K. Deoxidation characteristics and shape modification of deoxidation products with Al-Ce and Al-Y complex deoxidizers. *Tetsu-to-Hagane*. 1982;68(14):1915–1921. [https://doi.org/10.2355/tetsutohagane1955.68.14\\_1915](https://doi.org/10.2355/tetsutohagane1955.68.14_1915)
  11. Kwon S., Kong Y., Park J. Effect of Al deoxidation on the formation behavior of inclusions in Ce-added stainless steel melts. *Metals and Materials International*. 2014;20(5): 959–966. <https://doi.org/10.1007/s12540-014-5022-x>
  12. Fujikawa H., Morimoto T., Nishiyama Y., Newcomb S. The effects of small additions of yttrium on the high-temperature oxidation resistance of a Si-containing austenitic stainless steel. *Oxidation of Metals*. 2003;59(1):23–40. <https://doi.org/10.1023/A:1023061814413>
  13. Palleda T., Banoth S., Tanaka M., Murakami H., Kakehi K. The role of yttrium micro-alloying on microstructure evolution and high-temperature mechanical properties of additively manufactured Inconel 718. *Materials & Design*. 2023;225:111567. <https://doi.org/10.1016/j.matdes.2022.111567>
  14. Zhou P.J., Yu J.J., Sun X.F., Guan H.R., Hu Z.Q. Roles of Zr and Y in cast microstructure of M951 nickel-based superalloy. *Transactions of Nonferrous Metals Society of China*. 2012;22(7):1594–1598. [https://doi.org/10.1016/S1003-6326\(11\)61361-7](https://doi.org/10.1016/S1003-6326(11)61361-7)
  15. Kang D.S., Koizumi Y., Yamanaka K., Aoyagi K., Bian H., Chiba A. Significant impact of yttrium microaddition on high temperature tensile properties of Inconel 713C superalloy. *Materials Letters*. 2018;227:40–43. <https://doi.org/10.1016/j.matlet.2018.03.106>
  16. Chen L., Ma X., Wang L., Ye X. Effect of rare earth element yttrium addition on microstructures and properties of a 21Cr-11Ni austenitic heat-resistant stainless steel. *Materials & Design*. 2011;32(4):2206–2212. <https://doi.org/10.1016/j.matdes.2010.11.022>
  17. Guimarães A., Silveira R., Almeida L., Araujo L., Farina A., Dille J. Influence of yttrium addition on the microstructural evolution and mechanical properties of superalloy 718. *Materials Science and Engineering: A*. 2020;776:139023. <https://doi.org/10.1016/j.msea.2020.139023>
  18. Cao S., Yang Y., Chen B., Liu K., Ma Y., Ding L., Shi J. Influence of yttrium on purification and carbide precipitation of superalloy K4169. *Journal of Materials Science & Technology*. 2021;86:260–270. <https://doi.org/10.1016/j.jmst.2021.01.049>
  19. Tomio Yu., Sigara M. Ni-Cr alloy material and seamless oilfield pipe products made from it. Patent RF no. 2630131. MPK B21C 1/00. *Bulleten' izobretenii*. 2017;(25). (In Russ.). Пат. РФ № 2630131. МПК B21C 1/00. Материал сплава Ni–Cr и изготовленные из него бесшовные нефтепромысловые трубные изделия / Томио Ю., Сигара М. *Бюллетень изобретений*. 2017;(25).
  20. ISO 17475:2005. Corrosion of Metals and Alloys – Electrochemical Test Methods – Guidelines for Conducting Potentiostatic and Potentiodynamic Polarization Measurements.
  21. ASTM. G 28 Standard Test Methods for Detecting Susceptibility to Intergranular Corrosion in Wrought, Nickel-Rich, Chromium-Bearing Alloys. West Conshohocken, PA, USA: ASTM International; 2015.

## Information about the Authors

## Сведения об авторах

**Mariya A. Salynova**, Engineer, Peter the Great St. Petersburg Polytechnic University

**ORCID:** 0000-0002-8770-6908

**E-mail:** m.salynova21@gmail.com

**Tigran V. Uglunts**, Engineer, Peter the Great St. Petersburg Polytechnic University

**E-mail:** uglunts\_tv@spbstu.ru

**Oleg V. Tolochko**, Dr. Sci. (Eng.), Prof., Leading Researcher, Peter the Great St. Petersburg Polytechnic University; Head of the Chair, State Marine Technical University

**ORCID:** 0000-0001-9623-4001

**E-mail:** tolochko\_ov@spbstu.ru

**Мария Алексеевна Салынова**, инженер, Санкт-Петербургский политехнический университет Петра Великого

**ORCID:** 0000-0002-8770-6908

**E-mail:** m.salynova21@gmail.com

**Тигран Владимирович Углуниц**, инженер, Санкт-Петербургский политехнический университет Петра Великого

**E-mail:** uglunts\_tv@spbstu.ru

**Олег Викторович Толочко**, д.т.н., профессор, ведущий научный сотрудник, Санкт-Петербургский политехнический университет Петра Великого; заведующий кафедрой, Санкт-Петербургский государственный морской технический университет

**ORCID:** 0000-0001-9623-4001

**E-mail:** tolochko\_ov@spbstu.ru

## Contribution of the Authors

## Вклад авторов

**M. A. Salynova** – concept development, metallographic studies, writing and editing the text.

**T. V. Uglunts** – smelting of samples, conducting corrosion tests.

**O. V. Tolochko** – analysis, editing the text, approval of the final version.

**М. А. Салынова** – разработка концепции, проведение металлографических исследований, подготовка и редактирование текста.

**Т. В. Углуниц** – выплавка образцов, проведение коррозионных испытаний.

**О. В. Толочко** – анализ, редактирование текста, утверждение окончательного варианта.

Received 02.10.2023

Revised 10.10.2023

Accepted 11.12.2023

Поступила в редакцию 02.10.2023

После доработки 10.10.2023

Принята к публикации 11.12.2023

INFORMATION TECHNOLOGIES AND  
AUTOMATIC CONTROL IN FERROUS METALLURGYИНФОРМАЦИОННЫЕ ТЕХНОЛОГИИ  
И АВТОМАТИЗАЦИЯ В ЧЕРНОЙ МЕТАЛЛУРГИИ

UDC 621.793.5:620.191

DOI 10.17073/0368-0797-2024-1-89-105



Original article

Оригинальная статья

INVESTIGATION OF PERFORMANCE LIMITATIONS  
IN CONTINUOUS HOT-DIP GALVANIZING UNITS ASSOCIATED  
WITH PRODUCT DEFECTSM. Yu. Ryabchikov<sup>✉</sup>, E. S. Ryabchikova, V. S. Novak, A. E. Klimenko

■ Nosov Magnitogorsk State Technical University (38 Lenina Ave., Magnitogorsk, Chelyabinsk Region 455000, Russian Federation)

✉ mr\_mgn@mail.ru

**Abstract.** The goals of the work were to search and systematize the speed limits of the steel strip during hot-dip galvanizing, associated with the threat of product defects. Since speed can be combined with many other factors, this paper provides an overview of the known causes of common defects. The causes were grouped taking into account the operations of individual sections of continuous hot-dip galvanizing units. To determine the circumstances in which defects occur, a method was used that involved step-by-step stratification of retrospective data and comparison of the distribution density of influencing factors for defective and non-defective products. The method was applied in the analysis of the data on defects at the MMK Metallurgy plant in Turkey, obtained in 2020–2021. Twenty-one types of acceptable and unacceptable defects that occur during galvanizing of DX51D steel were selected for analysis. Twenty-two technological parameters were taken as factors, including the strip speed. For each selected type of the defects, a set of influencing factors is determined, and for some types of defects, the alleged causes of their occurrence are indicated. It is shown that the relationship observed for many types of defects with the strip speed can actually be caused by other factors. We determined the types of defects, the probability of which increases with an increase in the speed or the level of its change. The paper proposes measures aimed at preventing the increase in the proportion of defective products along with the performance gain.

**Keywords:** continuous hot-dip galvanizing, steel strip, defects, strip speed, performance

**Acknowledgements:** The work was supported by the Russian Science Foundation, grant No. 23-29-10058, <https://rscf.ru/project/23-29-10058/>.

**For citation:** Ryabchikov M.Yu., Ryabchikova E.S., Novak V.S., Klimenko A.E. Investigation of performance limitations in continuous hot-dip galvanizing units associated with product defects. *Izvestiya. Ferrous Metallurgy*. 2024;67(1):89–105.

<https://doi.org/10.17073/0368-0797-2024-1-89-105>

ИЗУЧЕНИЕ ОГРАНИЧЕНИЙ ПРОИЗВОДИТЕЛЬНОСТИ АГРЕГАТОВ  
НЕПРЕРЫВНОГО ГОРЯЧЕГО ОЦИНКОВАНИЯ,  
СВЯЗАННЫХ С ДЕФЕКТАМИ ПРОДУКЦИИМ. Ю. Рябчиков<sup>✉</sup>, Е. С. Рябчикова, В. С. Новак, А. Е. Клименко

■ Магнитогорский государственный технический университет им. Г.И. Носова (Россия, 455000, Челябинская обл., Магнитогорск, пр. Ленина, 38)

✉ mr\_mgn@mail.ru

**Аннотация.** Целями работы являлись поиск и систематизация ограничений скорости движения стальной полосы при горячем оцинковании, связанных с угрозой возникновения дефектов продукции. Поскольку скорость может оказывать совместное влияние с множеством других факторов, в работе проведен обзор известных причин возникновения распространенных дефектов. Выполнена группировка причин с учетом операций секций агрегатов непрерывного горячего оцинкования. Для определения обстоятельств возникновения дефектов применен способ, предполагающий поэтапную стратификацию ретроспективных данных и сопоставление плотности распределения влияющих факторов для дефектной и не дефектной продукции. Проведен анализ данных о дефектах на заводе «ММК Metallurgy» в Турции, полученных в 2020 – 2021 гг. Для анализа были отобраны допустимые и не допустимые дефекты двадцати одного вида, возникающие при оцинковании стали DX51D. В качестве факторов приняты двадцать два технологических параметра, включая скорость движения полосы. Для каждого отобранного вида дефектов определен набор влияющих факторов, для некоторых из них указаны предполагаемые причины их возникновения. Показано, что наблюдаемая для многих видов дефектов связь со скоростью движения полосы

в действительности может быть вызвана иными факторами. Определены виды дефектов, вероятность возникновения которых увеличивается с ростом скорости или уровнем ее изменения. Предложены мероприятия, направленные на предотвращение роста доли продукции с дефектами при увеличении производительности.

**Ключевые слова:** непрерывное горячее оцинкование, стальная полоса, дефекты, скорость движения полосы, производительность

**Благодарности:** Исследование выполнено за счет гранта Российского научного фонда № 23-29-10058, <https://rscf.ru/project/23-29-10058/>.

**Для цитирования:** Рябчиков М.Ю., Рябчикова Е.С., Новак В.С., Клименко А.Е. Изучение ограничений производительности агрегатов непрерывного горячего оцинкования, связанных с дефектами продукции. *Известия вузов. Черная металлургия*. 2024;67(1):89–105. <https://doi.org/10.17073/0368-0797-2024-1-89-105>

## INTRODUCTION

Galvanized sheet steel is a primary product of metallurgical companies. The production from continuous hot-dip galvanizing units (CHGUs) has increased significantly in recent decades. It is reported [1] that galvanized rolled steel accounts for approximately 10 % of the global metal product consumption. In developed countries, this figure can exceed 15 %. The automotive and construction sectors are the principal consumers of these products [2].

The efficiency of CHGUs is gauged by the speed of the steel strip and downtime. The optimal speed is selected based on the specifics of the automatic control system employed at various stages of the manufacturing process. For example, in the strip heat treatment phase, when fuel usage nears maximum capacity (determined by burner capabilities), regulating the process can become challenging [3].

Research highlights the significance of human judgment in selecting the strip speed [4]. It has been found that different operators may choose varying speeds, leading to significant discrepancies in CHGU efficiency. To address this, a consulting system has been suggested to allow staff to leverage the expertise of the most effective operators. However, the impact of these choices on product quality has not been assessed. It is noted [5] that operational complexities and constraints of the continuous annealing process play a crucial role, where the human factor often reduces efficiency. Moreover, there are line speed limits associated with product quality that lack systematic organization and are typically determined through empirical means.

## TYPICAL CAUSES OF THE LINE SPEED REDUCTION

Typically, equipment is engineered for a specific maximum line speed, which may be decreased either temporarily or for extended periods. For example, a study [6] suggests utilizing line speed adjustments to rapidly modify strip temperature in response to disruptions, such as changes in the type of steel being processed or alterations in annealing temperature requirements. Short-term reductions are often implemented as a regulatory measure.

On the other hand, long-term speed reductions may stem from the limited capacity of the heating and cooling systems in the strip heat treatment sections. For example,

the guidelines from the MMK Metallurgy plant provide specific line speed recommendations based on the strip's thickness, width, and the desired temperatures at the exit of the direct heating heat, indirect heating  $t_{\text{hold}}$ , and cooling  $t_{\text{cool}}$  stages (Fig. 1). According to these guidelines (Fig. 1), for strips thicker than 1 mm, the advised speed is considerably less than 180 m/min, which is the maximum.

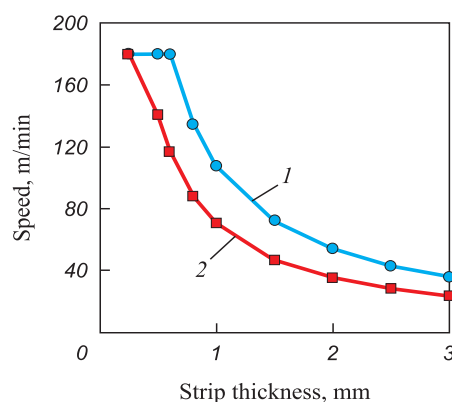
Enhancing the control of the continuous annealing process can lead to increased line speeds. Nevertheless, potential improvements are often constrained by defects arising from factors other than non-compliance with annealing specifications.

## CLASSIFICATION OF DEFECTS AT

### MMK METALLURGY PLANT

GOST 14918 – 2020, based on ISO 3575:2016 and additional standards, outlines allowable defects based on the type, category, and classification of the coating's finish. General acceptable defects include:

- marks from the strip and roller bends;
- scratches and abrasions that do not compromise the integrity of the coating;
- light and dead spots;
- inconsistent coloring of the passive film.



**Fig. 1.** Recommended speeds depending on heat treatment mode:

- 1 – CQ type ( $t_{\text{heat}} = 720\text{ }^{\circ}\text{C}$ ,  $t_{\text{hold}} = 750\text{ }^{\circ}\text{C}$ ,  $t_{\text{cool}} = 460\text{ }^{\circ}\text{C}$ );  
 2 – EDDQ type ( $t_{\text{heat}} = 750\text{ }^{\circ}\text{C}$ ,  $t_{\text{hold}} = 850\text{ }^{\circ}\text{C}$ ,  $t_{\text{cool}} = 460\text{ }^{\circ}\text{C}$ )

**Рис. 1.** Рекомендуемые скорости в зависимости от режима термической обработки:

- 1 – тип CQ ( $t_{\text{H}} = 720\text{ }^{\circ}\text{C}$ ,  $t_{\text{B}} = 750\text{ }^{\circ}\text{C}$ ,  $t_{\text{окл}} = 460\text{ }^{\circ}\text{C}$ );  
 2 – тип EDDQ ( $t_{\text{H}} = 750\text{ }^{\circ}\text{C}$ ,  $t_{\text{B}} = 850\text{ }^{\circ}\text{C}$ ,  $t_{\text{окл}} = 460\text{ }^{\circ}\text{C}$ )



For specific types and categories of coatings, the following imperfections are permitted:

- beads, runs, buildup without cracking;
- localized roughness of the coating;
- dross pimples or inclusions;
- uneven crystallization within the coating;
- dark dots and tracks (streaks).

The presence of cracks on minor beads situated on the steel substrate's flaws is prohibited. The standard also details unacceptable edge imperfections and establishes limits for the mass of the coating.

According to MMK Metallurgy's data for 2020 – 2021, as illustrated in Table 1, certain defects are significantly more prevalent in defective products ( $P_{\text{def}}$ ) compared to quality products ( $P_{\text{norm}}$ ). The most frequent defects

include uncoated areas (insufficient zinc coating and delamination) and uneven coating. Common defects of quality products are presented in Table 2.

#### IDENTIFIED CAUSES OF DEFECTS

The occurrence of defects in the continuous hot-dip galvanizing process can be attributed to both the technological aspects of the process and the characteristics of the initial steel strip being galvanized.

**Impact of steel strip properties on defect formation.** The properties of the steel base can be grouped into several categories:

- structural composition of the steel;
- chemical makeup of the steel;
- mechanical characteristics;

Table 1. Common defects in rejected products

Таблица 1. Распространенные дефекты отбракованной продукции

Number	Designation (English / Turkish)	Defect	$P_{\text{norm}}, \%$	$P_{\text{def}}^*, \%$
D1	Uncoated Spots / Kaplama Almama	Uncoated spots	0.46	25.90
D2	Rough Coating / Pas Kaynakli Puruzlu Kaplama	Uneven coating	0.12	22.29
D3	Damage Marks / Markalama Izi (Darbe Izi)	Damage marks	0.29	8.40
D4	Dent / Batik (Batma Boslugu)	Dents	0.31	4.88
D5	Edge Roughness / Kenar Puruzlulugu	Rough edges	1.06	2.71
D6	Coating Thickness Defect / Kaplama Uygunsuzlugu	Coating thickness nonconformity	0.58	1.63
D7	Macro Inclusion / Makro Inkluzyon	Macroinclusions	0.36	1.08
D8	Unappropriate Mechanical Test / Mekanik Test Uygunsuzlugu	Non-conforming mechanical properties	0.10	1.08

\* When probability was calculated, we excluded the defects occurring as the unit stopped/started.

Table 2. Common acceptable defects

Таблица 2. Распространенные дефекты качественной продукции

Number	Designation (English / Turkish)	Defect	$P_{\text{norm}}, \%$	$P_{\text{def}}^*, \%$
D9	Ridge / Ridge	Zinc bright edges	55.61	8.94
D10	Rough Coating / Puruzlu Kaplama	Rough coating	52.98	13.55
D11	Snout Marks / Surtunme Izi	Abrasions	49.21	6.23
D12	Sink Roll Marks / Sink Roll Merdane Izi	Roller marks	16.98	2.98
D13	Ocean Wave (Coating ripple) / Yuzey Akintisi (Dalgali Kaplama)	Wavelike coating	16.79	16.26
D14	Skin pass mill break-marks / SPM Kirigi	Marks related to skin-pass rolling	11.05	1.63
D15	Roll Shadow / Merdane Golgesi	Dark longitudinal streaks	5.07	0.27
D16	Chromate Stain / Kromat Lekesi	Chrome stains	4.45	4.34
D17	Matt Appearance / Mat Goruntu	Matte finish	4.39	4.34
D18	Scratch / Cizik	Scratches	2.73	4.07
D19	Orange Peel / Portakal Kabugu Olusumu	Micro-roughness (orange peel)	2.05	0.54
D20	Break Mark / Kirilma Izi	Cracks in the coating	1.67	0.54
D21	Blister / Blister	Blisters on the coating	0.79	0

– surface conditions, including levels of contamination [7; 8].

Research [9] points out the significant influence of steel's chemical composition on the zinc coating's development. Specifically, the silicon content plays a critical role. When the silicon concentration ranges between 0.06 and 0.10 %, an abnormal increase in zinc coating thickness occurs. This can result in a coating that is both fragile and possesses an unappealing gray hue. Notably, silicon content tolerances are relatively broad for many steel grades.

Further studies [10] have identified that certain marks on the coating can stem from the underlying steel's characteristics. For instance, small ferrite grains, approximately 1 – 2 mm in diameter, emerge on the surface. Chemical analyses have detected elevated levels of Ti and Mn within these grains, alongside thin layers (up to 150 nm) of Mn and Si oxides at the juncture between the coating and the base material.

Additionally, a steel phosphorus content exceeding 0.03 % has been linked to the coating's delamination.

According to [11], shape defects present in cold-rolled semi-finished products can directly influence the occurrence of coating defects. This is due to the abnormal effect of air knives on similar areas of the strip surface, leading to issues such as non-flatness, folds, corrugation, distortion, and scab.

Further research [8] indicates that surfaces marred by scratches, gouges, or mechanical damage exhibit significantly increased reactivity. This heightened reactivity can foster the growth of Zn–Fe crystallites as protrusions in the coating layer, resulting in areas with an excessively thick coating. Additionally, the process of galvanizing surfaces that are initially uneven is prone to result in a uneven coating thickness [12]. In attempts to counteract this, a thicker application of coating might be employed. However, such defects may still be inevitable, particularly when high zinc temperatures are involved or the immersion time in the zinc bath is extended.

The research articles [13 – 15], focusing on the development of steel for automotive body sheets, underscore the complexity of balancing a set of diverse and often conflicting requirements such as strength, ductility, formability, and corrosion resistance. The authors highlight the challenge in enhancing the steel's strength without a comprehensive understanding of the kinetics of phase and structural transformations. For instance, it has been observed that the presence of Cr, Ni, and Cu in the steel can delay recrystallization to higher temperatures. As a remedy, it's suggested to increase the annealing holding temperature by 30 – 50 °C to accommodate these effects.

Defects arising from the CHGU process are categorized based on the specific stages of the operation that lead to their occurrence.

**Cleaning section.** In the CHGU process, the steel strip is cleaned through immersion in an alkaline solu-

tion, brushed by rotating roller brushes, and subjected to electrolytic cleaning.

The primary contaminants on the strip include iron fines, oil, and dirt. As noted in the literature [8], the goal of the cleaning stage is to reduce the levels of iron fines and oil on the strip's surface to below 20 mg/m<sup>2</sup>. The presence of fine particles in the bath can lead to reduced zinc adhesion, resulting in dross formation, material adherence issues, and uncoated sections.

Research [10] into streaky mark defects, which are long (tens of meters), narrow (up to 15 mm wide), and run parallel to the rolling direction, suggests that these marks arise from a high concentration of oxides at the interface between the coating and the steel substrate. This condition suggests that the strip surface was not adequately cleaned, leading to ineffective removal of contaminants.

Another study [16] highlights that bare spots and coating delamination primarily result from residual oil on the steel substrate. This oil, when subjected to heating in direct and indirect heating furnaces, turns into carbonaceous deposits that manifest as defects. These issues can be mitigated through effective lubricant removal and appropriate adjustment of the bath's chemical composition.

Furthermore, the presence of uncoated cavities has been attributed to air knives failing to remove solid particles from the surface or to their inability to blow off particles that were not removed in time or were trapped, as indicated in [8].

**Heating and exposure.** The strip heating section in CHGU is designated for continuous recrystallization annealing. This section may consist of a furnace that utilizes indirect heating in an exothermic gas environment, or it may employ both direct and indirect heating methods. Reduction reactions occur in a protective atmosphere, aiding in the cleaning of the strip.

Research [8] indicates that inadequate management of the air/fuel mixture in the CHGU's direct heating furnace can lead to an excessively high concentration of CO, which may result in soot accumulation on the strip. These soot deposits can cause to bare spots in the zinc coating. In the case of indirect heating furnaces, where the strip is heated in a protective atmosphere of N<sub>2</sub> – H<sub>2</sub> maintaining low dew points and minimal oxygen levels is crucial for enhancing strip cleanliness. Failure to control these conditions can lead to contamination issues, such as those arising from the deterioration of radiant tubes, which negatively affect the zinc coating's adherence to the strip. Additionally, during the galvanization of low carbon steels, lubricant leaks from the hearth roll bearings can lead to surface carburization.

Moreover, it has been found [17] that when galvanizing dual-phase steels, annealing in environments with low dew points promotes significant external oxidation of trace alloying elements. This oxidation process impedes the molten zinc's ability to reactively wet

the steel surface effectively. An increase in the dew point leads to a reduction in the surface coverage of oxides.

The study [6] highlights that the thermal load in the heating section rises substantially with the increase in strip speed. This surge in thermal load amplifies the thermal crown effect of the rolls, attributed to the temperature variation within the rolls themselves, consequently heightening the likelihood of strip misalignment. Within the furnace, the strip experiences thermal buckling, a warping effect caused by uneven heat distribution, exacerbated by the strip's diminished yield strength at elevated temperatures.

According to [18], the phenomenon of strip buckling in the furnace is primarily due to the synergistic effects of elevated temperatures and tension applied to the strip. The risk of buckling escalates as the strip widens. Achieving a more even temperature distribution across the strip's width can mitigate buckling risks, but only within lower temperature ranges. At certain temperatures along the strip's length, tension reaching a first critical level induces buckling. Should the tension further escalate beyond a second critical threshold, buckling might reduce, provided deformation processes have not commenced.

The literature [6; 19; 20] underscores the significant influence of the steel's heat treatment conditions during annealing on the mechanical properties of products from CHGU. To avoid defects amid changes in production assortment or operational modes, it is advised to employ preemptive control models for strip temperature regulation [21].

**Closed-circuit cooling.** The closed-circuit cooling section is an integral component of the indirect heating furnace, where nitrogen-hydrogen gas serves as the cooling medium for the steel strip. This cooling process aims to reduce the strip's temperature to near that of the molten zinc in the bath, preparing it for the galvanizing process.

Research [22] conducted on the occurrence of zinc bright edges at Sheet-rolling Shop No. 11 of PJSC Magnitogorsk Iron and Steel Works identified the root cause as the accumulation of zinc dust within the snout of the CHGU furnace's outlet trough. This accumulation occurs when zinc dust particles evaporate from the bath and then condense on the snout, from where they subsequently fall onto the strip's surface, leading to zinc buildup. To address this issue, modifications to the furnace outlet trough's snout were suggested, specifically to enable dew point measurement and control within the area.

It has been observed [8] that a high strip temperature at the inlet of the zinc bath, following closed-circuit cooling, combined with a low dew point at the snout, can lead to zinc vaporization at elevated strip speeds. This vapor, upon condensing on the strip, may result in coating defects such as pimples and bulges. The significance of the strip temperature post-cooling on defect formation has also been highlighted [23]. To mitigate these issues, it is recommended [24] to minimize the temperature

difference between the cooled strip and the bath. When the strip temperature exceeds 470 °C, there is an increased risk of aluminum capture in the bath, heightened dissolution of the steel strip, and accelerated dross formation.

The study documented in [17] explores how the cooling rate influences the mechanical properties of dual-phase steels.

**Zinc bath.** The study in [9] highlights that the formation of bottom dross in the zinc bath increases the melt's viscosity, leading to uneven coating thickness and the appearance of bright edges. To mitigate these issues, the addition of aluminum to the bath is recommended.

Top-dross particles can become embedded in the coating if the bath's surface oxide film adheres to the strip, as noted in [8]. This underscores the necessity of maintaining a clean bath surface. Incorrect levels of aluminum in the bath, coupled with fluctuations in the melt temperature, can escalate dross formation. The resultant dross particles may adhere to both the coating and the rolls, with larger dross particles potentially causing indentations in the strip. An excessive iron content in the bath negatively impacts the fluidity of the molten zinc, leading to a matte coating finish.

Research in [25] examines how the melt temperature within a zinc bath affects the coating thickness, demonstrating that an increase in temperature leads to thinner coatings, particularly for steels with a high silicon content.

**Air knives.** After the bath, the strip passes through air knives that blow excessive zinc back into the bath. This ensures the required thickness and uniformity of the coating layer.

However, as [8] reveals, air knives can induce defects such as runs and folds in the coating. Runs typically occur on thicker strips with a heavy coating, whereas ripples are more likely on thinner strips with a light coating. Factors contributing to these defects include:

- the strip's overly smooth surface;
- elevated temperatures of either the strip or the zinc in the bath;
- excessive vibrations and the disruption of the oxide layer on the molten zinc.

The study in [26] discusses non-uniform coating issues, specifically check mark stains that create various patterns. These patterns result from differences in pressure within the air knife's alternating vortex, with higher pressure at the edges removing more molten zinc than the lower-pressure center. The movement of these vortices, driven by jet and pressure instability, influences the pattern formation, which varies with the strip's speed. According to [27], the characteristics of check-mark stains are affected by the initial distribution of coating thickness across the strip and the speed of the steel strip. The presence of such stains reduces the quality, productivity, and profitability of the final products [28]. Additionally, [29] demonstrates a significant drop in jet pres-



sure at the strip's edges compared to the peak pressure in the middle, affecting coating uniformity and leading to a thickening of the strip edge.

The studies referenced in [30; 31] delineate key variables influencing coating thickness, such as:

- strip speed;
- air knife pressure;
- height of the air knife from the bath;
- proximity of the air knife to the strip;
- opening of the gap;
- angle of air knife inclination.

Research presented in [32] highlights that deviations in coating thickness from the intended specification can often be attributed to vibrations of the strip near the air knives. These vibrations may stem from fluctuations in tension and the movement patterns of rollers within the zinc bath, suggesting that the effect of air knife settings on the quality is interlinked with strip speed and other parameters via strip vibrations. It has been observed that strip speed plays a significant role in the amplitude of vibrations near the air knife [33], with increased speeds making vibration mitigation more challenging. However, optimizing tension and controlling strip speed can limit peak vibration amplitudes. The utilization of the EMG eMASS electromagnetic strip stabilization system, as noted in [34], significantly reduces variation in coating thickness by minimizing vibration.

The authors of [11] identify severe strip vibrations, melt turbulence, and air knives clogging with the melt as causes for the appearance of zinc bright edges. They recommend adjusting the tension and strip speed to address these vibration-induced defects. Furthermore, modifications in the following areas can correct such defects:

- air knife pressure;
- proximity to the strip;
- jet angle;
- strip temperature and speed.

According to [35], when the strip exits the bath, the interaction between the molten zinc on the coating's outer surface and atmospheric oxygen results in a more viscous top oxide layer, leading to ripple formation. This phenomenon is more pronounced with thick coatings and lower strip speeds, which can be mitigated by increasing strip speed or employing nitrogen in the air knife process.

The paper [36] explores how air knives affect the flow of liquid zinc in the bath, showing that air knife jets can significantly alter the zinc flow around the strip's exit. This finding opens avenues for enhancing coating quality through strategic manipulation of air knife settings.

**Skin pass mill and tension leveller.** Following the air knives and deep cooling stages, the strip proceeds to the skin pass mill, where it undergoes rolling with a minimal elongation ratio. This process aims to maintain the steel's drawability, enhance surface smoothness, and

mitigate the zinc coating's texture. A tension leveler is utilized to improve the strip's flatness. It has been observed that the interaction between the hard surface of the work roll and the softer zinc coating leads to zinc transfer onto the work roll, resulting in dents on the strip's surface during rolling.

Research [37] identifies two distinct mechanisms for the formation of coating cracks in areas of the sheet that undergo the most extensive rolling. Macrocracks emerge from the infiltration of the coating material into the metal, which subsequently embrittles the grain boundaries. Microcracks develop during the skin-pass rolling of galvanized sheets under high tangential stress conditions and at minor strip bends.

The occurrence of the “orange peel” defect during skin-pass rolling, triggered when the elongation reaches the yield strength, has also been documented. Applying the correct annealing method can alleviate this issue [38].

**Combined effect of sections.** Numerous studies emphasize that defects often arise from a complex interplay of factors.

Research conducted by the authors of [11] delves into the causes of zinc bright edges, highlighting that operational downtime presents a significant challenge in mitigating such defects. The solidification of zinc at the point of contact between the strip and the zinc melt complicates the operation of air knives, which are crucial for achieving a specified coating thickness.

The study [10] identifies the co-occurrence of two specific conditions as a precursor to the development of cracks on the coating surface. Initially, flaws in the technological process lead to what is described as a “wavy pattern” of defects, including voids and cracks, primarily located at the center of the coating and not directly related to the presence of steel base surface oxides. The second condition involves the nuances of skin-pass rolling, during which the coating is prone to cracking.

The paper [39] outlines two scenarios frequently leading to diminished adhesion between the zinc layer and the steel substrate. The first scenario involves:

- low temperature in the zinc bath;
- reduced temperature in the furnace's sixth zone (the last one in the direction of metal flow);
- a sharp decrease in strip speed.

The second scenario includes:

- sudden speed alterations;
- low zinc bath temperature;
- decreased strip temperature at the furnace exit.

The researchers in [40] analyzed how various factors affect product quality, including:

- average elongation;
- strip speed;
- proximity of the air knives to the strip;
- air knife pressure.

Quality is defined by the absence of various defects, such as uneven or insufficient zinc coating due to buildup, streaks, pits, and dross inclusions. They identified specific conditions under which the incidence of defects markedly increases, namely:

- substantial elongation;
- speed over 57 m/min;
- air knife distance exceeding 1226 mm;
- elevated air knife pressure.

This analysis confirms that the strip speed plays a crucial role in the manifestation of various defects, making it challenging to simultaneously address all these aspects. Thus, identifying the root causes of defects with consideration of the line speed is crucial.

### INITIAL DATA

The analysis of performance and defects at MMK Metallurgy plant was conducted through a retrospective evaluation of data from CHGU subsystem operations and product defects identified during 2020 – 2021, specifically focusing on DX51D steel. The database for this period contains detailed records for each strip roll, including the maximum, minimum, and average values of each process parameter recorded during the processing of the roll.

### EFFECT OF STOPPAGES ON DEFECT OCCURRENCE

The research highlighted in [11] identifies downtime as a significant factor influencing the incidence of defects. Table 3 in the study details the ratio of rolls exhibiting defects that occurred during instances when the production unit was halted.

Out of the defects examined, only three showed a probable connection to the unit's stoppages. Among these, the defect categorized as *D1* – uncoated spots – exhibited the most significant correlation with unit downtime. The analysis suggests that for the range of defects considered, unit stoppages cannot be solely attributed as the cause for most defect occurrences. Consequently, rolls that experienced unit stoppages during their processing were subsequently removed from the analysis to maintain accuracy.

The data presented in Table 4 are considered as influencing factors in this context.

**Table 3. Proportion of rolls with defects during production of which there was a stoppage of the unit**

**Таблица 3. Доли рулонов с дефектами, при производстве которых возникала остановка**

Defect	Proportion, %
<i>D1</i> – Uncoated Spots	8.84
<i>D3</i> – Damage Marks	3.47
<i>D4</i> – Dent	1.50

### METHOD DETERMINING THE CIRCUMSTANCES

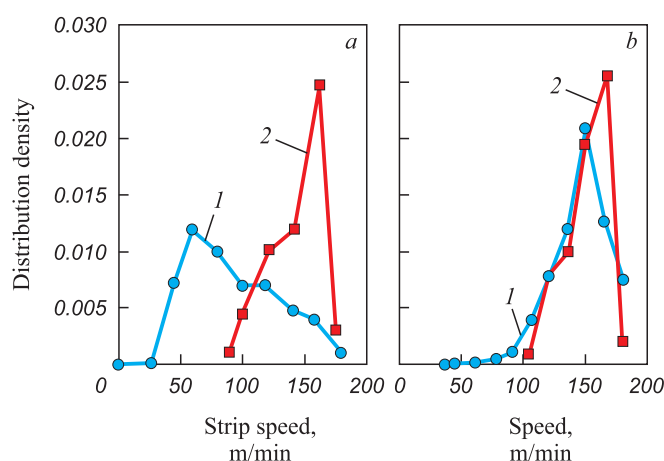
#### UNDER WHICH DEFECTS DEVELOPED

Identifying the precise conditions leading to defects is challenging due to the multitude of process parameters that could potentially influence outcomes, along with the interconnected changes among various signals.

For each specific defect, a particular set of factors was pinpointed to enable further data stratification. This approach involved initial assessments to compare the distribution laws of each parameter for defective versus non-defective products.

Stratification was employed to mitigate the effects of confounding factors amidst interdependent signal variations. Data were organized based on the conditions of their collection, and then analyzed within these groups separately to isolate and eliminate the influence of extraneous variables. For instance, the emergence of defect *D19* was linked to changes in strip thickness and line speed. To isolate the impact of speed, data were categorized by strip thickness. Subsequently, within each defined category (stratum), the effect of speed on the occurrence of defects was examined. Fig. 2, *a* presents the speed distribution density for products affected by defect *D19* without stratification, while Fig. 2, *b* shows the analysis for a specific stratum with stratification applied, indicating that the likelihood of defect occurrence is more closely related to strip thickness than to line speed.

The process of data stratification involved multiple stages. Initially, factors such as line speed and strip thickness were considered potential risk factors. Based



**Fig. 2. Speed distribution density for products with (2) and without (1) defect *D19*:**  
*a* – without stratification;  
*b* – with stratification (strip heights (0.40 – 0.65 mm))

**Рис. 2. Плотность распределения скорости для продукции с дефектом *D19* (2) и без такого дефекта (1):**  
*a* – без стратификации;  
*b* – при стратификации для страты толщиной 0,40 – 0,65 мм

Table 4. Factors explaining the causes of defects

Таблица 4. Факторы для объяснения причин дефектов

Number	Value
F1	Average strip speed
F2	Difference between maximum and minimum speed
F3	Average strip thickness
F4	Difference between maximum and minimum strip thicknesses
F5, F6	Minimum and maximum strip temperatures after the direct heating section
F7, F8	Minimum and maximum strip temperatures after the indirect heating section
F9, F10	Minimum and maximum strip temperatures after closed-circuit cooling
F11	Strip width
F12, F13	Minimum and maximum melt temperature in the zinc bath
F14, F15	Pressure on front and rear air knives*
F16, F17	Minimum and maximum dew point in the indirect heating section
F18, F19	Minimum and maximum dew point in the closed-circuit cooling section
F20	Minimum strip tension at the furnace inlet**
F21	Specified zinc coating thickness (coating mass)
F22	Elongation during rolling***
* When the coating thickness is stabilized, it characterizes melt viscosity in the zinc bath.	
** For some defects, the tension at different sections was considered.	
*** It was taken into account for defects D19, D20.	

on the outcomes of the initial analysis, these parameters were then classified as interfering factors if necessary.

#### FACTOR SETS FOR FURTHER STRATIFICATION

##### OF THE DATA

Table 5 presents the variations in distribution density between defective and non-defective products, correlating to each defect being investigated.

From the data in Table 5, it is apparent that there is no discernible link between factors F16 and F19 and any of the defects studied. Specifically, for defects D16 (*Chrome stains*) and D17 (*Matte finish*), the distribution densities of all factors for defective and non-defective products are notably similar, suggesting these factors do not significantly influence the emergence of these defects. Additionally, the pressures of the front and rear air knives (Factors F14 and F15) exhibit comparable partial distributions across all defects.

However, certain factors are identified as potentially influencing the occurrence of a broad range of defects:

- strip speed – 17 types of defects;
- strip thickness – 16 types of defects;
- strip tension – 12 types of defects;
- zinc coating thickness – 10 types of defects;
- air knife pressure – 9 types of defects;
- the minimum strip temperature after the direct heating section – 8 types of defects.

#### EVALUATION OF THE IMPACT OF FACTORS BASED ON THE RESULTS OF STRATIFICATION

Table 6 details the factors potentially affecting the incidence of various defects, with post-stratification analysis revealing that the relationship between defects and strip speed is often mediated by the effect of strip thickness. Beyond thickness, a significant array of defects can be attributed to several key factors:

- strip speed – 6 types of defects;
- air knife pressure and coating thickness – 5 types of defects;
- speed fluctuations and strip tension – 3 types of defects;
- dew point in the closed-circuit cooling section and strip temperature after this section – 2 types of defects.

Four specific defects were found to occur under conditions uniquely influenced by the distribution of strip thickness alone (D11 – abrasions, D12 – roller marks, D18 – scratches, D21 – blisters). Following strip thickness, speed emerges as the second most significant factor in the prevalence of a wide range of defect types.

#### ALIGNMENT OF THE RESULTS WITH THE KNOWN CAUSES OF DEFECTS

**D1 – Uncoated spots.** The findings indicate that variations in strip speed, in particular, are a probable cause



Table 5. Factors that can potentially affect the occurrence of a defect

Таблица 5. Факторы, которые потенциально могут влиять на возникновение дефекта

Defect	Factor number																					
	01	02	03	04	05	06	07	08	09	10	11	12	13	14	15	16	17	18	19	20	21	22
D1	+	+			+		+	+	+									+		+		
D2	+		+										+								+	
D3	+	+	+		+												+			+		
D4		+						+						+	+		+					
D5	+		+								+			+	+					+	+	
D6										+				+	+							
D7	+		+			+				+				+	+					+	+	
D8	+		+		+	+		+														
D9	+		+									+		+	+					+		
D10	+		+											+	+		+			+	+	
D11	+		+																	+	+	
D12	+		+																	+	+	
D13	+		+											+	+						+	
D14	+	+	+		+									+	+		+			+	+	
D15	+		+		+		+													+		
D16																						
D17																						
D18	+		+	+	+		+					+		+	+					+		
D19	+		+		+													+			+	+
D20	+		+																		+	
D21	+		+		+															+		
N	17	4	16	1	8	2	3	3	1	2	1	2	1	9	9	0	4	2	0	12	10	1

of uncoated spots (Fig. 3). This observation aligns with the insights from [39], highlighting the impact of speed changes on this type of defect. Nevertheless, only a minor portion of such defects can be attributed to unit stoppages, suggesting that uncoated spots are not directly linked to the unit's cessation of operation. The connection with tension suggests that these defects are likely due to mechanical factors. Contrary to the issues discussed in [8; 17], no significant effect from either high or low dew point values in the indirect-heating furnace on this type of defect was detected.

**D2 – Uneven coating.** The findings align with observations from [12], indicating that an elevated melt temperature complicates the achievement of a thick, uniform coating (Fig. 4). A higher melt temperature correlates with increased metal throughput in CHGU, presenting challenges in temperature control. This defect [41], adversely impacts the surface's wetting properties could be attributed to the diffusion of iron through the inhibitory Fe–Al interfacial layer, which, as reported in inhibiting Fe–Al interfacial layer, which, according to [41], negatively affects the surface wetting. When the aluminum content in the bath is at 0.2 %, the formation of the inhibiting layer is

complete, provided the strip temperature at the bath inlet is between 440 to 480 °C. Nonetheless [24] points out that the diffusion of iron through this inhibiting layer escalates

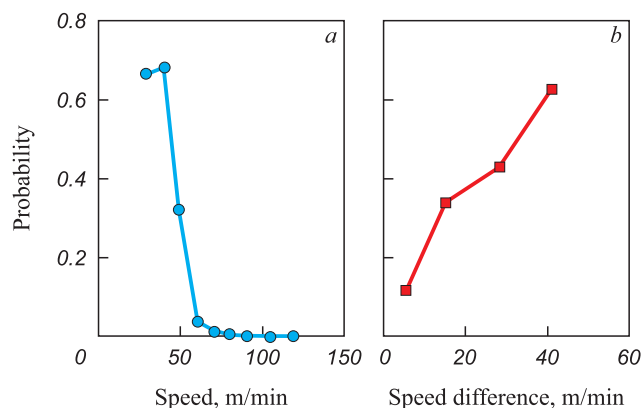


Fig. 3. Dependence of probability of uncoated spots (D1) on:  
a – speed at strip height  $h_{\text{met}} = 0.80 - 0.95$  mm;  
b – speed difference at  $h_{\text{met}} \approx 0.8$  mm and an average speed of 50 m/min

Рис. 3. Зависимость вероятности пятен без покрытия (D1) от:  
a – скорости при толщине полосы  $h_m = 0,80 - 0,95$  мм;  
b – перепада скорости при  $h_m \approx 0,8$  мм и средней скорости 50 м/мин

Table 6. Factors affecting the occurrence of a defect

Таблица 6. Факторы, влияющие на возникновение дефекта

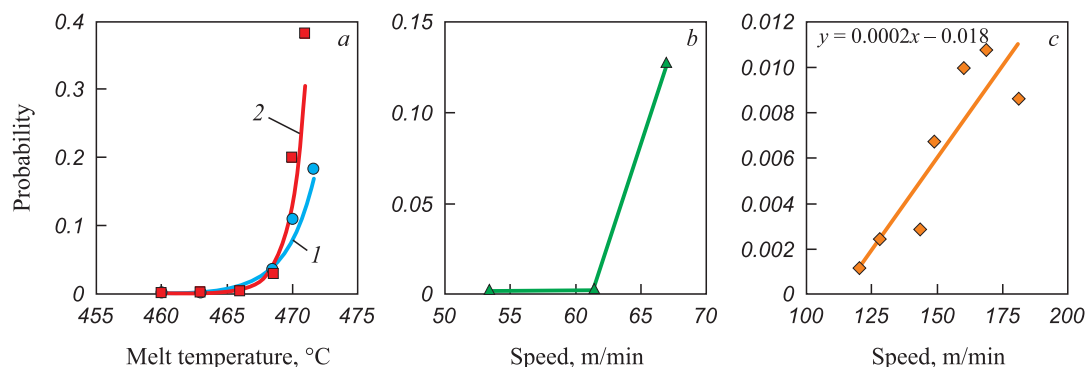
Defect	Impact		Circumstances in which the defect occurred
	strong	weak	
D1	F1, F2, F20	F3, F9, F18	On the strips of small height ( $h_{\text{met}}$ ) at low speed ( $v$ ). Large $v$ differences, especially when strips are thin. Low tension, thin strips. High dew point in the closed-circuit cooling section. Increased strip temperature after closed-circuit cooling at low $v$ , on the strips with $h_{\text{met}} < 1$ mm.
D2	F1, F3, F13, F21	None	High $v$ , thick strips. High melt temperature in the zinc bath when thin strips are processed at high $v$ or thick strips are processed at any $v$ . Very thick coating.
D3	F1, F2, F3, F20	F17	Thick strips, low $v$ . Thin strips, low $v$ and reduced tension. Considerable $v$ variations, except for high $v$ . Elevated dew point in the indirect heating furnace.
D4	F1, F2, F17	F8	Low $v$ . High dew point in the indirect heating furnace at low speed. Increased $v$ variations, high $v$ . Increased strip temperature after indirect heating
D5	F3, F14–15, F21	F11	High ( $> 2$ mm) or low ( $< 0.5$ mm) $h_{\text{met}}$ . Thick coating at high $h_{\text{met}}$ . Thin coating at high $h_{\text{met}}$ with strongly reduced pressure on the knives. The probability of a defect increases with growing strip width at high $h_{\text{met}}$ .
D6	None	F10	Increased (490 – 500 °C) strip temperature after closed-circuit cooling.
D7	F1, F3, F6, F10, F14–15, F21	None	At $h_{\text{met}}$ from 0.6 mm. More often at $h_{\text{met}} = 2$ mm. At $h_{\text{met}}$ up to 1 mm and high $v$ . At large $h_{\text{met}}$ no $v$ impact is observed. At $h_{\text{met}} > 1.8$ mm and elevated strip temperatures after direct heating and closed-circuit cooling section. Thick coating or low pressure on the air knives, the strips with $h_{\text{met}}$ up to 1 mm and $h_{\text{met}} > 2.5$ mm.
D8	Stratification is impossible due to small amount of data.		
D9	F1, F3	F14–15	More often at $h_{\text{met}} < 1.5$ mm. At $h_{\text{met}} < 1.2$ mm and high $v$ . At $h_{\text{met}} > 2.4$ mm and low knife pressure. When the tension at the inlet of the skin-pass rolling section is reduced.
D10	F3	F20	At $h_{\text{met}}$ from 1 to 2 mm and increased tension.
D11	F3	None	Often on the strips with $h_{\text{met}} < 1.5$ mm.
D12	None	F3	Very seldom on the strips with $h_{\text{met}} < 1$ mm.
D13	F1, F14–15, F21	None	When the coating is thick, regardless of $h_{\text{met}}$ . When the coating is thin, increasing $v$ reduces probability of a defect. When the coating is thin, reducing pressure on the knives increases probability of a defect.
D14	F3, F14–15, F21	F17	Typically at $h_{\text{met}} < 0.6$ mm with reduced knife pressure and thin coating. At $h_{\text{met}} > 1.2$ mm, an ambiguous effect of dew point in the closed-circuit cooling section was observed.
D15	F3, F7	None	Occurs at different $h_{\text{met}}$ . If $h_{\text{met}} > 2$ mm, the probability of a defect is 3 – 4 times higher. At $h_{\text{met}}$ 1.8 – 2.2 mm and reduced strip temperature after the indirect heating furnace.
D18	F3, F20	None	The probability grows with increasing $h_{\text{met}}$ ( $P = 0.0011 \exp(1.7856 h_{\text{met}})$ ) or with decreasing tension. Defects are rare at $h_{\text{met}} < 1$ mm.
D19	F3, F18, F22	F5	At $h_{\text{met}} < 1$ mm; very low dew point values in the closed-circuit cooling section; 1 % elongation during rolling; reduced strip temperature after the direct heating furnace. More often at $h_{\text{met}} \approx 0.3$ mm.
D20	F3, F21	None	Occurs at different $h_{\text{met}}$ . More frequent on the thin strips ( $P = -0.015 \ln(h_{\text{met}}) + 0.0196$ ). Up to $h_{\text{met}} = 0.9$ mm, the coating thickness does not affect the likelihood of defects. As $h_{\text{met}}$ grows, increasing coating thickness enhances the likelihood of defects.
D21	F1, F3	None	Mostly at $h_{\text{met}} < 1$ mm. The probability dramatically decreases at high $v$ .

as temperatures increase, recommending that strip temperatures should not surpass 470 °C. Given that aluminum content in the melt up to 0.3 % significantly influences the duration until Fe–Zn phases develop in a non-linear manner, the depletion of aluminum content in the bath, coupled with elevated temperatures of both the strip and the melt, may lead to the emergence of defects.

**D3, D4 – Damage marks, Dents.** Defects in rolled products are commonly the result of mechanical damage.

The findings imply that such damage can happen directly on the CHGU line, especially when there are abrupt changes in speed (Fig. 5, 6). The observation of a high dew point in products exhibiting dents leads to the suggestion that these defects may be due to contamination. Specifically, as mentioned in [8], dross particles in the bath can lead to the formation of dents on the rolled products.

**D5 – Rough edges.** Typical edge irregularities such as scab, corrugation, and ripple effect are linked to the char-



**Fig. 4.** Dependence of probability of obtaining an uneven coating (D2) on:

a – the temperature of the melt in the zinc bath ( $l - h_{\text{met}} = 0.5 - 0.6$  mm at a speed of 160 m/min; 2 –  $h_{\text{met}} \approx 2$  mm at a speed of 60 m/min);  
b – speed at  $h_{\text{met}} \approx 2$  mm; c – speed at  $h_{\text{met}} \approx 0.5$  mm

**Рис. 4.** Зависимость вероятности получения неравномерного покрытия (D2) от:

a – температуры расплава в цинковой ванне ( $l - h_{\text{мет}} = 0,5 - 0,6$  мм при скорости 160 м/мин; 2 –  $h_{\text{мет}} \approx 2$  мм при скорости 60 м/мин);  
b – скорости при  $h_{\text{мет}} \approx 2$  мм; c – скорости при  $h_{\text{мет}} \approx 0,5$  мм

acteristics of the original strip. The connection between these irregularities and factors like coating thickness and air knife pressure remains ambiguous.

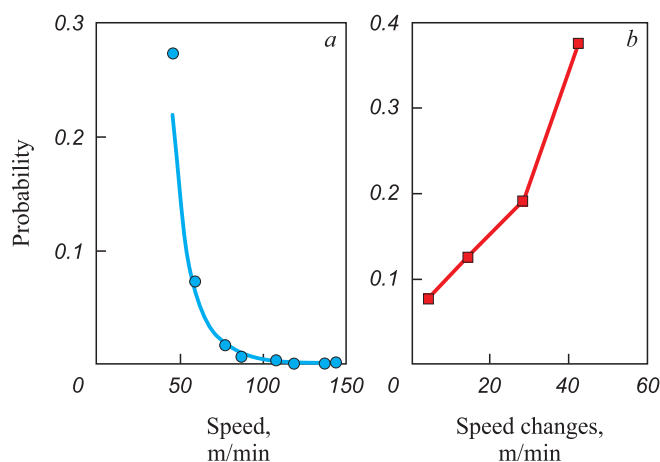
**D6 – Coating thickness defects.** It is postulated that as the strip temperature at the bath inlet increases, the absorption of aluminum from the bath also rises. This, as [24] suggests, can make the melt more viscous under similar conditions, potentially leading to inconsistencies in coating thickness, as [9] indicates.

**D7 – Macroinclusions.** According to [8], these defects may result from the strip capturing dross particles alongside the oxide film on the surface of the zinc bath, with a thicker coating more likely to retain larger dross particles (Fig. 7, b). It is theorized, based on [36], that lower air knife pressure has a diminished impact on the bath's melt near the strip's exit, where the oxide

film forms and gets entrapped. An increase in strip temperature at the bath inlet could facilitate the melt's contamination with zinc oxides. A thicker strip and strip speeds surpassing 125 m/min are believed to heighten the risk of this defect (Fig. 7, a, c). This phenomenon could be attributed to the dynamics of the melt and a greater influx of dross particles into the region where they are trapped.

#### D8 – Non-conforming mechanical properties.

The temperature distribution of the strip at the outlets of direct and indirect heating furnaces shows variations between defective and non-defective products. However, the limited amount of data complicates the verification of this difference through stratification. Given that this type of defect is not visible to the eye, adherence to the steel heat treatment protocol is imperative.

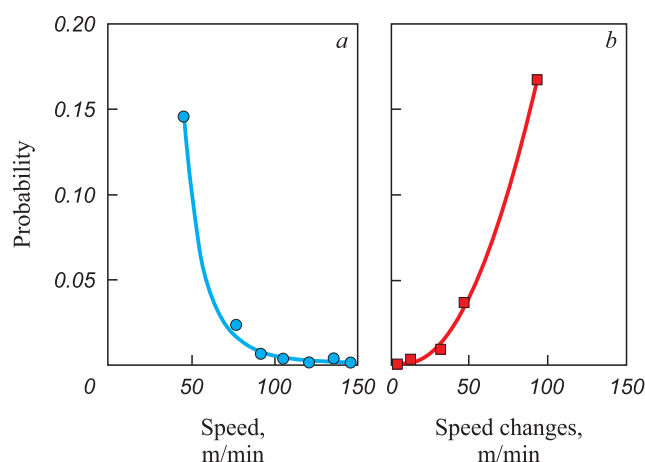


**Fig. 5.** Dependences of tail marks probability (D3) on:

a – speed at  $h_{\text{met}} \approx 0.8$  mm;  
b – speed changes at  $h_{\text{met}} \approx 0.8$  mm and a speed of 50 m/min

**Рис. 5.** Зависимости вероятности надавов (D3) от:

a – скорости при  $h_{\text{мет}} \approx 0,8$  мм;  
b – изменения скорости при  $h_{\text{мет}} \approx 0,8$  мм и скорости 50 м/мин



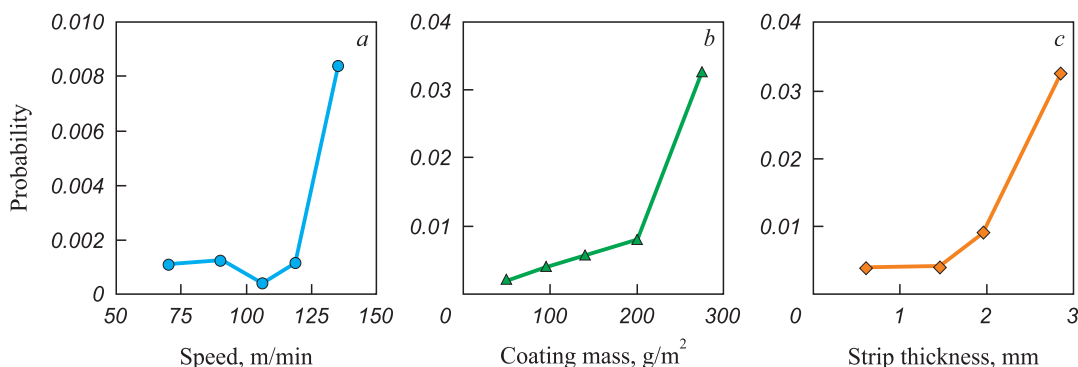
**Fig. 6.** Dependences of probability of imprints (D4) on:

a – speed at  $h_{\text{met}} = 0.8; 0.9$  mm;  
b – speed changes at  $h_{\text{met}} \approx 0.8$  mm and a speed of 110 m/min

**Рис. 6.** Зависимости вероятности отпечатков (D4) от:

a – скорости при  $h_{\text{мет}} = 0,8; 0,9$  мм;  
b – изменения скорости при  $h_{\text{мет}} \approx 0,8$  мм и скорости 110 м/мин





**Fig. 7.** Dependence of probability of macroinclusions (D7) on:  
*a* – strip speed at  $h_{\text{met}} \approx 0.9$  mm; *b* – coating mass at  $h_{\text{met}} = 2.5; 2.8$  mm and a speed of 45 m/min;  
*c* –  $h_{\text{met}}$  at a coating mass of 275 g/m² and a speed of 50 – 80 m/min

**Рис. 7.** Зависимость вероятности появления макровключений (D7) от:  
*a* – скорости движения полосы при  $h_{\text{мет}} \approx 0,9$  мм; *b* – массы покрытия при  $h_{\text{мет}} = 2,5; 2,8$  мм и скорости 45 м/мин;  
*c* –  $h_{\text{мет}}$  при массе покрытия 275 г/м² и скорости 50 – 80 м/мин

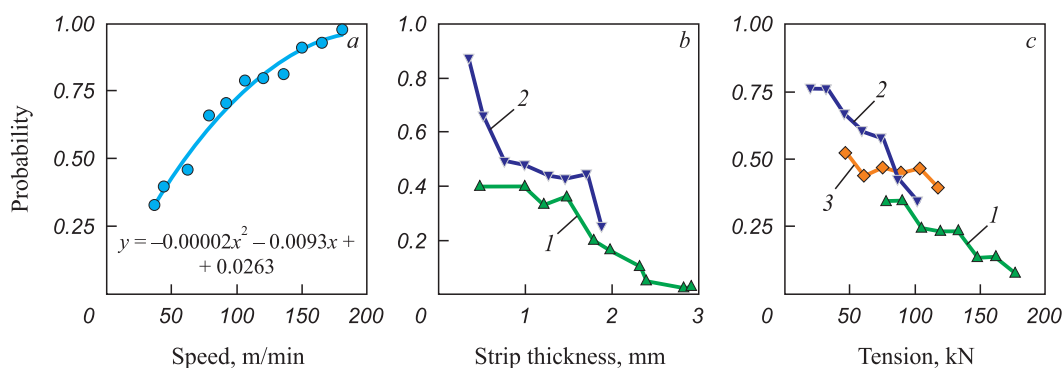
**D9 – Zinc bright edges.** Fig. 8, *a* illustrates the likelihood of defect occurrence in relation to strip speed for strips approximately 0.5 mm thick, indicating a decrease in defect probability with a reduction in speed. It has been determined that the occurrence of defects is dependent on strip thickness (Fig. 8, *b*) only at speeds below 90 m/min, while at higher speeds, the chance of defects occurring remains relatively unchanged. Low air knife pressure (indicative of low melt viscosity) influences defect formation predominantly at lower speeds for thicker strips, particularly at the initial stages of defect development. Increasing the tension at the inlet of the skin-pass section (Fig. 8, *c*) lowers the probability of defects, suggesting that vibration might contribute to the formation of bright edges.

**D10 – Rough coating.** The defect impacts the protective qualities, wear resistance, and visual appeal of the

galvanized strip, typically originating from the properties of the initial strip. The roughness of the base strip appears to correlate with its thickness. However, the reasons behind tension differences between defective and non-defective products remain ambiguous.

**D11, D12 – Abrasions and roller marks.** Abrasions are solely associated with thickness, aligning with findings from [10] that attribute the original strip's properties as the root cause of this defect. The occurrence of abrasions consistently diminishes as the thickness increases (Fig. 9). The probability of encountering roller marks ranges between 0.25 and 0.30 for most thicknesses, but the defect is virtually absent in strips thinner than 1 mm, with the underlying causes yet to be elucidated.

**D13 – Wavelike coating.** The likelihood of defects escalates with an increase in coating thickness, irrespective of the strip's thickness (Fig. 10, *a*). This observa-



**Fig. 8.** Dependence of probability of bright edges (D9) on:  
*a* – strip speed at  $h_{\text{met}} \approx 0.5$  mm; *b* –  $h_{\text{met}}$  at speed: 1 – 45 m/min; 2 – 75 m/min;  
*c* – tension at the inlet of the skin pass section (1 – thickness 1.8 – 2.0 mm, speed 60 m/min;  
 2, 3 – thickness 0.8 – 1.5 mm, speeds 100 – 130 m/min and 75 – 80 m/min)

**Рис. 8.** Зависимость вероятности появления напылов (D9) от:  
*a* – скорости движения полосы при  $h_{\text{мет}} \approx 0,5$  мм; *b* –  $h_{\text{м}}$  при скорости: 1 – 45 м/мин; 2 – 75 м/мин;  
*c* – натяжения на входе секции дрессировки (1 – толщина 1,8 – 2,0 мм, скорость 60 м/мин;  
 2, 3 – толщина 0,8 – 1,5 мм, скорость соответственно 100 – 130 и 75 – 80 м/мин)

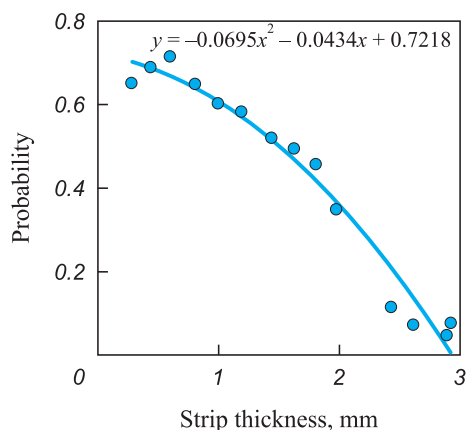


Fig. 9. Dependence of probability of abrasions (D11) on  $h_{\text{met}}$

Рис. 9. Зависимость вероятности появления потертостей (D11) от  $h_{\text{мет}}$

tion aligns with findings from [35]. Conversely, a higher speed diminishes the probability of defects, but only for thinner coatings (up to 140 g/m<sup>2</sup>), where defects emerge under reduced air knife pressure (Fig. 10, b). Thus, low melt viscosity with thin coatings may lead to a wavelike pattern on the coating.

**D14 – Marks related to skin-pass rolling.** It is suggested by [8] that such marks result from the coating adhering to the rollers. The defect manifests when the coating mass is above 80 g/m<sup>2</sup> (Fig. 11, a). At the coating mass of 80 – 140 g/m<sup>2</sup>, defects appear under diminished knife pressure (Fig. 11, b), with the wavelike coating potentially leading to sticking.

**D15 – Dark streaks.** According to [10], presence of oxides at the interface between the coating and steel is a contributing factor to the defect, although the connection between oxide formation, strip thickness, and temperature remains uncertain.

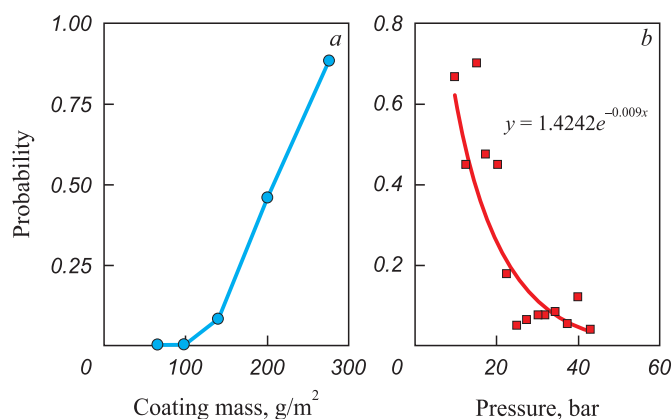


Fig. 10. Dependence of probability of D13 defect on: a – coating thickness; b – knives pressure at coating mass of 100 – 140 g/m<sup>2</sup>, a speed of 45 m/min and  $h_{\text{met}} \approx 2.5$  mm

Рис. 10. Зависимость вероятности дефекта D13 от: а – толщины покрытия; б – давления на ножах при массе покрытия 100 – 140 г/м<sup>2</sup>, скорости 45 м/мин и  $h_{\text{мет}} \approx 2,5$  мм

**D18 – Scratches.** Scratches are attributed to three potential sources:

- scratches on the original strip;
- the strip sagging educing friction with rollers, commonly in the zinc bath;
- dross sticking to the roller in the zinc bath.

It was discovered that the risk of scratches significantly increases when the strip thickness is over 2 mm. In analyzing this defect, the tension of the strip in various sections was considered as factor F20. For strips thicker than 2 mm, the defect probability diminishes as tension at the skin pass section's inlet increases (Fig. 12).

**D19 – Orange peel.** The occurrence of the defect is notably prevalent on thin strips that experience a significant reduction in dew point within the closed-circuit cooling section. This observation aligns with findings from [8], which link the formation of pimples to zinc evaporation prompted by a low dew point at the snout. The defect is most likely to manifest at approximately 1 % elongation (Fig. 13), corroborating the insights provided in [38].

**D20 – Cracks.** Such defects could originate from cracks in the original strip or internal stresses within the steel that annealing failed to resolve. Given the lack of correlation with annealing parameters, it's plausible to associate these defects with pre-existing cracks in the strip, a hypothesis supported by the marked variability in defect probability across different strip thicknesses and the observation that the issue is more pronounced with thicker coatings.

**D21 – Blisters.** Blisters may be linked to hydrogen absorbed during the etching process and released during galvanizing. Alternatively, they could result from dross particles becoming entrapped when the bath's bottom

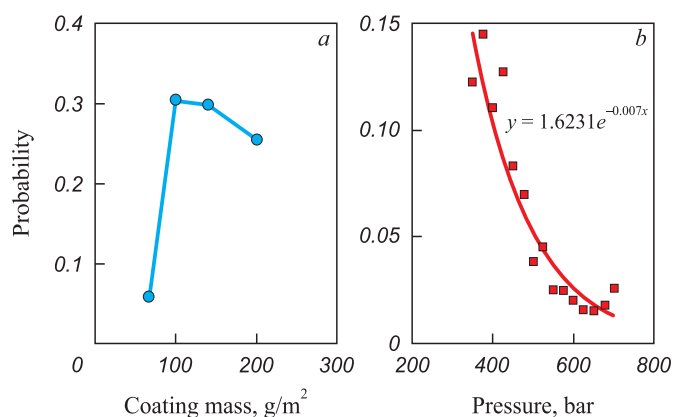
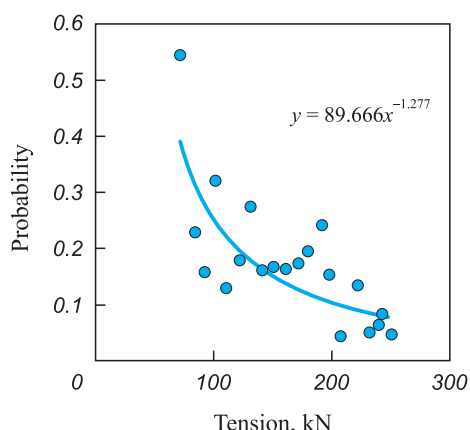


Fig. 11. Dependence of probability of D14 defect on: a – coating thickness at  $h_{\text{met}} \approx 0.45$  mm, speed of 150 m/min; b – knives pressure at coating mass of 100 g/m<sup>2</sup>, a speed of 125 m/min and  $h_{\text{met}} \approx 0.6$  mm

Рис. 11. Зависимость вероятности дефекта D14 от: а – массы покрытия при  $h_{\text{мет}} \approx 0,45$  мм, скорости 150 м/мин; б – давления на ножах при массе покрытия 100 г/м<sup>2</sup>, скорости 125 м/мин и  $h_{\text{мет}} \approx 0,6$  мм



**Fig. 12.** Dependence of probability of D18 defect on tension before tempering at  $h_{\text{met}} = 2.5; 3.0$  mm

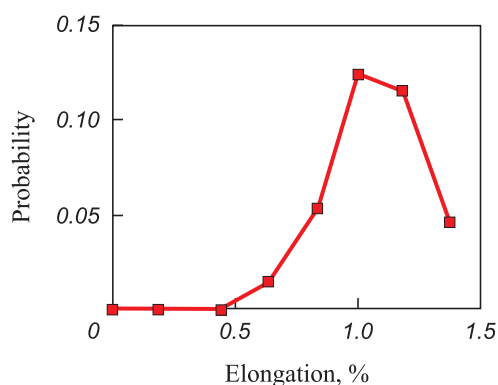
**Рис. 12.** Зависимость вероятности дефекта D18 от натяжения перед дроссировкой при  $h_{\text{мет}} = 2,5; 3,0$  мм

dross layer is disturbed. The absence of a relationship with coating thickness suggests the latter explanation might be more accurate. The dependencies on strip thickness (Fig. 14, *a*) and line speed (Fig. 14, *b*) could reflect the dynamics of strip movement within the zinc bath.

#### TYPES OF DEFECTS THAT LIMIT PERFORMANCE

The potential for enhancing the CHGU performance is primarily linked to increasing the processing speed of common-grade steel strips. Fig. 2 demonstrates that only the thinnest strips, with thicknesses up to 0.4 mm, are currently processed at the unit's maximum speed. However, these constitute just 4 % of the DX51D steel strip rolls. In contrast, approximately 60 % of the rolls have a strip thickness over 1 mm, indicating a significant opportunity to boost processing speeds for these thicker strips.

Considering this, it's possible to pinpoint defects that become more prevalent with increased speeds and could



**Fig. 13.** Dependence of probability of D19 defect on extension during rolling at  $h_{\text{met}} \approx 0.4$  mm and a speed of 160 m/min

**Рис. 13.** Зависимость вероятности D19 от удлинения при прокатке при  $h_{\text{мет}} \approx 0,4$  мм и скорости 160 м/мин

constrain performance even when heat treatment standards are adhered to:

- D2 – Uneven coating;
- D7 – Macroinclusions;
- D9 – Zinc bright edges.

The presence of an uneven coating restricts the ability to raise processing speeds. Findings suggest that the likelihood of this defect could be diminished by more accurately controlling the melt temperature in the zinc bath, achieved by reducing the temperature disparity between the strip after closed-circuit cooling and the melt.

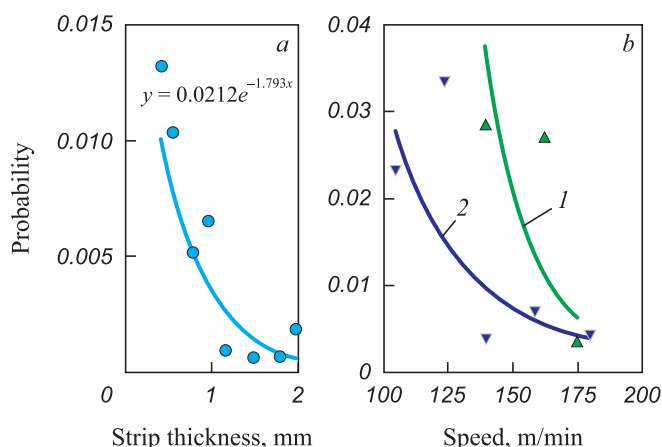
Macroinclusions represent another frequent defect, with their occurrence spiking notably as strip speeds surpass 125 m/min. The current operational parameters allow for processing strips thinner than 1 mm at such speeds, leaving uncertain the impact of increased speeds on thicker strips in terms of defect prevalence.

At exceedingly high speeds, the emergence of zinc bright edges on processed strips becomes inevitable, although this limitation might be less significant since bright edges are often deemed an acceptable defect. Optimizing the design of air knives could potentially address this issue.

Moreover, a rise in the speed may also increase the chances of encountering defects not extensively studied due to their rarity or limited data available. As noted in [6], an escalation in strip speed may induce corrugation in the strip.

Experimenting with different strip speeds to optimize current performance can lead to substantial and frequent single speed adjustments. However, such changes in speed significantly influence the likelihood of several defects:

- D1 – Uncoated spots;



**Fig. 14.** Dependence of probability of D21 effect on: *a* –  $h_{\text{met}}$ ; *b* – speed (at  $h_{\text{met}}$ : 1 – 0.4 mm; 2 – 0.5 mm)

**Рис. 14.** Зависимость вероятности D21 от: *a* –  $h_{\text{мет}}$ ; *b* – скорости при  $h_{\text{мет}}$  (1 – 0,4 мм; 2 – 0,5 мм)

- D3 – Damage marks;
- D4 – Dents.

The analysis identified similar patterns in how speed and its fluctuations affect the emergence of these three defects, suggesting they may share a common cause related to tension control amid changes in strip speed. Dents exhibit the least sensitivity to speed variations, with a high probability of occurrence only when speed alterations exceed 50 m/min. The chance of all three types of defects occurring diminishes to a minimal level as the speed increases.

## CONCLUSIONS

The findings indicate that enhancing the control over the temperature and chemical composition of the melt in the zinc bath, along with the temperature of the strip following the closed-circuit cooling section, is essential for increasing strip speed and, thereby, overall performance. Given that defects arising from frequent changes in strip speed are deemed unacceptable, there is a clear need to scrutinize and potentially refine the strip tension control systems across various sections of the unit.

## REFERENCES / СПИСОК ЛИТЕРАТУРЫ

1. Subbotina Yu.M., Radionova L.V. Technological features of continuous lines for hot-dip galvanizing of a steel strip. *Bulletin of the South Ural State University. Ser. Metallurgy*. 2016;16(1):112–119. (In Russ.).  
<https://doi.org/10.14529/met160116>  
Субботина Ю.М., Радионова Л.В. Технологические особенности агрегатов непрерывного горячего цинкования стальной полосы. *Вестник ЮУрГУ. Серия «Металлургия»*. 2016;16(1):112–119.  
<https://doi.org/10.14529/met160116>
2. Nikiforov B.A., Salganik V.M., Denisov S.V., Stekanov P.A. Commercial production of high-strength rolled products at MMK JSC for the automotive industry. *Vestnik of Novosibirsk State Technical University*. 2006;4(16):41–45. (In Russ.).  
Никифоров Б.А., Салганик В.М., Денисов С.В., Стеканов П.А. Освоение производства высокопрочного проката для автомобилестроения в ОАО «ММК». *Вестник Магнитогорского государственного технического университета им. Г.И. Носова*. 2006;4(16):41–45.
3. Ryabchikov M.Yu., Ryabchikova E.S., Kokorin I.D. System of temperature stabilization in a heating furnace based on sliding mode control and fuzzy logic. *Mekhatronika, Avtomatizatsiya, Upravlenie*. 2020;21(3):143–157. (In Russ.).  
<https://doi.org/10.17587/mau.21.143-157>  
Рябчиков М.Ю., Рябчикова Е.С., Кокорин И.Д. Система стабилизации температуры в нагревательной печи с применением скользящего регулирования и нечеткой логики. *Мехатроника, автоматизация, управление*. 2020;21(3):143–157. <https://doi.org/10.17587/mau.21.143-157>
4. Антоненко О. Как мы узнали, что одна из бригад оцинковщиков работала быстрее других и что было дальше. URL: <https://habr.com/ru/company/nlmk/blog/589267/> (accessed: 30.04.2023).
5. Sahay S.S., Kapur P.C. Model based scheduling of a continuous annealing furnace. *Ironmaking and Steelmaking*. 2007;34(3):262–268.  
<https://doi.org/10.1179/174328107X165708>
6. Yahiro K., Shigemori H., Hirohata K. Development of strip temperature control system for a continuous annealing line. *Proceedings of IECON '93 – 19th Annual Conf. of IEEE Industrial Electronics*. 2002:481–486.  
<https://doi.org/10.1109/IECON.1993.339029>
7. Mezin I.Yu., Zotov S.V., Kramzina L.V. Analysis and increase of quality of zinc coating on wire for automobiles. *Kachestvo v obrabotke materialov*. 2017;(1(7)):14–18. (In Russ.).  
Мезин И.Ю., Зотов С.В., Крамзина Л.В. Анализ и повышение качества нанесения цинкового покрытия на проволоку для автомобилей. *Качество в обработке материалов*. 2017;(1(7)):14–18.
8. Saravanan P., Srikanth S. Surface defects and their control in hot dip galvanized and galvanized sheets. *International Journal of Advanced Research in Chemical Science (IJARCS)*. 2018;5(11):11–23.
9. Radionova L.V., Subbotina Yu.M. Advantages and shortcomings of hot dip galvanizing steel sheet. *Galvanizing problems. Russian Internet Journal of Industrial Engineering*. 2013;(2):3–9. (In Russ.).  
Радионова Л.В., Субботина Ю.М. Преимущества и недостатки способа горячего оцинкования стальной полосы. *Проблемы цинкования. Машиностроение: сетевой электронный журнал*. 2013;(2):3–9.
10. Hong M.-H., Saka H. FIB and TEM observations of defects in hot-dip zinc coatings. *Journal of Electron Microscopy*. 2004;53(5):545–552. <https://doi.org/10.1093/jmicro/dfh053>
11. Berezhnaya G.A., Zarutskaya A.O., Karimova D.Yu. Quality analysis of hot-dip galvanized strip produced at plate rolling mill no 11 at MMK OJSC. *Kachestvo v obrabotke materialov*. 2016;(2(6)):39–42. (In Russ.).  
Бережная Г.А., Зарутская А.О., Каримова Д.Ю. Анализ качества горячеоцинкованной полосы в ЛПЦ-11 ОАО «ММК». *Качество в обработке материалов*. 2016;(2(6)):39–42.
12. İlhami Pektaş. Galvaniz hataları ve çözüm önerileri. *Ankara*; 2020:76. (In Turk.).
13. Rodionova I.G., Uglov V.A., Zaitsev A.I., Protasov A.V., Mishnev P.A., Adigamov R.R., Pavlov S.I., Las'kov S.A., Nikolaev O.A., Kiryushin A.A., Tikhonov A.K., Ryabchikov V.G. A new generation of economical automotive steel. *Steel in Translation*. 2016;46(1):65–73.  
<https://doi.org/10.3103/S0967091216010125>  
Родионова И.Г., Углов В.А., Зайцев А.И., Протасов А.В., Мишнев П.А., Адигамов Р.Р., Павлов С.И., Ласьков С.А., Николаев О.А., Кирюшин А.А., Тихонов А.К., Рябчиков В.Г. Разработка и освоение высококачественных экономичных автолистовых сталей нового поколения. *Сталь*. 2016;(1):46–54.
14. Zaitsev A.I., Koldaev A.V., Rodionova I.G., Stepanov A.B. A modern approach to improving the complex properties of automotive sheet and other types of steels. In: *Scientific and Technological Progress in Ferrous Metallurgy – 2019. Materials of the IV Int. Sci. Conf.* 2019:66–72. (In Russ.).



- Зайцев А.И., Колдаев А.В., Родионова И.Г., Степанов А.Б. Современный подход к повышению комплекса свойств автолистовых и других типов сталей. В сборнике: *Научно-технический прогресс в черной металлургии – 2019. Материалы IV Международной научной конференции*. 2019:66–72.
15. Tikhonov A.K., Rodionova I.G. Thermomechanical treatment in the recrystallizational annealing of automotive cold-rolled steel. *Steel in Translation*. 2022;52:451–459. <https://doi.org/10.3103/S0967091222040143>
16. Srikanth S., Sharma C.B., Bhattacharyya A., Amitava Ray. Metallurgical investigations into genesis of bare spots, exfoliation, and matte coating appearance in hot dip galvanized steel sheets. *JFAPBC*. 2005;(3):73–81. <https://doi.org/10.1361/15477020523509>
17. Liu H., Li F., Shi W., Swaminathan S., He Y., Rohwerder M., Li L. Challenges in hot-dip galvanizing of high strength dual phase steel: Surface selective oxidation and mechanical property degradation. *Surface & Coatings Technology*. 2012;206(16):3428–3436. <https://doi.org/10.1016/j.surfcoat.2012.02.001>
18. Luo H., Dunbar W.S., Moore J.E. Buckling analysis of a heated steel strip in a continuous annealing furnace. *Journal of Manufacturing Science and Engineering*. 1999;121(1):76–83. <https://doi.org/10.1115/1.2830578>
19. Wu H., Speets R., Ozcan G., Ekhardt R., Heijke R., Nederlof C., Boeder C.J. Non-linear model predictive control to improve transient production of a hot dip galvanising line. *Ironmaking & Steelmaking*. 2016;43(7):541–549. <https://doi.org/10.1080/03019233.2015.1126687>
20. Ryabchikov M.Yu. Selection of steel strip annealing energy-saving conditions in view of the substandard products share. *Journal of Chemical Technology and Metallurgy*. 2020;55(1):182–191.
21. Ryabchikov M.Yu., Ryabchikova E.S., Novak V.S. Hybrid model for metal temperature control during hot dip galvanizing of steel strip. *Mekhatronika, Avtomatizatsiya, Upravlenie*. 2023;24(8):421–432. (In Russ.). <https://doi.org/10.17587/mau.24.421-432>  
Рябчиков М.Ю., Рябчикова Е.С., Новак В.С. Гибридная модель для предупреждающего управления температурой металла при горячем оцинковании стальной полосы. *Мехатроника, автоматизация, управление*. 2023;24(8):421–432. <https://doi.org/10.17587/mau.24.421-432>
22. Kleshcheva S.E., Kasatkina E.G. Analysis of the quality level of galvanized metal in the sheet-rolling shop No. 11 of the PJSC “ММК”. *Kachestvo v obrabotke materialov*. 2019;(1(11)):18–23. (In Russ.).  
Клещева С.Е., Касаткина Е.Г. Анализ уровня качества оцинкованного металлопроката в ЛПЦ-11 ПАО «ММК». *Качество в обработке материалов*. 2019;(1(11)):18–23.
23. Ryabchikov M.Yu., Ryabchikova E.S., Shmanev D.E., Kokorin I.D. Strip cooling control for flexible production of galvanized flat steel. *Izvestiya. Ferrous Metallurgy*. 2021;64(7):519–529. (In Russ.). <https://doi.org/10.17073/0368-0797-2021-7-519-529>  
Рябчиков М.Ю., Рябчикова Е.С., Шманев Д.Е., Кокорин И.Д. Управление охлаждением стальной полосы при гибком производстве оцинкованного листового проката. *Известия вузов. Черная металлургия*. 2021;64(7):519–529. <https://doi.org/10.17073/0368-0797-2021-7-519-529>
24. Sawaitul P.B., Chowriwar S.A., Lade I.P. Minimization of dross formation during the continuous galvanizing process in the steel industry. *International Journal of Emerging Technology and Advanced Engineering*. 2012;2(1):45–51.
25. Bondareva O.S., Mel'nikov A.A. Influence of the temperature of a zinc melt on the coating thickness and structure during high-temperature zincplating steels with a high silicon content. *Powder Metallurgy and Functional Coatings*. 2015;(1):66–70. (In Russ.). <https://doi.org/10.17073/1997-308X-2015-1-66-70>  
Бондарева О.С., Мельников А.А. Влияние температуры цинкового расплава на толщину и структуру покрытия при высокотемпературном горячем цинковании сталей с высоким содержанием кремния. *Известия вузов. Порошковая металлургия и функциональные покрытия*. 2015;(1):66–70. <https://doi.org/10.17073/1997-308X-2015-1-66-70>
26. Yoon H.G., Ahn G.J., Chung M.K., Kim J.K. Aerodynamic investigation of air knife system to find out the mechanism of the check mark in a continuous hot-dip galvanizing process. *Proceedings of IMECE2008 2008 ASME Int. Mechanical Engineering Congress and Exposition*. 2008:1–7. <https://doi.org/10.1115/IMECE2008-68056>
27. Hongyun S., Gi Y.H., Kyoon C.M. CFD analysis of sag line formation on the zinc-coated steel strip after the gas-jet wiping in the continuous hot-dip galvanizing process. *ISIJ International*. 2011;51(1):115–123. <https://doi.org/10.2355/isijinternational.51.115>
28. Gi Y.H., Kyoon C.M. Development of novel air-knife system to prevent check-mark stain on galvanized strip surface. *ISIJ International*. 2010;50(5):752–759. <https://doi.org/10.2355/isijinternational.50.752>
29. Bao C., Kang Y., Li Y. Numerical analysis of edge over coating and baffle effect on hot-dip galvanizing. *Surface Review and Letters*. 2017;24(1):1750010. <https://doi.org/10.1142/S0218625X1750010X>
30. Mao K., Yang Y.-L., Huang Z., Yang D.-y. Coating thickness modeling and prediction for hot-dip galvanized steel strip based on GA-BP neural network. *2020 Chinese Control and Decision Conf. (CCDC 2020)*. 2020;3484–3489. <https://doi.org/10.1109/CCDC49329.2020.9164854>
31. Zhang Y., Cui Q.-p., Shao F.-q., Wang J.-s., Zhao H.-y. Influence of air-knife wiping on coating thickness in hot-dip galvanizing. *Journal of Iron and Steel Research International*. 2012;19(6):70–78. [https://doi.org/10.1016/S1006-706X\(12\)60130-7](https://doi.org/10.1016/S1006-706X(12)60130-7)
32. Xu P., Wang B., Ye J., Zhang H., Huang Z., Xu X. Research on the vibration of sheet metal near the zinc pot area in continuous hot-dip galvanizing line. *Applied Mechanics and Materials*. 2012;141:471–477. <https://doi.org/10.4028/www.scientific.net/AMM.141.471>
33. Li J., Yan Y.-H., Guo X.-H., Wang Y.-Q. Research on vibration control method of steel strip for a continuous hot-dip galvanizing line. *ISIJ International*. 2012;52(6):1072–1079. <https://doi.org/10.2355/isijinternational.52.1072>
34. Dombrowski S., Pereira A. Electromagnetic strip stabilization: EMG-EMASS® – technology, results, customer experiences, and future development. *50° Seminário de Laminação*. 2013:252–260.
35. Rajiv E.P., Jain N.C., Mahakalkar Nilesh, Pawar B.D. Defects in continuous hot dip galvanized steel sheet and their reme-

- dies. URL: <http://samoseyindia.in/web-english/galvn1.html> (accessed: 30.04.2023)
36. Yuan S., Zhou X., Huang Y., Yang P. Influence of air knives on liquid zinc flow in galvanising bath. *Ironmaking & Steelmaking*. 2016;43(2):83–87.  
<https://doi.org/10.1179/1743281215Y.0000000051>
  37. Belov V.K., Krivko O.V., Gubarev E.V., Demchuk F.A., Pogonin E.Yu., Samorodova E.G. Identification of causes of coating dusting during stamping of parts from hot-dip galvanized sheet. *Aktual'nye problemy sovremennoi nauki, tekhniki i obrazovaniya*. 2021;12(1):99–103. (In Russ.).  
Белов В.К., Кривко О.В., Губарев Е.В., Демчук Ф.А., Погонин Е.Ю., Самородова Э.Г. Выявление причин пыления покрытия при штамповке деталей из горячеоцинкованного листа. *Актуальные проблемы современной науки, техники и образования*. 2021;12(1):99–103.
  38. Wang L., Tang D., Liu X., Zhang Y., Zhou S. Analysis of orange peel defects on hot-dip galvanized high strength low alloy steel. *Advanced Materials Research*. 2014;1004–1005: 221–226.  
<https://doi.org/10.4028/www.scientific.net/AMR.1004-1005.221>
  39. Martínez-de-Pisón F.J., Sanz A., Martínez-de-Pisón E., Jiménez E., Conti D. Mining association rules from time series to explain failures in a hot-dip galvanizing steel line. *Computers & Industrial Engineering*. 2012;63(1):22–36.  
<https://doi.org/10.1016/j.cie.2012.01.013>
  40. Colla V., Matarese N., Cervigni F. Quality improvement in hot dip galvanizing line through hybrid case-based reasoning system. *UKSim 15<sup>th</sup> Int. Conf. on Computer Modelling and Simulation*. 2013:161–166.  
<https://doi.org/10.1109/UKSim.2013.24>
  41. Yang H., Zhang S., Li J., Liu X., Wang H. Effect of strip entry temperature on the formation of interfacial layer during hot-dip galvanizing of press-hardened steel. *Surface & Coatings Technology*. 2014;240:269–274.  
<http://dx.doi.org/10.1016/j.surfcoat.2013.12.040>

## Information about the Authors

## Сведения об авторах

**Mikhail Yu. Ryabchikov**, Cand. Sci. (Eng.), Assist. Prof. of the Chair of Automated Control Systems, Nosov Magnitogorsk State Technical University

ORCID: 0000-0001-5337-0951

E-mail: [mr\\_mgn@mail.ru](mailto:mr_mgn@mail.ru)

**Elena S. Ryabchikova**, Cand. Sci. (Eng.), Assist. Prof. of the Chair of Automated Control Systems, Nosov Magnitogorsk State Technical University

ORCID: 0000-0001-6441-1157

E-mail: [mika.elena@mail.ru](mailto:mika.elena@mail.ru)

**Vladimir S. Novak**, Bachelor of the Chair of Automated Control Systems, Nosov Magnitogorsk State Technical University

E-mail: [Vladimir.novak.02@mail.ru](mailto:Vladimir.novak.02@mail.ru)

**Aleksandr E. Klimenko**, Master Student of the Chair of Automated Control Systems, Nosov Magnitogorsk State Technical University

E-mail: [klimenko\\_alexandr@mail.ru](mailto:klimenko_alexandr@mail.ru)

**Михаил Юрьевич Рябчиков**, к.т.н., доцент кафедры автоматизированных систем управления, Магнитогорский государственный технический университет им. Г.И. Носова

ORCID: 0000-0001-5337-0951

E-mail: [mr\\_mgn@mail.ru](mailto:mr_mgn@mail.ru)

**Елена Сергеевна Рябчикова**, к.т.н., доцент кафедры автоматизированных систем управления, Магнитогорский государственный технический университет им. Г.И. Носова

ORCID: 0000-0001-6441-1157

E-mail: [mika.elena@mail.ru](mailto:mika.elena@mail.ru)

**Владимир Сергеевич Новак**, бакалавр кафедры автоматизированных систем управления, Магнитогорский государственный технический университет им. Г.И. Носова

E-mail: [Vladimir.novak.02@mail.ru](mailto:Vladimir.novak.02@mail.ru)

**Александр Евгеньевич Клименко**, магистр кафедры автоматизированных систем управления, Магнитогорский государственный технический университет им. Г.И. Носова

E-mail: [klimenko\\_alexandr@mail.ru](mailto:klimenko_alexandr@mail.ru)

## Contribution of the Authors

## Вклад авторов

**M. Yu. Ryabchikov** – developing the method for assessing the factors influence on defects occurrence, comparing the research results with the known causes of defects, identifying the alleged causes of defects.

**E. S. Ryabchikova** – analytical review on research topics, determining the defects probability dependences on accepted factors.

**V. S. Novak** – processing of experimental data, database preparation, design of graphic materials and text.

**A. E. Klimenko** – search for scientific papers on the research subject.

**М. Ю. Рябчиков** – разработка способа оценки влияния факторов на возникновение дефектов, сопоставление результатов исследования с известными причинами возникновения дефектов, выявление предполагаемых причин возникновения дефектов.

**Е. С. Рябчикова** – проведение аналитического обзора по тематике исследований, определение зависимостей вероятности возникновения дефектов от принятых факторов.

**В. С. Новак** – обработка экспериментальных данных, подготовка базы данных, оформление графических материалов и статьи.

**А. Е. Клименко** – поиск научных работ по тематике исследования.

Received 05.05.2023

Revised 29.10.2023

Accepted 12.12.2023

Поступила в редакцию 05.05.2023

После доработки 29.10.2023

Принята к публикации 12.12.2023



UDC 601.77

DOI 10.17073/0368-0797-2024-1-106-111



Original article

Оригинальная статья

## INVESTIGATING EFFECTIVENESS OF CHANGING CALIBRATION OF INPUT CONE OF ROLLS AND LINES OF A PIERCING MILL WITH TAPERED ROLLS USING COMPUTER MODELING

O. A. Panasenko<sup>1</sup>, A. O. Khalezov<sup>2</sup>, D. Sh. Nukhov<sup>2</sup> <sup>1</sup> JSC “Severskii Tube Steelworks” (7 Vershinina Str., Polevskoi, Sverdlovsk Region 623388, Russian Federation)<sup>2</sup> Ural Federal University named after the first President of Russia B.N. Yeltsin (19 Mira Str., Yekaterinburg 620002, Russian Federation)

dnukhov@mail.ru

**Abstract.** Screw piercing of a workpiece is a process with complex cyclical nature of metal flow in deformation center. Setting up the deformation tool and its calibration, as well as the accuracy of the workpiece feed and release of the hollow billet from deformation zone, have a significant impact on the quality of the hollow billet: dimensional accuracy and presence of defects on its inner and outer surface. In the paper, a technical solution was proposed to increase the stability of piercing a continuously cast workpiece on screw rolling mills. Implementation of the idea involves the use of an improved calibration of the piercing mill tool. For both in order to achieve the workpiece alignment and its stable feeding along rolling axis of the piercing mill, it was proposed to add a special thickening (hump) on the roll input cone and to change calibration of its input section on the ruler in order to meet the workpiece with the rolls earlier: before the initial capture of the workpiece by the rolls, that is, before deformation of metal of the continuously cast workpiece by the rolls. To check and correct the proposed solution, the tasks of FEM-modeling of screw piercing process with a modified design of the tapered roll and ruler were set and solved using the QForm 3D software package. Results of the finite element modeling (FEM) showed that the use of improved tool calibration makes it possible to improve the alignment of the workpiece and ensure its stable position along the rolling axis of the piercing mill, thereby reducing the runout of the workpiece in the deformation center and thereby reducing the force on the rolls from 8 to 5 MN. The results of measurements of the hollow billets' geometric parameters obtained by FEM showed insignificant relative deviations that fit within the regulatory limits.

**Keywords:** screw piercing, size accuracy of hollow billet, process power parameters, computer modeling, solid-state model, piercing stability, FEM

**For citation:** Panasenko O.A., Khalezov A.O., Nukhov D.Sh. Investigating the effectiveness of changing calibration of input cone of rolls and lines of a piercing mill with tapered rolls using computer modeling. *Izvestiya. Ferrous Metallurgy*. 2024;67(1):106–111.

<https://doi.org/10.17073/0368-0797-2024-1-106-111>

## ИССЛЕДОВАНИЕ ЭФФЕКТИВНОСТИ ИЗМЕНЕНИЯ КАЛИБРОВКИ ВХОДНОГО КОНУСА ВАЛКОВ И ЛИНЕЕК ПРОШИВНОГО СТАНА С ГРИБОВИДНЫМИ ВАЛКАМИ С ПОМОЩЬЮ КОМПЬЮТЕРНОГО МОДЕЛИРОВАНИЯ

О. А. Панасенко<sup>1</sup>, А. О. Халезов<sup>2</sup>, Д. Ш. Нухов<sup>2</sup> <sup>1</sup> АО «Северский трубный завод» (Россия, 623388, Свердловская обл., Полевской, ул. Вершинина, 7)<sup>2</sup> Уральский федеральный университет имени первого Президента России Б.Н. Ельцина (Россия, 620002, Екатеринбург, ул. Мира, 19)

dnukhov@mail.ru

**Аннотация.** Процесс винтовой прошивки заготовки – это процесс со сложным циклическим характером течения металла в очаге деформации. Настройка инструмента деформации и его калибровка, а также точность подачи заготовки и выдачи гильзы из очага деформации оказывают существенное влияние на качество гильзы: точность размеров и наличие дефектов на внутренней и наружной поверхности гильзы. В работе предложено техническое решение повышения стабильности ведения процесса прошивки непрерывнолитой заготовки на станах винтовой прокатки. Реализация идеи предполагает применение усовершенствованной калибровки инструмента прошивного

стана. Для обеспечения центровки заготовки и стабильной ее подачи по оси прокатки прошивного стана предложено добавить на входном конусе вала специальное его утолщение (гребень), а на линейке изменить калибровку входного ее участка с целью более ранней встречи заготовки с валками – до первичного захвата валками заготовки, т. е. до начала деформации валками металла непрерывнолитой заготовки. Для проверки и корректировки предлагаемого решения были поставлены и решены задачи конечно-элементного моделирования процесса винтовой прошивки с измененной конструкцией грибовидного вала и линейки. Решение задач осуществлялось в программном комплексе QForm 3D. Результаты конечно-элементного моделирования показали, что применение усовершенствованной калибровки инструмента позволяет улучшить центровку заготовки и обеспечить стабильную ее подачу по оси прокатки прошивного стана. За счет этого удастся снизить биение заготовки в очаге деформации и тем самым снизить усилие на валках с 8 до 5 МН. Результаты замеров геометрических параметров гильз, полученные при помощи конечно-элементного моделирования, показали незначительные относительные отклонения, которые укладываются в нормативные пределы.

**Ключевые слова:** винтовая прошивка, точность размеров гильз, энергосиловые параметры процесса, компьютерное моделирование, твердотельная модель, стабильность процесса прошивки, МКЭ-моделирование

**Для цитирования:** Панасенко О.А., Халезов А.О., Нухов Д.Ш. Исследование эффективности изменения калибровки входного конуса валков и линейки прошивного стана с грибовидными валками с помощью компьютерного моделирования. *Известия вузов. Черная металлургия*. 2024;67(1):106–111. <https://doi.org/10.17073/0368-0797-2024-1-106-111>

## INTRODUCTION

The critical step in producing hot-worked seamless pipes involves transforming a solid workpiece into a hollow billet [1 – 3]. The most effective method for this, both in terms of productivity and the accuracy of the hollow billet's geometry, is screw piercing of continuous cast workpieces (CCW) using rotary piercers [4 – 6]. The screw rolling process is modern and holds great promise; however, it is also exceptionally complex [7; 8]. This complexity arises from the unique way metal flows in the deformation zone, which makes the process particularly challenging [9; 10]. During screw rolling, the workpiece undergoes simultaneous rotation, axial movement, and radial compression by the rolls [2]. As a result, screw rolling is seen as a process with uncertain boundary conditions and a cyclic nature of deformation [5]. The setup and calibration of the deformation tool, along with the precision of the workpiece feed and the release of the hollow billet from the deformation zone, significantly affect its quality. This includes the dimensional accuracy and the presence of defects on its inner and outer surfaces [11 – 14].

## PECULIARITY OF THE WORKPIECE FEEDING INTO THE PIERCING MILL AND ITS IMPACT ON THE HOLLOW BILLET QUALITY

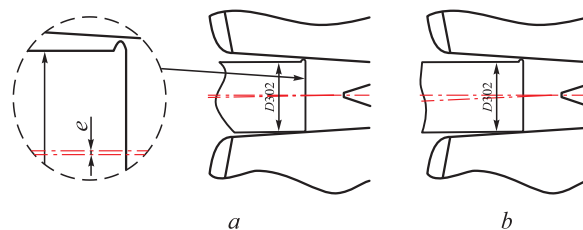
It is widely recognized that for a stable piercing process at the rotary piercers, it is crucial to meet the conditions for initial and secondary capture, as well as to ensure the reliable completion of the piercing process when the hollow billet is released from the mill rolls [1 – 3]. In practice, however, achieving capture can be challenging. The study mentioned in [3] highlights that to guarantee the forward and rotational movement of the workpiece during its initial capture by the rolls, an external axial force must be applied to the workpiece's rear end. In this scenario, the pushing force should be applied to the workpiece until its circumferential velo-

city hits a critical point. At this juncture, the metal is axially fed into the rolls, and both the speed and force of the device pushing the workpiece into the rolls should be kept to a minimum [3].

Moreover, during its initial capture by the rolls of the piercing mill, the workpiece exhibits a considerable degree of movement freedom. This is partly because the entry guide is manufactured to a set tolerance for the inner diameter, and the working surface that supports the workpiece is subject to wear (Fig. 1). These factors lead to an increase in wall thickness variation and the out-of-roundness of the hollow billet's front end [14 – 16]. The deviation of the workpiece from the rolling axis, as shown in Fig. 1, can be exacerbated by the curvature of the continuous cast workpieces (CCW) themselves, as well as by lapping or burrs on their front face.

Therefore, the stability of the piercing process in its early stages is compromised by two main issues: the failure to adhere to the required workpiece feeding mode and the inadequacies of the existing feeding devices.

To improve the alignment of the workpiece and ensure its stable feeding along the rolling axis of the EZTM piercing mill at Tube Rolling Shop-1 of JSC Seversty Pipe Plant, a novel approach was suggested. This method



**Fig. 1.** Misalignment of the workpiece from rolling axis during the primary capture: eccentricity of axes of the workpiece and rolling (a); angle of the workpiece inclination (b)

**Рис. 1.** Отклонение заготовки от оси прокатки при первичном захвате: эксцентриситет осей заготовки и прокатки (a); угол наклона заготовки (b)



involves adding a special thickening, or hump, on the roll input cone, along with adjusting the calibration of its input section on the guide shoe. The aim is for the workpiece to engage with the rolls sooner – before the initial capture of the workpiece by the rolls, and thus before the deformation of the CCW metal by the rolls.

To achieve this, an additional tapered section is introduced on the roll input cone. This section extends from the roll end to the point where the workpiece is first captured by the mill rolls and is aligned parallel to the rolling axis (assuming the rolls are rotated to the necessary angle for rolling and feeding). This design is intended to keep the workpiece centered within the deformation zone of the EZTM piercing mill, thereby enhancing the stability of the workpiece's initial capture by the rolls (Fig. 2).

### VERIFICATION OF THE TECHNICAL SOLUTION TO ENHANCE THE STABILITY OF THE SCREW PIERCING PROCESS IN THE MILL WITH TAPERED ROLLS

To validate and refine the proposed solution, tasks involving the FEM modeling of the screw piercing process at the rotary piercer with a modified design of the tapered roll and guide shoe were set up and conducted using the QForm 3D software package. This approach enabled the identification of workpiece shape change patterns within the deformation zone and facilitated the assessment of the hollow billet's dimensional accuracy [17].

To facilitate these tasks, a solid model of the piercing mill was developed using CAD modeling software, specifically KOMPAS-3D. The solid models of the rolls,

guide shoes, and the piercing head for the EZTM mill were prepared, aligning with the technological guidelines provided by JSC Seversky Pipe Plant. For the modeling process, a workpiece with a diameter of 290 mm was used. The positioning of the tools was determined based on the technological parameters of the piercing mill's configuration, as practiced at the production facility (refer to the Table).

As the modeling tasks were established, the following assumptions were made.

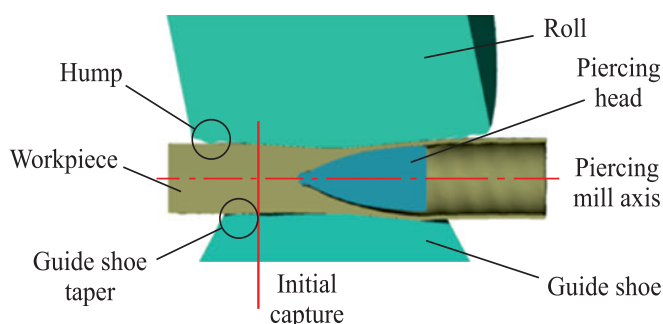
- The workpiece is 1000 mm long.
- The material of the workpiece is solid, isotropic, and incompressible AISI 1045 steel (equivalent to steel 45), for which the necessary parameters are available in the QForm 3D software database.
- In line with the specifications, the workpiece's temperature is set at 1200 °C, and the temperature of the working tools at 50 °C.
- The friction between the workpiece and the tool surfaces is described by the Siebel friction law:  $\tau = \psi \tau_s$ , where  $\tau$  is the friction stress, MPa,  $\psi$  is the friction index, and  $\tau_s$  is the shear deformation resistance of the material. For the surfaces in contact with the rolls, the friction index is presumed to be 0.8, while for those in contact with the piercing head and guide shoe, it's assumed to be 0.4 [5].

These assumptions were chosen to expedite the calculation process and are considered not to significantly affect the study's objectives. The solid model showcasing the workpiece piercing process and the process's initial stage, as visualized in the QForm 3D software, is illustrated in Fig. 3.

The results from the tasks solved using the QForm 3D software revealed several positive outcomes from applying the improved tool calibration:

- the stable initial capture of the workpiece by the mill rolls is achieved;
- significant compression of the workpiece in the deformation zone does not result in the premature opening of the CCW internal cavity;
- a consistent secondary capture without any workpiece runout in the deformation zone is assured.

As the calibration was refined, the optimal parameters for the input cone of rolls and guide shoes were determined (Fig. 4).



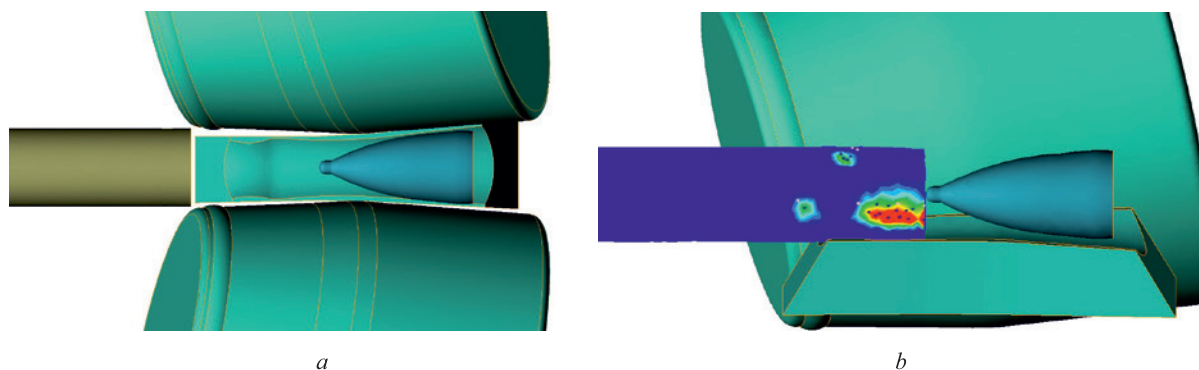
**Fig. 2.** Center of deformation during piercing of the workpiece in rolls with a hump on the input section

**Рис. 2.** Очаг деформации при прошивке заготовки в валках с гребнем на входном участке

### Settings of the piercing mill

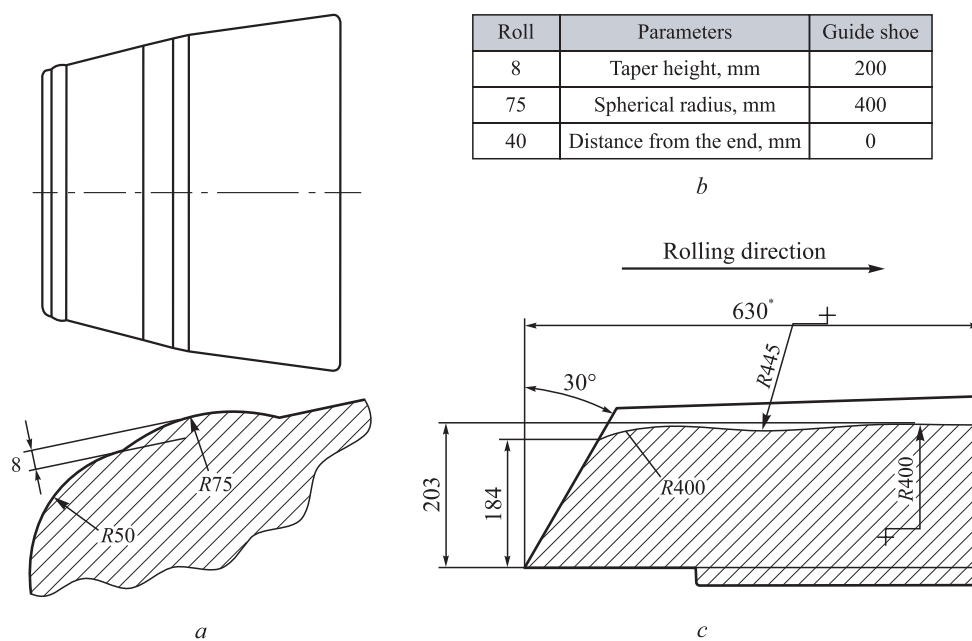
#### Параметры настройки прошивного стана

Distance between		The piercing head extending beyond the rolls overclamping, mm	Angle of, deg		Rolls speed, rpm
the rolls, mm	the guide shoes, mm		feeding	rolling	
253	286	100	9.5	12	30



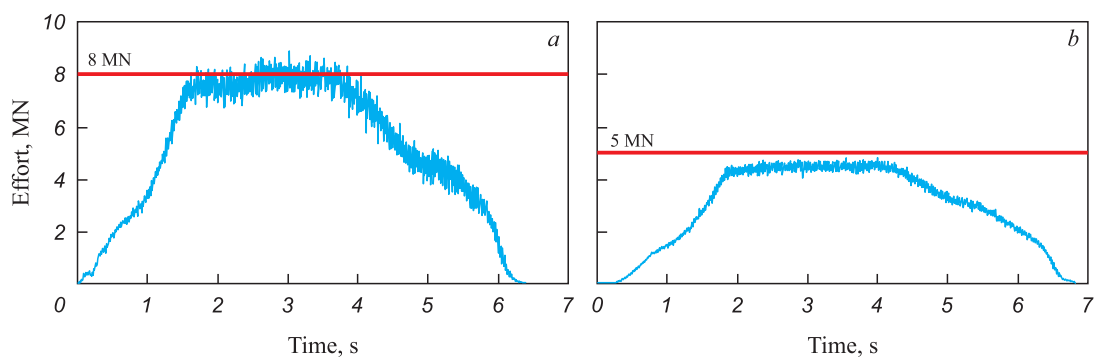
**Fig. 3.** Solid-state model of the workpiece piercing (a) and the initial stage of piercing process in rolls with a hump (b) in QForm 3D program

**Рис. 3.** Твёрдотельная модель процесса прошивки заготовки (a) и демонстрация стабильности первичного захвата и накопления деформации при прошивке в валках с гребнем (b) в программе QForm 3D



**Fig. 4.** Parameters of the hump on the roll and ruler: drawing of the roll with a hump (a); main parameters (b); drawing of the ruler with a taper (c)

**Рис. 4.** Параметры гребня на валке и линейки: чертеж валка с гребнем (a); основные параметры (b); чертеж линейки с конусностью (c)



**Fig. 5.** Graphs of force on the piercing mill rolls during computer modeling: basic model (a); model with modified calibration (b)

**Рис. 5.** Графики усилия на валки прошивного стана при компьютерном моделировании: базовая модель (a); модель с измененной калибровкой (b)

The force graph on the rolls of the piercing mill validates that the calibration was accurately performed (Fig. 5).

This enhanced tool calibration effectively minimizes workpiece runout along the piercing axis, as evidenced by a considerable reduction in the piercing force (Fig. 5). The graphs demonstrate that piercing the workpiece with improved tool calibration can reduce the force exerted on the rolls from 8 to 5 MN.

The results of the FEM measurements for the hollow billets' geometric parameters revealed minor relative deviations:

- the average outside diameter did not surpass 0.8 % (within the standard tolerance of  $\pm 1$  %);
- the wall thickness deviations did not exceed 1.4 % (with a standard tolerance of  $\pm 5$  %).

Blanks refined with improved roll and guide shoe calibration have been successfully tested at the EZTM piercing mill and are now being utilized to manufacture hollow billets in Shop No. 1 of JSC Seversky Pipe Plant.

## CONCLUSIONS

The paper proposes a technical solution to enhance the stability of piercing CCW on screw rolling mills. It suggested adding a special thickening (hump) on the roll input cone and altering the calibration of its input section on the guide shoe, enabling the workpiece to engage with the rolls sooner – before the initial capture and prior to the deformation of CCW metal by the rolls.

To evaluate and refine this solution, tasks for FEM modeling of the screw piercing process with a redesigned tapered roll and guide shoe were established and completed.

The FEM modeling results confirmed that utilizing improved tool calibration could significantly reduce workpiece runout in the deformation zone and lower the force on the rolls from 8 to 5 MN. The FEM-derived measurements of the hollow billets' geometric parameters showed negligible relative deviations, all within acceptable regulatory standards.

## REFERENCES / СПИСОК ЛИТЕРАТУРЫ

1. Potapov I.N. Theory of Pipe Production. Moscow: Metallurgiya; 1991:424. (In Russ.).  
Потапов И.Н. Теория трубного производства. Москва: Металлургия; 1991:424.
2. Danilov F.A. Hot Rolling and Pressing of Pipes. Moscow: Metallurgiya; 1972:591. (In Russ.).  
Данилов Ф.А. Горячая прокатка и прессование труб. Москва: Металлургия; 1972:591.
3. Teterin P.K. Theory of Transverse and Screw Rolling. Moscow: Metallurgiya; 1972:270. (In Russ.).

- Тетерин П.К. Теория поперечной и винтовой прокатки. Москва: Металлургия; 1983:270.
4. Osadchii V.Ya. Production and Quality of Steel Pipes: A Textbook for Universities. Moscow: MSUPI; 2012:370. (In Russ.).  
Осадчий В.Я. Производство и качество стальных труб: Учебное пособие для вузов. Москва: Издательство МГУПИ; 2012:370.
5. Bogatov A.A. Screw Rolling of Continuously Cast Billets from Structural Steel Grades: A Textbook. Yekaterinburg: UrFU; 2017:164. (In Russ.).  
Богатов А.А. Винтовая прокатка непрерывно-литых заготовок из конструкционных марок стали: Учебное пособие. Екатеринбург: Издательство УрФУ; 2017:164.
6. Wei Z., Wu C. A new analytical model to predict the profile and stress distribution of tube in three-roll continuous retained mandrel rolling. *Journal of Materials Processing Technology*. 2022;302:117491.  
<https://doi.org/10.1016/j.jmatprotec.2022.117491>
7. Gamin Yu.V., Galkin S.P., Romantsev B.A., Koshmin A.N., Goncharuk A.V., Kadach M.V. Influence of radial-shear rolling conditions on the metal consumption rate and properties of D16 aluminum alloy rods. *Metallurgist*. 2021; 65(5-6):650–659.  
<https://doi.org/10.1007/s11015-021-01202-0>
8. Topa A., Kim D.K., Kim Y. 3D numerical simulation of seamless pipe piercing process by fluid-structure interaction method. *MATEC Web of Conferences*. 2018;203:06016.  
<https://doi.org/10.1051/mateconf/201820306016>
9. Romantsev B.A., Skripalenko M.M., Ba Huy Tran, Skripalenko M.N., Gladkov Yu.A., Gartvig A.A. Computer simulation of piercing in a four-high screw rolling mill. *Metallurgist*. 2018;61(9–10):729–735.  
<http://doi.org/10.1007/s11015-018-0556-7>  
Романцев Б.А., Скрипаленко М.М., Чан Ба Хюи, Скрипаленко М.Н., Гладков Ю.А., Гартвиг А.А. Компьютерное моделирование прошивки заготовок в четырехвалковом стане винтовой прокатки. *Металлург*. 2017;(9):19–24.
10. Skripalenko M.M., Rogachov S.O., Romantsev B.A., Bazhenov V.E., Skripalenko M.N., Danilin A.V. Microstructure and hardness of hollow tube shells at piercing in two-high screw rolling mill with different plugs. *Materials*. 2022;15(6):2093.  
<https://doi.org/10.3390/ma15062093>
11. Nguyen Q., Aleshchenko A.S. Research on the mandrel wear of a screw rolling piercing mill by the finite element method. *Key Engineering Materials*. 2022;910:381–387.  
<https://doi.org/10.4028/p-4m4o75>
12. Goncharuk A.V., Fadeev V.A., Kadach M.V. Seamless pipes manufacturing process improvement using mandreling. *Solid State Phenomena*. 2021;316:402–407.  
<https://doi.org/10.4028/www.scientific.net/SSP.316.402>
13. Rotenberg Zh.Ya., Budnikov A.S. Modernization of screw rolling technology in a multi-roll mill. *Izvestiya. Ferrous Metallurgy*. 2022;65(1):28–34. (In Russ.).  
<https://doi.org/10.17073/0368-0797-2022-1-28-34>  
Ротенберг Ж.Я., Будников А.С. Модернизация технологии винтовой прокатки в многовалковом стане. *Известия вузов. Черная металлургия*. 2022;65(1):28–34.  
<https://doi.org/10.17073/0368-0797-2022-1-28-34>
14. Pavlova M.A., Zvonarev D.Yu., Akhmerov D.A. QFORM-based research how the accuracy settings of piercing mill

centering units axis influences hollow shell thickness. *Bulletin of the South Ural State University. Series: Metallurgy*. 2021;(4):56–62. (In Russ.).

Павлова М.А., Звонарев Д.Ю., Ахмеров Д.А. Исследование влияния точности настройки осей центрователей прошивного стана на разнотолщинность гильз с использованием QFORM. *Вестник Южно-Уральского государственного университета. Серия: Металлургия*. 2021;(4):56–62.

15. Galkin S.P., Aleshchenko A.S., Romantsev B.A., Gamin Yu.V., Iskhakov R.V. Effect of preliminary deformation of continuously cast billets by radial-shear rolling on the structure and properties of hot-rolled chromium-containing steel pipes. *Metallurgist*. 2021;65(1–2):9–12. <https://doi.org/10.1007/s11015-021-01147-4>

Галкин С.П., Алешенко А.С., Романцев Б.А., Гамин Ю.В., Исхаков Р.В. Влияние предварительной деформации непрерывнолитых заготовок радиально-сдвиговой про-

каткой на структуру и свойства горячекатаных труб из хромсодержащих сталей. *Металлург*. 2021;65(2):54–61.

16. Toporov V.A., Tolmachev V.S., P'yankov B.G., Bushin R.O., Panasenکو O.A., Ibragimov P.A. *Method of obtaining hollow sleeves on a sewing mill*. Patent RF no. 2578887. МРК В21В19/04. *Bulleten' izobretenii*. 2016;(33). (In Russ.).

Пат. 2578887 RU. *Способ получения полых гильз на прошивном стане* / Топоров В.А., Толмачев В.С., Пьянков Б.Г., Бушин Р.О., Панасенко О.А., Ибрагимов П.А.; заявл. 30.09.2014; опубл. 27.03.2016.

17. Toporov V.A., Stepanov A.I., Panasenکو O.A., Ibragimov P.A. Use of finite-element modeling to improve the piercing operation on a piercing mill. *Metallurgist*. 2014; 58(7–8):563–567. <http://doi.org/10.1007/s11015-014-9954-7>

Топоров В.А., Степанов А.И., Панасенко О.А., Ибрагимов П.А. Применение конечно-элементного моделирования для совершенствования процесса прошивки на прошивном стане. *Металлург*. 2014;58(7):28–31.

## Information about the Authors

**Oleg A. Panasenکو**, Head of the Pipe Rolling Laboratory of the Research Center, JSC "Severskii Tube Steelworks"

**E-mail:** [PanasenکوOA@stw.ru](mailto:PanasenکوOA@stw.ru)

**Aleksandr O. Khalezov**, Postgraduate of the Chair "Metal Forming", Ural Federal University named after the first President of Russia B.N. Yeltsin

**E-mail:** [alekssanja633@mail.ru](mailto:alekssanja633@mail.ru)

**Danis Sh. Nukhov**, Cand. Sci. (Eng.), Assist. Prof. of the Chair "Metal Forming", Ural Federal University named after the first President of Russia B.N. Yeltsin

**E-mail:** [d.s.nukhov@urfu.ru](mailto:d.s.nukhov@urfu.ru)

## Сведения об авторах

**Олег Александрович Панасенко**, начальник трубопрокатной лаборатории научно-исследовательского центра, АО «Северский трубный завод»

**E-mail:** [PanasenکوOA@stw.ru](mailto:PanasenکوOA@stw.ru)

**Александр Олегович Халезов**, аспирант кафедры «Обработка металлов давлением», Уральский федеральный университет имени первого Президента России Б.Н. Ельцина

**E-mail:** [alekssanja633@mail.ru](mailto:alekssanja633@mail.ru)

**Данис Шамильевич Нухов**, к.т.н., доцент кафедры «Обработка металлов давлением», Уральский федеральный университет имени первого Президента России Б.Н. Ельцина

**E-mail:** [d.s.nukhov@urfu.ru](mailto:d.s.nukhov@urfu.ru)

## Contribution of the Authors

**O. A. Panasenکو** – formulation of the research task, developing a technical solution for changing calibration of input cone of rolls and lines of a piercing mill, planning of a computational experiment.

**A. O. Khalezov** – development of calibration of piercing mill tools, formulation and solution of the problem of FEM of the screw piercing process with a modified design of tapered roll and ruler; measuring the geometric parameters of hollow billets.

**D. Sh. Nukhov** – processing the experimental results, design of the article, literary review, formulation of conclusions.

## Вклад авторов

**О. А. Панасенко** – формулировка задачи для проведения исследований, разработка технического решения по изменению калибровки входного конуса валков и линеек прошивного стана, планирование вычислительного эксперимента.

**А. О. Халезов** – разработка калибровки инструментов прошивного стана, постановка и решение задачи конечно-элементного моделирования процесса винтовой прошивки с измененной конструкцией грибовидного валка и линейки, проведение замеров геометрических параметров гильз.

**Д. Ш. Нухов** – обработка результатов экспериментов, оформление материалов статьи, анализ литературы по тематике статьи, формулировка выводов.

Received 06.04.2023

Revised 15.01.2024

Accepted 22.01.2024

Поступила в редакцию 06.04.2023

После доработки 15.01.2024

Принята к публикации 22.01.2024





UDC 004.94:621.745:662.61

DOI 10.17073/0368-0797-2024-1-112-120



Original article

Оригинальная статья

## MATHEMATICAL MODELING OF GAS DYNAMICS AND OFF-GAS POST-COMBUSTION ABOVE THE MELT IN A MELTER-GASIFIER FURNACE

T. V. Erokhov<sup>✉</sup>, I. A. Levitskii, G. S. Podgorodetskii, V. B. Gorbunov

National University of Science and Technology “MISIS” (4 Leninskii Ave., Moscow 119049, Russian Federation)

[✉ erohov.tv@isis.ru](mailto:erohov.tv@isis.ru)

**Abstract.** Organization of technological process and design of a furnace significantly affect the parameters of post-combustion, determining the need to develop a mathematical model of post-combustion zone. Modeling of gas dynamics, chemical reactions, convective diffusion and heat transfer in the gas phase above the melt was carried out in an experimental melter-gasifier furnace at three different values of mass flow rates and two positions of post-combustion tuyeres. Temperature distributions and off-gas components concentrations were obtained. It was found that at the lower position of the tuyere, post-combustion is carried out in the area of reflected jet, stagnant zones are formed around the tuyere and between the reflected jet and the melt surface, which decrease the post-combustion level. At the upper position of the tuyere, post-combustion occurs inside the primary jet, intensive mixing of all components of the furnace atmosphere occurs, post-combustion undergoes more completely, which leads to an increase in the off-gases temperature with an increase in uniformity of temperature fields and concentrations compared with the lower position of the tuyere. At the lower position of the tuyere, the flame zone turns out to be open, its shape significantly depends on the mass flow, and the flame zone volume increases with an increase in the mass flow. At the upper position of the tuyere, the flame zone is closed, with an increase in the mass flow, its shape does not change, but the flame zone volume decreases. For reduction processes in slag melt, the upper position of the tuyere is preferable, while for production of the producer gas at the furnace outlet, position of the tuyere closer to the melt surface is preferable.

**Keywords:** computational fluid dynamics, mathematical modeling, numerical modeling, temperature field, concentration field, flame zone, mass flow, post-combustion, experimental melter-gasifier furnace

**For citation:** Erokhov T.V., Levitskii I.A., Podgorodetskii G.S., Gorbunov V.B. Mathematical modeling of gas dynamics and off-gas post-combustion above the melt in a melter-gasifier furnace. *Izvestiya. Ferrous Metallurgy*. 2024;67(1):112–120.

<https://doi.org/10.17073/0368-0797-2024-1-112-120>

## МАТЕМАТИЧЕСКОЕ МОДЕЛИРОВАНИЕ ГАЗОДИНАМИКИ И ДОЖИГАНИЯ ГОРЮЧИХ КОМПОНЕНТОВ НАД РАСПЛАВОМ В ПЛАВИЛЬНОЙ ПЕЧИ-ГАЗИФИКАТОРЕ

Т. В. Ерохов<sup>✉</sup>, И. А. Левицкий, Г. С. Подгородецкий, В. Б. Горбунов

Национальный исследовательский технологический университет «МИСИС» (Россия, 119049, Москва, Ленинский пр., 4)

[✉ erohov.tv@isis.ru](mailto:erohov.tv@isis.ru)

**Аннотация.** Особенности организации технологического процесса и конструкции печи значительно влияют на параметры процессов дожигаания, тем самым определяя необходимость построения математической модели зоны дожигаания. В данном исследовании проведено моделирование газодинамики, химических реакций, конвективной диффузии и теплообмена в газовой среде над расплавом в экспериментальной плавильной печи-газификаторе при трех различных значениях расхода дутья и двух положениях фурмы для дожигаания. Получены распределения температур и концентраций продуктов дожигаания. При нижнем расположении фурмы процесс дожигаания осуществляется в области «отраженной» струи, образуются застойные зоны вокруг фурмы и между отраженной струей и поверхностью расплава, что ухудшает дожигаание. При верхнем расположении фурмы дожигаание происходит внутри первичной струи, осуществляется интенсивное перемешивание всех компонентов печной атмосферы и дожигаание проходит более полно, что приводит к увеличению температуры отходящих газов при увеличении однородности полей температуры и концентраций по сравнению с нижним положением фурмы. Установлено, что при нижнем положении фурмы факел оказывается разомкнутым, его форма существенно зависит от расхода дутья, а объем с ростом расхода дутья увеличивается. При верхнем расположении фурмы факел является замкнутым, с увеличением расхода дутья его

форма не изменяется, а объем уменьшается. Для процессов восстановления в шлаковом расплаве предпочтительно верхнее расположение фурмы, в то время как для получения генераторного газа с большим содержанием горючих компонентов на выходе из печи предпочтительно более близкое к поверхности расплава расположение фурмы.

**Ключевые слова:** вычислительная гидродинамика, математическое моделирование, численное моделирование, температурное поле, поле концентраций, расход дутья, факел, дожигание, экспериментальная плавильная печь-газификатор

**Для цитирования:** Ерохов Т.В., Левицкий И.А., Подгородецкий Г.С., Горбунов В.Б. Математическое моделирование газодинамики и дожигания горючих компонентов над расплавом в плавильной печи-газификаторе. *Известия вузов. Черная металлургия*. 2024;67(1):112–120. <https://doi.org/10.17073/0368-0797-2024-1-112-120>

## INTRODUCTION

High-temperature bath type smelting reduction furnaces stand out as the most promising technologies for extracting metals from low-grade raw materials (such as refractory ores and iron-containing waste) and for the gasification of coal, including varieties of low-grade coal. The thermal balance for the processes of metal reduction and/or gasification of low-grade coals occurring within the slag melt is achieved by reintroducing heat to the slag bath from the post-combustion of CO and H<sub>2</sub> over the slag. These gases, in turn, results from a series of reduction-oxidation processes taking place within the slag layer [1 – 3].

Mathematical modeling plays a crucial role in understanding the processes occurring during the post-combustion of gases in metallurgical furnaces. For example, studies [4 – 7] delve into modeling the post-combustion process in the electric arc furnace. Post-combustion models for the oxygen converter are outlined in [8], while modifications involving bottom blowing with inert gas, such as the AOD converter and KOBM converter, are discussed in [9 – 11]. Additionally, a significant number of research efforts focus on the modeling of post-combustion in direct iron reduction reactors [12 – 15]. These studies highlight how the specific organization of processes and the design of the furnace greatly influence post-combustion parameters, thereby underscoring the importance of developing mathematical models for the post-combustion zone (the furnace area above the melt) in various furnaces, including the Romelt furnace, Vanyukov furnace, and other bath type smelting reduction furnaces with designated off-gas post-combustion zone.

The aim of this research is to model the gas dynamics, chemical reactions, convective diffusion, and heat transfer in the gas phase above the melt within an experimental melter-gasifier furnace, considering three different blast flow rates and two post-combustion tuyere positions. Mathematical modeling was conducted using Ansys Fluent software, version 15.0.7.

## PROBLEM FORMULATION

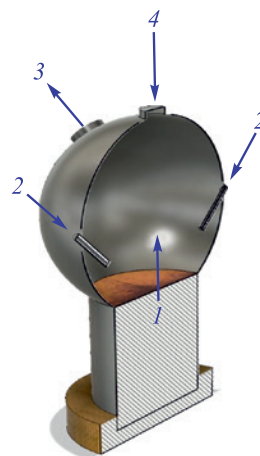
The geometry of the working space within the experimental melter-gasifier furnace is schematically presented in Fig. 1.

In its standard operational mode, the cylindrical part 1 of the furnace is filled with slag melt. The surface level of this slag melt aligns with the transition between the cylindrical and spherical sections of the furnace. The ongoing chemical reactions within the melt are driven by oxygen-air blast from the lower tuyeres (not depicted in the diagram or explored in this study). These processes generate high-temperature gases that rise into the space above the slag, where they fully combust with oxygen-rich air supplied through two upper tuyeres 2. These tuyeres enter the furnace at the center level of the spherical part, angled at 45°.

The flue gases are then emitted through two gas off-takes 3. The gas off-takes axes plane is perpendicular to the upper tuyeres' axes plane.

The primary geometric dimensions of the furnace (m) are detailed as follows:

Diameter of the spherical part of the furnace	3.00
Diameter of the cylindrical part of the furnace	1.80
Inner diameter of the gas offtake	0.50
Inner diameter of inlet bulk supply window	0.40
Internal diameter of the upper tuyere	0.02
External diameter of the upper tuyere	0.10



**Fig. 1.** Layout of the experimental melter-gasifier furnace:  
1 – melt zone; 2 – tuyeres; 3 – gas offtakes; 4 – bulk supply window

**Рис. 1.** Схема экспериментальной плавильной печи-газификатора:  
1 – область расплава; 2 – фурмы; 3 – газоотводы;  
4 – окно подачи сыпучих

## KEY ASSUMPTIONS

To simplify the calculations, the heat transfer through solid walls (including both the furnace itself and the tuyeres) was not considered. This approach allowed us to exclude the regions occupied by solid materials (the walls of the furnace and tuyeres) from detailed analysis, with the thermal boundary conditions merely acknowledging their existence.

Given that the paper examines the processes in the space above the slag of the furnace, the computational domain was limited to the gas-filled area of the working space – specifically, a sphere with a truncated segment at the bottom and three adjoining small cylindrical elements at the top. This domain includes three inlet cross-sections (the surface of the melt and the inlet cross-sections of the post-combustion tuyeres) and two outlet sections (the openings of the gas offtakes, assuming the bulk supply window is sealed with a lid).

Given that the geometry in question features two planes of symmetry and lacks any elements that would cause swirling in the flows, the modeled value fields exhibit the same symmetry. Consequently, it is sufficient to consider only a quarter of the working space, bounded by the planes of symmetry, as the computational domain for analysis.

In this computational domain, the areas of the inlet and outlet cross-sections are 4 times smaller. Consequently, the flow rates at the inlet sections must be proportionally reduced to reflect their scaled-down size compared to their actual counterparts.

The computational domain's geometry was outlined using Design Modeler, while the computational mesh was developed and the sections for applying boundary conditions were chosen in Ansys Meshing. The mesh was later converted to a polyhedral format within the Fluent application. This conversion improved the orthogonality of the cell faces and minimized errors associated with so-called schematic diffusion.

For the analysis, we employed several models, including:

- a convection-diffusion heat transfer model which involves solving the energy equation;
- a  $k$ - $\varepsilon$  turbulence model, specifically the Realizable variant with standard wall functions;
- a component transfer model, that solves the convective diffusion equation and incorporates chemical reactions occurring within the volume. The interaction between kinetics and turbulence adheres to the Finite-Rate/Eddy-Dissipation model.

This last model, which balances the impact of chemical kinetics and turbulent transfer to identify the limiting factor in the process, was utilized in studies [16 – 19]

to explore the combustion of methane introduced through a blast furnace tuyere.

Within the framework of this model, the convective diffusion equation for each constituent of the mixture within the computational domain is resolved with reference to its local mass fraction  $Y_i$  at every computational mesh node. The equation is as follows:

$$\frac{\partial}{\partial t}(\rho Y_i) + \vec{\nabla} \cdot (\rho \vec{\omega} Y_i) = -\vec{\nabla} \cdot \vec{J}_i + R_i, \quad (1)$$

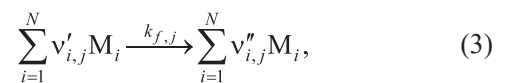
where  $\rho$  is the density of the mixture,  $\text{kg/m}^3$ ;  $\vec{\omega}$  is the velocity vector,  $\text{m/s}$ ;  $R_i$  is the rate of formation of the  $i^{\text{th}}$  component as a result of chemical reactions,  $\text{kg}/(\text{m}^3 \cdot \text{s})$ ;  $\vec{J}_i$  is the diffusion flow density of the  $i^{\text{th}}$  component,  $\text{kg}/(\text{m}^2 \cdot \text{s})$ . The latter is influenced by the concentration gradients of this component and temperature, which can be expressed as:

$$\vec{J}_i = -\left(\rho D_{i,m} + \frac{\mu_t}{Sc_t}\right) \vec{\nabla} Y_i - D_{T,i} \frac{\vec{\nabla} T}{T}, \quad (2)$$

where  $D_{i,m}$  and  $D_{T,i}$  are the mass diffusion and thermodiffusion coefficients (also known as Soret coefficients) for the component  $i^{\text{th}}$ ,  $\text{m}^2/\text{s}$ , respectively;  $Sc_t$  is the turbulent Schmidt number, typically defaulted to 0.7 ( $Sc_t = \frac{\mu_t}{\rho D_i}$ , where  $\mu_t$  is the dynamic coefficient of turbulent viscosity,  $\text{Pa} \cdot \text{s}$ ;  $D_i$  is the turbulent diffusion coefficient,  $\text{m}^2/\text{s}$ ).

For a component that is involved in multiple reactions  $R_i$  is the sum of the rates of formation of that component from all the reactions  $\hat{R}_{i,j}$ .

Assuming the reactions are irreversible for simplicity, the  $j^{\text{th}}$  reaction can be summarized as:



where  $N$  is the number of chemical components in the system;  $v'_{i,j}$  is the stoichiometric coefficient for the  $i^{\text{th}}$  reactant in the  $j^{\text{th}}$  reaction;  $v''_{i,j}$  is the stoichiometric coefficient for the  $i^{\text{th}}$  product in the  $j^{\text{th}}$  reaction;  $M_i$  symbolized the  $i^{\text{th}}$  component;  $k_{f,i}$  is the rate constant for the forward  $j^{\text{th}}$  reaction.

For irreversible reactions, the molar rate of formation/destruction of the  $i^{\text{th}}$  component in the  $j^{\text{th}}$  reaction is described by the expression:

$$\hat{R}_{i,j} = (v''_{i,j} - v'_{i,j}) \left( k_{f,j} \prod_{l=1}^N [C_{l,j}]^{\eta'_{l,j} + \eta''_{l,j}} \right), \quad (4)$$

where  $C_{l,j}$  is the molar concentration of the  $l^{\text{th}}$  component in the  $j^{\text{th}}$  reaction,  $\text{kmol}/\text{m}^3$ ;  $\eta'_{l,j}$  is the reaction rate index of the  $l^{\text{th}}$  component in the  $j^{\text{th}}$  reaction;  $\eta''_{l,j}$  is the reaction rate index of the  $l^{\text{th}}$  product in the  $j^{\text{th}}$  reaction.

Table 1. Kinetic constants for the studied chemical reactions [20]

Таблица 1. Значения кинетических констант для рассматриваемых реакций [20]

Reaction	$A_j$	$\beta_j$	$E_j$	Equation coefficient $\nu$	Order of reaction $\eta$
$\text{H}_2 + 0.5\text{O}_2 = \text{H}_2\text{O}$	$9.87 \cdot 10^8$	0	$3.1 \cdot 10^7$	$\nu'_{\text{H}_2} = 1.0; \nu'_{\text{O}_2} = 0.5; \nu''_{\text{H}_2\text{O}} = 1.0$	$\eta'_{\text{H}_2} = 1.00; \eta'_{\text{O}_2} = 1.00; \eta''_{\text{H}_2\text{O}} = 0$
$\text{CO} + 0.5\text{O}_2 = \text{CO}_2$	$2.239 \cdot 10^{12}$	0	$1.7 \cdot 10^8$	$\nu'_{\text{CO}} = 1.0; \nu'_{\text{O}_2} = 0.5; \nu''_{\text{CO}_2} = 1.0$	$\eta'_{\text{CO}} = 1.00; \eta'_{\text{O}_2} = 0.25; \eta''_{\text{CO}_2} = 0$

Table 2. Boundary conditions in the calculation

Таблица 2. Граничные условия, задаваемые при расчете

Cross-section	Cross-section type	Gas dynamics	Temperature, K	Composition, vol. % [2]
Melt surface	Mass-flow inlet	$\dot{M} = 0.2439 \text{ kg/s};$ $d_{\text{gh}} = 1.8 \text{ m};$ pulsations = 5 %	1773	$\text{CO} = 50; \text{H}_2 = 30; \text{CO}_2 = 2;$ $\text{H}_2\text{O} = 8; \text{N}_2 = 10$
Tuyere inlet cross-section	Mass-flow inlet	$\dot{M} = 0.03919 - 0.11757 \text{ kg/s};$ $d_{\text{gh}} = 0.02 \text{ m};$ pulsations = 15 %	293	$\text{O}_2 = 90; \text{N}_2 = 10$
Gas offtakes cross-section	Pressure outlet	$P = -160 \text{ Pa};$ $d_{\text{gh}} = 0.5 \text{ m};$ pulsations = 5 %	1773	$\text{O}_2 = 21; \text{N}_2 = 79$

The rate constant for the forward  $j^{\text{th}}$  reaction is computed using the Arrhenius equation:

$$k_{f,j} = A_j T^{\beta_j} e^{-\frac{E_j}{RT}}, \quad (5)$$

where  $A_j$  is the pre-exponential indicator (units vary based on the reaction order);  $\beta_j$  is the temperature exponent (dimensionless number);  $E_j$  is the activation energy for the reaction (J/kmol);  $R = 8.31$  is the universal gas constant (J/(kmol·K)).

This study considered just two combustion reactions, involving hydrogen and carbon monoxide; the equations

for these reactions, along with their parameters – some of which were derived from the Ansys Fluent database – are detailed in Table 1.

At the oxygen-air blast and off-gas inlet cross-sections, parameters such as temperature, mass flow rate, and inlet turbulence characteristics (which include hydraulic diameter and the level of turbulent pulsations) were defined. For the outlet cross-section, parameters set included rarefaction and the temperature and the turbulence characteristics of the external environment immediately adjacent to the outlet (Table 2).

The computational task was performed in two stages. Initially, the SIMPLE algorithm was used to solve the gas

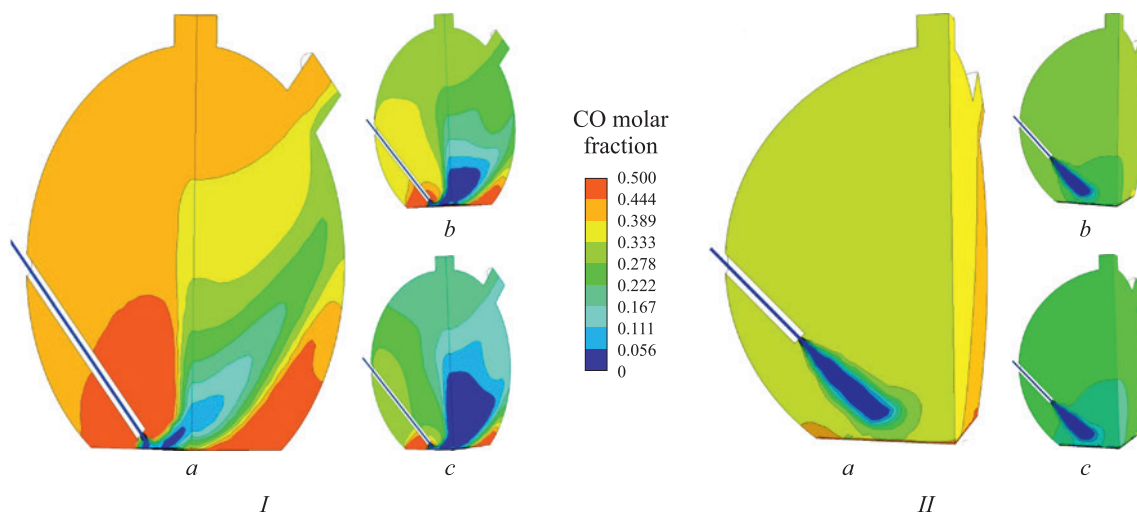
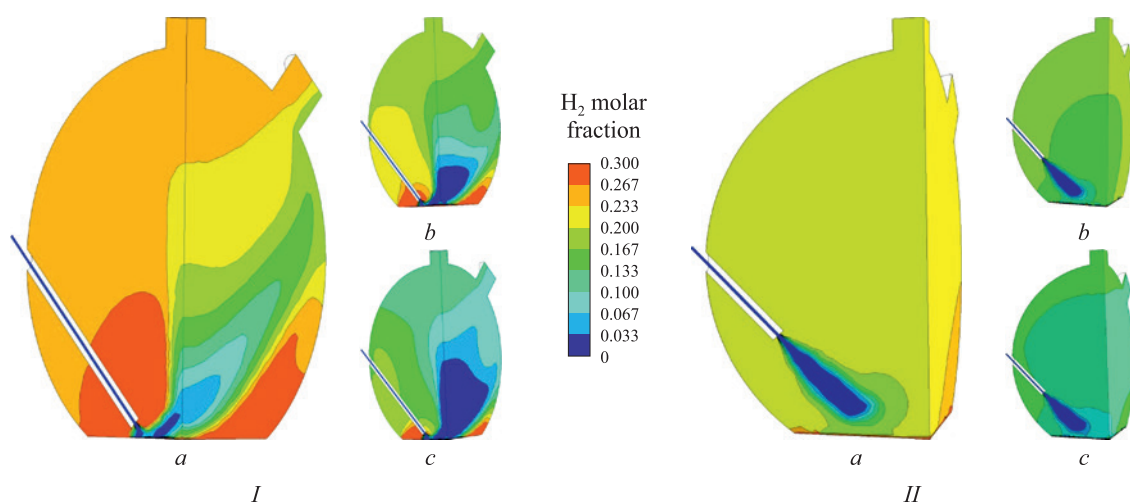


Fig. 2. Field of CO molar fraction for two variants of the tuyere position (I, II) and three values of the blast flow rate (a, b, c)

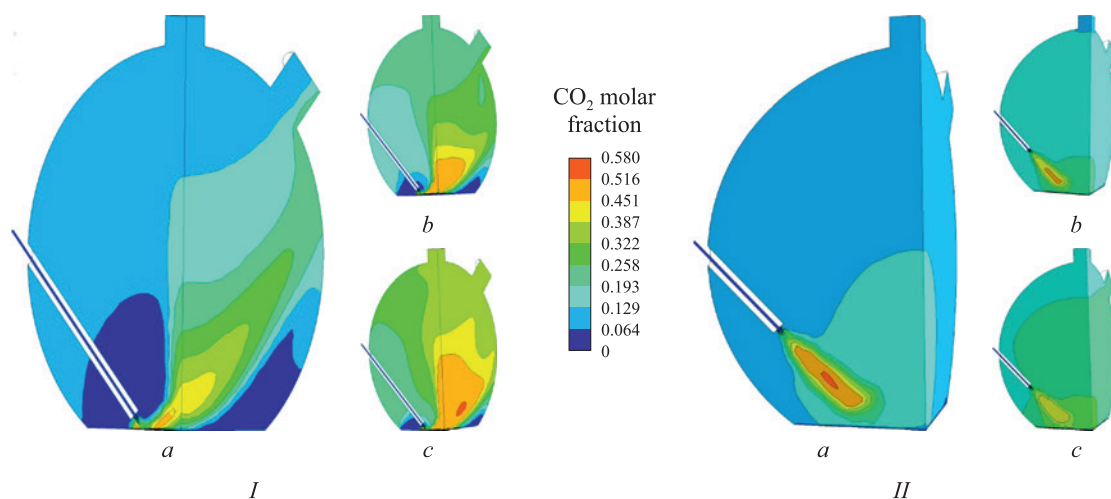
Рис. 2. Поле мольной доли CO для двух вариантов расположения фурмы (I, II) и трех значений расхода дутья (a, b, c)





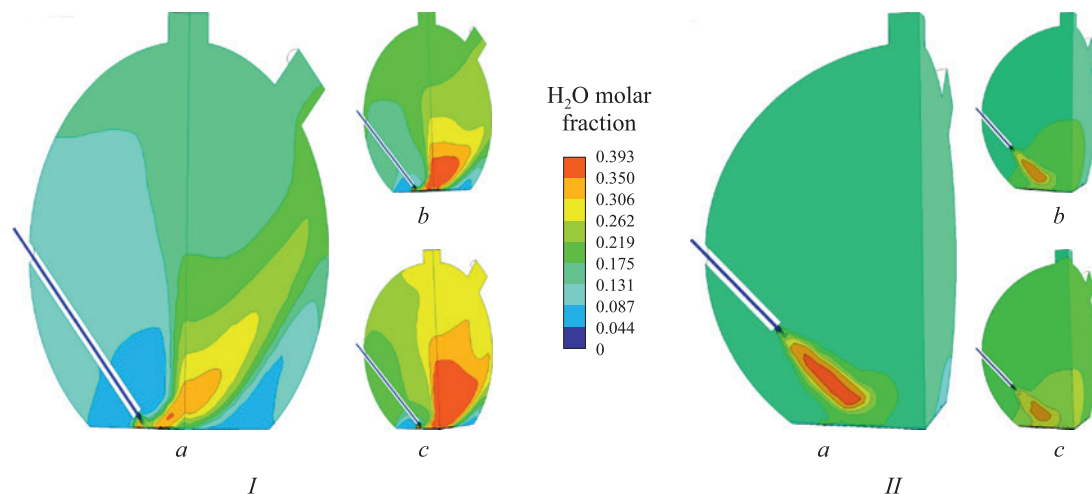
**Fig. 3.** Field of  $H_2$  molar fraction for two variants of the tuyere position (I, II) and three values of the blast flow rate (a, b, c)

**Рис. 3.** Поле мольной доли  $H_2$  для двух вариантов расположения фурмы (I, II) и трех значений расхода дутья (a, b, c)



**Fig. 4.** Field of  $CO_2$  molar fraction for two variants of the tuyere position (I, II) and three values of the blast flow rate (a, b, c)

**Рис. 4.** Поле мольной доли  $CO_2$  для двух вариантов расположения фурмы (I, II) и трех значений расхода дутья (a, b, c)



**Fig. 5.** Field of  $H_2O$  molar fraction for two variants of the tuyere position (I, II) and three values of the blast flow rate (a, b, c)

**Рис. 5.** Поле мольной доли  $H_2O$  для двух вариантов расположения фурмы (I, II) и трех значений расхода дутья (a, b, c)

dynamics equations, with first-order schemes being used for the other equations. Subsequently, the simulation progressed to using a coupled solver for pressure and momentum and second-order schemes for other variables.

The calculation results shown in Fig. 2 – 5 correspond to three blast flow rates  $\dot{M}_b$ : 0.03919 kg/s (a), 0.07838 kg/s (b), 0.11757 kg/s (c) – these figures should be quadrupled to reflect true values for the full-scale model – and two tuyere positions relative to the melt surface: the lower position *I*, at 0.1 m from the melt surface, and the upper position *II*, at 0.7 m from the melt surface.

Fig. 2 – 5 illustrate that increasing the blast flow rate leads to a decrease in the concentrations of post-combustion components (CO and H<sub>2</sub>) and a corresponding increase in the concentrations of combustion products (CO<sub>2</sub> and H<sub>2</sub>O). Moreover, the tuyere's position significantly impacts both the distribution of these components and the peak values of their concentrations.

With the tuyere positioned at the lower level, the only effective blast jet is the one “reflected” off the melt surface, where the highest concentrations of off-gases are found. These maximum concentrations of off-gases are located in the region near the tuyere above the nozzle and in the area farthest from the nozzle adjacent to the melt surface, influenced by the “reflected” jet.

With the tuyere elevated, the blast mixes more thoroughly with the surrounding components in the space above the slag, leading to most mixing and post-combustion processes happening before the jet reaches the melt surface. In this scenario, the zone of maximum off-gases concentrations forms within the primary blast jet and spreads toward the melt surface. The extreme concentrations are less marked compared to the lower tuyere position, owing to enhanced mixing and the lack of stag-

nant zones. Consequently, with the tuyere in its upper position, more complete post-combustion is attained, evidenced by the off-gases' composition at the furnace outlet and the temperature field, which aligns with the concentration field of the combustion products (Fig. 6). This suggests that for producing gas rich in combustible components, positioning the tuyere at a lower level is preferable, whereas for more efficient reduction, a higher tuyere position is advantageous.

Fig. 6 demonstrates that increasing the blast flow rate causes the high-temperature region to expand with the tuyere lowered, but to contract with the tuyere raised.

Ansys Fluent's Isovolumes visualization tool facilitates the creation of three-dimensional surfaces corresponding to specific values of a given quantity, calculated as part of the problem-solving process. Selecting temperature allows for the visualization of concepts such as the flare zone, with Figs. 7 and 8 showcasing isovolumes for temperatures of 2200 and 2600 K, respectively.

The findings indicate that with the tuyere in the upper position, the flame remains closed, its shape stays consistent with increased blast flow rates, and the volume enclosed by the isosurface decreases. In contrast, raising the blast flow rate significantly alters the configuration of the jet region “reflected” off the melt surface for the lower tuyere, increasing the volume enclosed by the isosurface and causing considerable scattering of the “reflected” jet. This results in an excessive heat flow to the water cooled panels, which is detrimental to the technological process.

## CONCLUSIONS

Using Ansys Fluent 15.0.7 software, we numerically analyzed the post-combustion of off-gases (CO,

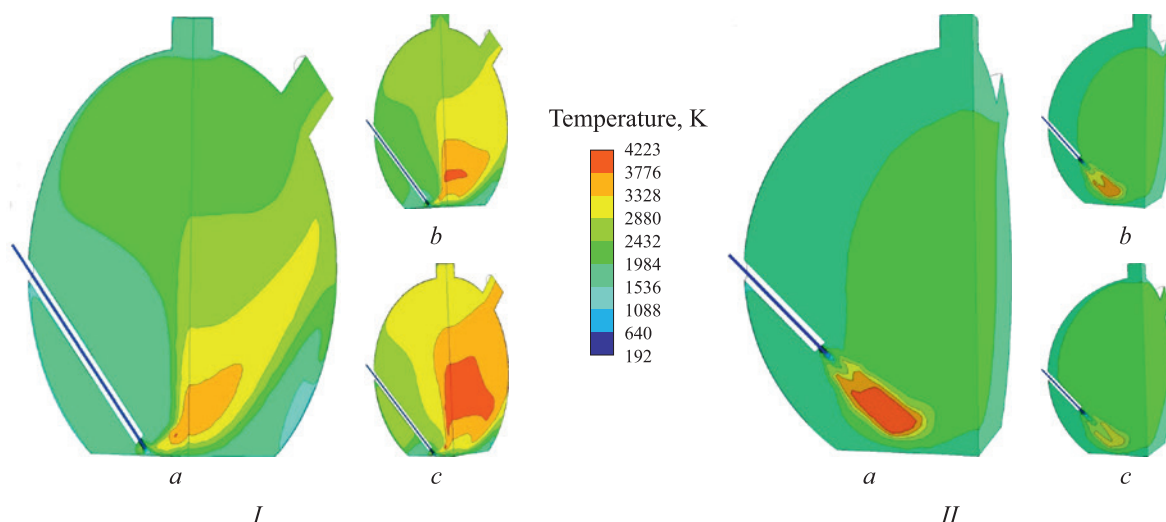
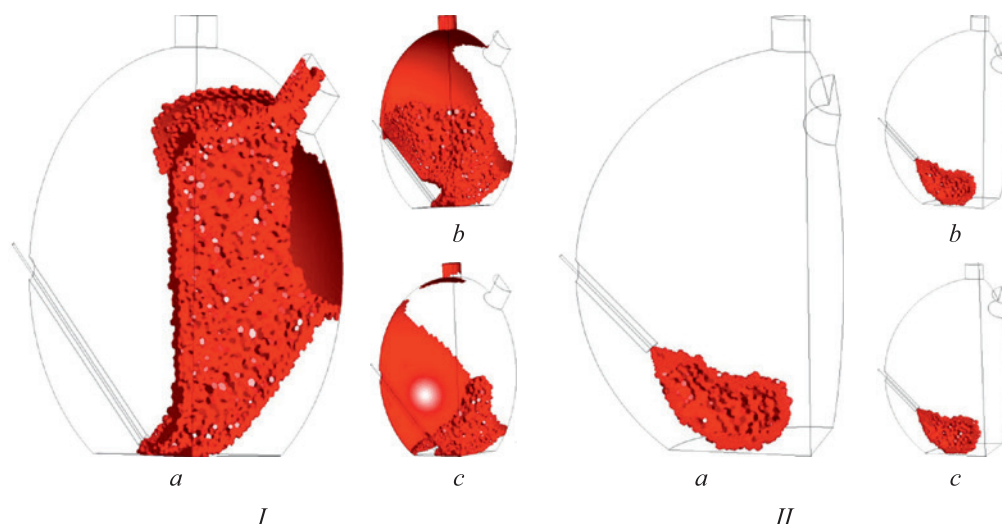


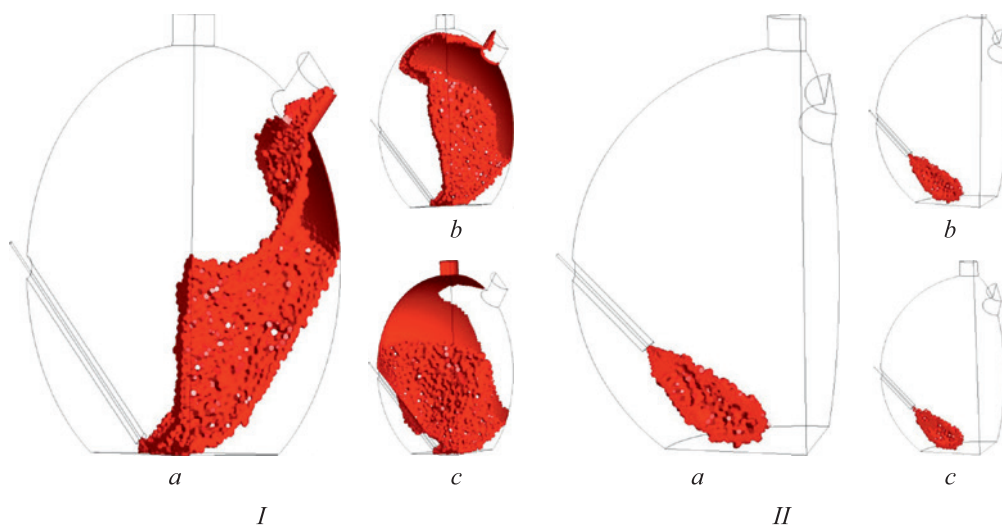
Fig. 6. Temperature field for two variants of the tuyere position (*I*, *II*) and three values of the blast flow rate (*a*, *b*, *c*)

Рис. 6. Температурное поле для двух вариантов расположения фурмы (*I*, *II*) и трех значений расхода дутья (*a*, *b*, *c*)



**Fig. 7.** Isovolumes for 2200 K with two variants of the tuyere position (*I, II*) and three values of the blast flow rate (*a, b, c*)

**Рис. 7.** Изообъемы для температуры 2200 К при двух вариантах расположения фурмы (*I, II*) и трех значений расхода дутья (*a, b, c*)



**Fig. 8.** Isovolumes for 2600 K with two variants of the tuyere position (*I, II*) and three values of the blast flow rate (*a, b, c*)

**Рис. 8.** Изообъемы для температуры 2600 К при двух вариантах расположения фурмы (*I, II*) и трех значений расхода дутья (*a, b, c*)

H<sub>2</sub>) released from the slag bath's surface in the experimental melter-gasifier furnace. Our study examined how the oxygen-enriched blast flow rate and the tuyeres' positioning affect the post-combustion process, including the off-gases' composition and temperature, flame configuration, and the distribution of temperature and component concentrations within the furnace atmosphere.

We discovered that with the tuyere positioned at the lower level (0.1 m from the nozzle to the melt), post-combustion primarily occurs in the “reflected” jet area. This creates stagnant zones around the tuyere and between the reflected jet and the melt surface, reducing the effectiveness of post-combustion. With the tuyere at the upper level (0.7 m from the nozzle to the melt), post-combustion happens inside the primary jet, leading

to intense mixing of all furnace atmosphere components. This results in more complete post-combustion, increasing the off-gas temperature and improving the uniformity of temperature fields and concentrations compared to when the tuyere is at a lower position.

At the lower tuyere position, the flame zone is open, significantly influenced by the mass flow, and its volume increases with the mass flow. With the tuyere in the upper position, the flame zone remains closed, and while its shape stays constant with increased mass flow, the volume of the flame zone decreases.

For reduction processes in the slag melt, higher position of the tuyere is preferable. However, for generating producer gas rich in combustible components at the furnace outlet, a location closer to the melt surface is more



advantageous, though it poses a risk of overheating some water cooled panels, potentially harming the furnace structure and affecting other process parameters adversely.

## REFERENCES / СПИСОК ЛИТЕРАТУРЫ

- Romenets V.A., Valavin V.S., Usachev A.B., Karabassov Yu.S., etc. Romelt Process. Moscow: MISIS; 2005:400.  
Роменец В.А., Валавин В.С., Усачев А.Б., Карабасов Ю.С. и др. Процесс Ромелт. Москва: МИСиС, ИД «Руда и Металлы»; 2005:400.
- Balasanov A.V., Lekherzak V.E., Romenets V.A., Usachev A.B. Coal Gasification in Slag Melt. Moscow: Institut Stal'proekt; 2008:288.  
Баласанов А.В., Лехерзак В.Е., Роменец В.А., Усачев А.Б. Газификация угля в шлаковом расплаве. Москва: «Институт Стальпроект»; 2008:288.
- Podgorodetskii G.S., Gorbunov V.B., Agapov E.A., Erokhov T.V., Kozlova O.N. Challenges and opportunities of utilization of ash and slag waste of TPP (Thermal Power Plant). Part 2. *Izvestiya. Ferrous Metallurgy*. 2018;61(7):557–563. (In Russ.). <https://doi.org/10.17073/0368-0797-2018-7-557-563>  
Подгородецкий Г.С., Горбунов В.Б., Агапов Е.А., Ерохов Т.В., Козлова О.Н. Проблемы и перспективы утилизации золошлаковых отходов ТЭЦ. Часть 2. *Известия вузов. Черная металлургия*. 2018;61(7):557–563. <https://doi.org/10.17073/0368-0797-2018-7-557-563>
- Li Y., Fruehan R.J. Computational fluid-dynamics simulation of postcombustion in the electric-arc furnace. *Metallurgical and Materials Transactions B*. 2003;34(3):333–343. <https://doi.org/10.1007/s11663-003-0079-9>
- Arzpeyma N., Ersson M., Jönsson P.G. Mathematical modeling of postcombustion in an electric arc furnace (EAF). *Metals*. 2019;9(5):547. <https://doi.org/10.3390/met9050547>
- Gruber J.C., Echtermann T., Pfeifer H. Investigation on the influence of the arc region on heat and mass transport in an EAF freeboard using numerical modeling. *Steel Research International*. 2016;87(1):15–28. <https://doi.org/10.1002/srin.201400513>
- Tang X., Kirschen M., Abel M., Pfeifer H. Modelling of EAF off-gas post combustion in dedusting systems using CFD methods. *Steel Research International*. 2003;74(4):201–210. <https://doi.org/10.1002/srin.200300182>
- Doh Y., Chapelle P., Jardy A., etc. Toward a full simulation of the basic oxygen furnace: Deformation of the bath free surface and coupled transfer processes associated with the post-combustion in the gas region. *Metallurgical and Materials Transactions B*. 2013;44(3):653–670. <https://doi.org/10.1007/s11663-013-9817-9>
- Tang Y., Fabritius T., Härkki J. Mathematical modeling of the argon oxygen decarburization converter exhaust gas system at the reduction stage. *Applied Mathematical Modelling*. 2005;29(5):497–514. <https://doi.org/10.1016/j.apm.2004.09.011>
- Song Z., Ersson M., Jönsson P. A study of post-combustion in an AOD flue. *Steel Research International*. 2014;85(7):1173–1184. <https://doi.org/10.1002/srin.201300307>
- Gou H., Irons G.A., Lu W.K. Mathematical modeling of postcombustion in a KOBM converter. *Metallurgical and Materials Transactions B*. 1993;24(1):179–188. <https://doi.org/10.1007/BF02657884>
- Panjovic V., Truelove J., Ostrovski O. Analysis of performance of an iron-bath reactor using computational fluid dynamics. *Applied Mathematical Modelling*. 2002;26(2):203–221. [https://doi.org/10.1016/S0307-904X\(01\)00056-7](https://doi.org/10.1016/S0307-904X(01)00056-7)
- Shin M.K., Lee S.D., Joo S.H., Yoon J.K. A numerical study on the combustion phenomena occurring at the post combustion stage in bath-type smelting reduction furnace. *ISIJ International*. 1993;33(3):369–375. <https://doi.org/10.2355/isijinternational.33.369>
- Becker-Lemgau U., Tacke K.-H. Mathematical model for post combustion in smelting reduction. *Steel Research*. 1996;67(4):27–137. <https://doi.org/10.1002/srin.199605469>
- Shinotake A., Takamoto Y. Combustion and heat transfer mechanism in iron bath smelting reduction furnace. *Metallurgical Research & Technology*. 1993;90(7–8):965–974. <https://doi.org/10.1051/metal/199390070965>
- Levitskii I.A., Radyuk A.G., Titlyanov A.E., Sidorova T.Yu. Influence of the method of natural gas supplying on gas dynamics and heat transfer in air tuyere of blast furnace. *Izvestiya. Ferrous Metallurgy*. 2018;61(5):357–363. (In Russ.). <https://doi.org/10.17073/0368-0797-2018-5-357-363>  
Левицкий И.А., Радюк А.Г., Титлянов А.Е., Сидорова Т.Ю. Влияние способа подачи природного газа на газодинамику и теплообмен в воздушной фурме доменной печи. *Известия вузов. Черная металлургия*. 2018;61(5):357–363. <https://doi.org/10.17073/0368-0797-2018-5-357-363>
- Gorbatyuk S.M., Tarasov Yu.S., Levitskii I.A., Radyuk A.G., Titlyanov A.E. Effect of a ceramic insert with swirler on gas dynamics and heat exchange in a blast furnace tuyere. *Izvestiya. Ferrous Metallurgy*. 2019;62(5):337–344. (In Russ.). <https://doi.org/10.17073/0368-0797-2019-5-337-344>  
Горбатьук С.М., Тарасов Ю.С., Левицкий И.А., Радюк А.Г., Титлянов А.Е. Влияние керамической вставки с завихрителем на газодинамику и теплообмен в воздушной фурме доменной печи. *Известия вузов. Черная металлургия*. 2019;62(5):337–344. <https://doi.org/10.17073/0368-0797-2019-5-337-344>
- Albul S.V., Kobelev O.A., Radyuk A.G., Titlyanov A.E., Levitskii I.A. Effect of natural gas flow rate and temperature on the processes occurring in a blast furnace tuyere with heat-insulating insert in blast channel. *Izvestiya. Ferrous Metallurgy*. 2022;65(11):778–785. (In Russ.). <https://doi.org/10.17073/0368-0797-2022-11-778-785>  
Албул С.В., Кобелев О.А., Радюк А.Г., Титлянов А.Е., Левицкий И.А. Влияние расхода и температуры природного газа на процессы, происходящие в воздушной фурме доменной печи с теплоизолирующей вставкой в дутьевом канале. *Известия вузов. Черная металлургия*. 2022;65(11):778–785. <https://doi.org/10.17073/0368-0797-2022-11-778-785>
- Radyuk A.G., Gorbatyuk S.M., Tarasov Yu.S., Titlyanov A.E., Aleksakhin A.V. Improvements to mixing of natural gas and hot-air blast in the air tuyeres of blast furnaces with thermal insulation of the blast duct. *Metallurgist*. 2019;63(5–6):433–440. <https://doi.org/10.1007/s11015-019-00843-6>
- Milewski J., Swirski K., Santarelli M., Leone P. Advanced Methods of Solid Oxide Fuel Cell Modeling. London, UK: Springer; 2011:201. <https://doi.org/10.1007/978-0-85729-262-9>



## Information about the Authors

## Сведения об авторах

**Timofei V. Erokhov**, Assistant of the Chair "Energy-Efficient and Resource-Saving Industrial Technologies", National University of Science and Technology "MISIS"

**ORCID:** 0000-0001-6926-9049

**E-mail:** erohov.tv@misis.ru

**Igor' A. Levitskii**, Cand. Sci. (Eng.), Assist. Prof. of the Chair "Energy-Efficient and Resource-Saving Industrial Technologies", National University of Science and Technology "MISIS"

**ORCID:** 0000-0002-9345-3628

**E-mail:** lewwwis@mail.ru

**G. S. Podgorodetskii**, Cand. Sci. (Eng.)

**V. B. Gorbunov**, Cand. Sci. (Eng.), National University of Science and Technology "MISIS"

**E-mail:** vbg1953@mail.ru

**Тимофей Витальевич Ерохов**, ассистент кафедры энергоэффективных и ресурсосберегающих промышленных технологий, Национальный исследовательский технологический университет «МИСиС»

**ORCID:** 0000-0001-6926-9049

**E-mail:** erohov.tv@misis.ru

**Игорь Анисимович Левицкий**, к.т.н., доцент кафедры энергоэффективных и ресурсосберегающих промышленных технологий, Национальный исследовательский технологический университет «МИСиС»

**ORCID:** 0000-0002-9345-3628

**E-mail:** lewwwis@mail.ru

**Г. С. Подгородецкий**, к.т.н.

**В. Б. Горбунов**, к.т.н., Национальный исследовательский технологический университет «МИСиС»

**E-mail:** vbg1953@mail.ru

## Contribution of the Authors

## Вклад авторов

**T. V. Erokhov** – calculations and modeling, analysis of the research results, text preparation.

**I. A. Levitskii** – setting the research goals and objectives, scientific consulting, text preparation.

**G. S. Podgorodetskii** – concept formation, scientific guidance.

**V. B. Gorbunov** – scientific guidance, conclusions formation.

**Т. В. Ерохов** – проведение расчетов и моделирования, анализ результатов исследований, подготовка текста.

**И. А. Левицкий** – постановка целей и задач исследования, научное консультирование, подготовка текста.

**Г. С. Подгородецкий** – формирование концепции, научное руководство.

**В. Б. Горбунов** – научное руководство, формирование выводов.

Received 04.06.2023

Revised 20.09.2023

Accepted 11.12.2023

Поступила в редакцию 04.06.2023

После доработки 20.09.2023

Принята к публикации 11.12.2023



UDC 658.562.012.7

DOI 10.17073/0368-0797-2024-1-121-131



Original article

Оригинальная статья

## SHEWHART CONTROL CHARTS – A SIMPLE BUT NOT EASY TOOL FOR DATA ANALYSIS

V. L. Shper<sup>1</sup>, S. A. Sheremetyeva<sup>1</sup>, V. Yu. Smelov<sup>1, 2</sup>, E. I. Khunuzidi<sup>1, 3</sup> <sup>1</sup> National University of Science and Technology “MISIS” (4 Leninskii Ave., Moscow 119049, Russian Federation)<sup>2</sup> GPB Complect (JSC) (6 Valovaya Str., Moscow 11505, Russian Federation)<sup>3</sup> LLC “AtomTekhnoTest” (13 bld. 37 2<sup>nd</sup> Zvenigorodskaya Str., Moscow 123022, Russian Federation)

el\_hun@mail.ru

**Abstract.** Shewhart control charts (ShCCs) are a powerful and technically simple tool for process variability analysis. However, simultaneously, they cannot be fully algorithmized and require deep process knowledge together with additional data analysis. ShCCs are well known, though, and the number of papers is great, as well as standards on ShCCs work in most countries, there are some serious obstacles for their effective application which are not being discussed in either educational or scientific literature. Just these problems are being considered in this paper. We analyzed two sides of standard assumption about data normality. First, we discuss the widely-spread misconception that measurement data are always distributed according Gauss law. Then, it is shown how the deviation from normality may impact the method of ShCCs’ constructing and interpreting. Using a specific process data, we debate on right and wrong ways to build ShCC. Further, the paper describes two new definitions of assignable causes of variation: not changing (*I*-type) and changing (*X*-type) the system. At the end, we discuss how the work with ShCCs should be organized effectively. It is outlined that creating and analyzing ShCCs is always a system question of interaction between the process and the person who tries to improve this process.

**Keywords:** Shewhart control charts, non-normality, capability indices, chart construction

**For citation:** Shper V.L., Sheremetyeva S.A., Smelov V.Yu., Khunuzidi E.I. Shewhart control charts – A simple but not easy tool for data analysis. *Izvestiya. Ferrous Metallurgy*. 2024;67(1):121–131. <https://doi.org/10.17073/0368-0797-2024-1-121-131>

## КОНТРОЛЬНЫЕ КАРТЫ ШУХАРТА – ПРОСТОЙ, НО НЕ ЛЁГКИЙ ДЛЯ ПРИМЕНЕНИЯ ИНСТРУМЕНТ АНАЛИЗА ДАННЫХ

В. Л. Шпер<sup>1</sup>, С. А. Шереметьева<sup>1</sup>, В. Ю. Смелов<sup>1, 2</sup>, Е. И. Хунузиди<sup>1, 3</sup> <sup>1</sup> Национальный исследовательский технологический университет «МИСИС» (Россия, 119049, Москва, Ленинский пр., 4)<sup>2</sup> «ГПБ Комплект» (АО) (Россия, 11505, Москва, Валовая ул., 6)<sup>3</sup> ООО «АтомТехноТест» (Россия, Москва, 123022, 2-я Звенигородская ул., 13, стр. 37)

el\_hun@mail.ru

**Аннотация.** Контрольные карты Шухарта (ККШ) – мощный и технически весьма простой инструмент анализа вариабельности процессов, но одновременно он не может быть полностью алгоритмизирован и требует глубокого знания процесса в сочетании с дополнительным анализом данных. Хотя сами по себе ККШ известны очень давно, число работ огромно и стандарты на применение карт внедрены в большинстве стран мира, существует несколько принципиально важных проблем их эффективного применения, которые практически не находят своего отражения ни в научно-исследовательской, ни в учебной литературе. Именно этим проблемам и посвящена данная работа. В частности, исследованы два аспекта стандартного допущения о нормальности закона распределения данных. Сначала авторы изучили широко распространенное заблуждение о том, что результаты измерений всегда распределены в соответствии с законом Гаусса. Затем показали, что отклонение реальной функции распределения данных от нормальности может при определенных условиях приводить к существенным изменениям в методике построения и интерпретации контрольных карт. Далее, на примере конкретного процесса, было рассмотрено, как правильно и как неправильно строить и интерпретировать ККШ, после чего исследована принципиально важная проблема операционного определения особых/специальных причин вариаций. Авторы предлагают ввести два типа особых причин: не меняющих (*I*-тип) и изменяющих (*X*-тип) систему. В конце работы рассмотрен вопрос о том, как правильно организовать работу с ККШ. Подчеркнуто, что построение и интерпре-

тация контрольной карты – это всегда системная проблема взаимодействия между процессами и людьми, работающими над улучшением этих процессов.

**Ключевые слова:** контрольные карты Шухарта, ненормальность, индексы воспроизводимости, построение карт

**Для цитирования:** Шпер В.Л., Шереметьева С.А., Смелов В.Ю., Хунузиди Е.И. Контрольные карты Шухарта – простой, но не легкий для применения инструмент анализа данных. *Известия вузов. Черная металлургия*. 2024;67(1):121–131.

<https://doi.org/10.17073/0368-0797-2024-1-121-131>

*All models are wrong,  
but some are useful.  
George Box*

## INTRODUCTION

Shewhart Control Charts (ShCCs) are widely recognized as a principal tool evaluating process stability at almost all fields of human activity. These charts were developed nearly a century ago by Walter Shewhart, who is acclaimed for his significant contributions to the field of quality management. His famous works, published in 1931 and 1939, have been reissued in facsimile editions by the American Society for Quality in 1980 and 1986, respectively [1; 2]. W. Edwards Deming, a close collaborator and friend of Shewhart, wrote a brief foreword to the 1939 publication, concluding with the following words: *“Another half-century may pass before the full spectrum of Dr. Shewhart’s contributions has been revealed in liberal education, science, and industry”* [2]. This paper aims to address some of the obstacles encountered in achieving the vision articulated by Deming. Firstly, we will examine the extent to which ShCCs have been adopted globally. Then, we will explain why, despite its apparent simplicity, the ShCCs remain a challenging tool to apply

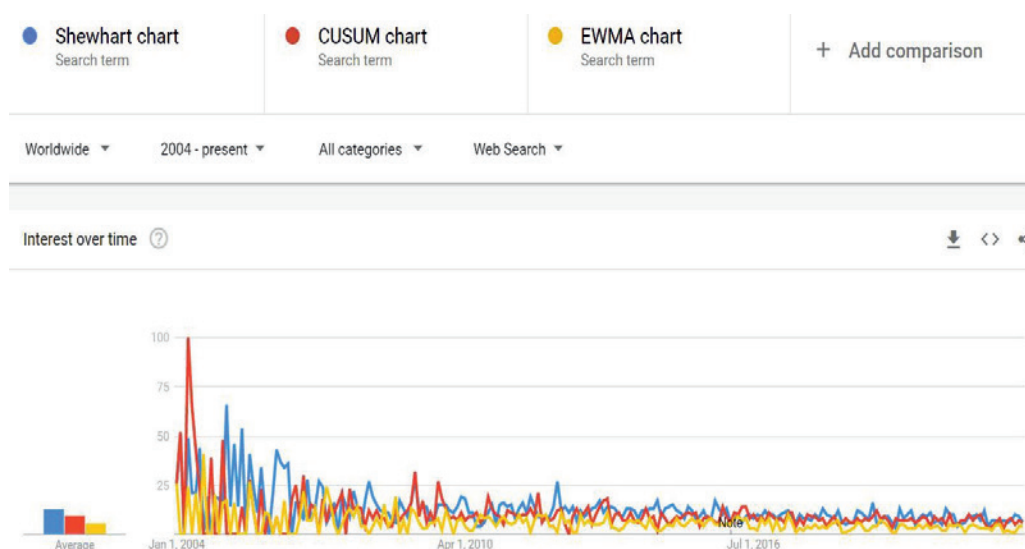
effectively. This analysis will draw upon both historical studies and recent research findings.

## CURRENT STATUS OF SHCCs USE

Upon first review, the use of ShCCs seems to be quite straightforward, finding application across diverse sectors such as metallurgy, automotive, semiconductor manufacturing, aviation, agriculture, government, health-care, and education.

ShCCs, as part of statistical process control (SPC), are widely cited in scholarly works [3 – 6], ranging from foundational texts that are considered classics to contemporary studies [7 – 10]. They are also supported by international standards like those mentioned in [11] and various online resources that provide instructions for their use.

However, there are at least two problems that cannot let us say “Everything is OK!” in the area of ShCCs. One notable issue is the declining interest in ShCCs among statisticians and industry professionals, as evidenced by the information depicted in Fig. 1 and a decrease in the volume of related scholarly publications in esteemed journals. The paper [12] recently addressed this topic.



**Fig. 1.** Dynamics of internet requests to ShCCs and two its competitors (cumulative charts and charts with exponentially weighted moving average) throughout the World since 2004

**Рис. 1.** Динамика интернет-запросов по ККШ и двум конкурирующим с ними инструментам (кумулятивным картам и картам с экспоненциально-взвешенным скользящим средним) в мире с 2004 г.

Part of this issue can be attributed to the formal and bureaucratic procedures for implementing ShCCs mandated by some international standards. Another concern is the noticeable scarcity of new research on ShCCs that goes beyond the conventional models of basic control charts. Our critique does not concern the creation of new types of charts – there is plenty of innovation in that area. Instead, we highlight the need for expanding the applications of charts beyond the traditional assumptions of ShCCs theory. Here are a few uncommon examples of such research. In 2011, the study “Assignable causes of variation and statistical models: another approach to an old topic” was published [13]. The authors, one of whom is a co-author of this article, suggested dividing the assignable causes of variation into two categories: those caused by an intervention with the same distribution function (DF) as the original process and those with a different DF. While the former approach has been used in all prior studies, the latter presents an operating characteristic (the probability of a point exceeding the chart limits) that significantly deviates from what is described in textbooks. The 2017 publication [14] brought up the significant issue regarding the sequence of points, highlighting that processes with random data are nearly non-existent. However, current ShCCs theory assumes that process data are completely random. In 2021, a paper was released detailing the effects of a transient shift in the process mean on ShCCs behavior [15]. The findings demonstrated that in cases of a transient shift, the chart for the mean might become less effective compared to the chart for individual values. This contradicts all standard SPC guidelines. These examples represent just a small fraction of the potential for broadening the scope of traditional ShCCs applications by challenging the assumptions that have underpinned standard models for decades.

This work further extends the exploration of traditionally overlooked conditions. This time, we will move beyond the common assumption that process parameters are normally distributed and will discuss several implications of this departure. Additionally, we will examine various types of assignable causes of variation and their effects on the utilization of ShCCs.

## EFFECTS OF NON-NORMAL DISTRIBUTION ON SHCCS

### PERFORMANCE

This section is divided into two parts. Firstly, we will examine whether measurement results are always normally distributed. Secondly, we will show how the limits of ShCCs change when the DF is non-normal and will describe the most user-friendly method to address this issue.

***Are the measurement results always normally distributed?*** This assumption is widely accepted

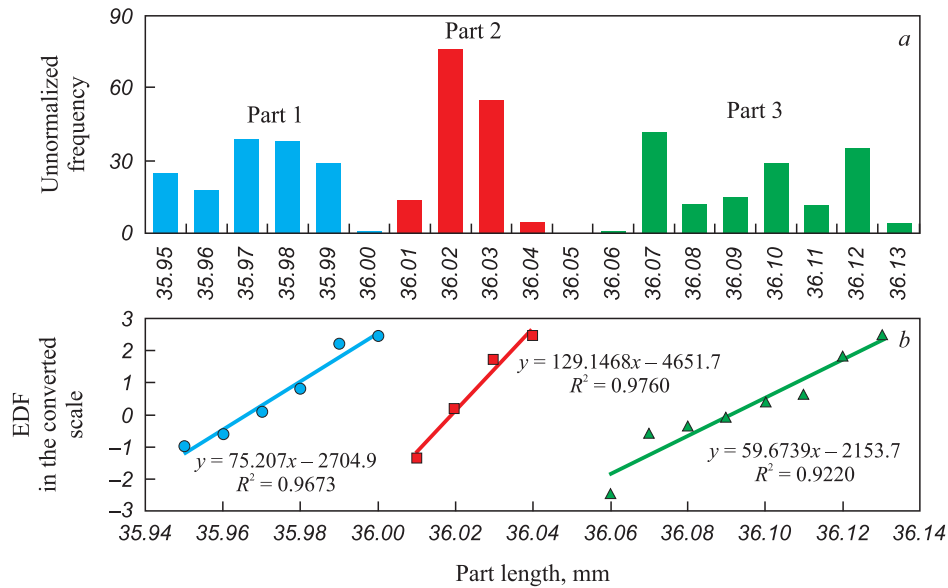
by numerous authors, texts, and even standards. For example, the standard [11] articulates: “According to this standard, the application of control charts for quantitative data presumes that the characteristic under surveillance adheres to a normal (Gaussian) distribution, and deviations from this norm can influence the effectiveness of the charts. The coefficients for calculating control limits are predicated on a normal distribution of characteristics. Given that control limits frequently serve as empirical benchmarks in decision-making, *reasonably small deviations from normality are conceivable*. The central limit theorem posits that sample mean values tend toward a normal distribution, even if individual observations deviate from this norm. This supports the premise of normality for  $\bar{X}$ -charts, even with sample sizes as small as 4 or 5 units. However, for assessments of process capabilities using individual observations, the actual distribution is crucial. Although the distributions of ranges and standard deviations deviate from normality, the calculation of control limits for range and standard deviation charts initially assumed normality. Nevertheless, *minor deviations* from a normal distribution in process characteristics should not prevent the employment of such charts for empirical decision-making” (emphasis ours).

But what exactly constitutes “*reasonably small deviations from normality*” or “*minor deviations*”? These terms do not provide a clear definition of what extent of change in the distribution law is deemed significant [16]. Recent findings [17] offer an operational definition for these terms and an algorithm for constructing ShCCs under the clear presence of non-normal DF.

A common misconception about the universal applicability of the normal law is the belief that measurement results always follow a Gaussian curve. To empirically test this assumption, three parts from the same process but from different points within the tolerance range were each measured 150 times using the same instrument. The outcomes are depicted in Fig. 2. ShCCs for the parts indicated that the processes for the first and second parts were stable, whereas for the third part, just three distinct categories were identified. All histograms were noticeably non-normal, and the hypothesis of normality was conclusively disproven through the testing procedure outlined in [18]. Therefore, it is reasonable to argue that the results of repeated measurements might not adhere to the normal distribution, akin to the measurement outcomes of various objects.

***How does non-normality of DFs affect ShCCs coefficients?*** Numerous DF processes markedly deviate from the Gaussian law. The question arises: how can the stability of such processes be assessed when a control chart is the sole instrument for ascertaining process stability? The study [17] offers an exhaustive literature review alongside the outcomes of simulating asymmetric data. It contrasts the results of analyzing non-normal data





**Fig. 2.** Histograms and empirical distribution functions (DFs) for many repeated measurements

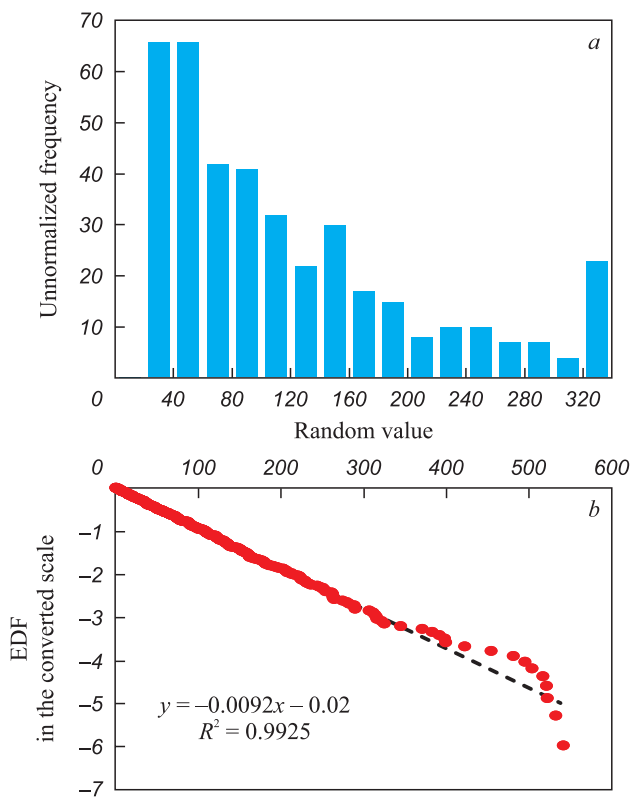
**Рис. 2.** Гистограммы и эмпирические ФР для многократных повторных замеров

through both the conventional method and the algorithm introduced in [17]. The conventional method adheres to the declaration cited from the standard [11]. Yet, what will empirical evidence disclose?

Initially, 400 samples of random numbers following an exponential distribution with the parameter  $\lambda = 0.01$  were generated, with each sample comprising 400 points. This was achieved by generating random numbers from a uniform distribution function using Excel, and then transforming these numbers by taking their logarithms and multiplying by  $(-100)$  to produce a set of exponentially distributed data samples.

The histogram for one of the generated samples is displayed in Fig. 3, *a*. Fig. 3, *b* illustrates the empirical DF on a probability plot for the exponential distribution. Both sections of Fig. 3 affirm that the sample's point distribution closely aligns with an exponential distribution<sup>1</sup>. The descriptive statistics parameters are as follows: the mean is 105.5; the standard deviation is 105.0; skewness is 1.82; kurtosis is 3.78 (Note: Excel 2013 calculates excess kurtosis); the minimum value is 0.51; the maximum value is 541.4; the median is 73.9; the first quartile is 31.1; the third quartile is 142.8; and the upper boundary for extreme outliers is determined to be 477.87, which allowed for the identification of eight extreme outlier (EO)<sup>2</sup> points (these are clearly visible in Fig. 3, *b*).

After removing EOs, the control chart for individual values and moving range ( $x-mR$ ) was created using stan-

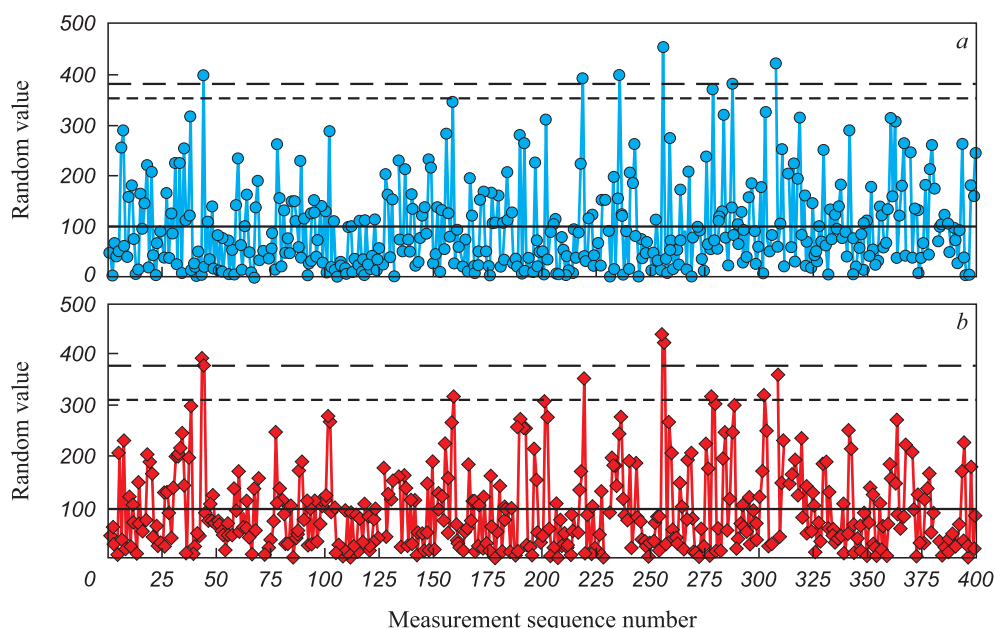


**Fig. 3.** Histogram (*a*) and empirical DF (EDF) (*b*) for simulated random data

**Рис. 3.** Гистограмма (*a*) и эмпирическая ФР (*b*) для смоделированных случайных данных

<sup>1</sup> Note to practitioners: When analyzing data, it's often unclear which distribution function (DF), if any, is appropriate to describe them. What should be done in such cases? Here's a solution: if the dataset contains more than 50 points, construct a histogram; if fewer, create a box-and-whisker plot. Often, these visual representations will indicate whether a normal approximation is feasible. Additionally, employing probability papers (such as normal, log-normal, or Weibull paper) can be beneficial help in some situations.

<sup>2</sup> The Tukey method was used to detect EOs, the coefficient 1.5 being replaced by 3.0.



**Fig. 4.** *x-mR* chart for simulated data:  
a – *x* chart; b – *mR* chart

**Рис. 4.** Карта *x-mR* для смоделированных данных:  
a – *x* карта; b – *mR* карта

dardized values of ShCCs coefficients [19]:  $E_2 = 2.66$ ;  $D_4 = 3.27$ . The resulting *x-mR* chart is depicted in Fig. 4, with the control limits illustrated by dashed lines. The process is identified as unstable, as seven points (representing 1.8 % of the total) in the chart for individual values (*x*) and nine points (accounting for 2.2 %) in the chart for moving range (*mR*) exceed the upper control limit (UCL). However, based on the findings in [17], the coefficient  $d_2$  for an exponential DF should be 2.99, not 2.66. The limit, recalculated using the revised coefficients, is also displayed in Fig. 4, marked by long dashes. It is observed that with this adjustment, only six points in the *x*-chart exceed the UCL. Similarly, on the *mR* chart, the count of points exceeding the upper control limit dropped to four from nine, nearly halving the number of signals. Therefore, in this scenario, the incidence of false alarms was reduced by 14 % on the chart for individual values and by 44 % on the moving range chart. Using a chart for medians, instead of means, would have produced identical outcomes.

In a second example, monthly data on the number of technological violations at a large mining and processing plant are presented in a Table.

The question arises: *Should the increased value in September be considered an assignable cause of variation, or in other words, is the process stable?*

To address this, an *x-mR* chart needs to be constructed. Using the traditional methodology for creating ShCCs, we obtain the following parameters for the chart: the center line (CL) is 20.7; the mean moving range (MMR) is 13.2; the UCL is 55.7. With the September value exceeding the UCL, it suggests that the process is unstable, and an interference cause should be identified. However, this conclusion comes from the traditional approach. The critical inquiry then is whether employing the traditional method was appropriate for this analysis.

Given the small sample size, a box-and-whisker plot was chosen over a histogram (Fig. 5). This plot clearly indicates that the data are asymmetric. The question then arises: Is this level of deviation from normality significant? One method to address this question involves calculating the skewness and kurtosis values. Excel reports skewness as 2.0 and kurtosis as 4.7. However, Excel calculates excess kurtosis, meaning the actual kurtosis value is 7.7. According to [17], for kurtosis values exceeding 7.0 –

#### Violations of technological discipline at the plant

#### Нарушения технологической дисциплины на комбинате

Dynamics of technology violations for the year											
January	February	March	April	May	June	July	August	September	October	November	December
13	14	8	11	14	8	33	24	60	15	22	26

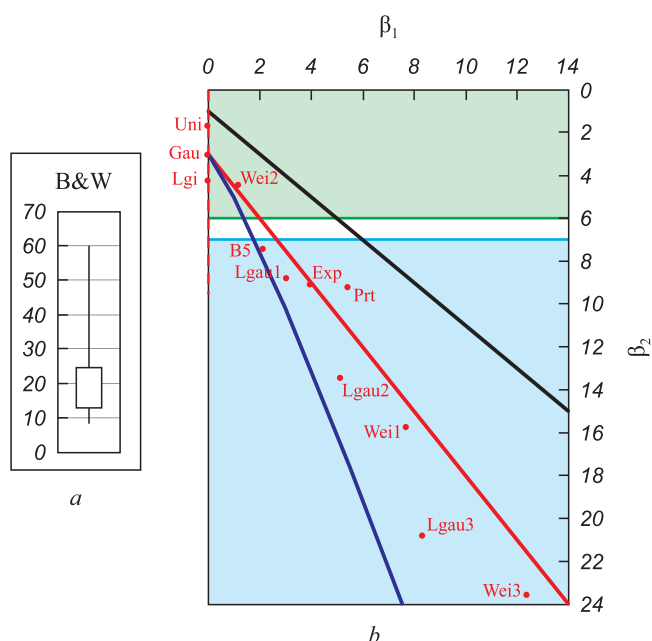


Fig. 5. Box-and-whisker plot for Table data (a) and Pearson curve plane from [17] (b)

Рис. 5. Ящик-с-усами для данных таблицы (a) и плоскость кривых Пирсона из работы [17] (b)

when the specific DF matching our data is unknown – it is recommended to use the coefficient value for the closest point on the plane of Pearson curves (Fig. 5, b). For the data in question, the nearest point is B5, corresponding to the Barr DF. The  $E_2$  value for this DF = 2.81 and adjusted UCL = 57.7 [17]. Therefore, the value for September still exceeds the UCL, leaving the assessment of process stability unchanged. However, if the data had been closer to an exponential distribution (for example, if the kurtosis were about 9), then the adjusted coefficient would be 2.99, the adjusted UCL would become 60.1, and the process would be considered stable, indicating no assignable causes of variation on the chart.

These examples demonstrate an important aspect of the ShCCs that is often overlooked by many scholars and not fully grasped by practitioners: ShCCs are the tool that necessitates direct interaction with the process. The construction of the ShCCs cannot be entirely reduced to an algorithm [20]. To use ShCCs effectively, one must possess a deep understanding of the process's nuances as well as a solid grasp of control chart theory. The authors claim that the absence of such a synergistic approach is likely the main reason why this potent tool frequently fails to give a practitioner a helping hand.

## REFLECTIONS ON PROCESS STABILITY AND ANALYSIS TECHNIQUES

As mentioned earlier, the Shewhart control chart is the only tool for determining process stability. However, different types of instability necessitate varied responses. Let us examine the process shown in Fig. 6, which comes from a real case with data collected from a machine-building plant in Russia. The manufacturing technology for the part being monitored did not change at all during the period of observation, and the production system remained the same. Fig. 6 illustrates that all manufactured parts met tolerance requirements (there were no rejections), which means the customer's standards were met. From the perspective of process stability, let us examine the subject first through the eyes of an engineer unfamiliar with SPC procedures, whom we will refer to as a novice, and then from the standpoint of a user well-versed in SPC methods, referred to as an expert.

A novice, without hesitation, will analyze all available data and derive the  $x\text{-}mR$  chart as illustrated in Fig. 7. The CL will be calculated at 40.865, the UCL at 40.913, and the lower control limit (LCL) at 40.817. This chart suggests that the process exhibits instability (with one point exceeding the UCL and four points surpassing the  $UCLmR$  on the  $mR$  chart). Alternatively,

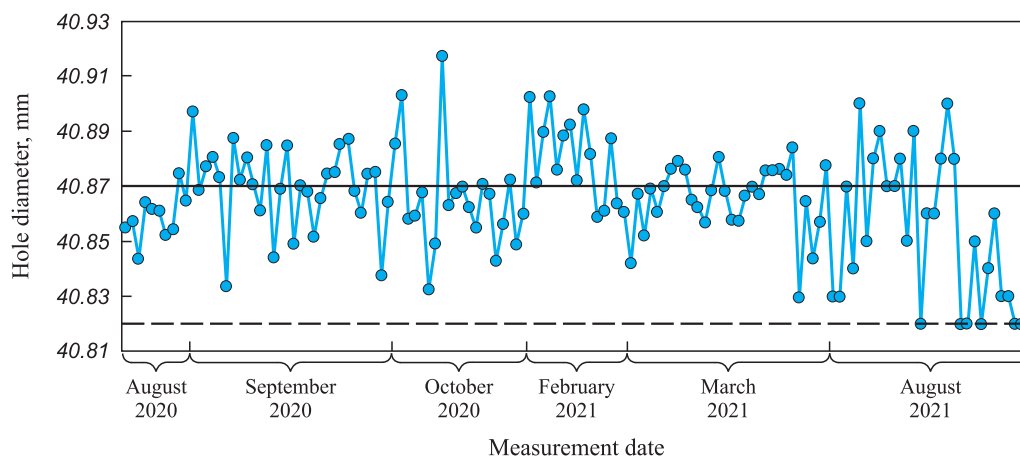


Fig. 6. Run chart for the hole diameter  $40.87 \pm 0.05$

Рис. 6. Карта хода процесса для отверстия диаметром  $40,87 \pm 0,05$

it could be interpreted that the process was stable during August and September 2021 and in March 2022 but entered a phase of instability in October 2021 and again in March 2022. For the novice, computing the Process Capability Index (PCI) also presents no challenge:  $C_p$  will be equal to 1.04 (0.1 divided by 6 sigma, with sigma being the mean moving range divided by  $d_2$ ). A  $C_p$  value of 1.04 equates to a potential non-conformity level (NL) of 0.18 % or a process yield (PY) of 99.82 %.

An expert would observe that the process is distinctly heterogeneous and recommend its division into homogeneous segments for more accurate analysis. This approach of stratification is depicted in Fig. 8, where four segments are identified, each with distinct CL values and control limits:

Section 1: August – October 2020.

CL = 40.8665; CLmR = 0.0173; UCL = 40.9124; LCL = 40.8206; UCLmR = 0.0564.

Section 2: February 2021.

CL = 40.8830; CLmR = 0.0189; UCL = 40.9331; LCL = 40.8329; UCLmR = 0.0616.

Section 3: March 2021.

CL = 40.8662; CLmR = 0.0123; UCL = 40.8990; LCL = 40.8334; UCLmR = 0.0403.

Section 4: end of March and August 2021.

CL = 40.8537; CLmR = 0.0256; UCL = 40.9218; LCL = 40.7856; UCLmR = 0.0837.

The PCI values for each section are as follows: section 1:  $C_p = 1.09$ ; section 2:  $C_p = 1.00$ ; section 3:  $C_p = 1.53$ ; section 4:  $C_p = 0.73$ . Calculating NL for each section yields values ranging from 4.7 to 27,525 ppm. Given such a jaw-dropping difference, two pressing questions arise:

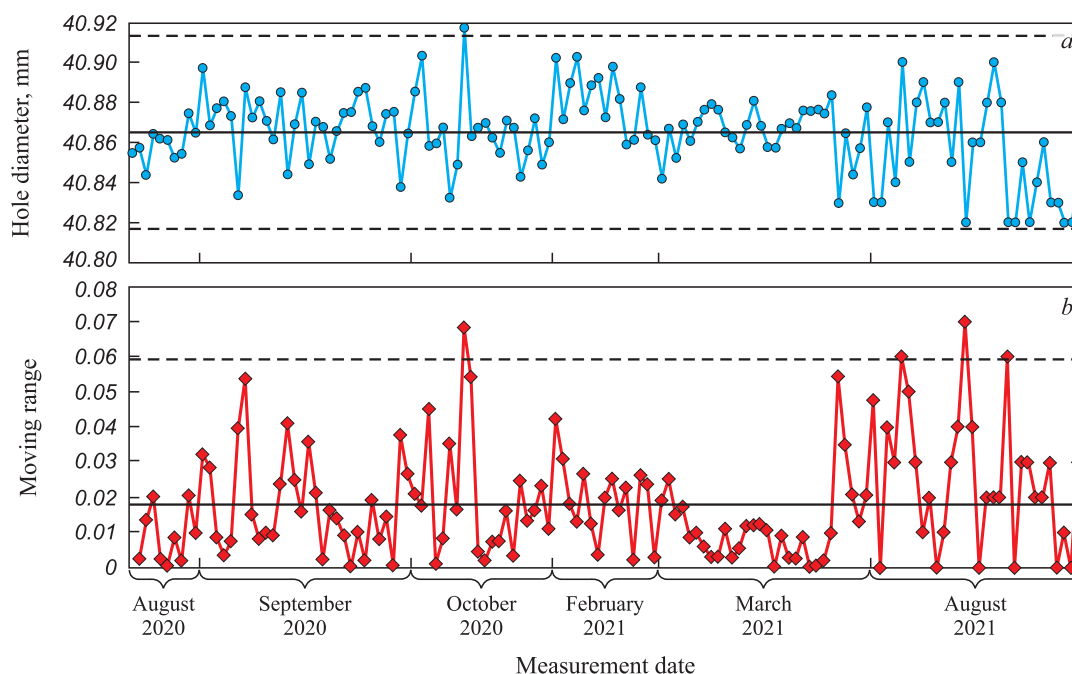
– Which analytical method is most appropriate for process improvement?

– How should the stability of such a process be interpreted?

Let us address the latter question first.

## VARIOUS FORMS OF PROCESS INSTABILITY

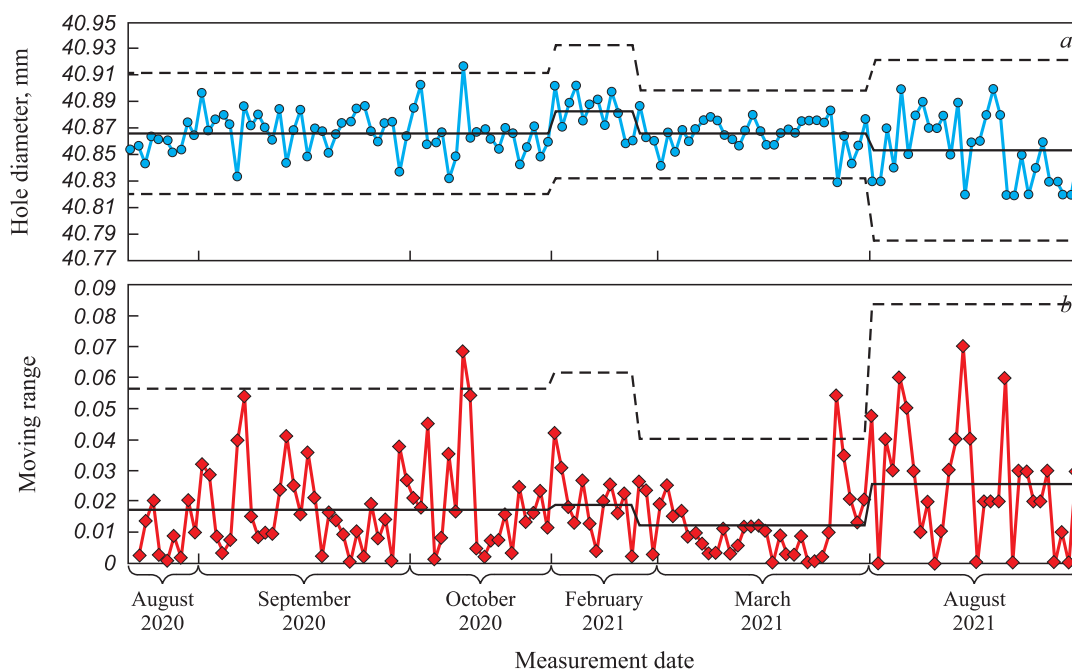
It's clear that instability can manifest itself in various forms. Dr. Deming highlighted this distinction in his introduction to Shewhart's 1939 book [2]: "A significant contribution of the control chart lies in its ability to methodically differentiate variation sources into two categories: (1) systemic causes ("change causes", as Dr. Shewhart termed them), which fall under management's purview; and (2) assignable causes, referred to by Deming as "special causes", which are tied to transient events and can typically be identified and eliminated by the process expert. A process is deemed to be in statistical control when it is free from the impact of special causes. Such a process, once in statistical control, exhibits predictable performance". Fig. 9, drawn from [21], explores various special causes of variation identified



**Fig. 7.**  $\bar{x}$ - $mR$  chart constructed by a novice:  
a – not stratified  $\bar{x}$  chart; b – not stratified  $mR$  chart

**Рис. 7.** Карта  $\bar{x}$ - $mR$ , построенная новичком:  
a – не стратифицированная  $\bar{x}$  карта; b – не стратифицированная  $mR$  карта





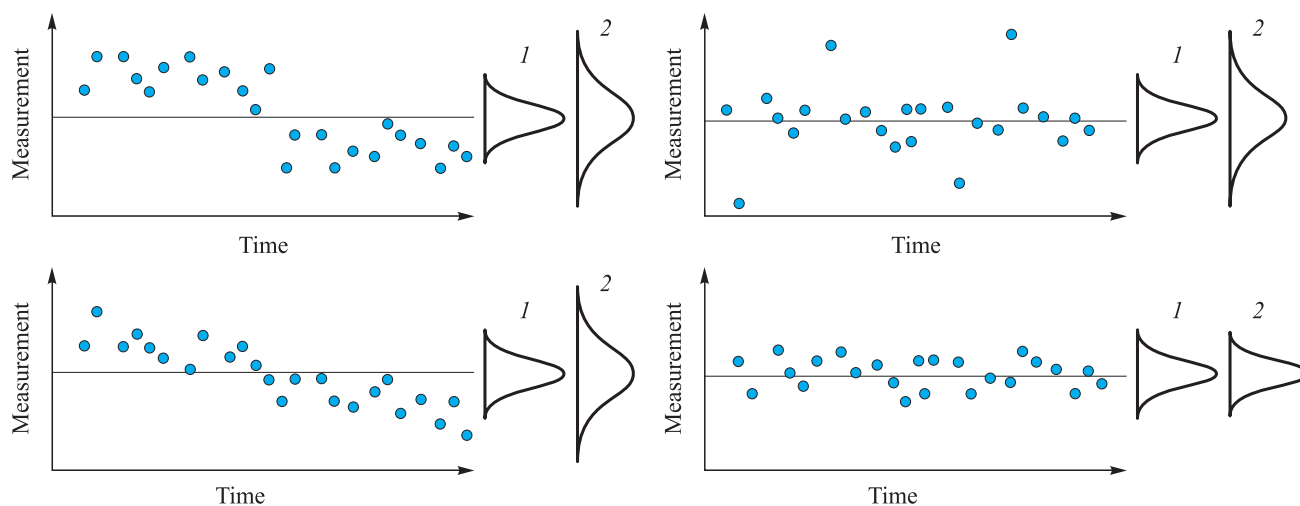
**Fig. 8.** *x-mR* chart constructed by an expert:  
a – stratified *x* chart; b – stratified *mR* chart

**Рис. 8.** Карта *x-mR*, построенная экспертом:  
a – стратифицированная *x* карта; b – стратифицированная *mR* карта

in different processes. In three of the four illustrations, a step change in the mean, outliers, and a drift in the mean are evident. However, only the illustration depicting outliers aligns with the “ephemeral event”. Deming mentioned in the previously quoted text. Deming wasn’t alone in this viewpoint. W. Woodall in the paper [22] provides this definition: “Common cause variation is attributed to the intrinsic characteristics of the process and cannot be modified without altering the process itself.

“Assignable (or special) causes” of variation are unusual shocks or other disruptions to the process, the causes of which can and should be removed”.

The two left images in Fig. 9 indicate that the process underwent a change due to some cause. The question arises: Is this cause common or assignable? Given that common causes are regarded as “constant” (a term used by Shewhart in his works [1; 2]) and inherent to the process itself, the causes for the variation seen in the left



**Fig. 9.** Different types of variation:  
1 – short-term; 2 – long-term

**Рис. 9.** Различные типы вариаций:  
1 – кратковременная; 2 – долговременная

part of Fig. 9 should be classified as assignable. However, these causes differ from outliers and other transient events. Thus, it appears suitable to acknowledge different types of assignable (special) causes. In reference [13], the authors suggest introducing two types of assignable causes of variation. After slightly altering the language of [13], we propose the following definitions:

**Definition 1.** An assignable cause of variation, Type *I* (*Intrinsic*) does not alter the system within which the process functions (for example, it does not change the type of the underlying DF). As a result, this kind of assignable cause can be naturally perceived as part of the system (though this is not a strict requirement).

**Definition 2.** An assignable cause, Type *X* (*eXtrinsic*) modifies the system in which the process operates (for example, it changes the type of the underlying DF). Consequently, this kind of assignable cause can be naturally viewed as external to the system (though this, too, is not an absolute necessity).

If the scientific community agree with this idea, the distinction between a novice and an expert will boil down to understanding the nuances between various types of assignable causes. Regardless, the process under study is unstable. However, the different forms of instability are fundamentally distinct. When confronted with Type *I* instability, it is crucial to search for the root causes of interference within the system. This responsibility should fall to the process team, as they possess deep insights into the process and system. Conversely, when dealing with Type *X* instability, identifying the root cause outside the system becomes necessary. Dr. Deming often stated, “A system must be managed; it will not manage itself” [23]. In such instances, the senior management responsible for overseeing the system as a whole should undertake the search for root causes.

#### WHICH ANALYSIS METHOD IS MORE SUITABLE FOR PROCESS IMPROVEMENT

The answer is obvious – it relies on the specific goal and current condition of the process. Each approach may be effective in one context yet ineffective in another, a notion that circles back to the initial discussion in the article. Technically, ShCCs might seem elementary, yet their practical use is more complex. Even a grade school student might grasp the basic formulas for chart parameter calculations. But proper use of ShCCs requires a deep understanding of the analyzed process and a keen awareness of the many assumptions and limitations that come into play in practical settings. Moreover, it demands the integration and effective application of knowledge from diverse areas. Collaborative efforts often lead to the most successful outcomes with ShCCs. We agree with the statement expressed in [12]: to get closer to G. Wells’ vision that statistical thinking

is as vital for competent citizenship as literacy, statistical thinking should be incorporated early in educational programs. This means that ShCCs fundamentals should be included in the elementary school curriculum.

#### CONCLUSIONS

Our examination of the usage of ShCCs has revealed that, despite their widespread use, several challenges obstruct their more effective practical application. To address some of these challenges, we suggest:

- ignoring the standard assumption that data are normally distributed when analyzing measurement systems;
- using alternative constants to calculate ShCCs control limits when it is evident that process data are non-normal;
- adopting a new method for identifying assignable causes of variation.

Implementing these recommendations could significantly refine the application of ShCCs, leading to more accurate decisions when analyzing real data and, therefore, enhancing the management quality of the processes in question.

Our research revealed a significant insight: the proper deployment of ShCCs cannot be algorithmized automatically. A deep understanding of the process details and additional analyses, such as understanding the distribution function or the sequencing of data points, is essential. This understanding is crucial for choosing the right sections of the process, deciding on the chart type, setting the length of phase 1, or picking the right coefficients for calculating control limits. Such understanding can’t be programmed into statistical software; it comes from the interaction between the person managing the process and the process itself.

We hope that this article will help convey a straightforward yet overlooked point: the Shewhart control chart may seem simple as an SPC tool, but that simplicity is deceptive. To use it effectively, one needs a thorough understanding of the process and solid knowledge of the theories underlying variability.

#### REFERENCES / СПИСОК ЛИТЕРАТУРЫ

1. Shewhart W. Economic Control of Quality of Manufactured Product. Milwaukee: ASQ Quality Press.; 1980:501.
2. Shewhart W. Statistical Methods from the Viewpoint of Quality Control. N.Y.: Dover Publications, Inc.; 1986:163.
3. Kume H. Statistical Methods for Quality Improvement. The Association for Overseas Technical Scholarship (AOTS); 1985:231.
4. Wheeler D. Advanced Topics in Statistical Process Control. Knoxville: SPC Press, Inc.; 1995:484.
5. Alwan L.C. Statistical Process Analysis. Irwin: McGraw-Hill series in operations and decision sciences; 2000:768.

6. Rinne H., Mittag H.-J. Statistische Methoden der Qualitätssicherung. Fernuniversität-Gesamthochschule-in-Hagen, Deutschland, Fachbereich Wirtschaftswissenschaft; 1993: 615. (In Germ.).
7. Schindowski E., Schürz O. Statistische Qualitätskontrolle. Berlin: Veb Verlag Technik; 1974:636. (In Germ.).
8. Murdoch J. Control Charts. The Macmillan Press, Ltd; 1979:150.
9. Montgomery D.C. Introduction to Statistical Quality Control. 6<sup>th</sup> ed. John Wiley & Sons; 2009:752.
10. Balestracci D. Data Sanity: A Quantum Leap to Unprecedented Results. Medical Group Management Association; 2009:326.
11. ISO 7870-2:2013. Control Charts – part 2: Shewhart Control Charts.  
ГОСТ Р ИСО 7870-2-2015. Статистические методы. Контрольные карты. Часть 2. Контрольные карты Шухарта. М.: ФГУП «СТАНДАРТИНФОРМ»; 2016:46.
12. Шереметьева С.А., Шпер В.Л. Бизнес и теория вариативности: дружба или непонимание. *Стандарты и качество*. 2022;(2):92–97.  
<http://doi.org/10.35400/0038-9692-2022-2-72-21>  
Sheremetyeva S.A., Shper V.L. Business and variation: friendship or misunderstanding. *Standards and Quality*. 2022;(2):92–97. (In Russ.).  
<http://doi.org/10.35400/0038-9692-2022-2-72-21>
13. Adler Y., Shper V., Maksimova O. Assignable causes of variation and statistical models: Another approach to an old topic. *Quality and Reliability Engineering International*. 2011;27(5):623–628. <https://doi.org/10.1002/qre.1207>
14. Shper V., Adler Y. The importance of time order with Shewhart control charts. *Quality and Reliability Engineering International*. 2017;33(6):1169–1177.  
<http://doi.org/10.1002/qre.2185>
15. Shper V., Gracheva A. Simple Shewhart control charts: Are they really so simple? *International Journal of Industrial and Operations Research*. 2021;4(1):010.  
<http://doi.org/10.35840/2633-8947/6510>
16. Deming W. Out of Crisis. Cambridge, Massachusetts: The MIT Press; 1987:524.
17. Shper V., Sheremetyeva S. The impact of non-normality on the control limits of Shewhart's charts. *Тяжелое машиностроение*. 2022;(1–2):16–29.  
Shper V., Sheremetyeva S. The impact of non-normality on the control limits of Shewhart's charts. *Tyazheloye Mashinostroyeniye*. 2022;(1–2):16–29.
18. Ryan T.A., Joiner B.L. *Normal Probability Plots and Tests for Normality*. Available at: <https://www.additive-net.de/de/component/jdownloads/send/70-support/236-normal-probability-plots-and-tests-for-normality-thomas-a-ryan-jr-bryan-l-joiner>
19. Wheeler D.J., Chambers D.S. Understanding Statistical Process Control. 2<sup>nd</sup> ed. Knoxville: SPC Press, Inc.; 1992:428.  
Уилер Д., Чамберс Д. Статистическое управление процессами. Оптимизация бизнеса с использованием контрольных карт Шухарта. Москва: Альпина Бизнес Букс; 2009:409.
20. Адлер Ю.П. Алгоритмически неразрешимые задачи и искусственный интеллект. *Экономика и управление: проблемы, решения*. 2018;7/77(5):17–24.  
Adler Yu.P. Algorithmically unsolvable problems and artificial intellect. *Economics and management: problems, solutions*. 2018;7/77(5):17–24. (In Russ.).
21. Jensen W., Szarka J. III, White K. A better picture. *Quality Progress*. 2020;53(1):41–49.
22. Woodall W. Controversies and contradictions in statistical process control. *Journal of Quality Technology*. 2000;32(4):341–350.  
<https://doi.org/10.1080/00224065.2000.11980013>
23. Deming W. The Essential Deming. Leadership Principles from the Father of Quality. Orsini J. ed. N.Y.: McGraw-Hill; 2013:336.

## Information about the Authors

## Сведения об авторах

**Vladimir L. Shper**, Cand. Sci. (Eng.), Assist. Prof. of the Chair of Certification and Analytical Control, National University of Science and Technology "MISIS"

E-mail: [vlad.shper@gmail.com](mailto:vlad.shper@gmail.com)

**Svetlana A. Sheremetyeva**, Postgraduate of the Chair of Certification and Analytical Control, National University of Science and Technology "MISIS"

E-mail: [prosto\\_sveta92@mail.ru](mailto:prosto_sveta92@mail.ru)

**Vladimir Yu. Smelov**, Cand. Sci. (Eng.), Assist. Prof. of the Chair of Certification and Analytical Control, National University of Science and Technology "MISIS"; Technical Director, GPB Complect (JSC)

ORCID: 0000-0002-9438-4054

E-mail: [b.c.21@mail.ru](mailto:b.c.21@mail.ru)

**Elena I. Khunuzidi**, Cand. Sci. (Eng.), Assist. Prof. of the Chair of Certification and Analytical Control, National University of Science and Technology "MISIS"; Head of Division of Quality Assurance, LLC "Atom-TekhnTest"

ORCID: 0000-0002-2396-6911

E-mail: [el\\_hun@mail.ru](mailto:el_hun@mail.ru)

**Владимир Львович Шпер**, к.т.н., доцент кафедры сертификации и аналитического контроля, Национальный исследовательский технологический университет «МИСИС»

E-mail: [vlad.shper@gmail.com](mailto:vlad.shper@gmail.com)

**Светлана Алексеевна Шереметьева**, аспирант кафедры сертификации и аналитического контроля, Национальный исследовательский технологический университет «МИСИС»

E-mail: [prosto\\_sveta92@mail.ru](mailto:prosto_sveta92@mail.ru)

**Владимир Юрьевич Смелов**, к.т.н., доцент кафедры сертификации и аналитического контроля, Национальный исследовательский технологический университет «МИСИС»; технический директор, «ГПБ Комплект» (АО)

ORCID: 0000-0002-9438-4054

E-mail: [b.c.21@mail.ru](mailto:b.c.21@mail.ru)

**Елена Ивановна Хунузиди**, к.т.н., доцент кафедры сертификации и аналитического контроля, Национальный исследовательский технологический университет «МИСИС»; руководитель отдела по обеспечению качества, ООО «АтомТехноТест»

ORCID: 0000-0002-2396-6911

E-mail: [el\\_hun@mail.ru](mailto:el_hun@mail.ru)

## Contribution of the Authors

## Вклад авторов

**V. L. Shper** – formation of the basic concept, research goal and objectives; formulation of conclusions.

**S. A. Sheremetyeva** – planning and making simulation, calculations, revision of the text.

**V. Yu. Smelov** – writing the text, graphic design, discussion of conclusions.

**E. I. Khunuzidi** – scientific guidance, analysis of results, correction of conclusions.

**В. Л. Шпер** – формирование основной концепции, цели и задачи исследования, формирование выводов.

**С. А. Шереметьева** – планирование и выполнение численного моделирования, проведение сопутствующих расчетов, доработка текста.

**В. Ю. Смелов** – подготовка текста, оформление графических материалов, обсуждение выводов.

**Е. И. Хунузиди** – научное руководство, анализ результатов исследований, корректировка выводов.

Received 04.03.2023

Revised 20.11.2023

Accepted 11.12.2023

Поступила в редакцию 04.03.2023

После доработки 20.11.2023

Принята к публикации 11.12.2023



Над номером работали:

Л.И. Леонтьев, главный редактор

Е.В. Протопопов, заместитель главного редактора

Е.А. Ивани, заместитель главного редактора

Л.П. Бащенко, заместитель ответственного секретаря

Е.Ю. Потапова, заместитель главного редактора по развитию

О.А. Долицкая, научный редактор

Е.М. Запольская, ведущий редактор

А.О. Гашникова, ведущий редактор

В.В. Расенец, верстка, иллюстрации

Г.Ю. Острогорская, менеджер по работе с клиентами

---

Подписано в печать 25.02.2024. Формат 60×90 <sup>1</sup>/<sub>8</sub>. Бум. офсетная № 1.  
Печать цифровая. Усл. печ. л. 16,5. Заказ 19252. Цена свободная.

---

Отпечатано в типографии Издательского Дома МИСИС.  
119049, Москва, Ленинский пр-кт, д. 4, стр. 1.  
Тел./факс: +7 (499) 236-76-17



Features of iron foundry production in Belarus and its prospects

Possibilities of heat-power spraying of wet charge during formation of structural properties of agglomerated iron ore materials

Joint processing of perovskite and ilmenite concentrates. Part 1. Chemical-mineralogical (material) characteristics of perovskite and ilmenite concentrates

Mechanical properties and microstructure of Al-Mg (5052) alloy processed by equal-channel angular pressing (ECAP) with variation of ECAP routes and heat treatment

Effect of hydrogen on steels in hydrogen sulfide-containing and other environments at gas facilities

Improvement of the Cantor alloy's mechanical properties by alloying with niobium and zirconium

Structure and its defects in additive manufacturing of stainless steels by laser melting and electric arc surfacing

Influence of copper and silicon on phase transformations in the iron – carbon system

Experience in implementing machine learning to calculate the quality and production of agglomerate

Effect of yttrium additions on microstructure and corrosion resistance of Incoloy 825 alloy

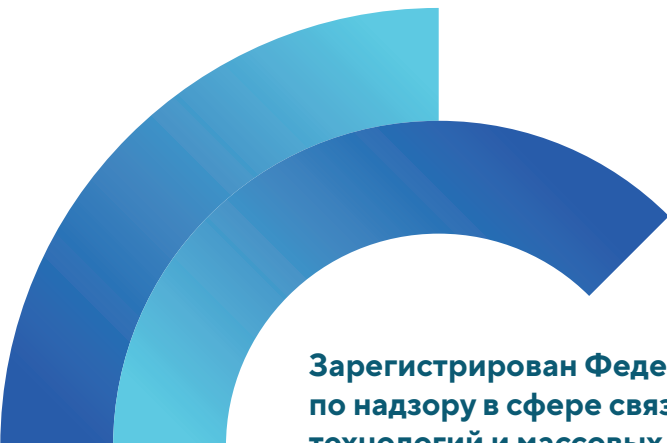
Investigation of performance limitations in continuous hot-dip galvanizing units associated with product defects

Investigating the effectiveness of changing calibration of input cone of rolls and lines of a piercing mill with tapered rolls using computer modeling

Mathematical modeling of gas dynamics and off-gas post-combustion above the melt in a melter-gasifier furnace

Shewhart control charts – A simple but not easy tool for data analysis

To the 100<sup>th</sup> Anniversary of Vuli Arshakovich Grogoryan



**Зарегистрирован Федеральной службой  
по надзору в сфере связи, информационных  
технологий и массовых коммуникаций.  
Свидетельство о регистрации  
ПИ № ФС77-35456.**

**Подписной индекс 70383.**

